A Theoretical Approach To The Prediction Of Haemolysis In Centrifugal Blood Pumps

by

Catrin Bludszuweit, Dipl.-Ing.

A thesis submitted in accordance with the regulations governing the award of the Degree of Doctor of Philosophy in Bioengineering.

Bioengineering Unit
University of Strathclyde
Glasgow; Scotland; UK

October 1994

Copyright Declaration

Abstract

The successful use of centrifugal pumps as temporary cardiac assist devices strongly depends on the extent to which they damage blood. The development of a theoretical pump evaluation model was performed in this study to facilitate an effective pump optimisation. The optimisation process seeks to maximise flow performance and minimise blood trauma which is primarily caused by hydrodynamic stresses. A general mechanical blood damage theory was developed which comprises a combination of the information about mechanical loading of blood with the knowledge of its resistance properties. In this theory arbitrary loading-time functions are reduced to simple loading functions for which the damage behaviour is known. A linear damage accumulation theory contributes towards the determination of partial damages and their correlation in the overall damage process.

The application of this novel blood damage prediction theory was demonstrated for haemolysis prediction in a commercial centrifugal blood pump. Particle loading-time functions were determined with a 3-dimensional numerical flow analysis of the entire pump domain by means of assigning scalar stress values to particle streaklines. Scalar stress values were obtained by a theory which enables the comparison of a six-component stress tensor with uniaxial stresses as applied in blood damage tests. It was shown that particles undergo a complex, irregularly fluctuating stress loading and that turbulent stresses and flow conditions in the outlet domain are the most critical factors.

Haemolysis tests using an oscillating capillary tube setup were performed to investigate blood damage resistance properties under cyclic stress loading in hitherto unexplored amplitude and frequency ranges. A non-linear damage curve for stress amplitude-cycle number was derived which indicated the existence of an endurance strength for red blood cells.

For the first time, detailed information about the mechanical loading of blood within a centrifugal pump has been obtained and linked to its traumatic effect. It offers the possibility for an effective, multi-parameter optimisation of blood pumps in the design phase.

Acknowledgements

I would like to express my sincerest gratitude to Dr. J.D.S. Gaylor for showing me how to approach medical-related problems from an engineering view point. His multi-talented and systematic approach, accuracy and critical assessment gave me strong motivation.

Thank you very much, John, for the attention and support you gave to this study as well as for your friendship.

I am very grateful to Professors J.P. Paul, J.C. Barbenel and J.M. Courtney who facilitated the conduction of these studies at the Bioengineering Unit. I appreciate your attention and understanding of the complicated situation of my stay, and for incorporating me into the scientific and social activities of the Department.

In the course of this project I received help and advice from many members of staff and students from the Bioengineering Unit for which I am very grateful.

In connection with my experimental work, I would like to mention Mrs. E. Smith, Dr. R. Wilkinson, Ms. C. Nugent and the members of the workshops.

I would like to thank all the secretaries, in particular Mrs. J.D. Wilson, for lending a helping hand on many occasions.

Numerous fruitful discussions and a kind and social atmosphere within the Bioengineering Unit provided excellent conditions for my studies.

This thesis incorporates the thoughts and cooperation of a variety of people outside the Bioengineering Unit:

The Abacus Division of the Architecture Department kindly allowed me access to their computer facilities and were always friendly hosts. I am extremely grateful especially to Mr. P.M. Grant who patiently assisted with my numerous enquiries and troubles, competently solved all kinds of hardware and software

related problems and was an invaluable partner for discussions.

I am indebted to ASC GmbH Holzkirchen, Germany, in particular, Dr. G. Scheuerer amd Mr. M. Britsch, for providing the CFD software and computer facilities for the numerical flow simulation.

I also received support from present and former staff and students of the Mechanical Engineering Department, in particular, Professor S.M. Fraser, Dr. Zhang Yi (Computational Fluid Dynamics), Mr. A. Cairney (Dynamics & Control Division) who provided the vibrator unit for the blood experiments and Mr. D.A. Johnson (Metallurgy) for fruitful discussions regarding physical phenomena and theories.

Special help and support in the experimental part of the project was provided by Dr. S. Hickey from Glasgow Royal Infirmary and Dr. B.F. McHugh from the National Centre for Training in Prosthetics and Orthotics.

I would like to thank St.Jude Medical and Sarns/3M for providing the blood pumps.

Financial support was given to me during the past years by The British Council, the Deutscher Akademischer Austauschdienst (DAAD) and the Stifterverband für die Deutsche Wissenschaft for which I am very grateful.

Many thanks to my friends in Glasgow and around the globe for giving me a warm social environment and for contributing to recharge my batteries.

The real home and origin of the presented work lies within my family. The selfless love, understanding, encouragement, help and inspiration I received from my parents, my brother Mark and my grandparents was the most valuable contribution to this thesis, I extend my love and gratitude to you. Your share will always be remembered.

To my dear parents to whom I owe so much.

The Doubter

Whenever we seemed
To have found the answer to a question
One of us untied the string of the old rolled-up
Chinese scroll on the wall, so that it fell down and
Revealed to us the man on the bench who
Doubted so much.

I, he said to us
Am the doubter. I am doubtful whether
The work was well done that devoured your days.
Whether what you said would still have value for anyone if it were less well said.
Whether you said it well perhaps
Were not convinced of the truth of what you said.
Whether it is not ambiguous; each possible misunderstanding
Is your responsibility. Or it can be unambiguous
And take the contradictions out of things; is it too unambiguous?
If so, what you say is useless. Your thing has no life in it.
Are you truly in the stream of happening? Do you accept
All that develops? Are you developing? Who are you? To whom
Do you speak? Who finds what you say useful? And, by the way,
Is it sobering? Can it be read in the morning?
Is it also linked to what is already there? Are the sentences that were
Spoken before you made use of, or at least refuted? Is everything verifiable?
By experience? By which one? But above all
Always above all else: how does one act
If one believes what you say? Above all: how does one act?

Reflectively, curiously, we studied the doubting
Blue man on the scroll, looked at each other and
Made a fresh start.

Bertolt Brecht

Contents

Nomenclature

A	–	*Light absorbance*
a	–	*Acceleration*
c_m	–	*Meridional velocity component*
D	–	*Damage*
	–	*Diameter*
E	–	*Young's modulus*
F	–	*Force*
fHb	–	*Plasma free haemoglobin concentration*
G	–	*Shear modulus*
g	–	*Gravitational acceleration*
H	–	*Pressure head*
Hct	–	*Haematocrit*
J_n	–	*Bessel function of first kind of order n*
K	–	*Bulk modulus*
L	–	*Length*
N	–	*Number of cycles*
n	–	*Number of cycles*
	–	*Rotational speed*
P	–	*Pressure*
p	–	*Pressure*
Q	–	*Flow rate*
R	–	*Radius*
r	–	*Radius*
r, ϕ, z	–	*Cylindrical coordinates*
S	–	*Stress*
	–	*Source term*

T – *Time (range, duration, period)*
t – *Time*
U – *Voltage*
U, V, W – *Velocity components*
u, v, w – *Velocity components*
V – *Volume*
W – *Work*
– *Resilience*
W_s – *Shear resilience*
x, y, z – *Cartesian coordinates*
x – *Displacement*
Y – *Yield criterion*
Y_n – *Bessel function of second kind of order n*

Γ – *Diffusion coefficient*
$\dot{\gamma}$ – *Shear rate*
δ – *Specific diameter*
ϵ – *Strain*
η – *Molecular dynamic viscosity*
μ – *Molecular dynamic viscosity*
μ_t – *Turbulent dynamic viscosity*
ν – *Kinematic viscosity*
– *Poisson's ratio*
ϱ – *Density*
σ – *Stress*
τ – *Shear stress*
Φ – *Transport variable*
ϕ – *Capacity coefficient*
ψ – *Head coefficient*
Ω – *Angular velocity*
ω – *angular velocity*

List of Figures

List of Tables

Chapter 1

Introduction

'The medical man, indeed, is the engineer pre-eminently; for it is in the animal body that true perfection and the greatest variety of mechanisms are found' [1]. This concept of engineering postulated in 1827 by the Scottish physician, Neil Arnott, bears no similarity to that found in any encyclopedia. The body with its complex structure and function must be regarded as a most successful design. It can, however, be subject to 'failure'. The desire to repair such 'failures' has led to a strong interaction of surgeons and physicians with scientists and engineers. This interdisciplinary liaison is particularly important in the new area of design, production and application of artificial devices which perform the functions of body organs.

The heart is an important part of the cardiovascular system and often subject to dysfunction and failure through disease. Cardiovascular diseases are still the major cause of death in the western world. In the USA 2.3 million people were reported in 1988 to be suffering from chronic heart failure with the number being on the rise [2]. Treatment of cardiac failure in particular has often been made possible by an enormous progress in medical and bioengineering research in the last quarter century. The number of heart operations per year in the UK more than doubled from 11,000 in 1977 to 26,000 in 1991 with a concomitant decrease in mortality rate from 9.8 % to 5.4 % [3]. The nature of the treatment will depend on whether the heart dysfunction is reversible or irreversible. With

the irreversibly damaged heart replacement by a donor organ transplant is the most effective solution and ranks second to kidney transplantation with respect to long-term survival. However, only a small proportion of patients requiring transplants can be treated as demand greatly exceeds supply. Implantable artificial hearts offering an alternative approach and have been the subject of intensive studies [4]. Although the first implantation of a pneumatically driven artificial heart was undertaken in 1957 by Kolff and Akutsu [5], relatively reliable devices were not available until the late 1980s [6]. Apart from these long-term mechanical blood pumps, temporary heart replacement or assist devices are needed in the treatment of reversible heart failure, as a bridge to transplantation and for extracorporeal perfusion techniques, in particular, haemodialysis and cardiopulmonary bypass. Membrane type pumps imitating the natural heart's structure and function and rotary blood pumps represent the two major groups of current heart replacement or assist devices. A variety of different pumping principles employing a rotating mechanism have been realised; the most common being roller and centrifugal types. These designs dominate the field of short-term extracorporeal circulation due to their relatively low cost and ease of handling and operation.

The replacement of physiological functions by artificial blood pumps has to go hand in hand with the maintenance of the biological equilibrium of the body. Blood, which is in direct contact with the mechanical device, should be allowed to be altered only to a physiologically 'repairable' degree. Blood trauma can be caused by a variety of factors, including abnormal biochemical or physical conditions. In artificial organs like blood pumps, hydrodynamic stresses play a major role in the blood damage process [7]. Centrifugal blood pumps have a particularly high potential for blood trauma due to their high level of energy transmission from the rotor to the blood. An assessment of blood pumps requires the evaluation of hydraulic parameters as well as their haematological interaction.

In the development phase, haematological characteristics are usually determined by measuring blood destruction in *in-vitro* tests or in animal tests. This

leads to an iterative process between experimental pump evaluation and design improvement before the design is finalised, an approach which is extremely costly both in materials and time. It also considers the pump in terms of its traumatic characteristics as a 'black box', thus preventing a mechanistic approach to optimisation.

An optimal design of a mechanical assist or replacement device for the heart has not been realised so far, partly because of the inability of purely empirical methods to account for the complex haemodynamic and hydrodynamic requirements.

An effective optimisation procedure which seeks to maximise flow performance and minimise blood trauma should be incorporated into the design phase. A combination of a powerful pump flow analysis with a numerical optimization technique is seen as an appropriate way to address these issues. The quantification of blood destruction under particular flow conditions and the optimization of responsible design parameters requires the knowledge of their functional relationship.

Chapter 2 will review current blood pump designs, concentrating on the centrifugal pump type, and include assessment of their haematological and hydrodynamic performances. Present mechanical blood damage theories will be discussed. It will be shown that neither a detailed flow analysis of centrifugal blood pumps nor an appropriate model to relate flow characteristics to blood destruction have been reported in literature.

As a consequence, the formulation of a complex and comprehensive model for mechanically-induced blood trauma will be undertaken in this thesis. It enables the relation of an arbitrary mechanical loading function to damage resistance properties of the blood and results in an overall damage prediction considering cumulative effects of damage caused by single loading functions.

The application of this theory will be demonstrated for a centrifugal blood pump. The required information about stress-loading functions of blood components on their passage through the pump will be obtained by a 3-dimensional

Computational Fluid Dynamics (CFD) analysis of the entire stator-rotor configuration.

A detailed description of the objectives of this thesis and solution strategies is given in Chapter 3.

The application of the methodology for the damage prediction is not restricted to the case of centrifugal blood pumps. The generality of the proposed theory would allow a new approach towards a satisfactory solution to any kind of flow related blood destruction problem. Haematological complications caused by a variety of artificial devices (e.g. blood oxygenators, haemodialysers, heart valves), and by abnormalities in the natural circulation (e.g. stenosis, aneurysms) could also be theoretically predicted and reduced on a well-defined and systematic basis.

Chapter 2

State of the Art

2.1 Centrifugal Blood Pump Designs

The human heart functions as a muscular pump pushing blood through the pulmonary and systemic circulation. Carrying out this function by an artificial device in the event of total or partial cardiac failure requires the production of a similar cardiac output sufficient to maintain blood flow against the circulatory resistance.

Different kinds of artificial blood pumps with specific pumping principles have been developed for this purpose. Besides the 'physiological' membrane pump and the intra-aortic balloon pump, rotary blood pumps offer another alternative. This group includes the simple roller pump [8], the spindle pump [9], the eccentric rotor pump [10, 11] and the nutational pump [12, 13] as well as rotary impeller pumps with axial, mixed and radial flow directions (Fig 2.1).

In all pumps energy is transmitted from the moving parts to the fluid and appears as an increase in either velocity or pressure. In radial centrifugal pumps with axial inflow and radially directed outflow the pressure rise between inflow and outflow is mainly produced by centrifugal force. Additionally, the kinetic energy of the fluid due to its circumferential velocity can be converted into a pressure rise by means of a diffuser. The recovery of the kinetic energy imparted to the fluid in form of pressure in the exit diffuser creates the pressure head

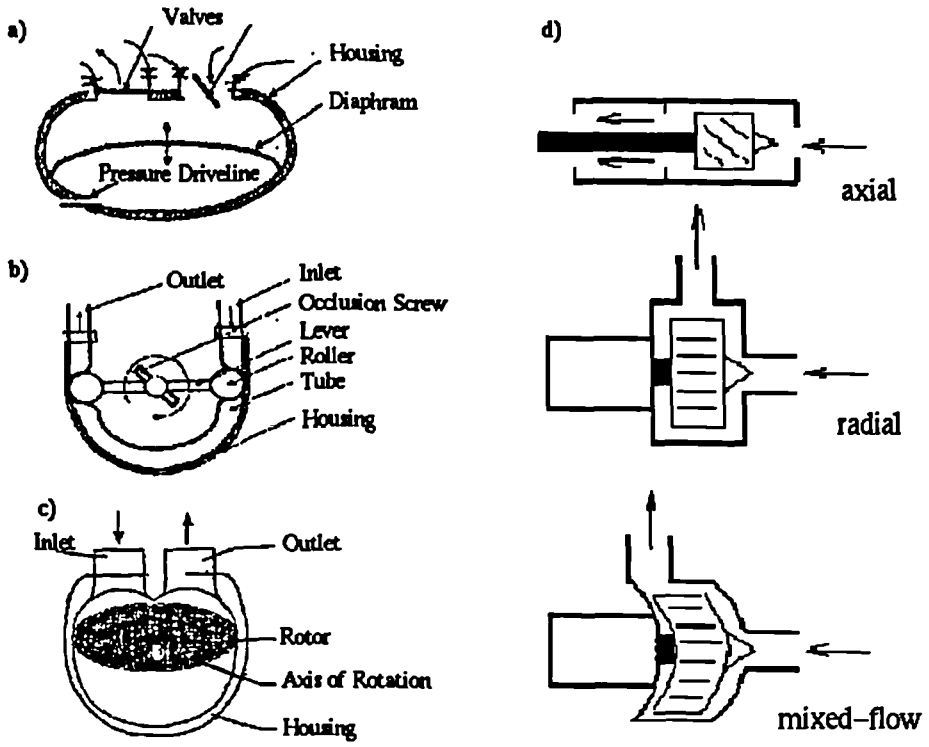

Figure 2.1: Blood pump types: a) membrane, b) roller, c) eccentric rotor, d) impeller pumps with axial, radial and mixed flow directions.

in axial centrifugal pumps, i.e. pumps where inflow and outflow are aligned with the rotor axis and the flow runs essentially parallel to it. The mixed-flow pump combines radial and axial configurations with the fluid running diagonally between two conical surfaces.

Pump characteristics such as specific speed n_s, specific diameter δ, head coefficient ψ and capacity coefficient ϕ which are dimensionless with exception of n_s and are defined as

$$n_s = n\frac{Q^{\frac{1}{2}}}{H^{\frac{3}{4}}} \;\; ; \;\; \delta = \frac{\sqrt{\pi}}{2}\left(\frac{2gH}{Q^2}\right)^{\frac{1}{4}} D_2 \;\; ; \;\; \psi = \frac{2gH}{u_2^2} \;\; ; \;\; \phi = \frac{c_{m_2}}{u_2} \,, \qquad (2.1)$$

where

n – *rotational speed*

Q – *flow rate*

H – *pressure head*

D_2 – *outer impeller diameter*

u_2 – *circumferential velocity at* D_2

c_{m_2} – *meridional component of absolute velocity at* D_2

enable the correlation of pumps of different type, characteristic and size. A fundamental diagram for pump design is represented by the Cordier diagram where experimentally evaluated efficiencies are plotted as a function of the specific speed [14]. Radial centrifugal pumps work most efficiently with low speed rotors, suitable for high pressure coefficients and low flow coefficients. In contrast, efficient pumps with axial flow employ high speed rotors and create a small pressure rise with large quantities of flow. Mixed-flow pumps are suitable for the region in between.

All of the above centrifugal pumps have been utilised for the purpose of assisting or replacing the heart. This study will concentrate on the analysis of radial centrifugal pumps (hereafter termed as centrifugal pumps). However, existing axial and mixed-flow pumps will be briefly described for the sake of completeness.

Design criteria for centrifugal blood pumps are derived from physiological requirements.

a) The flow rate and pressure head are determined by the requirements of the circulatory system:

1. Flow rate : 2 - 10 l/min

2. Pressure head :

   (a) approx. 20 kPa (150 mmHg) for replacing the left ventricle

   (b) approx. 4 kPa (30 mmHg) for replacing the right ventricle

b) The necessity of a pulsatile flow for maintaining physiological perfusion has been refuted and experimental evidence has indicated that non-pulsatile perfusion can be sustained for a period of up to 100 days without harmful physiological effects [15].

Figure 2.2: Aries Medical Isoflow ^{TM}, Sarns/3M Delphin ^{TM} and Medtronic Bio-Pump ^{TM} (from left to right).

c) Considerations of pump and therefore impeller size are strongly related to the intended location of the device. Intracorporeal pumps need to be fitted into a limited space whereas extracorporeal devices have a far higher size tolerance.

d) Blood as the medium being pumped requires that consideration be made of mechanical, thermal and chemical factors which could lead to undesirable blood destruction. In particular, high mechanical forces, abnormal temperatures and blood incompatible surfaces should be reduced or avoided.

Three commercially available centrifugal blood pumps are the Sarns/3M Delphin ^{TM}, the Aries Medical Isoflow ^{TM} and the Medtronic Bio-Pump ^{TM}, see Fig 2.2.

Common to all the pumps is the magnetic coupling of the external AC drive motor to the disposable pump head. The need for rotary shaft seals and their potential problems of leakage and loss of sterility is thus avoided. The Delphin

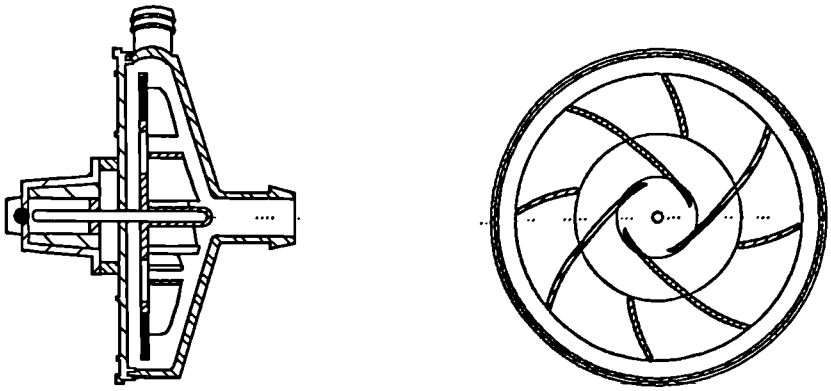

Figure 2.3: Isoflow ^{TM} Centrifugal Pump.

^{TM} pump is an unshrouded impeller pump, the rotor comprising six long vanes interposed by six short vanes. The vanes are straight, inclined backwards and attached to a segmented disc. Pump priming volume is 48 ml and the operating

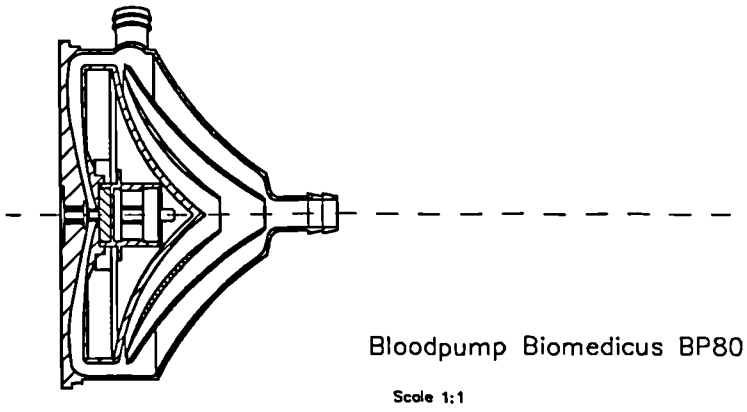

Figure 2.4: Bio-Pump Centrifugal Pump BP80.

ranges of pressure, flow rate and rotational speed are 0 - 700 mm Hg, 0 - 10 l/min and 0 - 3600 rpm, respectively. The performance curves (Fig 2.5) show a slight decrease in pressure with increasing flow rate at a constant rotational speed.

The impeller of the Isoflow ^{TM} pump consists of a segmented disk mounting

four long vanes alternating with four short vanes. The impeller is unshrouded and all vanes are slightly bent in the radial plane and inclined backwards (Fig 2.3). The priming volume is 65 ml and operating ranges of pressure, flow rate and

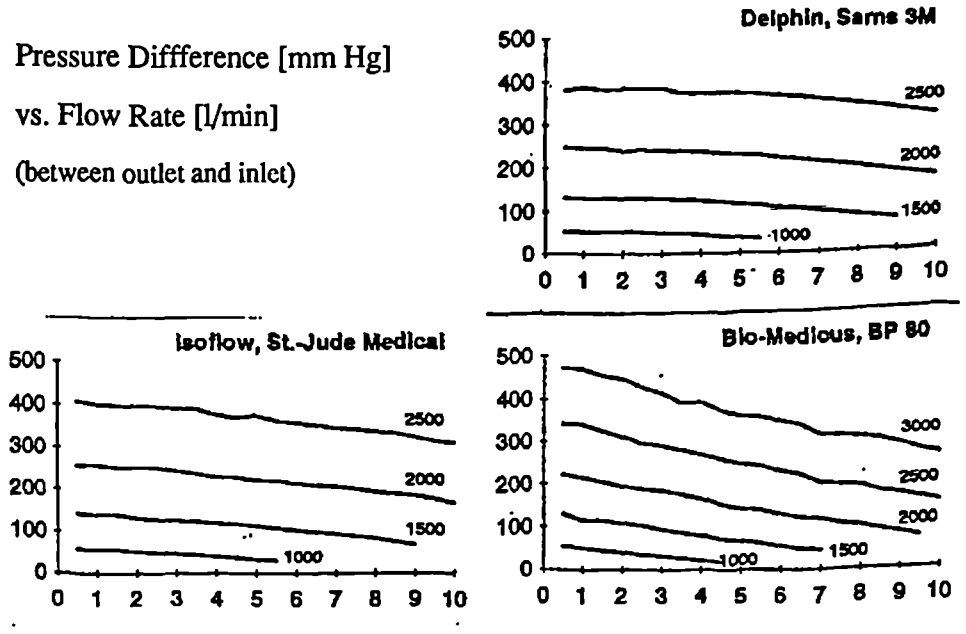

Figure 2.5: Performance curves at different rotational speeds (in rpm) for Delphin ^{TM}, Isoflow ^{TM} and Bio-Pump ^{TM}.

rotational speed are 0 - 850 mm Hg, 0 - 10 l/min and 0 - 3500 rpm, respectively. Performance curves are similar to those for the Delphin ^{TM} pump (Fig 2.5).

A different design approach is followed with the Bio-Pump ^{TM}. A set of three concentric intercalated hyperboloids of revolution constitute the pump rotor (Fig 2.4). The transfer of the rotor momentum to the fluid is achieved by viscous coupling. Two versions of the Bio-Pump ^{TM}, the BP50 and the BP80 have priming volumes of 50ml and 80ml, respectively. Pump performance curves, shown for the BP50 in Fig 2.5, have a larger slope than that for the Delphin ^{TM} or Isoflow ^{TM} models, i.e. the pressure head is more sensitive to a flow rate change. Higher rotational speeds are required to obtain similar flow rate - pressure head levels compared to the impeller pumps.

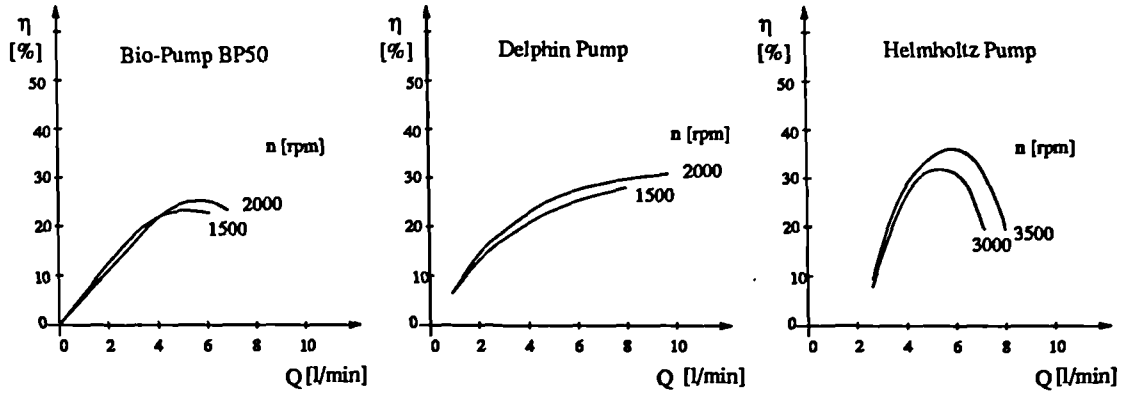

Figure 2.6: Efficiency curves for Bio-Pump ^{TM}, Delphin ^{TM} and Helmholtz pumps.

Different concepts of centrifugal blood pumps have been investigated and tested in the past. Only the most distinctive designs will be mentioned here. The Helmholtz centrifugal pump [16] has a shrouded impeller with seven vanes. The shrouding of the impeller increases pump efficiency (Fig 2.6).

A straight path rotor, i.e. a rotor with six straight fluid paths arranged radially was designed by Nishida [17] with the intention of achieving the required hydraulic output with low rotational speeds. Performance curves, however, do

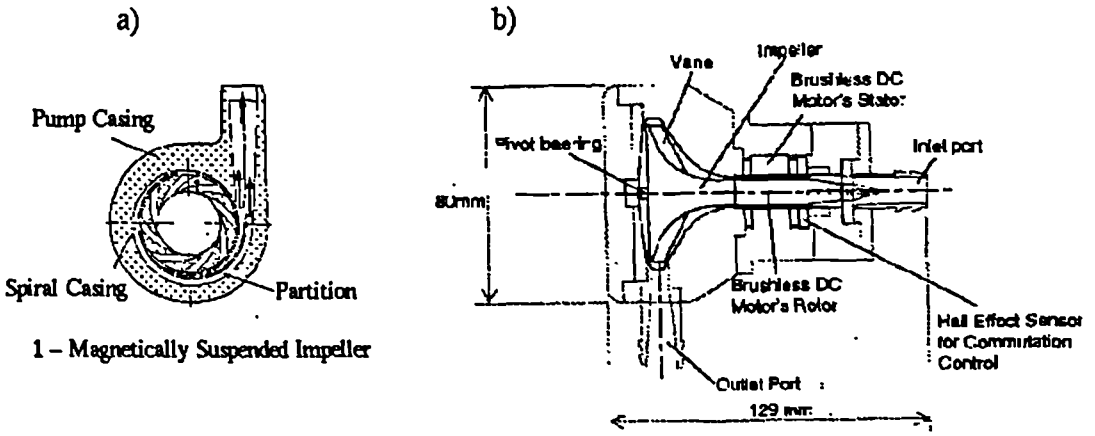

Figure 2.7: a) Magnetically suspended impeller pump by Akamatsu, b) Baylor Gyro pump.

not show relevant differences between this pump and the Delphin ^{TM} or Isoflow

^{TM} pump. Different methods of sealing and bearing the rotor have been reported. Employing a direct drive system instead of the indirect magnetic coupling mechanism, Takatani et al [18] showed an increase in pump efficiency but at a cost of considerably higher heat generation. A magnetically suspended impeller is a feature of the centrifugal pump developed by Akamatsu et al [19]. In this design the impeller rotates by magnetic coupling with the outer rotor of the motor. Elimination of unbalanced radial forces is achieved by division of the outlet part (Fig 2.7a). The Baylor Gyropump [20] implements the gyroscopic principle, the motor-impeller being made through a brushless DC motor with its rotor placed inside the impeller (Fig 2.7b).

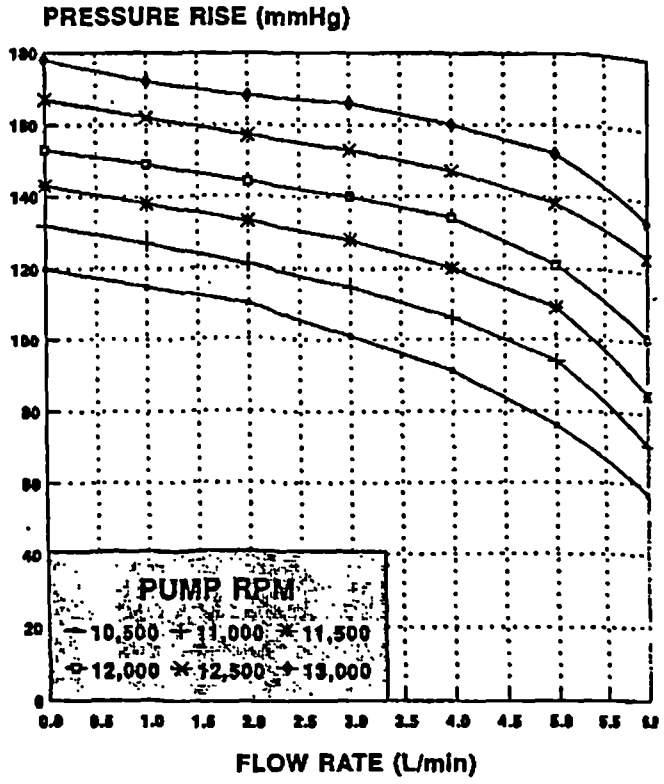

Figure 2.8: Flow performance curves for axial blood pump by Butler.

The axial flow pump concept has been utilised in the Hemopump ^{TM} [21] and an axial flow pump by Butler et al [22]. According to efficiency and performance criteria mentioned above, they operate in a high speed and low pressure range. Performance curves for the axial pump by Butler are given in Fig 2.8.

Small specific diameters are required to create the desired output and allow the Hemopump to be operated inside human arteries or vascular grafts.

A diagonal blood pump design intermediate in size as well as pump performance characteristics between radial and axial version was realised by Quian [23, 24].

2.2 Haematological and Hydrodynamic Assessment of Centrifugal Blood Pumps

Mechanical circulatory assist devices must not only achieve a physiologically adequate pump output, but also an acceptable degree of bio-compatibility. Besides the effects an intracorporeal use of blood pumps has on the surrounding tissue, most studies have focussed on the interaction between pump and blood. Causes of blood destruction or trauma can be manifold and include biochemical and physical factors. Since it has been established that the latter is mainly responsible for traumatic events in blood pumps [7, 25], a survey of haematological pump assessment will be given under this aspect.

Blood trauma is usually expressed with direct or indirect changes to its cellular components, in particular red blood cells (RBCs), platelets and white blood cells (WBCs), closely related to their structure and function.

RBCs have a very thin membrane (~10 nm) [26] that encapsulates the haemoglobin solution. Biaxial membrane strain due to mechanical forces can lead to an opening of pores in the membrane enabling an osmotic leakage of haemoglobin. It can also cause an irreversible tearing of the membrane with release of the cell content, a process called haemolysis [27]. Prediction methods of red blood cell damage therefore consist in the measurement of free haemoglobin in the plasma and of cell lifespan, microscopic observations of morphological changes of the cell and, less frequently, in the detection of leakage of K^+ ions. Platelets are evaluated by total cell counts, decreasing with cell aggregation and segmentation, the measurement of beta-thromboglobin as an indicator for

platelet release reaction, lactic dehydrogenase (LDH) as a cytoplasmic marker enzyme indicating unspecific platelet destruction, platelet factor 3 for procoagulant activity, released serotonin and also by morphological changes [28, 29]. WBCs are assessed by detection of their phagocytic activity and total cell count [30]. It should be mentioned that interactive cell responses can also occur. For example, the release of ADP or ATP converted to ADP from haemolysed red cells cause platelet stickiness and thus accelerates platelet aggregation in flowing blood [27, 28, 31].

The haematological performance of centrifugal blood pumps has been evaluated in numerous *in vitro* and *in vivo* tests both in animals and humans [32, 33, 34, 35, 36, 37, 38, 39, 40]. In summarising the results of haemodynamic evaluation studies, a disturbance of the haematological system can be generally observed. This is expressed as a monotonic increase in free plasma haemoglobin (fHb) as well as an increase in platelet activity and release reaction with time. Reduction of platelet population was often found to terminate and recover after a certain period of time [17, 21, 35, 40]. Differences in the degree of blood trauma between various types of centrifugal pumps were observed in these tests, however, contradictory results prohibit a generalisation of haemodynamic pump evaluation. Comparison of the quantitative outcome is extremely difficult and precise assessment of effects of mechanical devices on the haematological condition is a risky venture.

A fair uniformity of experimental conditions can be achieved by a standardization of test methods for *in vitro* tests [37]. *In vivo* examinations will always, despite showing a statistical significance, involve a large deviation due to biological differences between individuals and the haematological response to an artificial device used under a range of operating conditions.

The question if the amount of blood trauma caused by an artificial organ is physiologically bearable may often be answered positively. Plasma haptoglobins can, for example, bind 100-140 mg/dl of fHb forming a complex which is removed by the reticuloendothelial system at a clearance rate of 15 mg HB/dl/h

[41]. Not only with regard to a longer term application and a further safety increase but also for a better understanding of the mechanisms, there is the need to know the device related causes of blood destruction. Centrifugal blood pumps deliver high kinetic energies to the blood via their high speed rotors and particular attention must be given to mechanically induced blood trauma in these devices. The analysis of this damage process contains two major subproblems: the identification of the mechanical loading acting upon the blood within the pump and the determination of the correlation between mechanical loading and blood damage. Prior knowledge of the latter is discussed in detail in the following section.

The analysis of flow conditions with the option of subsequent optimisation of the pump design will facilitate the development of a highly efficient design with lower energy dissipation leading to a decrease in blood trauma. Mechanical loading of a fluid within a pump can be divided into its hydrodynamic part and its thermodynamic part. Although related, a distinction between the two parts still has to be made. Heat generation results both from dissipation of kinetic energy of the bulk fluid as well as from friction within bearings and seals of the pump rotating parts.

Analysis of flow conditions within centrifugal blood pumps has been attempted using different approaches. An analytical solution of the Navier-Stokes equations, describing the motion of a viscous fluid, does not exist for the complex internal flow in turbomachines. However, for the simpler case of a disc spinning in an infinite fluid an analytical solution may be obtained (Karman) [42, p. 102]. The flow field for this configuration is presented in Fig 2.9.

The above solution has been applied by Affeld [43] to model the flow in a cone-type centrifugal pump. The axial distribution of the wall shear stress at the cone surface was obtained. Furthermore, the fluid volume and the residence time in the boundary layer, the area of highest laminar shear stresses were predicted. (It should be noted that the magnitude and duration of shear stresses acting upon blood cells are important determinants in blood trauma as shall be shown

below.) Affeld's studies are therefore of great interest for an initial identification of mechanical loading parameters and their location in this type of blood pump. However, a reported discrepancy of 50 % between the actual flow rate and that derived from the analytical solution highlights the idealised representation of the actual pump geometry. The hyperboloidal shape of the impeller, the flow field boundaries due to the pump housing and the inlet and outlet design are not taken into account. Realistic modelling of the geometrical and fluid dynamic conditions

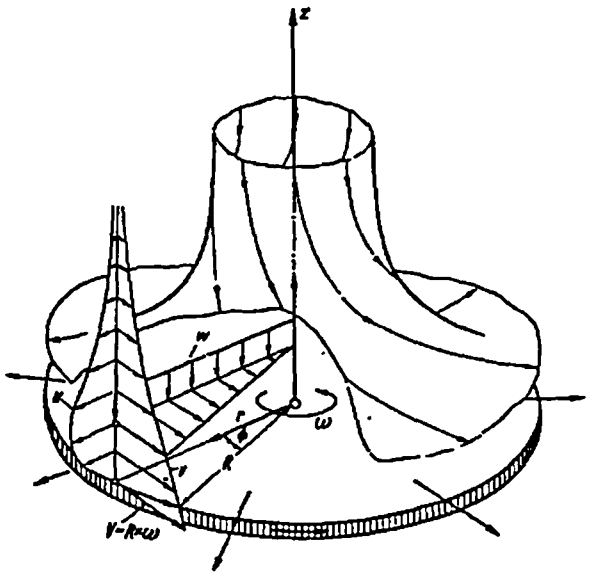

Figure 2.9: Flow in the neighbourhood of a disk rotating in a fluid at rest (from [42,p.102]).

are desirable to enable the evaluation of shear stresses at all boundaries and of arbitrary turbulent stresses for the case of turbulent flow.

Where analytical solutions are not possible for complex hydrodynamic problems, numerical methods can often be employed. They present a fast and less costly option compared to experiments for determining complicated flows. However, computer related limitations may lead to important drawbacks of numerical methods, for example the need to treat turbulence by simplifying models.

The only numerical prediction of the flow field within a centrifugal blood pump has been undertaken by Papantonis [44, 45]. Straight vaned impeller

pumps designed by the Bioengineering Research Laboratory of the University of Vienna [33] were analysed by the Finite-Volume-Method. The full Navier-Stokes equation for the velocity relative to the rotating impeller was solved in a two-dimensional blade-to-blade plane. Assumptions relating to the third dimension were made, such as omission of the axial velocity as well as axial gradients of all kinematic parameters. However, the radial change in the axial height of the impeller was taken into account. The relative velocity components were calculated as were the wall shear stresses along the blade (Figs 2.10 and 2.11).

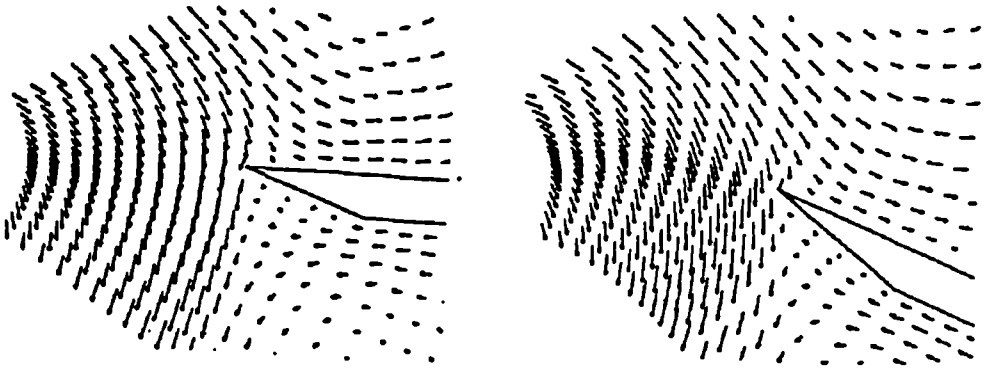

Figure 2.10: Relative velocity vectors in near-blade for a) straight radial blade and b) straight inclined blade (from [45]).

Trajectories of fluid particles in the absolute flow field issuing from various points at the inlet section were determined and used to calculate the residence time of particles in the impeller domain. The deviation of residence times between different trajectories was taken as an indication of the non-uniformity of the flow.

Papantonis also solved the problem of relating flow parameters to a blood damage criterion by application of the experimental results of Wurzinger [25] who found that haemolysis is a function of approximately $\tau^2 t$ where τ represents the shear stress and t the duration of application of a constant τ (for details see Chapter 2.3). Papantonis introduced an index for quantitative comparison of different impellers in terms of blood traumatisation by summation of the term $\tau^2 t$ along a streamline located within the boundary layer of the blades.

The contribution of Papantonis' pioneering studies towards an understanding

of flow phenomena within centrifugal blood pumps and their variation with changes in geometry and operating conditions is very significant. Of particular

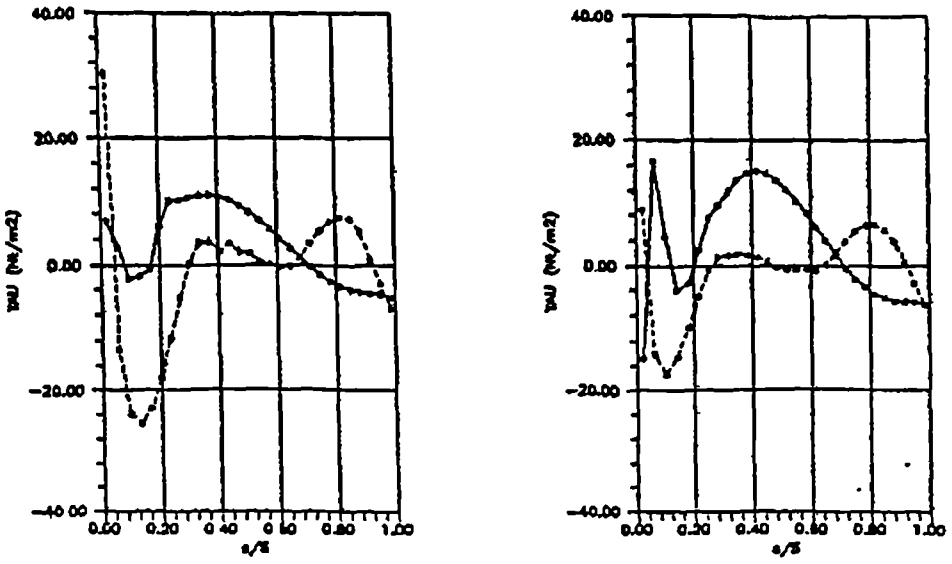

Figure 2.11: Distribution of laminar wall shear stresses along a blade (from [45]).

note is the attempt to relate pump flow parameters to blood damage criteria. One major shortcoming of the investigations undertaken is associated with the use of a two-dimensional model. Areas of expected high velocity gradients and stresses especially at the front and back housing, non-uniformities and secondary flows due to the change of flow direction at the inlet and to flow over the blades are not taken into consideration. Papantonis did not incorporate a turbulence model since the Reynolds number based on the relative velocity at the outer impeller circumference was estimated to be in the order of 1000, and hence in the laminar region. This way of estimating turbulent flow seems very uncertain. Reynolds numbers calculated, for example, for the flow relative to the housing related to the gap between blade and housing indicate turbulent conditions. The inclusion of turbulence models would enable the prediction of turbulent or Reynolds stresses as an important source of blood trauma. Furthermore, the quantitative criterion for trauma potential of an impeller by Papantonis would not be applicable in a three-dimensional flow with a six component stress tensor. Clearly, consideration of particles undergoing a non-constant stress regime needs

to be paid in future for blood damage predictions based on the knowledge of the mechanical loading of the blood.

Experimental flow investigations are necessary for the development of physical models, for the validation of theoretical boundary conditions, for the verification of numerical flow simulations and for a detailed final design of a product. Only recently have serious experimental flow investigations of centrifugal blood pumps been performed. Flow visualization techniques are relatively simple and inexpensive. These include the oil film method [46] and tuft method [46] and the commonly used particle tracking method [46, 47, 48, 49]. Although these studies used non-invasive recording or observing techniques, they cannot be considered non-interacting due to the addition of particles, tufts or additional surface layers. As a result, qualitative observations of flow patterns with identification of recirculation zones and separation [46, 47] and secondary flows [48] were obtained and suggested certain changes in the pump design to smooth the flow. A quantitative analysis of flow visualization studies in the outlet tube section was attempted by Treichler et al [49] and produced two-dimensional velocity profiles and values for laminar shear stresses. This study made a valuable contribution to the understanding of the complex outflow domain. Apart from the inability to quantify the flow in the direct impeller area, the main limitations of these visualization studies is the planar recording of particle motion with consequent neglect of the motion in the third direction. This may be overcome with additionally higher accuracies by use of more sophisticated experimental methods, e.g. laser Doppler anemometry. However, such methods involve much higher costs. It should be noted that no experimental flow investigations of the three commercial centrifugal blood pumps, Bio-pump ^{TM}, Isoflow ^{TM} and Delphin ^{TM} pumps, have been reported in literature.

An interesting thermodynamic investigation of two centrifugal blood pumps was undertaken by Belenger et al [50]. Using infrared emission thermograms and measuring the overall heat generation within the pump , it showed major differences in the thermodynamic behaviour between the cone-type Bio-pump

^{TM} and an open impeller pump. In the Bio-pump ^{TM} significant global heating occurred with an estimated partition of fluid frictional effects of 80 %. The overall heat generation of the impeller pump was significantly lower than in the cone pump under all operating conditions. Only small variations in heat generation took place with a change in viscosity suggesting that fluid frictional energy dissipation does not present a major problem in the impeller pump.

2.3 Mechanical Blood Trauma

2.3.1 General Aspects

Artificial devices used in circulatory support procedures, e.g. blood pumps, valves, tubing, oxygenators may produce levels of blood trauma which exceed the haemostatic mechanisms of the body resulting in cessation of the procedure or the occurrence of abnormal physiological states. Shedding light on the mechanisms of blood degradation is essential for the optimisation of those devices with respect to their haematological performance.

Blood trauma is often classified as being physical or chemical, although it has been pointed out [30] that both act in a coupled fashion in real flow situations. Bearing in mind the complexity of trauma mechanisms, single parameter studies are desirable. To ensure repeatable and controllable conditions, mechanical blood damage experiments are preferably performed *in vitro*.

As stated earlier, the cellular components of blood are of particular interest as a measure of its degradation. The majority of investigations has concentrated on erythrocytes (RBCs), fewer on thrombocytes (platelets). Leucocytes (WBCs) have received the least attention regarding their mechanical resistance. Flow-related loading parameters in question are stresses and pressure. Newtonian shear stresses and negligible normal stresses [42] in laminar flow are accompanied by Reynolds normal and shear stresses as an expression of energy dissipation due to velocity fluctuations in turbulent flow. Idealization of the complex time-dependency of stress and pressure regimes in real flow is conveniently undertaken

by consideration of steady flow with time-constant mechanical parameters or by a controlled time-dependent loading function, e.g. sinusoidal or stepwise.

The common methods of measuring the response of cellular blood components to an imposed mechanical loading are mentioned in detail in Section 2.2.

In the following section a survey of experimental investigations of mechanical blood trauma is presented and organised according to cell type. Emphasis is placed on red blood cells. Thereafter, theories of the interaction between mechanical loading and blood destruction obtained from experiments and from theoretical analysis of cell rheology and cell mechanical properties are discussed.

2.3.2 Experimental Investigations

Erythrocytes:

A considerable amount of basic experimental research has been reported on various factors that influence haemolysis under well-defined hydrodynamic conditions. In terms of shear stresses these conditions are obtained by applying a Couette-type flow in a concentric cylinder or a cone-and-plate apparatus, or Poiseuille flow in a capillary tube. Shear stress distributions are constant with the assumptions of a small gap and non-existence of secondary flows (Taylor vortices) in the former and linear with maxima at the walls for the latter. Despite being based on a velocity distribution of ideal homogeneous fluids and not corresponding exactly with particle motion in the two-phase flow of blood or blood cell suspensions [51], they still represent a sufficiently exact approximation of the real flow conditions. The literature on haemolysis under a time-constant shear stress of this type is very extensive. Shear stresses of a defined magnitude acting for a certain duration of time were studied and their effect on haemolysis evaluated, usually in terms of plasma free haemoglobin. A threshold of the onset of haemolysis, e.g. the destruction of the most vulnerable cells, has been predicted in these studies. Comparison is, however, difficult due to the non-uniformity of experimental conditions. Table 2.1 summarizes results of these investigations.

A controversial debate on the haemolytic effect of cell-wall-interactions and its extent has accompanied these investigations. Formation of tethered cells anchored to the wall, possible chemical interactions and mechanical surface imperfections causing lysis have been cited as cell-solid surface mechanisms [52].

Investigator	*Apparatus*	*Exposure time*	*Shear stress* threshold [Pa]	*Hct* [%]	*Remarks*
Bacher, Williams [53]	capillary tubes	10 ms	500	20-40	bovine blood
Williams [54]	cone-&-plate; capillaries	5 min	60	*	human cell suspensions
Beissinger, Williams [55]	cone-&-plate and parallel plates	10 min	<13	*	whole human blood
Solen [56]	coni-cylindrical	2 h	1.5	*	dog blood, surface effects
Nevaril [57]	concentric & cone-&-plate cylinder	2 min	300	*	human & rabbit blood, morphological changes
Wurzinger [28]	concentric cylinder	700 ms	120	40-45	human cell suspension
		14 ms	450	40-45	
Leverett [58]	concentric cylinder	2 min	150	0.3-60	whole human blood laminar flow
Sutera [59]	concentric cylinder	4 min	150	0.2	human blood suspension turbulent flow

Table 2.1: Experimental investigations of threshold for haemolysis under constant shear stress loading (* - Hct not mentioned).

Wall effects mediated by flow processes were discussed by several investigators [53, 56]. Blackshear [27] and Solen [56] concluded that the main influence for the haemolysis produced were due to effects of contained surfaces, whereas bulk

stresses were favoured by Leverett [58], Sutera [59], Wiliams [54] and Beissinger [55]. An experimental design was used by Blackshear [60] to eliminate foreign surfaces in the high shear zone by using a liquid jet injected into a suspension of erythrocytes. For an estimated average exposure time of 0.01 ms the author reported a threshold turbulent stress of 4 kPa. An improved jet test by Sallam [61] with correct mapping of the Reynolds stress distribution and with blood collection from selected locations, this stress magnitude was corrected to approximately 400 Pa.

It is generally agreed that for tests conducted under constant shear loading there are two primary determinants of in-bulk haemolysis: shear stress magnitude and exposure time. Fig 2.12 displays the threshold for constant shear-induced haemolysis and its dependency on these two determinants. No clear evidence is given on the dominance of either laminar or turbulent stresses for lysis processes. Investigations by Bluestein et al [62] of a continuous power functional relationship between local rate of energy dissipation and rates of haemolysis for four types of flow including laminar and turbulent supports the former statement.

Haemolytic tests under unsteady shear stress conditions were performed by Rooney [63], Williams and Hughes [64] and Hashimoto [65]. The physical concepts of the first two studies, pulsation of a gas bubble and transverse oscillation of a wire in a suspension of cells, are closely related. In both cases microstreaming near to the vibrating medium is formed and resultant tangential stresses are related to the measured haemolysis. Operational frequency was 20 kHz for a duration of 5 min in both studies. A threshold for haemolytic shear stress of 450 to 560 Pa was calculated. The strong non-uniformity of the flow conditions and the small blood volumes involved in the microstreaming zone make an assessment difficult. Interestingly, the time a particle spends in the region of maximum shear stress next to the wire tip is only in the range of 5.E-5 s to 2.E-3 s correspondingly to a wire displacement of 30 μm to 10 μm , respectively [64]. The product of the time spent in this region and the number of passes was stated to be constant and approximately 1.0 ms. The question arises as to

whether the shear stress amplitude or the frequency of application of the maximum shear stress is responsible for observed haemolysis. This question has not been answered by the authors.

Hashimoto examined the haemodynamic effect of periodically fluctuating shear rates in a Couette-flow device. Results showed distinct dependencies of haemolysis rates on frequency (0-1 Hz), shear rate amplitude (up to 1000 s^{-1}, corresponding laminar shear stress amplitude of approximately 3 Pa) and mean shear rates (up to 700 s^{-1}).

Effect of a constant pressure and pressure fluctuations on haemolysis have been studied by several investigators. According to Blackshear [52], positive pressures up to 3 bar had no effect but a negative pressure of 0.34 bar caused haemolysis. Yarborough [66], however, found no negative pressure effect provided that gas bubbles were absent. Nevaril [67] concluded that periodic pressure fluctuations of max. 10 bar with a frequency up to 30 Hz for a period of 1 h were harmless, but Nakahara [68] found a haemolytic response with the effect of the pressure amplitude being dominated by that of the frequency.

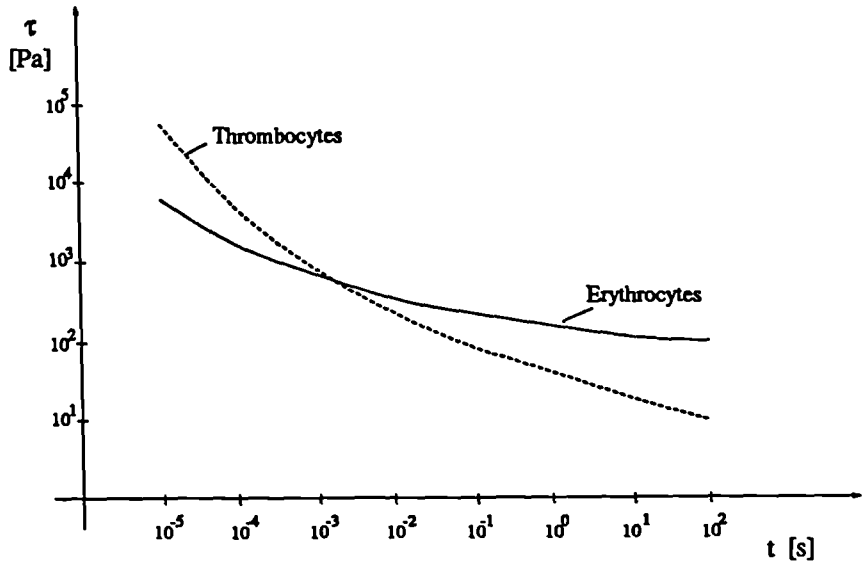

Figure 2.12: Threshold for extensive haemolysis (erythrocytes) and incipient serotonin release (thrombocytes) under constant shear stress loading (from [69]).

Platelets:

Studies of platelet response to mechanical forces are closely related in methodology to those for erythrocytes. Application of a constant shear stress in capillary tubes [29, 69, 70], Couette-type devices [28, 69] and jet tests [71] substantiated the correlation between cell lysis and shear stress magnitudes as well as exposure times. Fig 2.13 shows serotonin release induced by shear stress at different exposure times [69].

There is evidence that platelet release reaction and shear induced aggregation occurs at lower shear stresses than those which cause measurable platelet lysis (LDH release) [29, 69, 70, 71]. Shear stress related platelet activation and lysis were observed for laminar and turbulent flow [30, 72]. As shown in Fig 2.12 Hellums [69] compared the shear stress-time dependency of incipient serotonin release of platelets to the haemolysis threshold for red blood cells. Comparison of the two graphs shows higher mechanical resistance of erythrocytes at higher exposure times, whereas the converse relationship is apparent for short duration shear stresses. Regarding the influence of wall surface effects discrepancies exist among different research teams [69, 70].

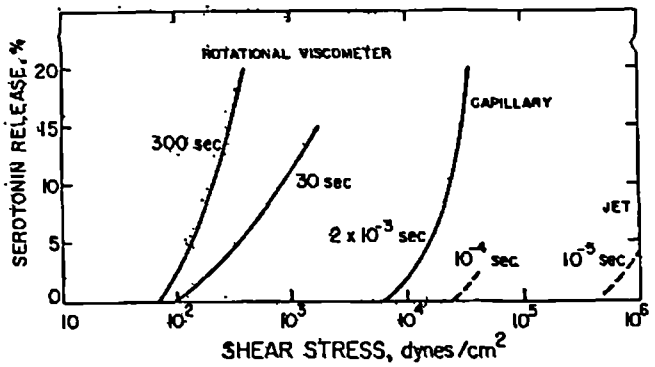

Figure 2.13: Serotonin release (thrombocytes) under constant shear stress loading at different exposure times (from [69] ; here 10 dyn/cm^2= 1 Pa).

Unsteady shear stress regimes were applied by Williams [73] utilising a transversely oscillating wire for 5 min at a frequency of 20 kHz as described above for erythrocytes. Shear stresses in the microstreaming field above a threshold of

80 Pa ± 4 Pa were found to cause serotonin release. The exposure of platelets to physiologically oscillating tube flow, carried out by Yu [74], with shear stress maxima of 2.62 Pa at the walls at a frequency of 1.2 Hz showed enhancement in platelet aggregation but no changes in release reactions. A similar test at lower shear stress maxima of 1.65 Pa [75] produced no signs of platelet aggregation.

Little is known about the effects of pressure as such or pressure fluctuations on platelet destruction. Schmid-Schoenbein [31] mentioned that high pressure (up to 3 bar) failed to affect platelet behaviour.

Leucocytes:

Knowledge about the role of fluid mechanical forces in the activation and lysis of white blood cells is extremely sparse. Studies by Dewitz et al [76] indicated that leucocytes are susceptible to flow-induced trauma. Significant cell damage was observed after 10 min exposure at a shear stress of 100 Pa.

2.3.3 Models of Blood Trauma

The formulation of a generally valid model to describe the relation between hydromechanic stresses acting on blood cells and their structural and functional response is a demanding task.

The difficulty in modelling cell lysis dependency on mechanical parameters follows from the specific conditions under which the bulk flow experiments were performed and the influence of non-mechanical parameters. Despite problems of relating those phenomenological examinations quantitatively to each other, important trends can be observed, e.g. the shear magnitude and exposure time dependency of RBC and platelet lysis. A mathematical analysis by Wurzinger [25] of the experimental data for constant shear-induced damage of platelets and RBCs gave the following correlations (Eqns.(2.2),(2.3)) for the percentage of released LDH and HB, related to the overall amount of LDH and HB in the suspension, respectively.

$$\%\ LDH-\ Liberation\ = 3.31 * 10^{-6} * t^{0.77} * \tau^{3.1} \qquad (2.2)$$

$$\%\ HB-\ Liberation\ = 3.62 * 10^{-5} * t^{0.79} * \tau^{2.4} \tag{2.3}$$

where t is the time in s and τ is the shear stress in Pa.

From these relationships the shear stress magnitude was evaluated by Wurzinger as the major determinant of damage. Platelets are more susceptible to shear destruction than erythrocytes as reflected in the higher exponent for τ. These correlations besides specifying particular experimental conditions, are also limited in the range of application for the mechanical parameters. A 2%-Hb-liberation curve calculated from Eqn. (2.3), for example, showed fair agreement with the well-established haemolysis curve by Leverett [58] within the time interval investigated by Wurzinger but considerable discrepancies outside this range, as displayed in Fig 2.14.

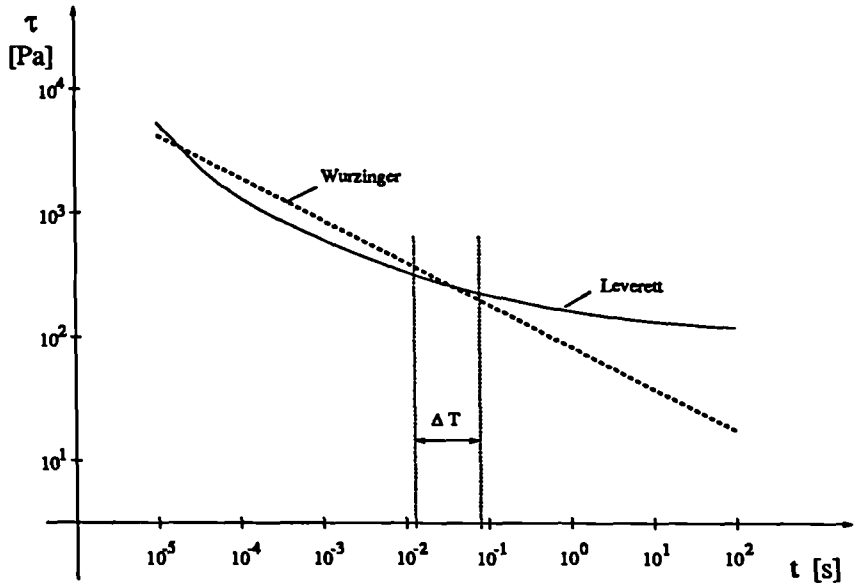

Figure 2.14: Comparison of 2%-Hb-release calculated from Equation (2.3) by Wurzinger with experimental haemolysis-threshold curve by Leverett [58]. ΔT is the time range of application of a constant shear stress by Wurzinger

A different, microscopic approach for identifying critical mechanical parameters using rheological models and continuum mechanics assumptions has been undertaken for the red cell membrane. The RBC is amenable to this type of approach because it may be treated as a relatively simple structure consisting of a continuous membrane enclosing an apparently homogeneous fluid [54]. The

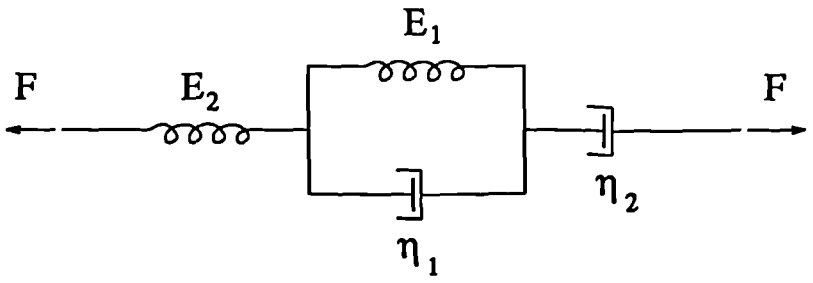

Figure 2.15: Viscoelastic model of RBC membrane

red cell membrane is an anisotropic material, which as a composite of molecular monolayers can be treated as continuum in the two-dimensional membrane plane, but has discontinuous, molecular character in the third dimension [77].

Constitutive assumptions for red cell membranes have been the subject of debate. A purely elastic model for the stress-strain relationship at low rates of strain [78] was followed by a hyperelastic material concept accounting for the large resistance to area increase of red cells [77, 79]. Time-dependent deformation of the membrane under applied forces has been considered in viscoelastic [77, 80] and viscoplastic [81] models. Rand [80] proposed viscoelastic membrane behaviour, described in model terms by a single spring and dashpot acting in parallel (i.e. a Kelvin body) and an additional spring and dashpot mounted in series (Burgers body) (Fig 2.15) to account for cell lysis processes.

The strain response of the combination of these elements to a step function applied force is shown in Eqn (2.4).

$$\epsilon = F\left[\frac{1}{E_2} + \frac{1}{E_1}\left(1 - exp\left(-\frac{E_1}{\eta_1}t\right)\right) + \frac{1}{\eta_2}t\right] \tag{2.4}$$

where ϵ - strain, F - applied force, E_1,E_2 - Young's moduli of springs and η_1,η_2 - viscosities of dashpots.

The empirical curve representing mechanical strain and breakdown of the membrane of an erythrocyte sucked into a micropipette fitted well with the postulated viscoelastic model [80]. Since molecular interpretation of this model

has not been established, Rand considered it as purely describing experimental data. A viscoplastic theory for two-dimensional membrane surfaces was applied by [81] to the analysis of irreversible growth of a microtether from a red cell which was attached to a wall and acted upon by fluid shear stresses.

Modelling the dynamic and kinematic behaviour of red blood cells in a flowing medium is a very complicated task due to its complex geometrical and rheological properties and has been approached with considerable simplifications and idealizations. From microscopic observations of deformation and behaviour of RBCs in uniform shear flow at subhaemolytic shear rates exceeding approximately 200 s^{-1}, it is known that they change their shape from biconcave discs into irregular ellipsoidal structure with their major axis at 5 - 25 degrees to the direction of flow. The cell membrane rotates around the interior, known as 'tank-treading motion' [82, 83]. Simple mathematical models describing the motion of RBCs in shear flow considering a single, two-dimensional, elliptical microcapsule were used for determining the velocity field external to the cell by Sutera et al [84] and for predicting the deformation by viscous forces with maintenance of the elliptical shape by Sugihara et al [85]. Richardson [86], assuming a flexible, elastic membrane, evaluated forces on the ellipsoid in uniform shear and determined the displacements for an elastic material by solving linear membrane equations. She then proceeded to a haemolysis prediction by taking the maximum membrane stresses predicted as input parameter into Rand's viscoelastic membrane breakdown model. This revealed a strain superpositioned from a term linear in time, a bounded periodic term and terms exponentially decreasing with time. Thus, it was concluded that as long as this model applies a cell would always experience haemolysis by merely remaining in the shear flow long enough for the linear term to reach the critical strain. A different approach of explaining time-dependent haemolysis behaviour was applied by Niimi [87]. The motion of a single rotating cell membrane in a two-dimensional uniform shear flow was analysed and shear stresses acting on both sides of the membrane were estimated. A cyclic change of external stress distribution along the circumference was predicted, essentially associated with the flow field at the presence of the

rotating membrane. A fixed membrane element would thus experience a cyclic shear loading, with stress amplitude and frequency possibly increasing with increasing shear rate. It was suggested by Niimi that cyclic loading conditions of the cell membrane could explain the time dependent relation between shear stresses and haemolysis in bulk flow experiments with shear-induced haemolysis due to a fatigue process of the cell membrane. Estimated values for rupture of RBC's under cyclic loading as a function of stress amplitude and stress cycles showed a strong similarity to the haemolysis threshold curve obtained in bulk shear experiments as a function of shear stress and exposure time. An investigation modifying the single-cell model by placing two parallel walls in the vicinity of the cell was undertaken by Sugihara [88]. The channel width was found to influence shape, tank-treading frequency and inclination angle of the cell, thus, suggesting the need of incorporating cell-cell or cell-wall interaction into a mathematical model.

2.4 Summary

Centrifugal blood pumps as temporary heart assist or replacement devices have been evaluated with regard to their hydraulic performance and blood trauma potential. The latter task is itself an extremely complex problem, involving the establishment of trauma causing mechanisms on the one hand and identifying them for the case of the blood pump on the other.

Singular hydrodynamic forces have been investigated in *in-vitro* bulk flow experiments with regard to their relation to lysis of blood cells. These studies show that laminar and turbulent shear stresses are major trauma sources and that consideration of the time history of the mechanical loading process is absolutely necessary. Applying constant shear stresses has attracted most attention, the strongly unsteady nature of all blood flow processes in reality demands, however, intensive studies of time-dependent mechanical loading and their haemodynamic effects. However, the *in-vitro* experiments involving oscillating stresses and fluctuating pressure regimes are too few in number and

limited to normal physiological conditions that one is unable to draw satisfactory conclusions about the influence of frequency and amplitude of a mechanical parameter on blood cell degradation. Microscopic studies, mathematic modelling of constitutive relationships and of dynamic and kinematic behaviour of red blood cell membranes in particular have explained the time-related haemolysis process under constant shear stresses by the viscoelastic properties of the membrane as well as by a fatigue process it undergoes under the cyclic shear loading of a membrane element. The approximation of a two-dimensional single cell neglecting cell-cell interactions limited to uniform shear flow reveals the initial state of these investigations. Haemolytic in-bulk-flow phenomena cannot be satisfactorily explained by current cell damage models.

The identification of the mechanical loading which the blood undergoes with transit through a centrifugal blood pump requires knowledge of the flow field within the device. For the complex geometry and flow conditions encountered, numerical methods are necessary to solve the governing equations. Although the flow field in a two-dimensional blade-to-blade analysis of a radial impeller pump has been reported and linked to the pump design, the determination of the complex three-dimensional flow field has not yet been undertaken.

The experimental flow investigations so far reported have not been able to give a quantitative analysis of the flow conditions within the pump.

Correlation between mechanical loading of blood cells within the pump and their damage potential has only be done in an oversimplified manner. This is due to the absence of the exact information about the flow field and hence mechanical loading parameters and of a complex damage theory which considers cumulative or synergistic effects of simple, damage-causing mechanical loading functions.

Chapter 3

Thesis Objectives and Solution Strategy

The optimisation of centrifugal blood pumps with respect to blood compatibility requires methods for their evaluation which are generally applicable, comprehensive and efficient. A solely experimental approach to design optimisation is only performable on a trial-and-error basis. In contrast, a theoretical model that relates pump design and performance characteristics to their biological effects would allow undesirable features to be traced to their origins and consequently would yield a directed approach to improvement. The development of a theoretical pump evaluation model forms the main objective of this thesis. Assuming blood trauma as a measure for the biological response to the pump, a correlation between trauma and the mechanical conditions within the device is needed. Concentrating on mechanically caused blood destruction the information required for a general trauma prediction theory can be divided as follows:

1. The mechanical loading of the blood and its constituents has to be obtained and because of its complex nature conveniently classified into simple loading-time-functions.

2. The knowledge of the damage behaviour of blood under those simple loading-time-functions is desired.

3. A classification of the loading functions into damage-causing and non-damaging as well as their frequency of appearance is followed by:

4. an overall damage prediction considering cumulative effects of partial damage caused by single loading functions.

The damage behaviour of blood or its components and its causal relationship to an arbitrary mechanical loading have neither been experimentally explored nor stated within any theory. Because of this lack of information, the adaptation of damage prediction theories for engineering materials and equipment will be considered. The prediction of service life for machine elements using a combination of mechanical loading analysis and material-based damage hypothesis shows a strong similarity with the problem in question.

An additional problem is whether to choose a single or multiple blood components to represent damage to whole blood. Although a definitive answer cannot be given, a close relation between the mechanical behaviour of the membranes of red blood cells and platelets has been shown in tests of cell lysis due to external mechanical forces. This similarity as well as the fact that mechanical haemolysis has been studied most extensively, point to the selection of the RBC as the cell type for the blood damage theory.

However, an adaptation of traditional mechanical damage concepts has to be undertaken with care, taking into consideration the specific rheological properties of blood cells, their suspension in a liquid solution and their biochemical nature and compensation mechanisms.

The commercially available centrifugal pump, the Isoflow ^{TM} Pump (Aries Medical), is selected for the mechanical blood loading investigation. Its complex impeller geometry (see Chapter 2) presents a challenge for flow analysis.

The determination of the mechanical loading of the blood particles can generally be performed in three different ways:

a) Calculation

b) Measurement within a physical model of the pump

c) Measurement within the actual pump

The experimental evaluation of stresses and pressure acting upon blood elements within a centrifugal pump is extremely difficult. Non-invasive methods for measuring the entire flow field of a blood-cell suspension, such as sophisticated laser Doppler anemometry or ultrasound studies are extremely costly. Less accurate methods, such as flow visualization studies of blood-simulating translucent fluids represent a compromise between cost and accuracy. Optical particle tracking within the actual pump head can be seen as an appropriate form of picturing the flow field. However, numerical flow calculations are preferred due to difficulties in obtaining optically useful information and three-dimensional velocity and stress distributions, especially in the frame of reference of rotation with the impeller. In this thesis, a Computational Fluid Dynamics software package will be utilized for the determination of three-dimensional flow parameters considering the exact and entire pump geometry and incorporating an appropriate turbulence model. Viscous and turbulent stresses and particle paths through the pump in the rotating impeller domain as well as in the stationary outlet area will be obtained to provide insight into the required time-dependent mechanical loading functions of particles.

Damage behaviour of red blood cells in bulk-flow, comparable to the strength property of engineering materials, has been well explored for the static mechanical loading case. However, the time-dependency of this process prohibits a simple comparison with the static strength of those materials. The damaging effects of a dynamic loading, as anticipated in the pump flow, are not known. Thus, experimental investigations of the haemolytic effects of a cyclic, sinusoidal laminar shear stress loading will be undertaken. Given the rheological properties of the cell membrane, haemolysis will not only be dependent on the stress amplitude and number of cycles but also on the frequency of loading. To study the effect of these three parameters a shearing device will be designed and operated within the shear stress amplitude and frequency ranges relevant to the conditions in a centrifugal pump.

Uniaxial stress regimes employed for haemolysis prediction under cyclic mechanical loading as well as for cell damage investigations under static loading need to be correlated to the three-dimensional stress condition in real blood flow phenomena. An analogy from solid mechanics in form of yield criteria will be taken. A suitable criterion will be chosen, modified and applied for the formation of a comparative stress theory for liquids. Thus, a comparative stress-time function of particles on their path through the pump will be established using the results of the numerical pump flow calculations. Being extremely irregular, these functions then need to be reduced to simple loading functions for which the haemolytic response is known by adoption of an appropriate classification method.

A hypothetical approach of correlating numerically obtained and classified mechanical loading functions of particles within a pump to an overall damage prediction with the help of a cumulative damage theory is the final aim of this work.

Chapter 4

General Blood Damage Prediction Model

4.1 Blood Damage Prediction Procedure

The knowledge of the correlation between an arbitrary mechanical loading of the blood and the amount of blood destruction in artificial circulatory devices and the natural circulation is vital for the prediction of lysis rates and the minimization of its causes. As stated previously, a general theoretical description of the damage process is very complicated if not impossible. Experimental data which could substantiate complex variants of the theory are difficult to obtain, especially under multiaxial loading. A general blood damage prediction model can therefore only have a hypothetical character. However, similar problems encountered with damage prediction models for engineering materials and equipment have not prevented the successful applicability of such models in practice.

Only the macroscopic or phenomenological plane, e.g. blood bulk flow phenomena, shall be considered within this model, consideration at the microscopic or cellular level takes place only in terms of rheological or constitutional properties of the blood cell membrane. Otherwise, cell-cell interactions have been insufficiently investigated to incorporate any results in the damage prediction model.

A definition of what is considered as damage in terms of blood cells has to

be made. In this thesis, the blood damage criterion will be that of detectable haemolysis of RBCs. A physiologically accurate definition of red cell damage would need to direct itself to the premature removal of cells by the spleen and the liver. This effect has been stated to occur at lower thresholds than those for haemolysis predictions [67]. Because of the lack of sufficient information on this process and given the advantages in predicting cell haemolysis, the above damage criterion was chosen. Failure, e.g. damage up to the degree of loss of function of the object, is considered as that level of critical haemolysis above which the body is unable to maintain haemostasis.

Influencing factors other than mechanical, such as temperature, blood pH, haematocrit, anticoagulant type and biochemical factors are referred to as non-mechanical parameters. There exists considerable variation in blood damage behaviour between individuals due in part to variations in these parameters. Prediction statements can therefore only be made within a statistical frame of probability.

The methodical procedure of a general blood damage prediction is schematically presented in Fig 4.1.

The starting point is the determination of the mechanical loading of the blood from the external loading imposed by output pressure head and rotational speed of the rotor, the pump geometry and the fluid material properties which effect flow and therefore loading conditions, i.e. density and viscosity. As a result the time-dependent stress distribution of the blood is obtained. These very complex and irregular functions need to be reduced to basic functions for which the response of blood is known from experimental investigations.

Since uniaxial stresses are applied in these experiments, a method of relating them to the three-dimensional stress tensor in real flow phenomena needs to be employed, for example by means of a comparative stress theory as described in Section 4.3. Having obtained mechanical loading functions of the blood volume of a classified basic order, the question, 'do they cause damage ?' has to be answered. This data reduction process is directly related to the damage resistance properties of the blood with respect to that particular mechanical

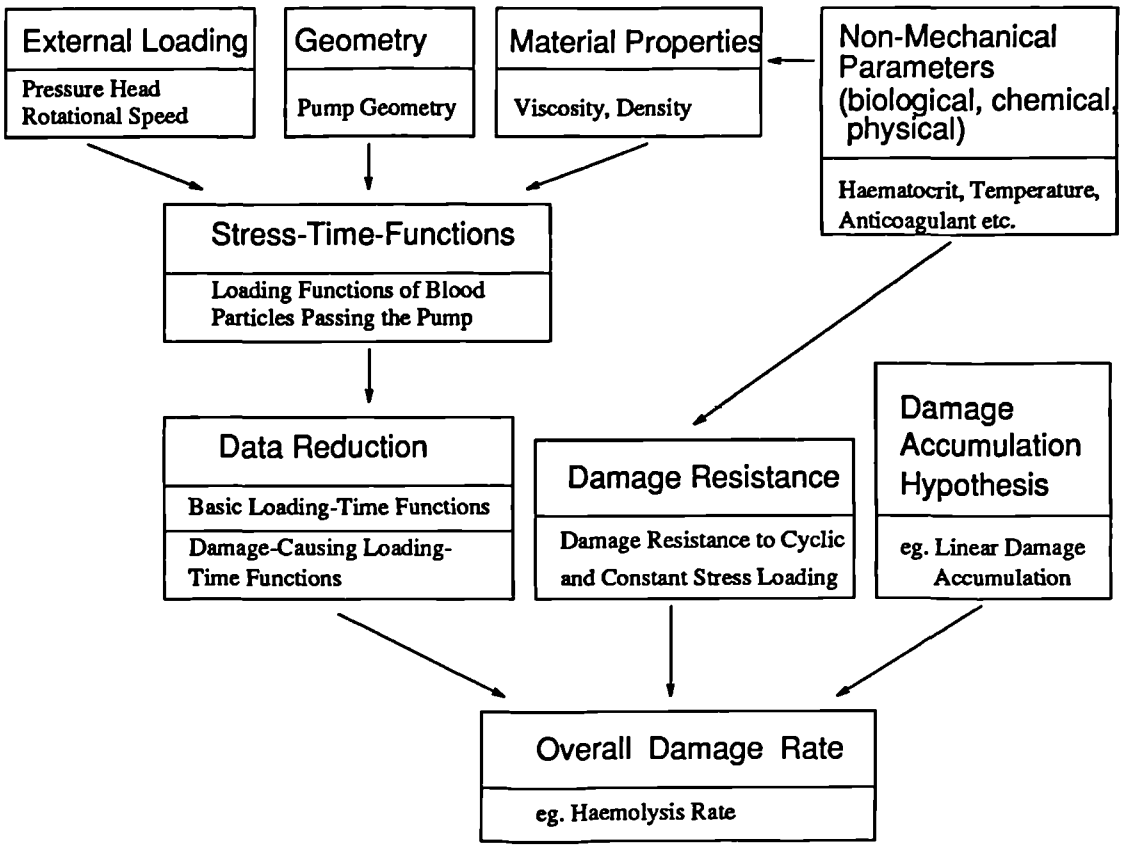

Figure 4.1: General mechanical blood damage prediction procedure.

loading. The data reduction procedure with its classification into damaging and non-damaging partial loadings has to take into account cumulative effects, e.g. the damage caused by combination of several different loading functions, which by themselves may not act in a destructive way.

The formulation of a damage accumulation hypothesis is undertaken in close relation to classical engineering approaches, aiming at generality and simplicity. Applying the damage accumulation hypothesis to the damaging partial loading functions, an estimation of the overall blood damage is thus made possible.

Non-mechanical parameters, as defined above, have a strong influence on the material properties within the stress analysis process as well as on the blood damage resistance behaviour. It emphasizes the individual character which a damage prediction theory must have when applied to a particular clinical case and the significance of a careful statistical analysis of the results.

4.2 Classification of Mechanical Loading

Throughout the proposed blood damage prediction theory, loading of blood particles will be referred to as the stresses and pressures in the bulk-blood-fluid acting externally upon the blood components. Stresses developed within the cell membranes in response to its mechanical environment are not considered because of the phenomenological approach chosen. They are, however, believed to act in an appropriate manner. Mechanical loading experienced by blood components can generally be treated as loading-time-functions and can be classified into monotonic, periodic and arbitrary functions with possible subdivisions according to Fig 4.2.

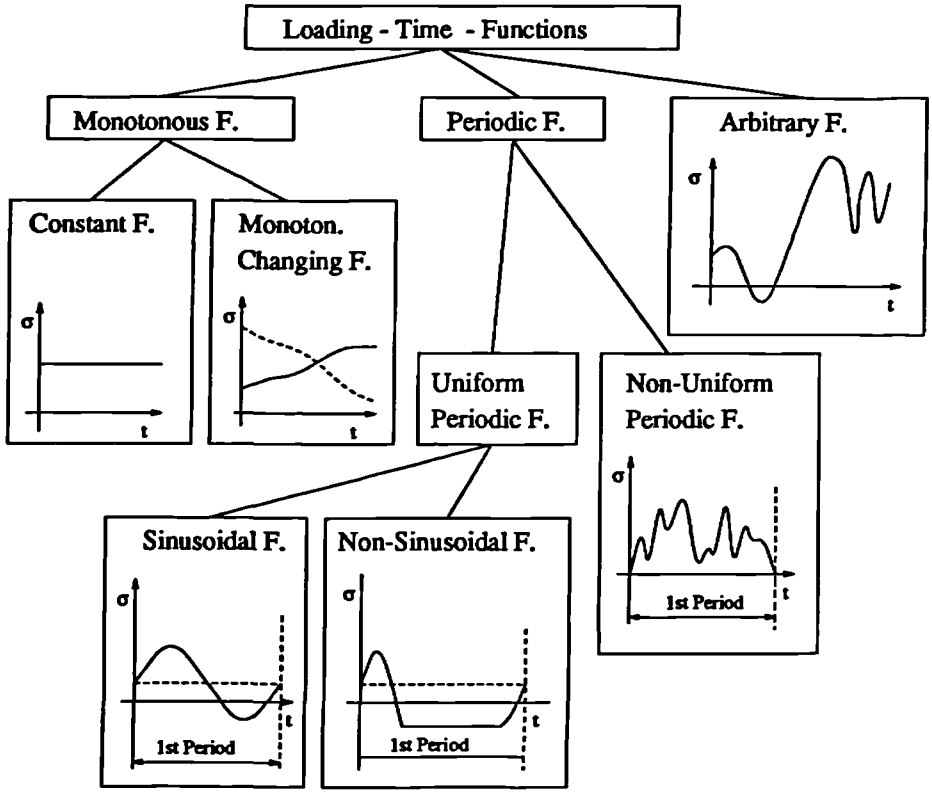

Figure 4.2: Classification of mechanical loading.

Mechanical loading of blood particles within the organism or an artificial device is most likely to be of an arbitrary nature. Monotonic and periodic time-functions are ideal cases possessing the property of easy reproducibility as required for systematic studies of the effects of mechanical loading on haemoly-

sis. In order to perform an assessment of the effects of an arbitrary loading, a reduction to those simpler functions is desirable.

Flow conditions existing, for example, in straight, unbranched arterial vessel segments or in the microcirculation may be reasonably represented as simple sinusoidal or constant flow, respectively. Geometrical and flow conditions in blood pumping devices , natural as well as artificial, lead to far more complex and irregular mechanical loading of blood particles and can not be simply assigned to one of the basic load-time functions. A reduction of these irregular time functions can be undertaken by means of a classification method. A filtering of harmonic functions with a particular amplitude and cycle number of appearance out of the complex function, for example, would thus allow a haemolytic assessment of the decomposed functions. which would in turn require a theory to predict the combined effect of those singular, harmonic blood loading functions.

Hydrodynamical stresses as the major mechanical loading parameter appear under the relevant blood flow conditions in the form of a three-dimensional tensor which would have to be set in relation to the uniaxial stresses applied in capillary or rotational viscometer haemolysis tests. A theory developed to obtain a representative one-dimensional stress parameter (scalar stress value) from the six components of the tensor is presented in the following section.

4.3 Comparative Stress Theory for Liquids

In general, the state of stress in the fluid must be specified by a knowledge of the six components of the stress tensor. A theory to relate this three-dimensional stress tensor to the known uniaxial stress responsible for damage processes is therefore needed.

This may be accomplished for engineering materials (metals, plastics and elastomers) from yield criteria which describe the yield stress as a function of the general state-of-stress [89, p. 63].

It is proposed that from the different yield criteria available, the Mises criterion would be the most suitable for addressing blood cell damage. This criterion

describes an overall resilience composed of the shear resilience and volume resilience. The volume resilience (hydrostatic state of stress) does not cause material destruction, so that only the shear resilience is considered for the comparison between one-dimensional and three-dimensional state of stress. The application of this assumption is supported by investigations which attribute shear stresses rather then hydrostatic pressures as the cause of blood cell damage [52].

The main assumptions of the Mises Criterion are as follows:

If σ_i are the principal stresses and ε_i the principal elastic strains, then the work done on an isotropic block in loading it from zero to σ_i is

$$\begin{aligned} W &= \frac{1}{2}\sum \sigma_i \varepsilon_i \\ &= \frac{1}{2E}\sum \sigma_i (\sigma_i - \nu\sigma_j - \nu\sigma_k) \\ &= \frac{1}{2E}\sum \sigma_i\sigma_i - \frac{\nu}{E}\sum \sigma_i\sigma_j \end{aligned} \tag{4.1}$$

$$i, j, k = 1, 2, 3; i \neq j \neq k$$

where E (Young's Modulus) and ν (Poisson's ratio) can be expressed by K (bulk modulus) and G (shear modulus) as

$$E = \frac{9KG}{3K + G} \tag{4.2}$$

and

$$\nu = \frac{3K - 2G}{6K - 2G}\,. \tag{4.3}$$

Thus,

$$W = \frac{\sum \sigma_i\sigma_i - \sum \sigma_i\sigma_j}{6G} + \frac{\sum \sigma_i\sigma_i + 2\sum \sigma_i\sigma_j}{18K} \tag{4.4}$$

The Yield Criteria Y by hypothesis of change of shape can then be expressed as

$$Y = W_s = \frac{\sum \sigma_i\sigma_i - \sum \sigma_i\sigma_j}{6G}\,. \tag{4.5}$$

The appropriate work rate done on a volume element of a viscous, incompressible fluid in laminar motion can be expressed similarly to Eqn. (4.1) with the Poisson's ration ν equal to 0.5 and $E = 2\mu$ in order to satisfy the equations for the three normal principal stresses in the fluid

$$\sigma_i = 2\mu \frac{\partial u_i}{\partial x_i}$$
$$i = 1, 2, 3 .$$

Considering that $K \rightarrow \infty$ for an incompressible material a boundary-value analysis yields values for $G = \frac{1}{3}E = \frac{2}{3}\mu$ and $\nu = \frac{1}{2}$, as stated above. The infinite bulk modulus justifies the reduction of the resilience to a mere shear resilience since the volumetric resilience is equal to zero.

Employing the relations between principal stresses and stresses in an arbitrary direction of the coordinate system [89, p. 71]

$$\sum \sigma_1 = \sum \sigma_{xx} \text{ and } \sum \sigma_1 \sigma_2 = \sum \sigma_{xx}\sigma_{yy} - \sum \sigma_{xy}^2,$$

Eqn. (4.5) can be rewritten using the six components of the arbitrary stress tensor in the following form

$$W_s = \frac{1}{12G}\left[\sum (\sigma_{ii} - \sigma_{jj})(\sigma_{ii} - \sigma_{jj}) + 6\sum \sigma_{ij}\sigma_{ij}\right] \tag{4.6}$$

$$i, j = r, \phi, z .$$

For the uniaxial shear experiments in a tube (steady or unsteady laminar flow) the following is relevant:

$$\begin{aligned} u_r = u_\phi &= 0 \\ \frac{\partial u_z}{\partial z} &= 0 \\ \sigma_{ii} &= -p \\ \sigma_{z\phi} = \sigma_{r\phi} &= 0 \\ \sigma_{rz} &= \sigma \end{aligned}$$

Hence, Eqn. (4.6) reduces to

$$W_s = \frac{1}{12G}\left[6\sigma^2\right] \tag{4.7}$$

Combining Eqns. (4.6) and (4.7), the yield criterion or comparative stress value is expressed as

$$\sigma = [2GW_s]^{\frac{1}{2}} = [\frac{1}{6}\sum(\sigma_{ii}-\sigma_{jj})(\sigma_{ii}-\sigma_{jj}) + 6\sum\sigma_{ij}\sigma_{ij}]^{\frac{1}{2}} \tag{4.8}$$

Equation (4.8) is derivable only for laminar flow. It was, however, applied in the same form for determining scalar stress values under turbulent flow conditions. The components of the overall stress tensor in this case are obtained merely from summation of the components of the viscous and Reynolds stress tensor. This expression now provides a means to assign a scalar value to a stress tensor at any point of the flow field.

4.4 Blood Resistance to Mechanical Loading

Failure behaviour of engineering materials is generally assessed by static and dynamic loading tests. Accordingly, the static and dynamic strength are those material characteristics to represent thresholds up to which the loading is withstood by the material or structure component without loss of its function.

Dynamical or endurance strength characteristics are often represented by a stress-service life-diagram named after Wöhler who performed endurance limit tests of locomotive rails in the last century [90, p. 51]. The characteristic for the service life is chosen as the number of cycles N of a uniform stress cycle sequence plotted on the log-scaled absissa of the diagram. The ordinate is a representative stress value, such as stress amplitude, often in logarithmic scale. The so-called Wöhler line divides the stress-cycle-domain into failure and non-failure, where the line itself represents values of a certain probability. Consideration of a third parameter, like temperature, environmental medium or frequency, leads to a band of lines. Change in frequency is often associated with thermal fatigue [91].

It has also been shown to influence service life under isothermal conditions [92, p. 87].

An example of a Wöhler line is shown in Fig 4.3. The stress axis is associated with three domains:

- Instantaneous failure if stresses are higher than the static strength σ_S
- Short-life time-strength with intermediate stresses between static and dynamic strength σ_D with strong dependency of the point of failure on the cycle number
- Long life or endurance strength with stresses below the dynamic strength which either cause no damage or lead to fatigue damage only after a very large number of cycles.

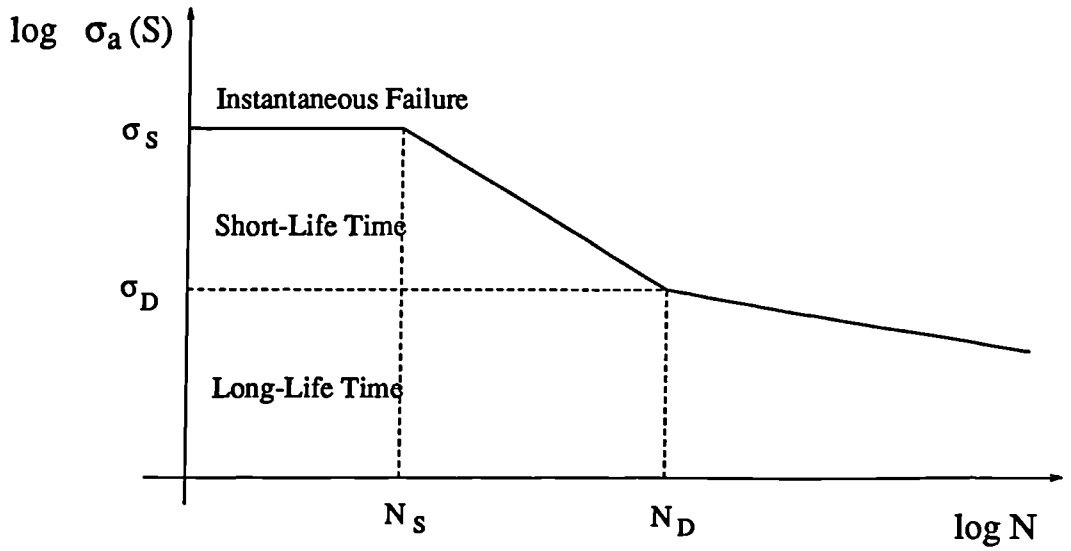

Figure 4.3: Wöhler line representing σ_a-N-dependency of material failure under cyclic mechanical loading.

Caution needs to be taken with application of these engineering methods to mechanical strength prediction of blood components, e.g. RBCs. One major obstacle lies in the complicated nature of stresses within the cell membrane in response to the external stress conditions applied. Even if the latter are uniform,

the responding membrane stresses are believed to be unsteady and location-dependent due to deformation and 'tank-treading' motion of the cell membrane around the cytoplasm. Interactions between cells and cell-wall contacts, as well as migration perpendicular to the flow axis are further factors of membrane stress instability. Nevertheless, the classification of external mechanical loading into well-defined, reproducible regimes appears to be the most favourable approach for blood damage predictions.

Studies on the haemolytic response to a constant shear stress loading have been performed extensively, see Chapt.2.3. Using different principles and devices for creating the constant shear stress loading, fair agreement was reached in observing a haemolytic response which differed from damage behaviour of engineering elastic materials. Damages commences not only at a certain value of shear stress but is also dependent on the exposure time of the cells to that stress. A satisfactory theoretical explanation for this behaviour does not yet exist, although the viscoelastic membrane property as well as non-constant membrane stress distributions have been proposed. Remaining at the phenomenological level and considering the well established haemolysis curve, presented in Fig 2.12 from [58], quantitative relations between extensive red cell lysis and a constant external (laminar or turbulent) shear stress and its duration can be obtained. Stress values below 50 Pa can be referred to as non-damaging for a duration of up to 100s. For the progression of haemolysis beyond its initial point Wurzinger [25] presented a quantitative expression (Eqn. 2.2). This formula should be only applied for the range in which it was predicted (15-700 ms exposure time; shear stresses up to 535 Pa).

Red blood cell resistance to a cyclic external shear loading has been investigated in the physiological vascular frequency and shear rate range (f $<$ 1Hz; $\dot{\gamma}$ $<$ 1000 $s^{-1} \cong \tau \simeq$ 3 Pa) [65]. Onset of haemolysis was recorded as a function of frequency, mean shear rate and shear rate amplitude. For example, haemolysis was observed after 3.6×10^3 cycles at a shear stress amplitude of 1 Pa with a frequency of 0.5 Hz. However frequencies of fluctuating shear stresses and stress

amplitudes acting upon blood particles which pass through a centrifugal blood pump are far higher. For example, the frequency with which a particle located at the stationary casing of a four-bladed impeller pump would experience the passage of the blades would be 130 Hz for a rotational speed of 2000 rpm. Maximal laminar shear stresses along an impeller blade were estimated by Papantonis [45] to be in the order of 50 Pa.

To provide information on damage behaviour of red blood cells under cyclic loads appropriate to centrifugal pump operation, experimental haemolysis tests are undertaken, as described in Chapter 5. Apart from the dependency of cell destruction on a representative stress magnitude and the number of cycles, the loading frequency is believed to be a third major parameter of influence with respect to the viscoelastic membrane properties. Bearing in mind that these cyclic shear stress loading experiments are at an early stage and that the nature of haemolysis under a constant shear stress load is largely unexplained, one should not expect an unambiguous, quantifiable outcome. They are, however, necessary and even qualitative results are a step forward in the analysis of complex, time-dependent mechanical blood damage phenomena.

The incorporation of a quantitative relation between haemolysis and a steady or unsteady pressure loading into a blood damage model has not been considered because of the highly contradictory reports on the matter in the literature. However, extreme values of pressure ($<$- 1/3 bar or $>$ 3 bar) should be implicated in the damage process.

4.5 Damage Accumulation Hypothesis

Whereas blood tested in a conventional apparatus, e.g. rotational viscometer or capillary tube, is subjected to a cyclic shear stress of constant amplitude or a steady constant shear stress, it experiences under *in-vivo* flow conditions an irregular shaped loading function. A reduction of this arbitrary load into a set of simple time functions, as described in Chapt 4.2., provides a means of correlating those singular loading functions to their damaging effects. Their interaction and

partial influences in the overall destruction process is, however, unknown.

In the life prediction process of engineering materials and structural components the investigation of fatigue under varying stress amplitudes has come to be known as the study of cumulative damage, because of the interest of how fatigue damage at various stress levels accumulated [90, pp. 58–61], [92, pp. 307–330]. A damage accumulation hypothesis provides a connection between results from one-level loading tests and the multi-level load under working conditions on the basic assumption that damage is accumulated at the various load levels. In cumulative damage tests varying from simple two-level step tests, repeated block tests to random load tests, as described by Frost [92, pp. 307–330], data were obtained for deriving appropriate empirical relationships or to prove or disprove theoretical predictions.

A life prediction hypothesis which is based on the assumption of a linear damage accumulation was suggested by Palmgren and Miner [93]. It assumes that during the action of a uniform stress cycle sequence an uniformly progressing damage occurs. If a dimensionless damage parameter D is defined which initially equals zero and reaches the value 1 at the point of failure (or fracture) at the failure cycle number N, then the partial damage after n cycles will be n/N of the damage failure, termed as the cycle ratio. Based on this assumption, failure of materials under a multi-level stress with stress amplitudes S_i is expressed as

$$1 = \frac{n_1}{N_1} + \frac{n_2}{N_2} + \frac{n_3}{N_3} + \ \ldots \ = \sum \frac{n_i}{N_i} \ . \tag{4.9}$$

Eqn. (4.9) is referred to as cumulative linear damage law or Palmgren-Miner law.

Inaccuracies of the linear damage accumulation hypothesis and the lack of its sufficient physical explanation led to a number of alternative theories to predict service life under varying amplitudes, some wholly empirical, others with some physical basis. For example, a power-law relationship between damage and

cycle ratio has been suggested [92, pp. 307–330], thus considering a non-linear, cycle-number dependent damage process where the degree of non-linearity is a function of the stress amplitude. Two imaginary damage curves for two applied stress levels are presented in Fig 4.4a, where the damage is calculated as

$$D = (n_1/N_1)^a = (n_2/N_2)^b \ , \ (b > a) \ .$$

If a=b=1, the relations reduce to the linear damage law.

Another exponential damage progress theory was developed by Cortan and Dolan, who assumed that the number of damage initiation nuclei m is dependent on the stress level and that at the same time the progression of damage occurs with a velocity r, increasing with duration and amplitude of loading, see Fig 4.4b. However, the amount of total damage is constant for all cyclic loading levels and can be expressed for two different levels as

$$D_{tot} = m_1 r_1 N_1{}^{a_1} = m_2 r_2 N_2{}^{a_2}$$

where a_1, a_2 are exponents which express the degree of non-linearity.

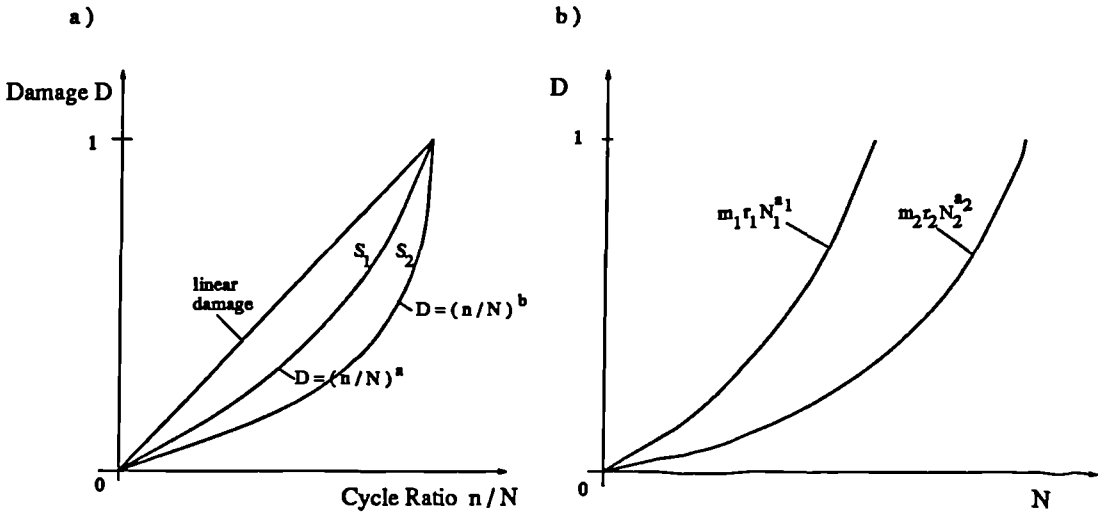

Figure 4.4: a) Power-Law damage accumulation, b) Damage accumulation after Cortan, Dolan.

Possible interactive effects between one stress level and another, such as change of fatigue properties of materials under the action of a cyclic preloading

are considered in the so-called secondary Wöhler lines or sequential Wöhler lines [94].

It has been stated, however, that the more complex the rules for a damage accumulation hypothesis are, the more cumbersome they are to apply and the more restricted they are to certain conditions or materials. Considerable experience is required in their application in order to achieve accurate predictions [92].

Returning to the task of predicting blood cell damage under a mechanical load varying in amplitude and frequency, common and distinctive features of the two areas need to be examined in order to establish an appropriate blood damage theory.

Current knowledge of blood cell behaviour under mechanical loading is, unquestionable, very immature and limited, especially under dynamical loading conditions.

To the author's knowledge no attempt has been made so far to correlate different loading mechanisms regarding their combined effect on cell destruction neither for singular cases nor on a general basis. For this lack of information, a damage accumulation theory can only have a mere hypothetical character. Such a hypothesis must, however, meet the requirement to be universal applicable and physically sensible in a broadest sense by taking into account basic relations which were observed and established with sufficient confidence.

A damage accumulation hypothesis of red blood cells as representative of blood components is formulated in the following.

Without anticipating the results of the dynamic load tests performed in this thesis, the amount of red blood cell damage is expected to be dependent on the amplitude of acting stresses, on their duration or cycle number and on the frequency. Amplitude and duration dependencies have been confirmed by static loading tests. Haemolysis progresses with the duration of applied constant shear stress where the exposure time necessary to reach a certain degree of haemol-

ysis decreases with increasing stress magnitude (see Chapter 2.3. for details). The exact form of this functional relationship is not known, although Wurzinger [25] obtained a power-law relationship between the amount of haemoglobin liberation and the stress magnitude and exposure time. However, limitations in the experimental range of parameters and discrepancies with the established haemolysis-threshold curve, see Fig 2.14, cast doubts about the accuracy and general applicability of this relationship. For the purpose of simplicity and generality an assumption is made here, that a linear relation between haemolysis as the damage D with $0 \leq D \leq 1$ and constant stress exposure time exists and may be expressed by

$$D = \frac{t}{T_{crit}(\tau_{mag})} \tag{4.10}$$

with T_{crit} being referred to as critical exposure time at which the failure in form of unrepairable amount of haemolysis occurs, itself a function of the stress magnitude. Values for T_{crit} are obtained from the haemolysis-threshold curve in Fig 2.12.

Assuming a positive cycle number dependency of haemolysis in cyclic shear stress experiments, a similar damage function may be formulated as

$$D = \frac{n}{N_{crit}(\tau_{ampl}, f)} \tag{4.11}$$

where N_{crit} is the analogous critical cycle number, being a function of the stress amplitude and frequency. This latter assumption will have to be verified by the cyclic loading experiments described in Chapter 5.

The question of how damage of different stress amplitudes and frequencies accumulates cannot be answered at this point. To keep the cell damage accumulation hypothesis as simple as possible a linear damage accumulation of different single load regimes will be assumed. Using the definition of the Miner rule, the overall damage may be imagined as the sum of damages under different constant

and cyclic shear stresses each having their critical exposure time or critical cycle number

$$D = \sum_{i=1}^{M_{\sigma con}} \frac{t_i}{T_i} + \sum_{j=1}^{K_{\sigma cyc}} \frac{n_j}{N_j(f)} \,. \tag{4.12}$$

In Eqn. (4.12), the critical cycle number at a given stress amplitude is shown as a function of the frequency of the applied stress, an assumption which will require verification and evaluation by the cyclic stress experiments. Applying Eqn. (4.12) for haemolysis prediction of cells under a varying mechanical loading, one has to be aware of the high degree of idealization and additive effects of simplifying assumptions.

A wide open field is also the influence of non-mechanical parameters on the progression of blood damage as well as on the damage accumulation properties. A precise, more generally valid damage accumulation hypothesis is seen as a necessity for future investigations. However, for the time being, the proposed theory is a simple and useful tool for a general damage prediction and enables consideration of real blood flow conditions.

Chapter 5

Blood Trauma under Cyclic Mechanical Loading

5.1 Selection of Loading Principle

Blood flow in the natural circulatory system and in artificial devices is of an unsteady nature, leading to a time-dependency of its mechanical loading parameters, namely shear stresses and pressure. Damage models therefore need to take account of a dynamic loading process in assessing the haematological response. According to the general mechanical damage prediction procedure, formulated in Chapter 4, the task consists in combining information about the actual loading conditions, as performed for the particular case of blood flow through a centrifugal blood pump in Chapter 6, with blood damage resistance properties.

Systematic tests to investigate haematological responses require the application of well-defined loading conditions, such as a constant or an uniform-periodic time function. Knowledge of blood destruction behaviour especially under a sinusoidal mechanical loading is important since an arbitrary time-dependent function can be decomposed into a set of harmonic functions.

With respect to the selection of haemolysis to represent blood trauma in the general damage prediction model, special attention will be paid in this study to the lysis of RBCs under an oscillating mechanical load. Investigations will

be concentrated on shear stress as a mechanical loading parameter. Pressure fluctuations, although omitted in this approach, will certainly need a closer look in the future.

The frequency and amplitude ranges of existing haemolysis investigations under an oscillating shear stress loading were limited to a 'physiological' level of f $\leq$ 1 Hz and shear rates $\dot{\gamma} < 1000$ s^{-1} corresponding to shear stresses $\tau \leq$ 3 Pa [65]. The actual stress loading of blood particles that occurs within the strongly non-uniform flow of a blood pump (as determined in Chapter 6) or during passage through a heart valve [95, 96] is, however, of far higher amplitude and frequency.

In order to examine the haemolytic response to an oscillating stress with an extended range of parameters (for instance $\tau_a < 100$ Pa, f < 100 Hz), an appropriate shearing principle and device have to be selected. Besides achieving the desired performance, an important mechanical requirement in such an apparatus is to produce a well-defined, analysable flow regime.

Couette-type viscometers employing an oscillatory driving mechanism as described by Billington [97], Copley [98] and Hashimoto [65] are unable to produce the required shear rate amplitudes and frequencies. Also, a well-defined flow might not be ensured in an oscillatory circular Couette device. Instabilities of the flow field which lead to a variety of regimes differing strongly from Couette flow have been observed and analysed . A transition diagram of those flow regimes for the case of concentric cylinders, which rotate independently with a constant rotational speed, is given by Andereck [99] (Fig 5.1).

Dependent parameters are the inner- and outer-cylinder Reynolds numbers R_i and R_o calculated as $R_i\{R_o\} = a\{b\}(b\text{-}a)\,\Omega_i\{\Omega_o\}/\nu$ with a and b being the inner- and outer-cylinder radii, $\Omega_i\{\Omega_o\}$ the angular velocity of the inner {outer} cylinder and ν the kinematic viscosity. The Couette flow developed with the inner cylinder being at rest and for a certain range of low Reynolds numbers was obtained with a slow acceleration of the outer cylinder from rest to its final rotational rate. Transition boundaries were defined as stable for average angular

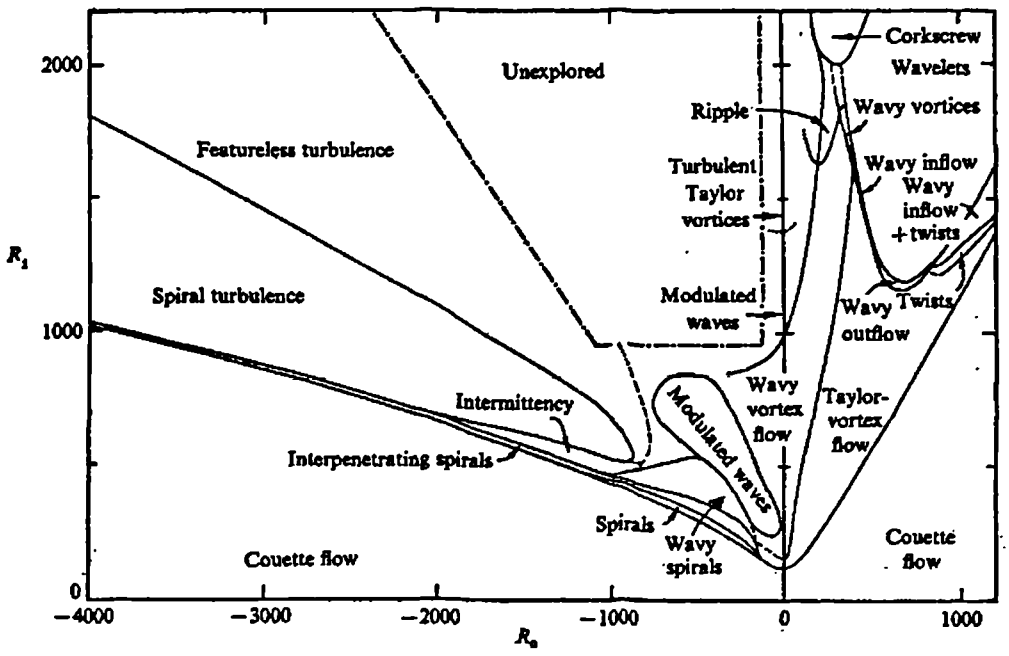

Figure 5.1: Regimes observed in flow between independently rotating concentric cylinders.

accelerations of less than 0.15 rad/min^2 [99]. Since high acceleration rates are unavoidable in the considered frequency range, caution needs to be taken in stating the existence of a pure Couette flow even in the case of rotating the outer cylinder (cone, disc).

Couette flow within transversely oscillating parallel walls presents a possible alternative. However, the need to produce a highly accurate device and practical difficulties in sealing the translating part as well priming the system and withdrawal of blood samples led to the rejection of this otherwise physically acceptable concept.

Capillary tube viscometers with a developed Poiseuille flow are not subjected to secondary flow phenomena. The flow is well-defined for the steady-flow case as well as for an axial oscillatory movement. The disadvantage of a non-constant shear stress distribution over the radius compared to its uniformity for Couette flow in a constant flow regime, vanishes for a time-dependent motion. Fluid

particles in both cases are subjected to radius-dependent amplitudes.

Considering the above facts, a capillary tube geometry was found suitable to perform oscillating shearing experiments with the necessary accuracy and reproducibility.

To produce the desired shear stress distribution by creating a harmonic axial motion of the blood column relative to the capillary walls, two main principles can be distinguished. Firstly, the movement of the fluid within a stationary capillary tube can be achieved by applying an external oscillating pressure gradient. Secondly, an oscillating movement of the capillary tube itself results in the desired relative motion between blood column and walls due to inertia effects. A combination of both concepts may, of course, be considered.

The oscillating tube principle was selected as this avoids problems of critical tube entrance and exit effects [27] as well as problems of sealing and heat development (for example in a piston-drive unit) that are associated with a pressure driven system.

The hydrodynamic theory for the flow within an oscillating capillary tube and examples of velocity and shear stress distributions are given in the following section. The experimental setup as well as the selection of the optimal geometrical and kinematic parameters are described in Section 5.3.

5.2 Physical Model of Flow Within An Oscillating Capillary

The basic equations describing the motion of a viscous, incompressible, Newtonian fluid under the influence of internal forces (pressure and shear stresses) are:

$$\rho\left(\frac{\partial \mathbf{v}}{\partial t} + (\mathbf{v}\cdot\nabla)\mathbf{v}\right) = -\nabla p + \eta\nabla^2\mathbf{v} \tag{5.1}$$

Here, the simplifying assumption of neglecting the surface tension forces has been made.

For the case of fluid motion in a rigid tube of circular cross section, cylindrical

symmetry (no ϕ-dependence) can be assumed, in which the fluid flow is always parallel to the tube axis ($\mathbf{v} = v\hat{\mathbf{k}}$). We find

$$\frac{\partial p}{\partial r} = 0 \quad ; \quad \frac{\partial p}{\partial \phi} = 0$$

$$\rho\left(\frac{\partial v}{\partial t} + v\frac{\partial v}{\partial z}\right) = -\frac{\partial p}{\partial z} + \eta\left(\frac{1}{r}\frac{\partial}{\partial r}\left(r\frac{\partial v}{\partial r}\right) + \frac{\partial^2 v}{\partial z^2}\right). \tag{5.2}$$

The continuity condition $\nabla \cdot \mathbf{v} = 0$ allows us to deduce that $\dfrac{\partial v}{\partial z} = 0$. In addition, for the non-existence of an external pressure gradient, physical constraints at the endpoints of the tube ensure that $\dfrac{\partial p}{\partial z} = 0$. Hence, Eqn. (5.2) becomes

$$\rho\frac{\partial v}{\partial t} = \frac{\eta}{r}\frac{\partial}{\partial r}\left(r\frac{\partial v}{\partial r}\right). \tag{5.3}$$

Separation of Eqn. (5.3) into independent time and spatial equations is achieved by setting $v(r,t) = v_r(r)v_t(t)$:

$$\frac{1}{v_t(t)}\,\frac{dv_t}{dt} = \frac{\eta}{\rho}\,\frac{1}{v_r(r)}\,\frac{1}{r}\,\frac{d}{dr}\left(r\frac{dv_r}{dr}\right). \tag{5.4}$$

Since the left hand side of this equation depends only upon t while the right hand side is determined by r, the two halves may independently be equated to a constant value, $-k$:

$$\begin{aligned} \frac{dv_t}{dt} &= -k\,v_t \\ r^2\,\frac{d^2v_r}{dr^2} + r\,\frac{dv_r}{dr} &= -\frac{k\rho}{\eta}\,r^2\,v_r. \end{aligned} \tag{5.5}$$

The first of these yields the time dependent part of the solution,

$$v_t(t) = e^{-kt}. \tag{5.6}$$

Clearly, this formula only leads to acceptable solutions if $k > 0$. In this case, the second equation is recognizable as Bessel's equation of order zero, and may be solved in terms of Bessel functions [100, 101], see Appendix A, to find the radial solution

$$v_r(r) = A\,J_0(\lambda r) + B\,Y_0(\lambda r), \tag{5.7}$$

where $\lambda^2 = k\rho/\eta$. Physical constraints require that the Y_0 function does not appear in the solution ($B = 0$), so that

$$v(r,t) = v_r(r)v_t(t) = A\,J_0(\lambda r)\,e^{-kt}. \tag{5.8}$$

Steady-state solutions may be found by eliminating the time dependence, that is, by choosing $k = 0$. In this case $\lambda = 0$ and solution (5.8) becomes

$$v(r,t) = v_0. \tag{5.9}$$

Oscillating solutions may be found almost as simply. If both sides of equation (5.4) are equated to an imaginary value $i\omega$, $\omega > 0$, the solutions (5.6) and (5.7) then take the form below:

$$\begin{aligned} v_t(t) &= e^{i\omega t} \\ v_r(r) &= A\,J_0(i^{3/2}\lambda r) = A\,[\,\mathrm{ber}(\lambda r) + i\,\mathrm{bei}(\lambda r)\,], \end{aligned} \tag{5.10}$$

where λ is now given by $\lambda^2 = \omega\rho/\eta$. In (5.10), ber and bei denote the real and imaginary parts of the Bessel function, respectively, which are listed in Appendix A. The independent solution, $v_r(r) = A\,K_0(i^{1/2}\lambda r)$, must be rejected due to physical considerations. If $\omega < 0$, we set $\lambda^2 = -\omega\rho/\eta$, leading to the solution:

$$v_r(r) = A\,J_0(i^{1/2}\lambda r) = A\,[\,\mathrm{ber}(\lambda r) - i\,\mathrm{bei}(\lambda r)\,]. \tag{5.11}$$

Combining both time and space parts of the former solution, we find

$$v(r,t) = A\,J_0(i^{3/2}\lambda r)\,e^{i\omega t}. \tag{5.12}$$

That is,

$$\begin{aligned} v(r,t) = A\,\Big[\,&\mathrm{ber}(\lambda r)\cos(\omega t) - \mathrm{bei}(\lambda r)\sin(\omega t) \\ &+ i\,(\mathrm{ber}(\lambda r)\sin(\omega t) + \mathrm{bei}(\lambda r)\cos(\omega t))\,\Big]. \end{aligned} \tag{5.13}$$

If the velocity of the moving tube is given with $v(R,t) = v_0 e^{i\omega t}$ then the coefficient A becomes

$$A = \frac{v_0}{J_0(i^{3/2}\lambda R)} = v_0\,\frac{\mathrm{ber}(\lambda R) - i\,\mathrm{bei}(\lambda R)}{\mathrm{ber}(\lambda R)^2 + \mathrm{bei}(\lambda R)^2}\,. \tag{5.14}$$

with R denoting the tubes's inner radius.

Taking only the real part of solution (5.13), we find eventually the velocity distribution within the tube,

$$
\begin{aligned}
v(r,t) = & \frac{v_0}{\mathrm{ber}(\lambda R)^2 + \mathrm{bei}(\lambda R)^2} \cdot \\
& \Big[\mathrm{ber}(\lambda R) \ \{ \ \mathrm{ber}(\lambda r)\cos(\omega t) - \mathrm{bei}(\lambda r)\sin(\omega t) \ \} + \\
& \quad \mathrm{bei}(\lambda R) \ \{ \ \mathrm{ber}(\lambda r)\sin(\omega t) + \mathrm{bei}(\lambda R)\cos(\omega t) \ \} \Big] .
\end{aligned}
\tag{5.15}
$$

The time-dependent radial shear stress distribution is obtained by

$$
\begin{aligned}
\tau_{xr}(r,t) = & \ \mu \ \frac{\partial v(r,t)}{\partial r} \\
= & \ \mu \cdot \frac{v_0}{\mathrm{ber}(\lambda R)^2 + \mathrm{bei}(\lambda R)^2} \cdot \lambda \cdot \\
& \Big[\mathrm{ber}(\lambda R) \{ \ \mathrm{ber'}(\lambda r)\cos(\omega t) - \mathrm{bei'}(\lambda r)\sin(\omega t) \ \} + \\
& \quad \mathrm{bei}(\lambda R) \ \{ \ \mathrm{ber'}(\lambda r)\sin(\omega t) + \mathrm{bei'}(\lambda R)\cos(\omega t) \ \} \Big] .
\end{aligned}
\tag{5.16}
$$

where ber' and bei' denote the derivative of the real and imaginary part of the Bessel function of first order with respect to the radius, listed in Appendix A.

In order to assign a characteristic shear stress value to a cross section of the fluid column where its elements experience a radius-dependent shear stress loading, a bulk shear stress is defined as follows:

$$
\tau_b(t) = \frac{1}{\tau_m(t)} \frac{2\pi L}{V} \int_0^R \tau(r,t)^2 r dr \tag{5.17}
$$

with

L – *length of the fluid column*

V – *volume of the fluid column*

τ_m – *arithmetic mean value of absolute shear stress magnitude*

A similar approach was used by Ramstack [70] for steady tube flow.

The weighting factor r in the shear stress integration over the radius ensures the consideration of the volume portion exposed to a particular radial stress value. Integration of the square values instead of absolute magnitudes of

the shear stress is performed to avoid difficulties in the numerical integration procedure. They are normalised by their arithmetic mean value.

Velocity and shear stress distributions over one time period for a certain oscillation frequency, tube radius and viscosity are plotted in Figs B.1 and B.2 in Appendix B. The graph of the corresponding bulk shear stress over one time period is shown in Fig B.3.

The restriction on positive bulk shear stress values must be seen as a result of the idealizations used, bearing in mind that every radial fluid layer experiences in fact an oscillating shear loading with a mean value equal to zero. The maximum value of the periodic bulk shear stress τ_b is therefore taken as the representative radial value of the shear stress amplitudes of the different radial layers.

The applicability of the proposed theory for the specific case of the motion of a blood column in an oscillating capillary tube will now be discussed.

Blood as a cell-plasma suspension does not satisfy the assumption of a homogeneous fluid. Also, constitutional relations reveal a non-Newtonian behaviour at shear rates below approx. 100 s^{-1} [102]. Studies of the former property of a cell suspension in a steady tube flow by Goldsmith [51] showed axial centerline velocities being smaller than for Poiseuille flow at the same flow rate. It is assumed that differences under dynamic flow conditions are determined by inertia effects, therefore strongly influenced by acceleration and deceleration values and hence, for a harmonic movement, frequency-dependent. Shear rate values below the critical threshold for Newtonian behaviour exist only in the axial region which is associated with a very small portion of the overall fluid volume.

The existence of a merely axial tube flow has been disproved for steady blood flow in small capillaries ($d < 500\mu m$) [102]. A tendency of radial migration of cellular blood components was observed under these conditions (Fahraeus effect), so flow does not obey Poiseuille's equation for flow of Newtonian fluids through tubes. For tubes with a diameter exceeding 500 μm this effect has not been shown.

In summary, the formulation of a continuum mechanics theory for the motion of a Newtonian fluid in an oscillating capillary tube presents an ideal case.

Deviation of blood flow from the postulated theory can be expected, but is assumed minimal when the conditions mentioned above are satisfied. Furthermore, with the simplification of a bulk shear stress as the representative value across the tube radius, the effort involved in formulating a more accurate, blood flow-specific theory is not warranted, especially when basic relations under dynamic conditions have not yet been sufficiently investigated.

5.3 Experimental Setup

In order to perform an axial oscillating motion with high amplitude and frequency ranges, an appropriate driving mechanism had to be chosen. The electromagnetic vibrator Derritron VP4 (Derritron Electronic Vibrators Ltd.) was found suitable for this task. This high performance, wide frequency range (1.5

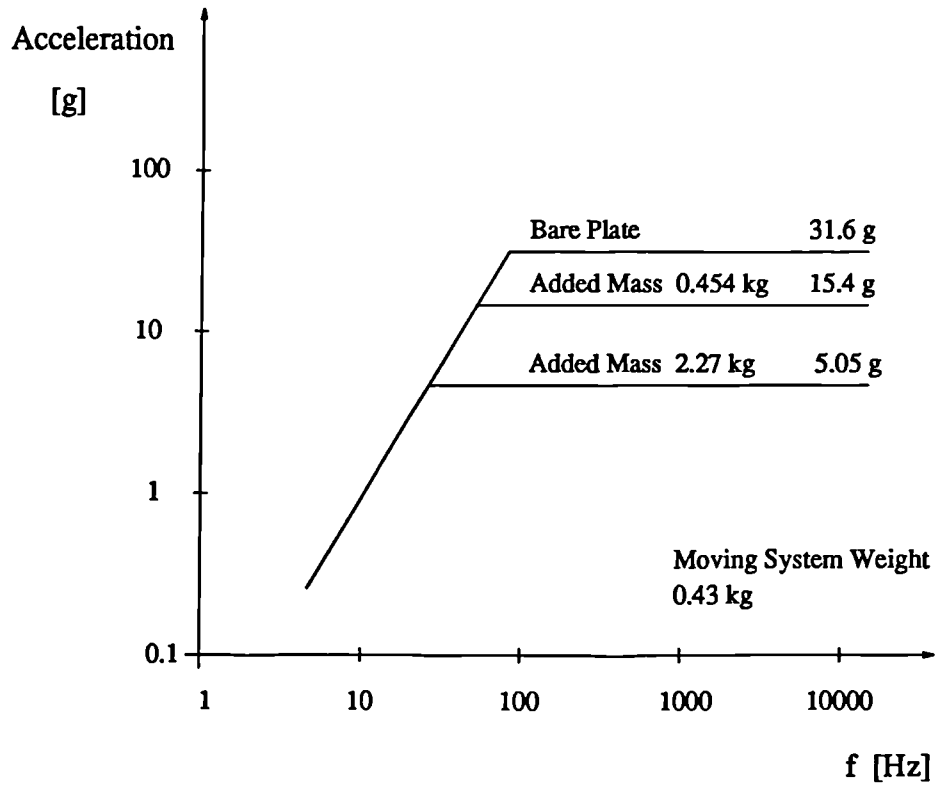

Figure 5.2: Performance curve of vibrator VP4 (Derritron Electronic Vibrators Ltd.).

Hz-10 kHz), permanent magnetic field vibrator with the lightweight moving

Frequency $[Hz]$	*Max. displacement* $[mm]$	*Corresp.* τ_{bmax} $[Pa]$
20	7.40	11.7
25	6.40	15.1
30	5.50	17.8
40	5.60	28.3
50	5.00	35.1
60	3.45	30.7
70	2.28	24.3
80	1.60	20.1
90	1.20	17.3
100	1.00	16.2

Table 5.1: Frequency-dependent maximum displacement amplitudes of vibrator Derritron VP4 and corresponding bulk shear stress amplitude for tube radius R=0.315 mm and haematocrit Hct=0.42.

plate cast in a heavy magnesium alloy provides a stiff and robust assembly with a smooth and useful frequency response. Driven by a 100 W amplifier, the moving table, weighing 0.43 kg, is accelerated at 31.6 g (see performance curve in Fig 5.2) with a stated maximum peak-to-peak displacement of 6.35 mm. The actual maximum displacement amplitudes in operation were found to be higher and dependent on the frequency within the range of interest (Table 5.1). A device to hold the capillary tubes and in turn connected to the vibrator plate was designed. Geometrical requirements of this design were determined by several parameters. The capillary diameter was chosen in order to achieve a maximum shear stress, according to values presented in Appendix B (Fig B.4). The amount of blood volume and therefore capillary length and number of capillaries were determined by the minimum volume of blood plasma necessary for the haemoglobin analysis procedure. Furthermore, undesired vertical vibrations in a horizontal position of the capillaries increase with increasing length of the capillaries. A higher statistical significance of the results is achieved with a larger number of capillaries.

As a result of these considerations, an aluminium box was fabricated which could be mounted on a shaft providing the connection to the moving plate of the vibrator. Slots were milled into the box base to hold 10 capillaries of 0.63

mm inner diameter and a length of 12.5 cm (CAMLAB Ltd.). The technical drawing of the box and the connection piece to the vibrator plate are shown in Figs 5.3 and 5.4, respectively. Silicone rubber tubes are slipped on the ends of the capillary and angled upwards to prevent blood spillage. The box is closed with a plastic plate screwed onto the box for safety reasons as well as to enable control of environmental conditions for the blood-air interface.

Since fresh human venous blood was used for the study, haemolytic effects due to oxygenation processes [58] may occur because the blood column is exposed to atmosphere at the capillary ends. This effect was minimised by purging the box with a constant flow rate of a 5% O_2/5% CO_2/N_2 gas mixture. Gas flow was measured with a variable area flowmeter (Rotameter, Brooks Instruments) and maintained at 200 ml/min. Adequate gas outflow was ensured by a hole in the opposite corner of the box.

A simultaneous measurement and monitoring of the vibrator's motion was provided by attaching acceleration sensors, SUPER-G (Hakuto International (UK) Ltd.), to the box and displaying acceleration curves on an oscilloscope. SUPER-G is a low frequency, compact and light sensor made of a piezoelectric plastic material showing high sensitivity with good separation in horizontal and vertical directions. In a frequency range of 0.5-500 Hz acceleration values of 0.1-25 g (g - gravity acceleration) are detected. The sensitivity of the accelerator is S=200 mV/g. Acceleration, displacement and velocity amplitude values can thus be obtained using Eqn. (5.18).

$$a = \frac{U}{S} \qquad x = \frac{a}{\omega^2} \qquad v_0 = \omega \cdot x_0 \tag{5.18}$$

with a -acceleration, U - accelerator voltage output, $x(_0)$ - displacement (amplitude), v_0 - velocity amplitude, ω - angular frequency.

Measured oscillations in the vertical direction at the outer end of the box showed magnitudes of up to a quarter of the horizontal values. In order to prevent those undesired off-line movements, a damping mechanism consisting of a thick-walled silicone rubber tube was fixed vertically to the box reducing vertical vibrations to a maximum value of 5% of the horizontal vibrations.

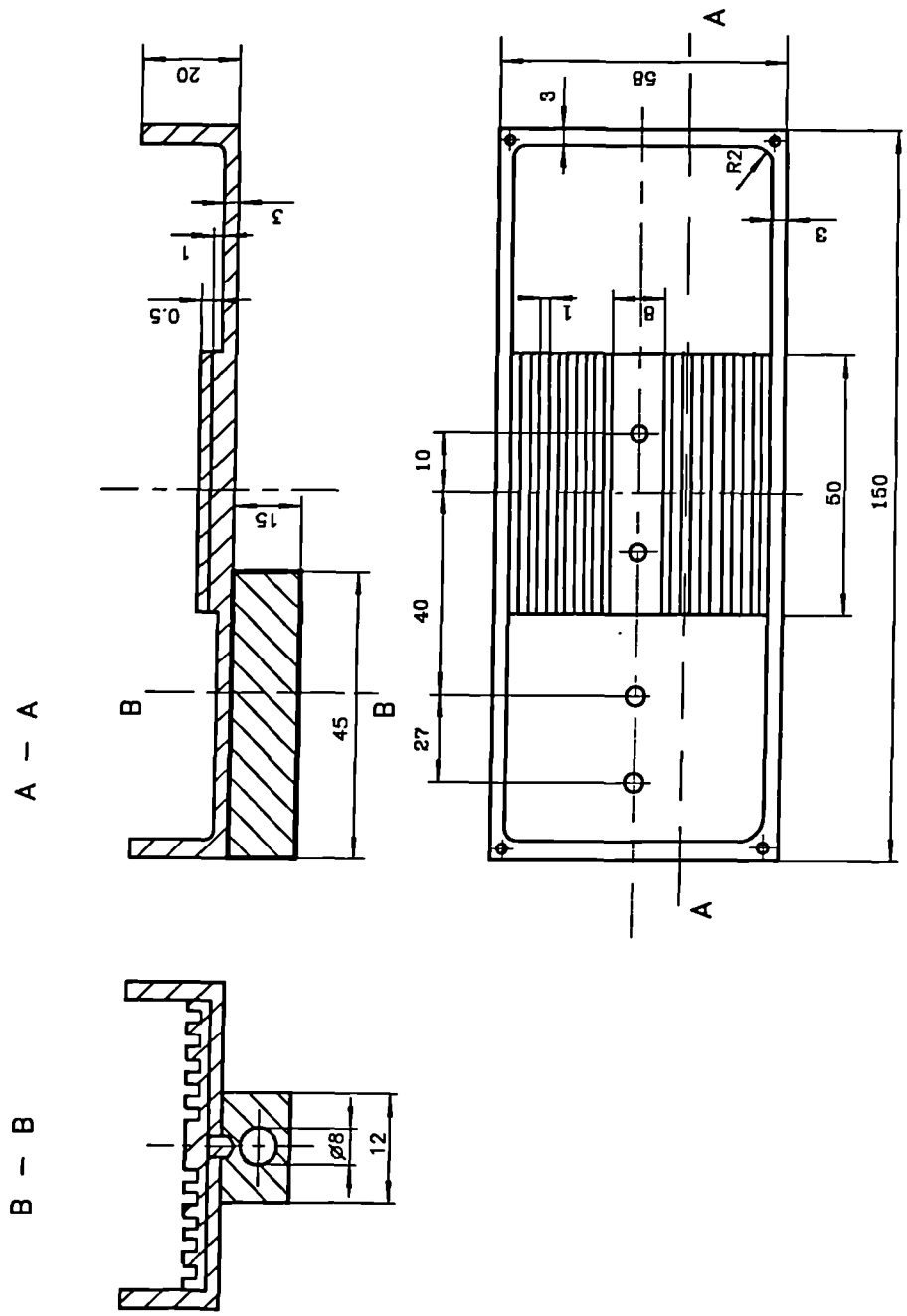

Figure 5.3: Box to hold capillary for oscillating shear stress experiments. All dimensions in mm.

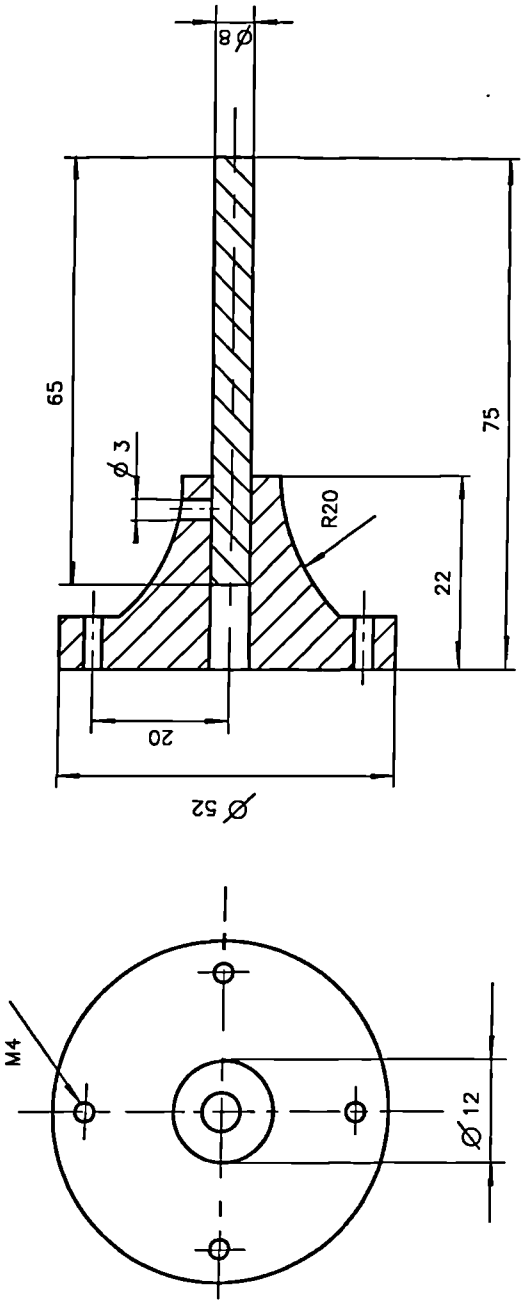

Figure 5.4: Connecting piece between vibrator and box. All dimensions in mm.

Fig 5.5 shows the layout of the entire experimental setup.

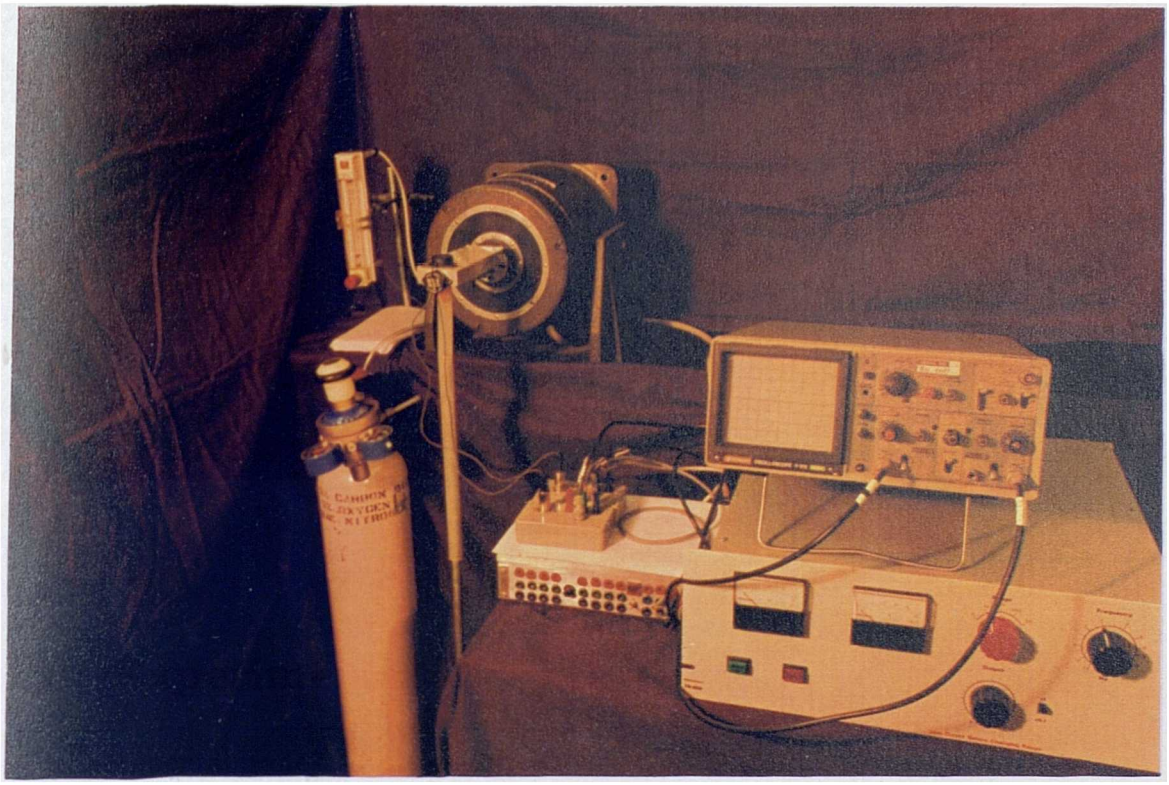

Figure 5.5: Experimental setup.

5.4 Experimental Regime

The experimental protocol for haemolysis evaluation under an oscillating shear stress loading comprised the following phases: pre-experimental, i.e. blood collection and preparation; experimental, which is the sequence of performing the tests, and post-experimental, i.e. blood analysis.

Pre-Experimental Phase

Haemolysis studies were performed with human blood obtained by venepuncture from two healthy, non-smoking volunteers. Immediately after withdrawal, the blood was anticoagulated by filling it into standard heparinized 5-ml or

10-ml tubes containing 9-11 units (75 μg) and 18-22 units (150 μg) heparin, respectively. Heparin was preferred to EDTA, another standard anticoagulant, since test runs in which blood was anticoagulated by the latter showed generally higher haemolysis values.

The haematocrit of the blood sample was determined prior to the shear tests using a microhaematocrit centrifuge.

Experimental Phase

Experiments were undertaken in the following order of steps:

1. Gentle mixing of blood in heparinized tube to reverse sedimentation.
2. Filling of capillaries with blood by capillary action from tube [*1].
3. Slipping silicone rubber tubes over the capillary ends and placing them into the box (which is connected to the vibrator).
4. Closure of box and perfusion of box with low-oxygen gas mixture.
5. Performance of shearing procedure with certain displacement amplitude, frequency and cycle number [*2].
6. Opening of box, taking capillaries out.
7. Cutting capillaries to separate middle part of blood column from end parts [*3].
8. Sealing one end of middle part.
9. Centrifugation for 8 min at 1000 g acceleration in microhaematocrit centrifuge.
10. Collection of plasma by cutting capillary and blowing plasma column out with pipette holder [*4].

Steps 1-10 were repeated with variation of the kinematic parameters within a time period of approximately 3.5 hours after blood withdrawal. This time limit was set by the rise in plasma free haemoglobin (fHb) of the unsheared control sample. Continuous monitoring of those values over the period of experimentation revealed a non-linear, exponentially rising trend, see Fig 5.6.

An assumption for this repetitive approach is the independency of shear-induced haemolysis on the time at which the experiment is performed. A series of shear experiments undertaken with constant parameters over a period of 4 hours revealed that there was a constant difference between fHb values for sheared and unsheared samples.

*1 Capillary tubes having a length of 12.5 cm are filled with a blood column of 7.5 cm length, thus ensuring that blood remains within the capillary during axial oscillation.

*2 Axial oscillations were performed at two frequencies, 40 Hz and 70 Hz. The displacement amplitude was varied in order to obtain a representative range of the corresponding bulk shear stress amplitude. The number of cycles was set to 350, 800, 2000, 4200 or 8000. Table 5.2 lists the variations of these kinematic parameters.

	$f = 40\ Hz$	$f = 70\ Hz$
$x_0\ [mm]$	5.6 ; 4.5 ; 2.5 ; 0.5	2.28 ; 11.65 ; 1.0
N_{cycle}	8000 ; 4200 ; 2000 ; 800	4200 ; 2000 ; 350

Table 5.2: Kinematic parameters chosen for oscillating shear stress experiments.

Whole blood viscosity values were obtained by applying the following relation postulated by Mockros [103]:

$$\eta_B = \eta_{Plasma} \cdot e^{2.31 \cdot Hct} \tag{5.19}$$

with Hct - Haematocrit

and η_{Plasma} = 1.6 mPa s at 20 °C

(20 °C - room temperature at which all experiments were performed).

*3 Despite creating a low-oxygen environment for the blood column, higher fHb values of the end pieces of the sheared samples could be recorded. In order to eliminate these end-effects, systematic studies on the extension of this non-shear stress related lysis process were undertaken. Stepwise reduction of the portion of the blood column examined for fHb revealed a decrease in the values reaching a constant value at a specific length (5.5 cm). Thus, only a 5.5cm length of the blood column centred about its mid-point was processed for the haemolysis analysis.

*4 To ensure that the centrifugation had led to a clear separation of plasma and blood cells, microscopic observations of the plasma at the cut capillary end adjacent to the cellular phase were undertaken. Neither blood cells nor cell fragments within the plasma were observed.

Post-Experimental Phase

Plasma samples were either analysed immediately after collection or stored at -20°C before analysis. Both treatments showed no differences in the results.

A quantitative, colorimetric determination of haemoglobin in plasma was performed using the Sigma Procedure No.527. The method is based on the catalytic action of haemoglobin on the oxidation of 3,3',5,5'-tetramethylbenzidene by hydrogen peroxide. The colour formed in the reaction is proportional to the haemoglobin concentration in the test sample.

Absorbance of the reacted sample was performed with a UV-VIS spectrophotometer at 600 nm (UV-1201 Spectrophotometer, Shimadzu Corp., Japan). Calibration is not required since a standard is included in each series of assays. Plasma free haemoglobin was calculated as

$$fHb = \frac{A_{Test} - A_{Blank}}{A_{Standard} - A_{Blank}} \cdot 30\ mg/dl$$

with a concentration of haemoglobin in the standard of 30 mg/dl and A - light absorbtion.

The procedure is stated to be linear over a haemoglobin concentration range of 0-50 mg/dl. If fHb values were expected to extend beyond this linearity threshold, an appropriate dilution of the plasma with 0.9%-NaCl-solution was performed.

Each plasma sample was analysed in duplicate. Thus, by averaging readings, the effect of subjective errors in the analysing procedure could be reduced.

5.5 Results

5.5.1 Plasma Free Haemoglobin

Haemolysis due to the applied stress is calculated as the free plasma haemoglobin value of the sheared sample less the value of the unsheared control sample.

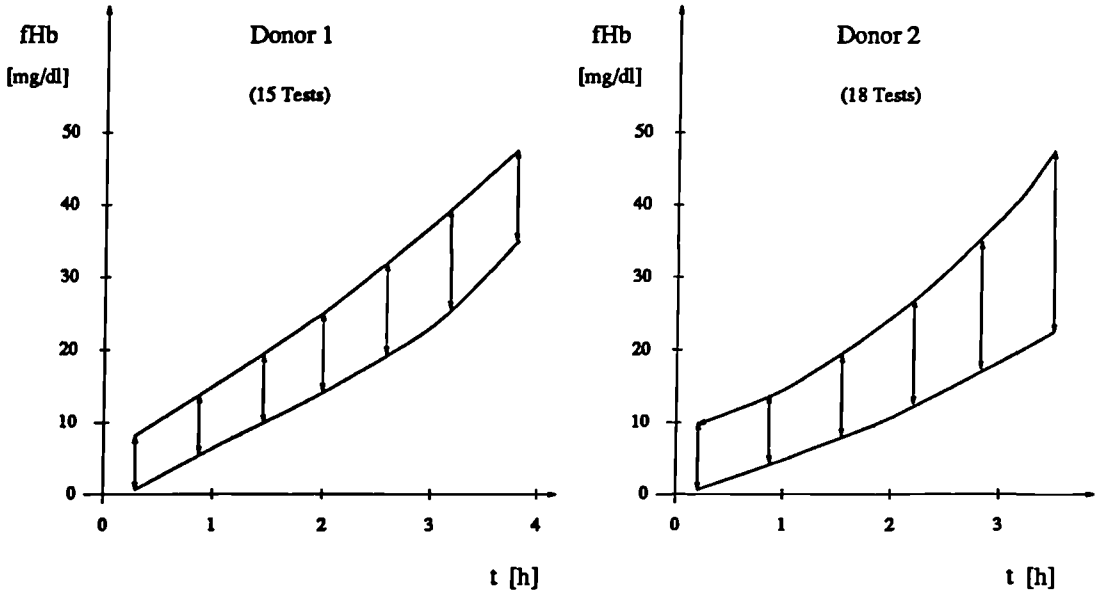

Figure 5.6: Haemoglobin release of unsheared control samples versus time for both donors.

The fHb values of the unsheared control samples representing non-shear stress-related destruction of red blood cells for both donors are given in Fig 5.6. Here, a similar increase of haemolysis with time was observed for every test run varying within a certain 'band width' which is presented in this graphical diagram.

According to the experimental regime listed in Table 5.2 in Section 5.4, a dependency of blood trauma on the stress amplitude, the number of stress cycles and the frequency of oscillation was examined under the action of an oscillating shear stress. Values for bulk shear stress amplitudes were obtained by applying Eqns. (5.16) and (5.17).

Results are represented separately for the two donors as well as combining both together.

Figs 5.7 to 5.18 illustrate the test results for the experimental conditions examined. Each data point represents the arithmetic mean value and standard deviation of a population of n test samples, with n specified within the figure.

In general, a large variation of data was found to exist for both donors and this, together with the relatively small number of data, made interpretation of the data difficult. Certain trends could however be observed.

The dependency of RBC damage on the shear stress amplitude is shown in Figs 5.7, 5.8 and 5.9 with the number of cycles as a variable and the frequency is kept constant at 40 Hz. These figures show a gradual increase in haemoglobin liberation with increasing stress amplitude. This tendency was found for both donors.

For a higher oscillating frequency of 70 Hz, a rise of fHb value with increase in stress amplitude was also found, Figs 5.10 and 5.11. It was, however, not as significant as for the lower frequency.

Haemolysis values for both frequencies are compared in Fig 5.12 for a cycle number, N = 4200. Unfortunately, the range of stress amplitudes was more restricted for f=70 Hz due to operational conditions of the vibrator, namely maximum displacement amplitude x_0 = 2.28 mm for f = 70 Hz compared to x_0 = 5.6 mm for f = 40 Hz.

Figs 5.13 to 5.15 depict dependency of fHb values on the cycle number (with the stress amplitude as the variable). The expected dependency of haemolysis on this parameter can be stated clearly for the frequency of 40 Hz, it is however, not so obvious for a frequency of f = 70 Hz, as illustrated in Figs 5.16 to 5.18. Also apparent in these figures is the increase in fHb with increasing stress amplitude

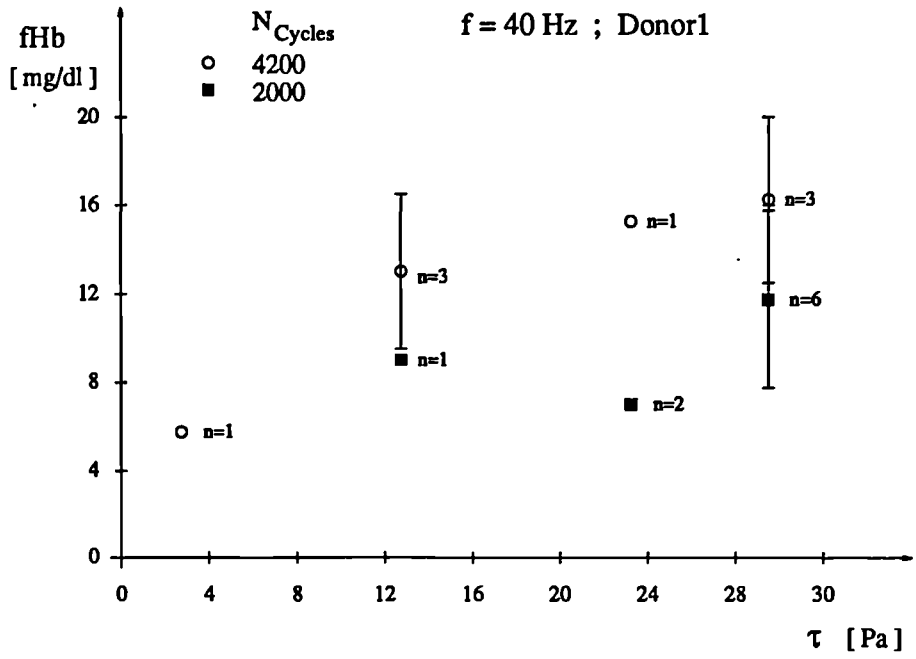

Figure 5.7: Haemoglobin release at f=40 Hz versus shear stress amplitude for donor 1.

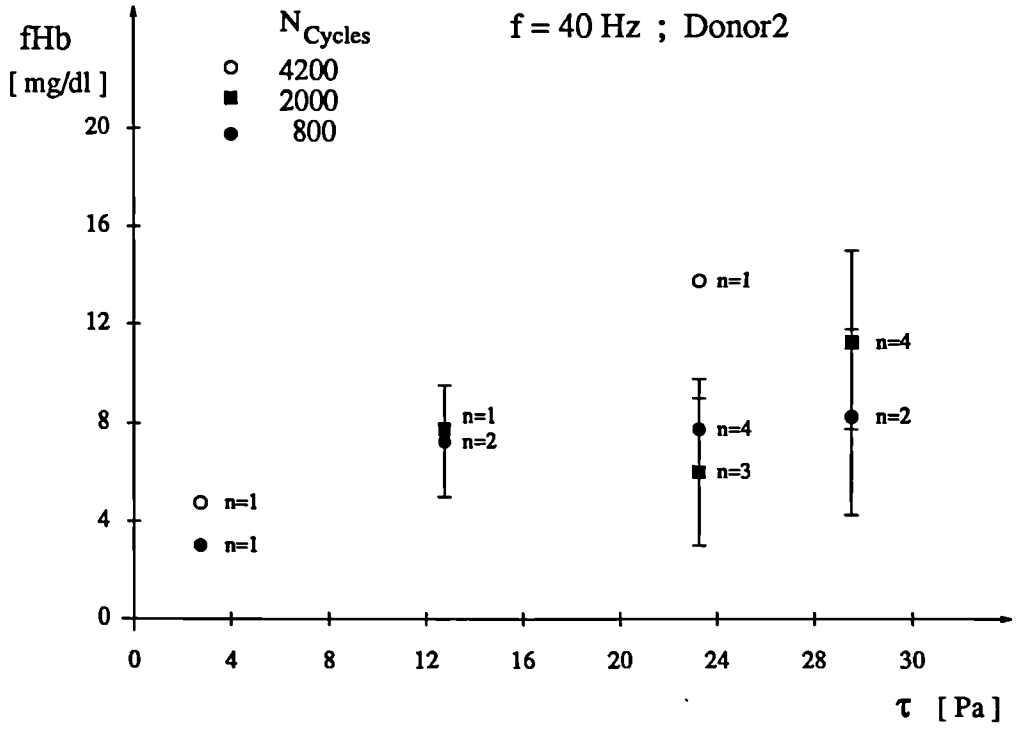

Figure 5.8: Haemoglobin release at f=40 Hz versus shear stress amplitude for donor 2.

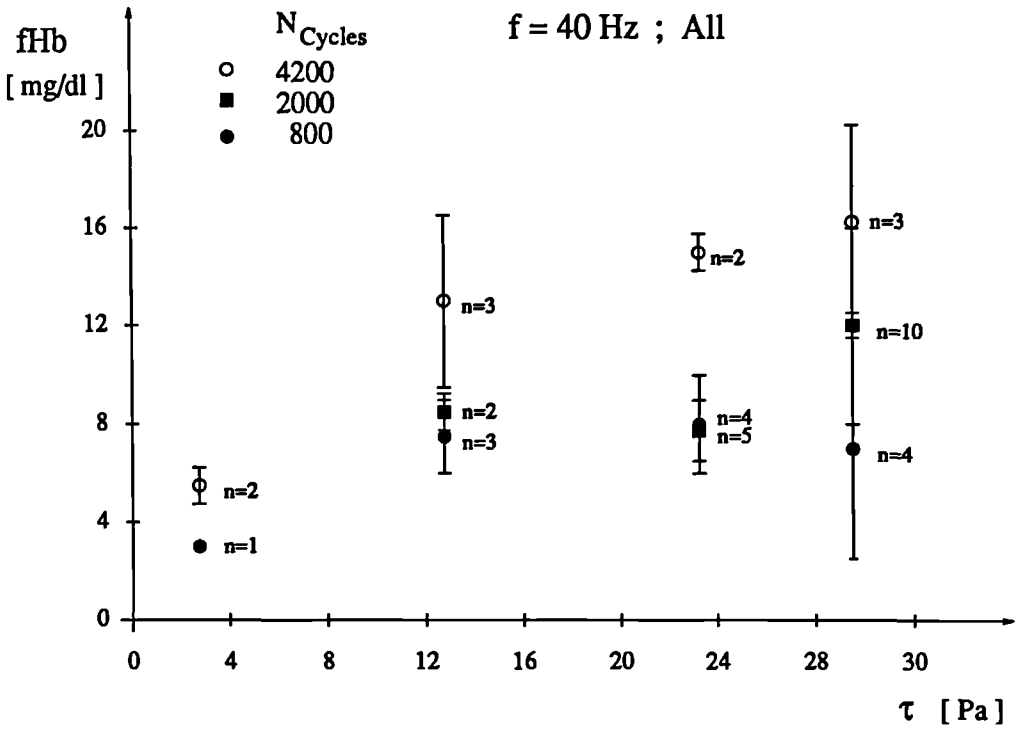

Figure 5.9: Haemoglobin release at f=40 Hz versus shear stress amplitude combining all data.

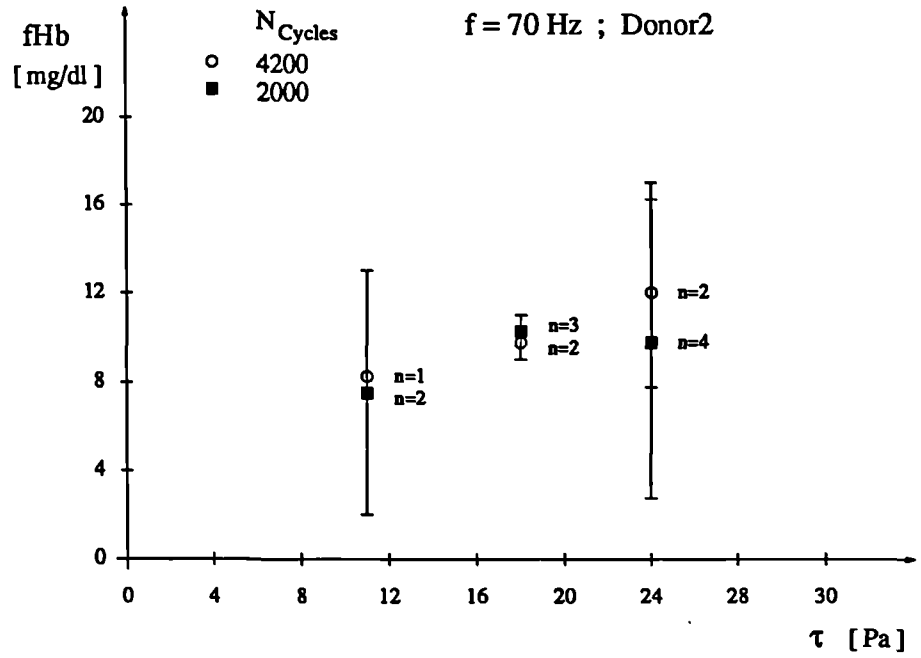

Figure 5.10: Haemoglobin release at f=70 Hz versus shear stress amplitude for donor 1.

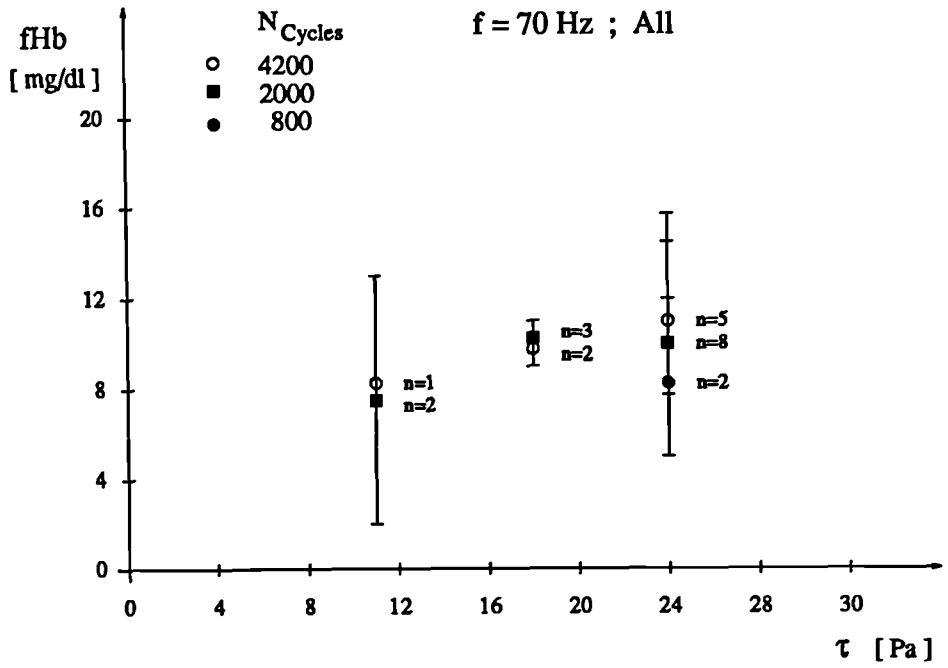

Figure 5.11: Haemoglobin release at f=70 Hz versus shear stress amplitude combining all data.

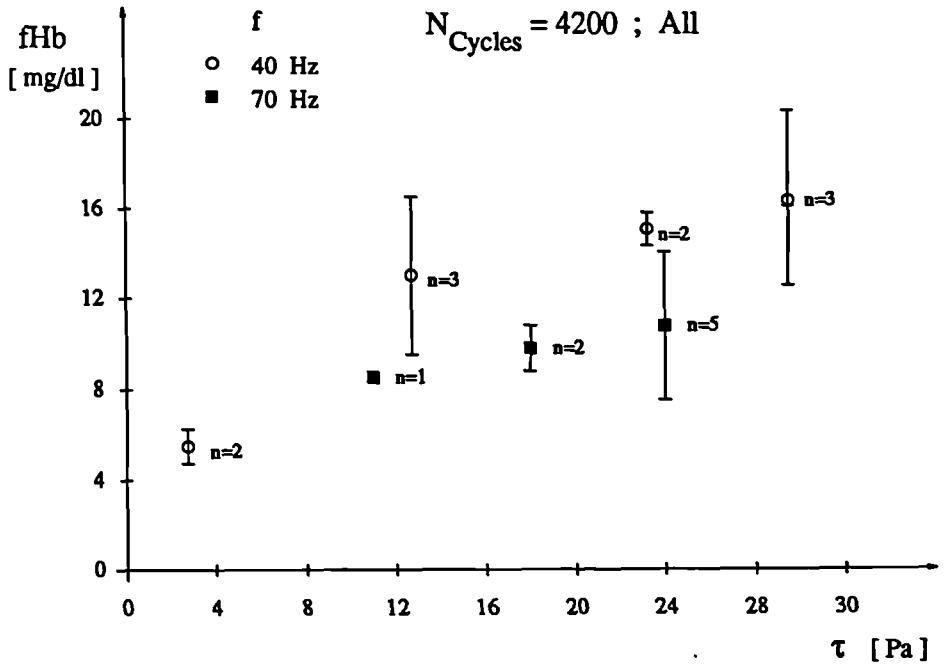

Figure 5.12: Haemoglobin release at f=70 Hz and f=40 Hz versus shear stress amplitude combining all data.

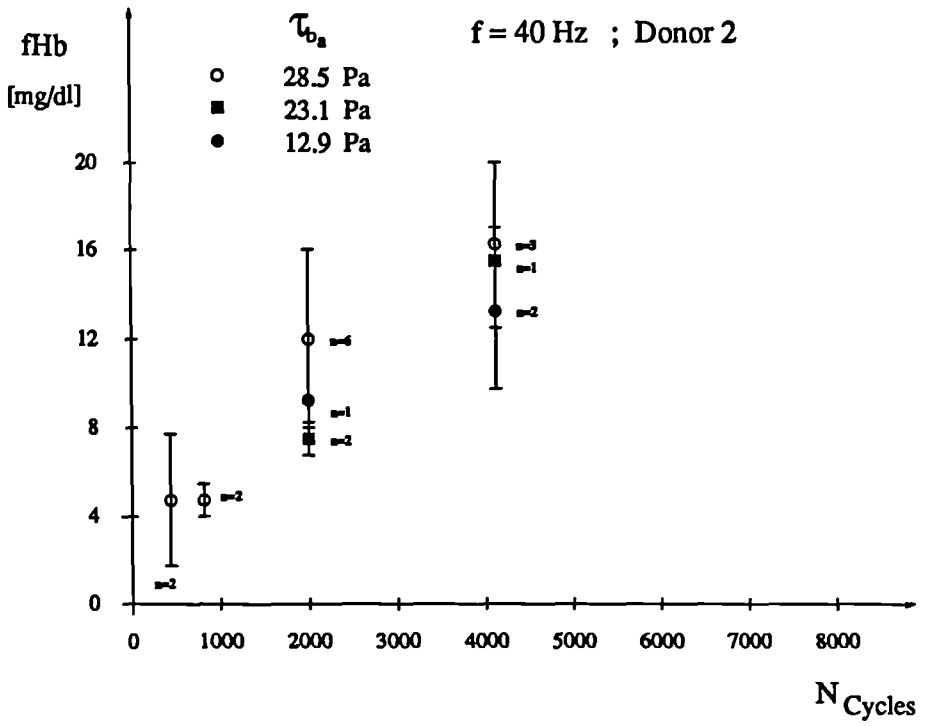

Figure 5.13: Haemoglobin release at f=40 Hz versus cycle number for donor 1.

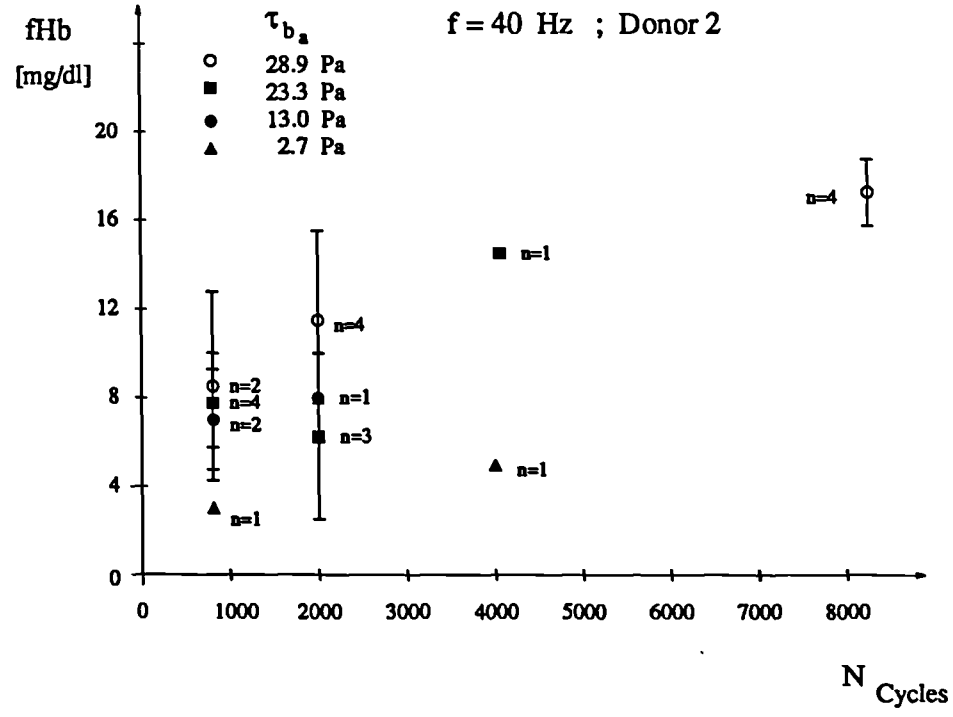

Figure 5.14: Haemoglobin release at f=40 Hz versus cycle number for donor 2.

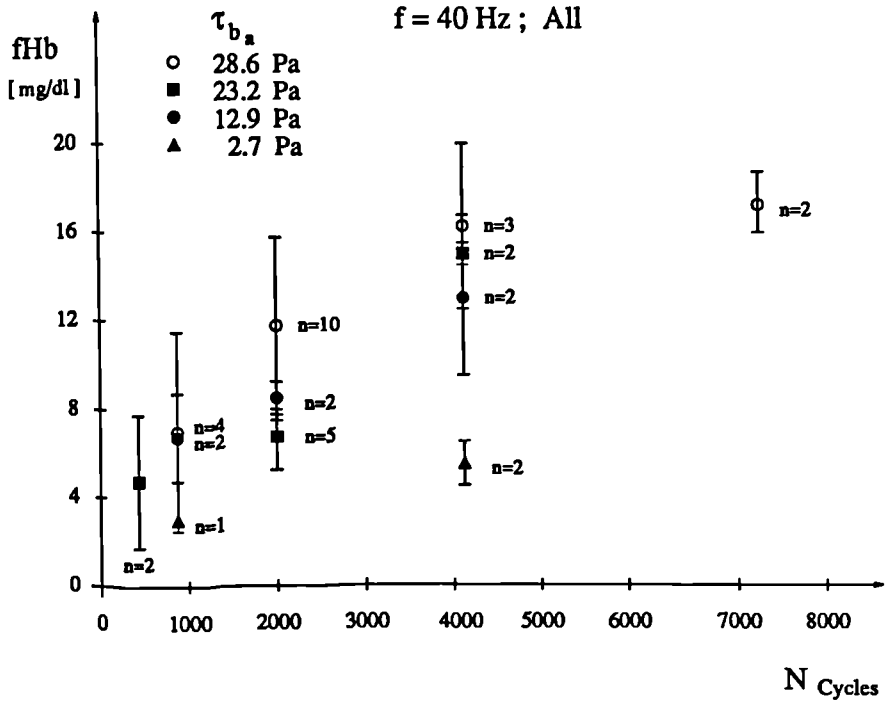

Figure 5.15: Haemoglobin release at f=40 Hz versus cycle number combining all data.

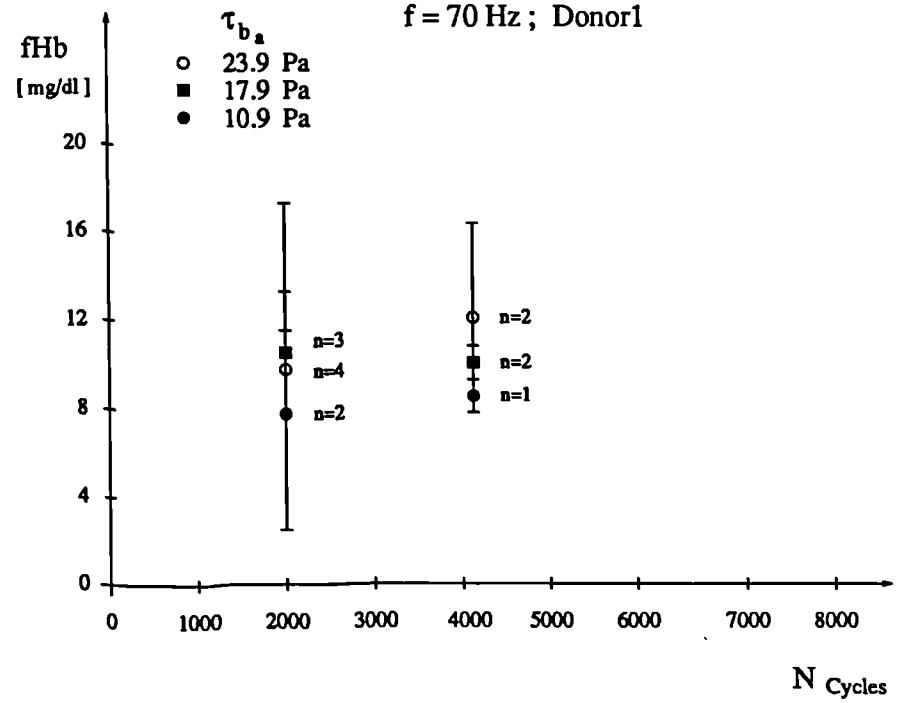

Figure 5.16: Haemoglobin release at f=70 Hz versus cycle number for donor 1.

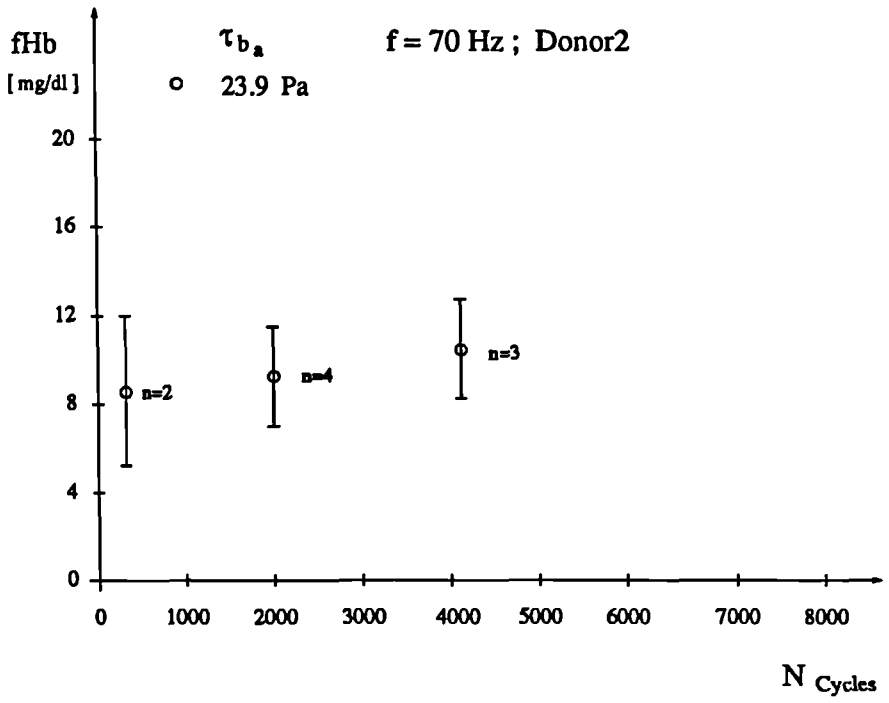

Figure 5.17: Haemoglobin release at f=70 Hz versus cycle number for donor 2.

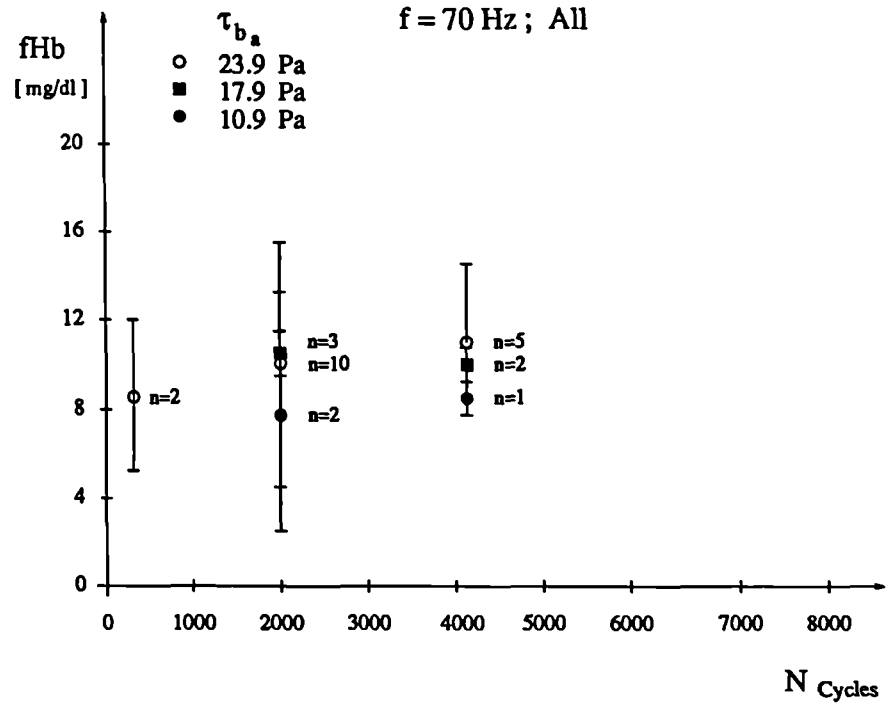

Figure 5.18: Haemoglobin release at f=70 Hz versus cycle number combining all data.

for any given f and N combination. This direct dependency of fHb-values on the two parameters, shear stress amplitude and number of cycles is made more explicit by a combined representation in a 3D-plot obtained by bilinear interpolation from the discrete mean fHb values of all data for both frequencies as shown in Figs 5.19 and 5.20.

Similar to S-N-diagrams for fatigue behaviour of engineering materials (Section 4.4), the 3-dimensional interpolations of haemolysis values shown in Figs 5.19 and 5.20 are used to determine a S-N-damage curve for red blood cells. The lines which approximate 0.05 % of haemoglobin liberation corresponding to a plasma haemoglobin value of 7.5 mg/dl with a whole blood haemoglobin concentration of 15.0 g/dl are shown in Fig 5.21. Here, the frequency represents the third parameter. This representation reveals three distinct sections of different damage behaviour: Cycle numbers up to approx. 600 did not cause damage within the shear stress range examined considering 0.05 % Hb liberation as a damage threshold. For cycle numbers in the range of 600-1500 a strong dependency of the damaging stress amplitude on the cycle number can be discerned. For cycle numbers exceeding this range these threshold amplitudes vary only little. The existence of an endurance strength τ_D of the cell membrane analogous to that of engineering materials appears possible from this diagram. Stresses below such an endurance strength would cause damage only after a very large cycle number. This hypothesis needs to be verified by examination of cell trauma at far higher cycle numbers. Results of a statistical analysis of the

Source	*DF*	*Seq SS*	*Adj.SS*	*Adj.MS*	*F*	*P*
$\tau_{amplit.}$	1	60.07	52.74	52.74	3.07	0.087
N_{cycle}	1	65.84	70.27	70.27	4.09	0.049
f	1	13.82	13.82	13.82	0.81	0.375
Error	42	721.06	721.06	17.17		
Total	45	860.79				

Table 5.3: Analysis of Variance for fHb.

experimental fHb data for the two frequencies at two cycle numbers over the

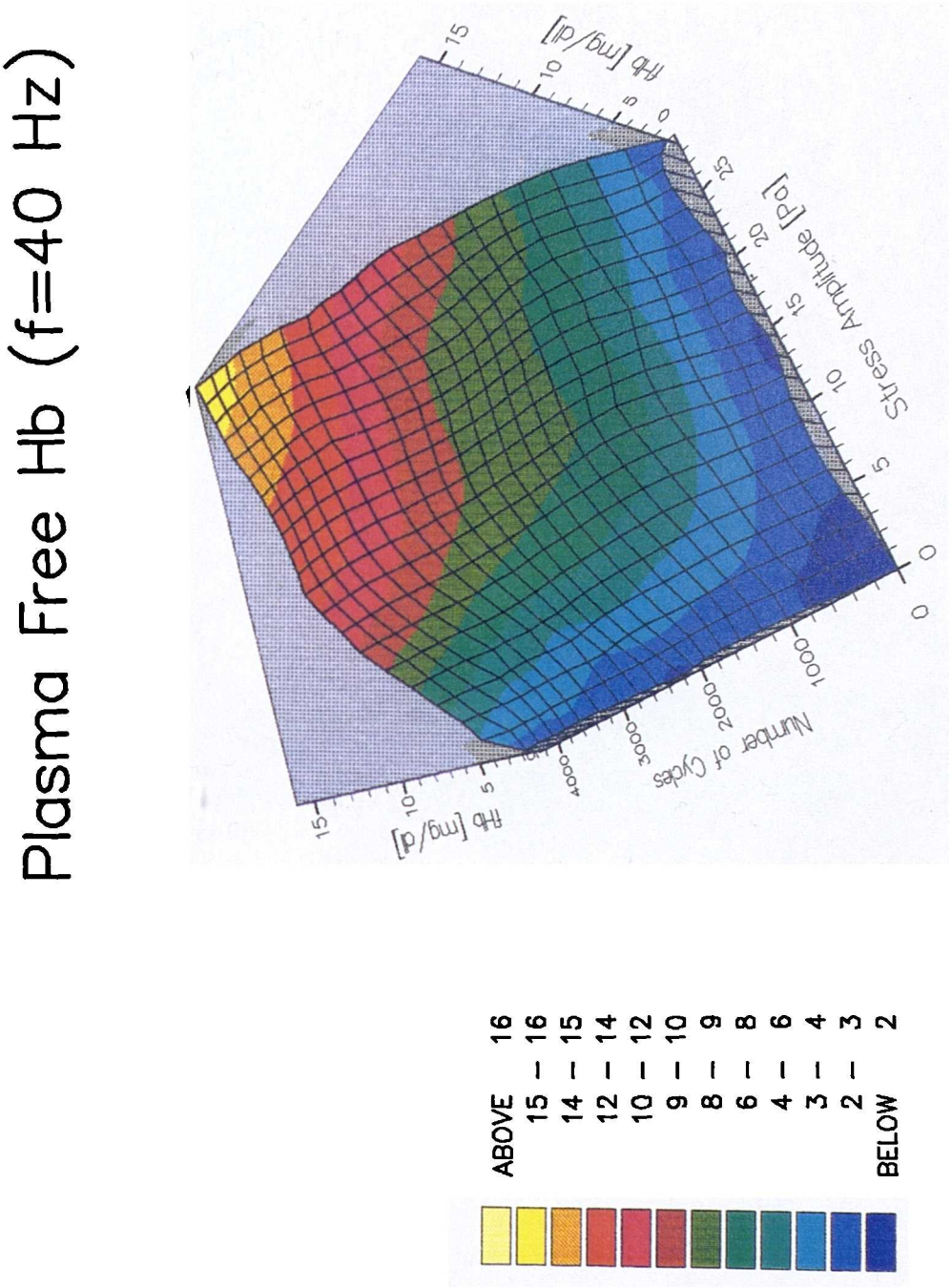

Figure 5.19: Dependency of Hb-liberation on shear stress amplitude and number of cycles at a frequency of 40 Hz.

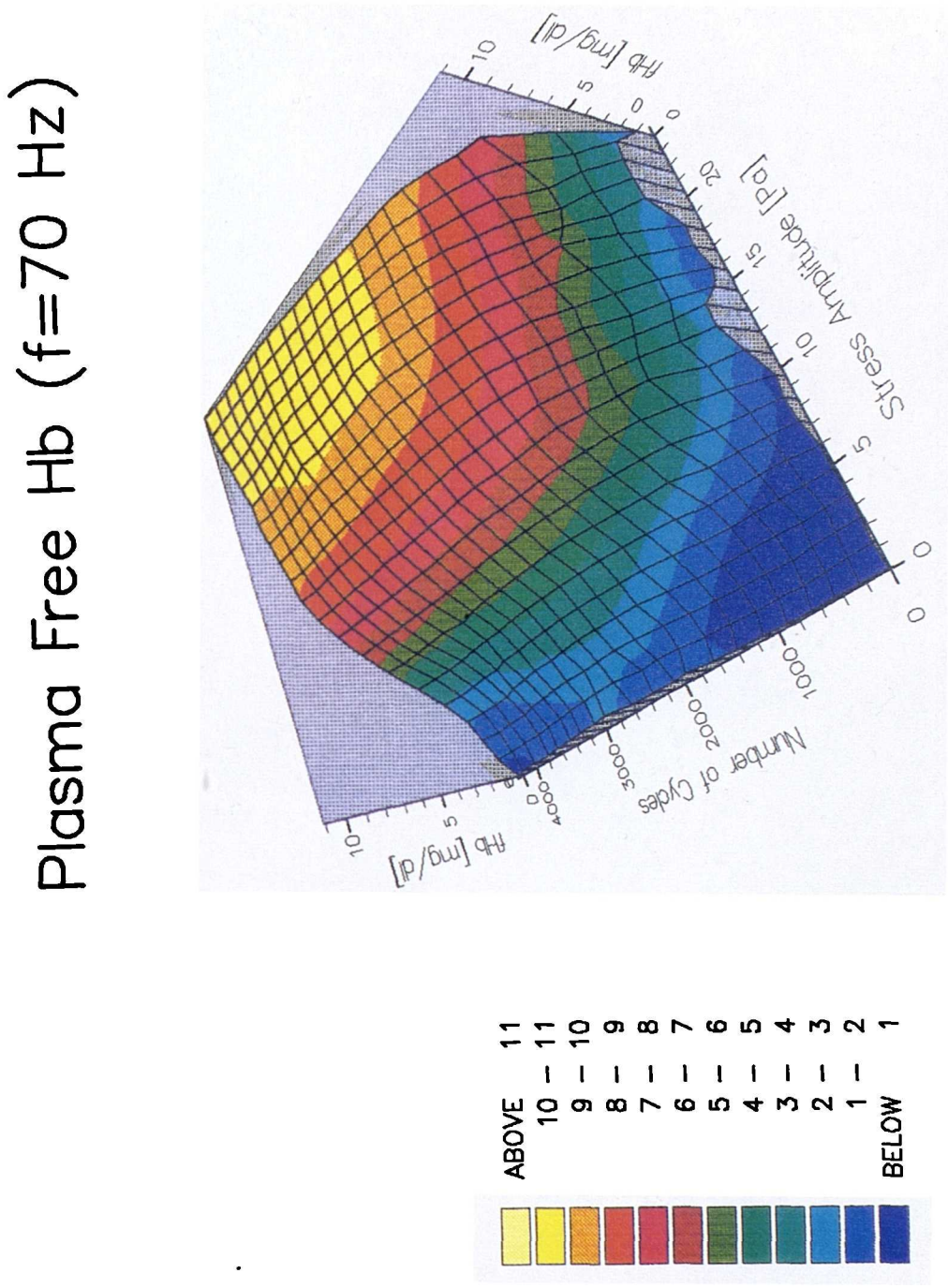

Figure 5.20: Dependency of Hb-liberation on shear stress amplitude and number of cycles at a frequency of 70 Hz.

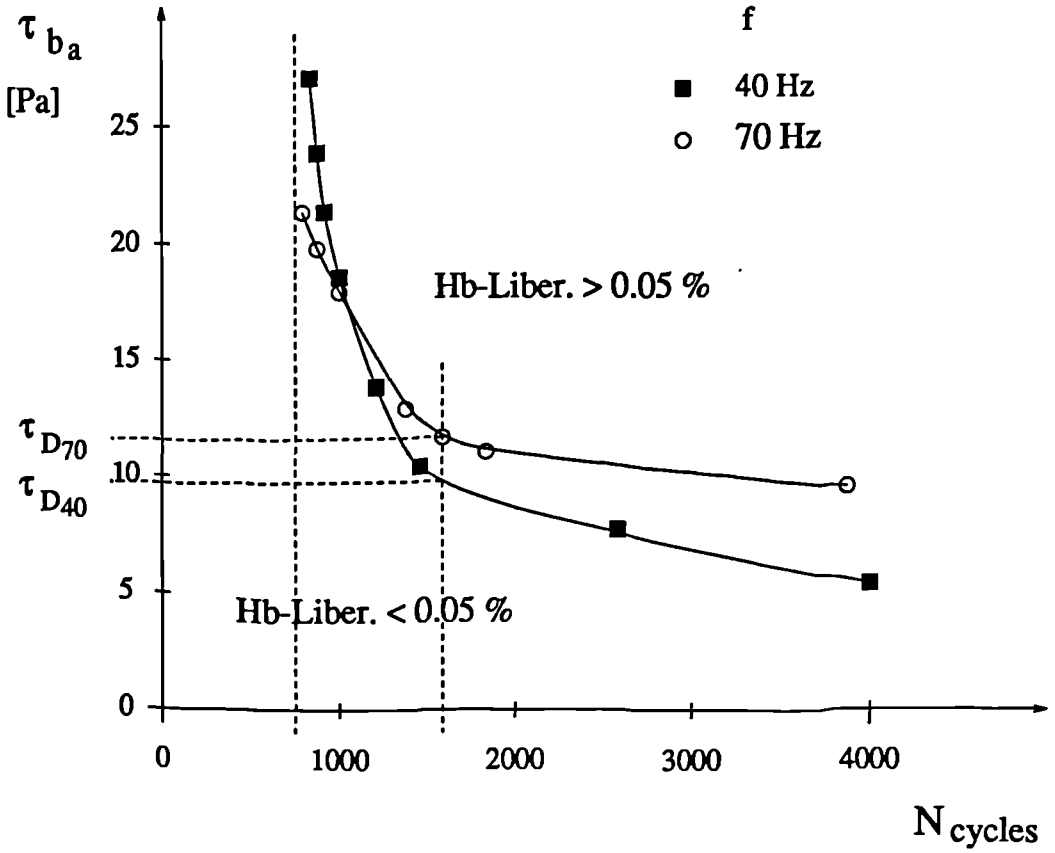

Figure 5.21: S-N damage curve for 0.05 % Hb liberation.

whole range of stress amplitudes by means of an 'unbalanced analysis of variance' [104] are presented in Table 5.3. Differences of fHb values for the two cycle numbers (2000; 4200) are statistically significant ($F > 4$; $P < 0.05$); the τ_a-dependency is only of marginal significance and that of a frequency dependency could not be shown. However, these results must be viewed in terms of a very small cycle number.

5.5.2 Error Analysis

For the assessment of accuracy of the experimental data, a comprehensive error analysis is indispensable. Only the detection of error sources and if possible, their qualitative or quantitative determination, allows a realistic interpretation of data and conclusions for an improved experimental technique. Generally, experimental errors are divided into systematic and random errors, with the

latter being subdivided into subjective, i.e caused by the experimenter, and non-subjective. Possible errors associated with the oscillating shear stress studies are examined below according to the above classification.

Systematic Errors

- Non-axial vibrations: Due to the need for a horizontal axis of vibration and the design of a free end of the moving apparatus, vertical vibrations could not be prevented. They were, however, largely reduced by the damping device described in Chapter 5.3. The maximum vertical displacement could thus be kept at a small fraction of the horizontal displacement with $y_0 \leq 0.05\ x_0$.

- Instrument accuracy

  - vibrator (amplifier) distortion $< 0.5\%$
  - accelerometer accuracy $\pm 5\%$
  - spectrophotometer for plasma Hb analysis

    wavelength accuracy ± 1.0 nm ; photometer accuracy $\pm 0.15\%$
  - pipette accuracy $\pm 1\%$

- Deviation of actual movement of blood column from theoretically calculated. Measured maximum values of blood column displacement were in good agreement with theory within the accuracy of measurement ($\pm$ 0.5 mm).

Subjective Random Errors

- Carelessness in blood withdrawal, leading to higher initial haemolysis rates.

- Time delay between end of shearing procedure and cutting of oxygenated ends from middle part of capillary.

- Inaccuracy in timing duration of test (maximum $\pm$ 0.5s) for shearing procedure.
- Inaccurate handling of chemicals in plasma Hb determination analysis. This error was reduced by taking the arithmetic mean values of two assays of each plasma sample.

Non-Subjective Random Errors

- Variations in the haematological conditions between individuals and on different days. The latter were found to be an important source of data deviation.
- End effects resulting from blood-air-interface were sought to be eliminated largely by examining only the middle part of the blood column. The mechanisms of haemolysis caused by the dynamic exposure to a low-oxygen environment are, however, not identified, so negative effects cannot be ruled out.
- Radial migration, sedimentation and a relative motion between blood and wall at the capillary wall as possible consequences of an inhomogeneous plasma-cell-suspension can lead to inaccuracies of the proposed theory. However, they could not be specified.
- Viscous heating of the blood column during the shearing procedure can have undesirable haemolysis as a consequence. Temperature changes are believed not to exceed 1^0 C.

From this tabulation of different error sources for the haemolysis experiments performed, it can be seen that they are manifold. Systematic errors play an unimportant role in data variation. Fluctuating biological conditions and other non-subjective random errors, which are strongly related to the special properties of blood and the shearing principle, are believed to have the major impact on inaccuracies. Subjective random errors are unavoidable, but can be kept to a minimum.

5.6 Discussion

A method was proposed which allows the investigation of blood damage behaviour under a time-dependent, oscillating shear stress loading. The analysis of the axial oscillation of a capillary tube containing a blood column was shown to have a closed form solution and yields a reproducable flow field and hence shear stress distribution. It was therefore chosen as the loading principle. The definition of a bulk shear stress allowed the assignment of a representative shear stress value at every time step, with an identical motion of every cross-section. The use of an averaged shear stress value presents a departure from an accurate analysis. It is, however, a necessary means to assess the loading-damage relation of a non-uniform radial stress distribution unless a layer-specific blood analysis is able to be performed. The elimination of these restrictions would improve the accuracy of future oscillating shear stress-damage experiments.

Blood trauma was specified with red cell damage documented by haemoglobin liberation. A variation of three kinematic parameters, namely bulk shear stress amplitude, cycle number and frequency of oscillation, characterising a sinusoidal stress loading with a zero mean stress, was performed. Whole blood samples of two healthy donors were analysed.

In summarising the results, the studies revealed an increased release of haemoglobin with increasing shear stress amplitudes and with an increasing number of stress cycles. These findings are not unexpected, since related dependencies are well established for stress magnitude and exposure time under a constant shear stress loading.

A major result of the study was the establishment of a characteristic S-N-damage curve. It supports the hypothesis that the damage behaviour of red blood cells under a cyclic mechanical loading can be characterised as a fatigue process. Oscillating stresses with amplitudes above a limiting threshold or endurance strength cause the membrane to deform extremely or rupture after a certain number of stress cycles with a consequent haemoglobin release. S-N curves representing a specific amount of Hb-liberation at different oscillating

frequencies showed similar tendencies.

Time-dependent constitutive relationships for the cell membrane could be responsible for this frequency-dependency. A transition from the phenomenological kind of investigation to a cell-based microscopic examination is, however, indispensable in order to postulate mechanisms for the macroscopic damage observations. Knowledge of the motion of the cell membrane in the oscillating flow field , for example, would yield predictions of the time-dependent stress distribution within the membrane, allowing conclusions to be made on the intrinsic membrane fatigue behaviour. Furthermore, interactions between single cells and cell-wall contacts with their effect on membrane stresses require detailed investigations to explain possible discrepancies between microscopic, single-cell studies and phenomenological observations.

Although the mechanical damage behaviour studies performed by the author have shown interesting trends they must be viewed with caution. Large deviations of the data and the prevalence of random errors will require that a far higher number of samples be tested in future in order to obtain statistically significant results. Consideration needs to be given on an improved oscillating shear stress loading principle and device to further minimize non-subjective random errors. The creation of a uniform stress distribution across the gap or a layer-related blood analysis is deemed important. Blood-air interfaces need to be avoided or minimized as also should be wall contacts for their disturbing influences. A verification of the applicability of theoretical flow models to practical conditions by accurate flow measurements is desirable.

Investigations of damage behaviour with extended stress amplitude, frequency and cycle number are necessary to obtain a more comprehensive picture.

The influence of non-mechanical parameters was not considered in these studies. Anticoagulant, pH-value, temperature differences, blood gas contents, etc. must be systematically checked for their effect on damage processes.

In conclusion, it can be said that some progress has been made with these experimental investigations in the determination of red cell damage behaviour under a time-dependent, oscillating shear stress loading.

Chapter 6

Numerical Simulation of Flow Within Centrifugal Blood Pumps

6.1 General Aspects

Flow processes may be identified by two different approaches: experimental investigation and theoretical calculation.

Theoretical calculations offer benefits in giving detailed and complete hydrodynamic information, like velocity and pressure fields, turbulence values and wall shear stresses. Furthermore, realistic conditions can be simulated in situations where scaled or simplified models need to be used for experimental investigations. Speed and cost factors are especially important for studying complicated physical situations, parameter variations or a large number of design variants in an optimization process.

The solution of a set of partial differential equations representing the mathematical model of flow processes by numerical methods has become increasingly attractive. They offer a cost and time effective method to calculate complex flows due to falling hardware costs, rising computer capacities as well as faster and more sophisticated numerical algorithms. On the minus side, computer capacities are still too limited to solve extremely fast and small-scale phenomena

such as turbulence. The necessary model assumptions and simplifications, for instance turbulence models, are the main disadvantage associated with numerical fluid dynamics.

Experimental investigations are, however, inevitable, to observe basic phenomena, to provide information about initial and boundary conditions for numerical calculations, to sufficiently validate them and to backup mathematical flow models.

The full Navier-Stokes equations are the most general description of fluid flow. For an isotropic, one-phase fluid they contain four coupled non-linear differential equations of second order which describe the conservation of mass and momentum. Using tensor notation (Einstein summation convention) they are presented in equations (6.1) and (6.2). Further detailed information about their derivation may be found in [42, pp. 64–65],[105].

$$\frac{\partial \rho}{\partial t} + \frac{\partial}{\partial x_j}(\rho u_j) = 0 \tag{6.1}$$

$$\frac{\partial}{\partial t}(\rho u_i) + \frac{\partial}{\partial x_j}(\rho u_j u_i) = -\frac{\partial p}{\partial x_i} + \frac{\partial \tau_{ij}}{\partial x_j} + S_i \tag{6.2}$$

In the above equations, u_i represents the velocities in x_i-coordinate directions, p is the static pressure, ρ is the density, τ_{ij} is the viscous stress tensor, and the S terms are additional source terms. The molecular fluxes τ_{ij} are expressed in terms of velocity gradients,

$$\tau_{ij} = \mu\left(\frac{\partial u_i}{\partial x_j} + \frac{\partial u_j}{\partial x_i}\right) + \frac{2}{3}\mu\frac{\partial u_l}{\partial x_l}\delta_{ij} \tag{6.3}$$

where μ is the dynamic viscosity of the fluid.

Approximations of the full Navier-Stokes equations are undertaken by component wise simplifications known as dynamic approximations or by dimensional simplifications, in particular spatial and time approximations [106].

Neglect of viscous forces leads to a system of four coupled, non-linear differential equations of first order, called Euler equations. They provide a valid approximation far from solid walls or when the influence of boundary layers can

be neglected. The assumption of irrotational flow leads to a single, second-order, non-linear differential equation, the Laplace equation of the velocity potential. As such it represents a major barrier in simulating internal flows.

Spatial approximations are undertaken by considering flow in only one or two dimensions which leads to a related reduction of the number of equations to be solved and hence minimization of computing space and time.

For incompressible flow the full Navier-Stokes equations simplify to:

$$\frac{\partial u_i}{\partial x_i} = 0 \tag{6.4}$$

$$\rho\frac{\partial u_i}{\partial t} + \rho\frac{\partial}{\partial x_j}(u_j u_i) = -\frac{\partial p}{\partial x_i} + \frac{\partial \tau_{ij}}{\partial x_j} + S_i \tag{6.5}$$

For the description of fluid motion in rotating elements it is advantageous to relate the conservation equations to a rotating coordinate system. For unsteady, incompressible flows the equations of mass and momentum conservation take the following form in the relative system:

$$\frac{\partial v_i}{\partial x_i} = 0 \tag{6.6}$$

$$\rho\frac{\partial v_i}{\partial t} + \rho\frac{\partial}{\partial x_j}(v_j v_i) + \rho e_{ijk}\omega_j e_{klm}\omega_l x_m + 2\rho e_{ijk}\omega_j v_k = -\frac{\partial p}{\partial x_i} + \frac{\partial \tau_{ij}}{\partial x_j} + S_i \,. \tag{6.7}$$

In these equations, v_i represents the relative velocity component in x_i-direction. The symbol ω_j designates the components of the angular velocity of the rotating system in the three coordinate directions and the permutation symbol e_{ijk} is defined as follows

$$e_{ijk} = \begin{cases} +1 & ,\textit{with } ijk \textit{ being an even permutation } (e.g.\ 123, 231, 312) \\ -1 & ,\textit{with } ijk \textit{ being an odd permutation } (e.g.\ 321, 213, 132) \\ 0 & ,\textit{if at least two indices are equal} \,. \end{cases}$$

Many of the flows encountered in engineering problems are turbulent. They are characterised by stochastic fluctuations of all dependent parameters. Since a direct simulation with a time and spatial resolution of turbulence structures is currently not possible for most flows of interest, a modelling of instantaneous scalar values is made. They are expressed in terms of mean and fluctuating components through a process of time averaging, called Reynolds-stress averaging [107]. Each dependent variable in the original conservation equation is decomposed into these two components by

$$\phi = \Phi + \phi' \,. \tag{6.8}$$

The mean component Φ is,

$$\Phi = \frac{1}{\Delta t}\int_t^{t+\Delta t} \phi \; dt \,, \tag{6.9}$$

where the time interval Δt is long compared to the time scale of turbulent fluctuations.

The time-averaged original momentum conservation equations contain also correlations of the turbulent fluctuations $-\overline{\rho u_i' u_j'}$, called Reynolds stresses, and take for incompressible flow the form:

$$\rho\frac{\partial U_i}{\partial t} + \rho\frac{\partial}{\partial x_j}(U_j U_i) \;=\; -\frac{\partial P}{\partial x_i} + \frac{\partial}{\partial x_j}\left[\tau_{ij} - \rho\overline{u_i' u_j'}\right] + S_i \tag{6.10}$$

or for the rotating frame of reference:

$$\begin{aligned}\rho\frac{\partial V_i}{\partial t} + \rho\frac{\partial}{\partial x_j}(V_j V_i) + \rho e_{ijk}\omega_j e_{klm}\omega_l x_m + 2\rho e_{ijk}\omega_j V_k = \\ -\frac{\partial P}{\partial x_i} + \frac{\partial}{\partial x_j}\left[\tau_{ij} - \rho\overline{v_i' v_j'}\right] + S_i \,.\end{aligned} \tag{6.11}$$

These additional terms must be related to the mean flow variables and the fluid properties using a turbulence model before a closed solution of the above equation system becomes possible. A detailed listing of existing turbulence models is beyond the scope of this work, but can be found in [108, 109]. A widely used two-equation model is the $k-\epsilon$ model. This model is based on the gradient diffusion hypothesis by Boussinesq which expresses Reynolds stresses as

$$-\overline{\rho u_i' u_j'} \;=\; \mu_t\left[\frac{\partial U_i}{\partial x_j} + \frac{\partial U_j}{\partial x_i}\right] - \frac{2}{3}\rho\delta_{ij}k \tag{6.12}$$

where μ_t, the turbulent viscosity, and k, the turbulent kinetic energy, are defined as

$$\mu_t = \frac{c_\mu \rho k^2}{\varepsilon} \quad ; \quad k = \frac{1}{2}\overline{u_i' u_i'} \, .$$

Local values for k and ε, the rate of dissipation of k, are obtained from the semi-empirical transport Eqns. (6.13) and (6.14):

$$\rho \frac{\partial k}{\partial t} + \rho \frac{\partial}{\partial x_j}(U_j k) = \frac{\partial}{\partial x_j}\left(\frac{\mu_t}{\sigma_k}\frac{\partial k}{\partial x_j}\right) + \mu_t G - \rho\varepsilon \tag{6.13}$$

$$\rho \frac{\partial \varepsilon}{\partial t} + \rho \frac{\partial}{\partial x_j}(U_j \varepsilon) = \frac{\partial}{\partial x_j}\left(\frac{\mu_t}{\sigma_\varepsilon}\frac{\partial \varepsilon}{\partial x_j}\right) + \frac{\varepsilon}{k}(c_1 \mu_t G - c_2 \rho\varepsilon) \tag{6.14}$$

where

$$G = \left(\frac{\partial U_i}{\partial x_j} + \frac{\partial U_j}{\partial x_i}\right)\frac{\partial U_i}{\partial x_j} \, .$$

The empirical constants $c_\mu, c_1, c_2, \sigma_k, \sigma_\varepsilon$ have values of 0.09, 1.44, 1.92, 1.0, 1.3, respectively.

Since an analytical solution of the Reynolds-averaged Navier-Stokes equations does not exist for most practical flow problems, numerical methods are employed. The basis of the numerical approach is to convert the governing set of continuum differential equations by discretization methods into algebraic equations which can be solved by traditional mathematical methods. This contains three main problems:

1. Discretization of the flow domain, e.g. construction of a numerical grid.

2. Discretization of the partial differential equations.

3. Solution of the resulting system of algebraic equations.

Numerous numerical methods have been developed to perform the above task, of which the main representatives are Finite-Difference, Finite-Element and Finite-Volume methods. A detailed description of these methods and discussion of their common features and differences can be found in [110]. All of

them have been applied to solve hydrodynamic problems, and no method is necessarily superior in terms of accuracy and geometric flexibility. The property of a discretization method to implicitly satisfy global conservation constraints, especially desirable for fluid flow, is best facilitated by a finite-volume approach.

For the task of quantifying flow field variables within a centrifugal blood pump, their numerical calculation is seen as the appropriately accurate and effective approach. Complex geometries and a rotating body make experimental investigations difficult and costly. However, sophisticated measurements are desirable for the validation of numerically obtained flow parameters.

A computational fluid dynamics (CFD) software package, TASCflow ^{TM}, was found to provide modelling capabilities with respect to numerical grid generation, numerical discretization and solution algorithms that made it suited to the above task. The main concepts incorporated into this code are presented in the following section, (6.2).

The mathematical models derived in section 6.2 are based on the assumption of a homogeneous, Newtonian fluid, whereas blood consists of an non-homogeneous cell-plasma suspension which shows non-Newtonian characteristics in the low shear rate region ($\dot{\gamma} < 100s^{-1}$) [102]. Neglect of non-Newtonian behaviour for flow calculations within centrifugal blood pumps is justified considering the average shear rates which are above that critical threshold. Incorporation of flow inhomogeneities was considered to be a too difficult task to be achieved within the timescale of this study.

6.2 TASCflow ^{TM} - a Computational Fluid Dynamics Software Package

The commercial code TASCflow ^{TM} (Advanced Scientific Computing Ltd.) incorporates an element-based finite-volume method for computing viscous flow. Its ability to model flow in a rotating frame of reference involving complex geometries with a high robustness, accuracy and efficiency [111, 112] made the

code especially suitable for calculating the flow within centrifugal blood pumps. The fundamental features and concepts offered by TASCflow ^{TM} with regards to discretization of the flow domain and of the governing differential equations as well as solution strategies of the algebraic equations will be introduced.

Computational Grid

The subdivision of the computational domain is performed with a general non-orthogonal, boundary-fitted, structured grid. The code permits the separate generation of several grids and consequent connection of interfaces of these sub-grids. This multi-grid capability prevents very distorted non-orthogonal grids or large block-off portions of the domain. The possibility to specify subregions of the domain which are to be discretized using a locally finer grid is given. The so-called grid 'embedding' enables the resolution of small length scale regions without adding a large number of unnecessary nodes elsewhere. Internal boundaries can be defined as block-off regions. Fig 6.1 is an example of grid-embedding and a block-off region [113].

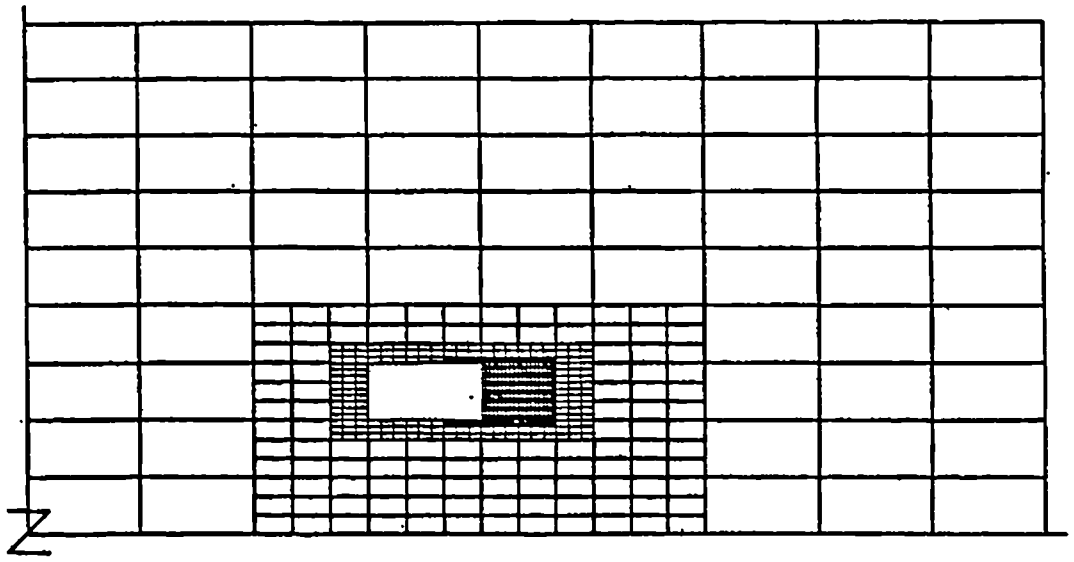

Figure 6.1: Example of grid embedding in TASCflow ^{TM}.

Fig 6.1 shows an elemental discretization of the domain. The definition of finite volumes in terms of these elements (called 'flux elements') is given in Fig

6.2. The subdivision of hexahedral flux elements (in the 3D case) into eight octants, each of them associated with one of the eight nodes, allows a high geometrical flexibility and the formulation of accurate discrete equations.

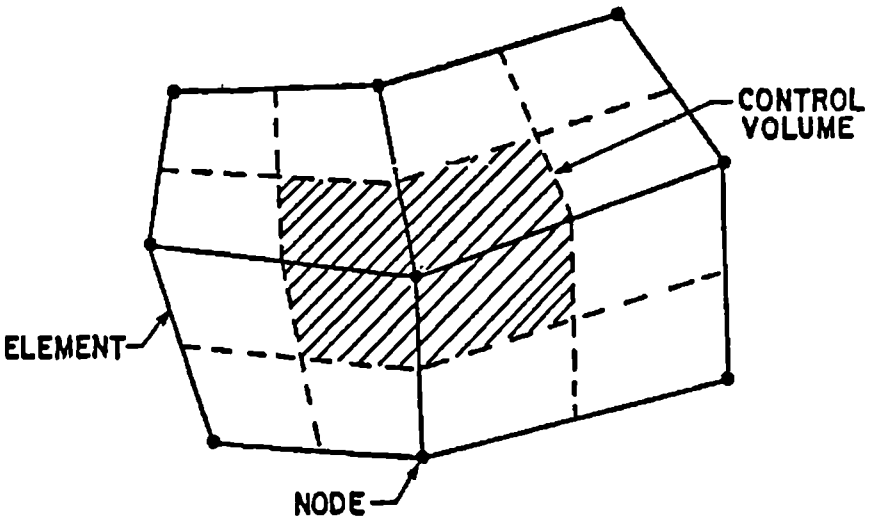

Figure 6.2: Definition of the finite volume.

Discretization of the Differential Equation

The transport equation for the general variable Φ can be expressed in differential equation form as

$$\begin{aligned} L(\Phi) = &\frac{\partial}{\partial x}(\rho u \Phi) + \frac{\partial}{\partial y}(\rho v \Phi) + \frac{\partial}{\partial z}(\rho w \Phi) + \\ &-\frac{\partial}{\partial x}\left(\Gamma \frac{\partial \Phi}{\partial x}\right) - \frac{\partial}{\partial y}\left(\Gamma \frac{\partial \Phi}{\partial y}\right) - \frac{\partial}{\partial z}\left(\Gamma \frac{\partial \Phi}{\partial z}\right) - S^{\Phi} = 0 \end{aligned} \tag{6.15}$$

where Γ is the diffusion coefficient.

Eqn. (6.15) is also written in a convenient form for conservative discretization as

$$\vec{\nabla} \cdot \vec{j}^{\Phi} = S^{\Phi} \tag{6.16}$$

with

$$\vec{j}^{\Phi} = \rho \vec{v} \Phi - \Gamma \vec{\nabla} \Phi \tag{6.17}$$

where $\vec{j}^{\Phi}$ is the vector flux of Φ by advection and diffusion.

Integrating (6.16) over the volume $\forall$ yields

$$\int_{\forall} \vec{\nabla} \cdot \vec{j}^{\Phi} d\forall = \int_{A} \vec{j}^{\Phi} \cdot \vec{n} dA = \int_{\forall} S^{\Phi} d\forall \tag{6.18}$$

where A is the surface area of this volume and **n** the unit normal vector to the surface.

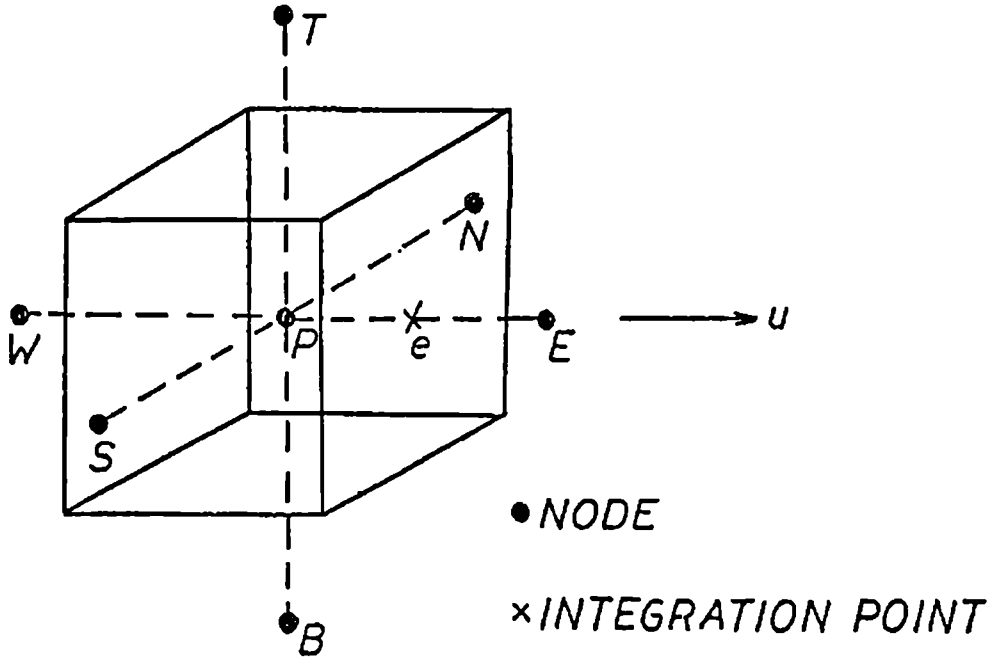

Figure 6.3: Representative control volume, node and integration point layout.

For a single 3D control volume, shown in Fig 6.3, with its west, east, south, north, bottom and top neighbouring points, Eqn. (6.18) can be approximated by

$$J_e + J_n + J_t - J_w - J_s - J_b = \overline{S}^{\Phi} \cdot \forall \tag{6.19}$$

where J_e for example is the total advection and diffusion flux across the east face of the control volume

$$J_e \approx \dot{m}_e \Phi_e - \Gamma_e A_e \left(\frac{\partial \Phi}{\partial x} \right)_e$$

and $\overline{S}^{\Phi}$ the average value of S^{Φ} over $\forall$.

The flux terms in Eqn. (6.19) are approximated through algebraic relations involving the nodal variables and assuming a spatial distribution of Φ between the nodes. In TASCflow discretization of advective fluxes is performed by either 'Mass Weighted Skew upstream differencing' (MWS) or 'Linear Profile Skew upstream differencing' (LPS) [114, 115]. The skewed upstream differencing reduces, for Mass Weighting, or eliminates, for Linear Profile, the possibility of false diffusion due to flows not aligned with the grid. Additionally, advective flux terms thus obtained can be corrected in TASCflow with the so-called 'Physical Advection Correction' (PAC) term to obtain a spatial second order truncation error. The diffusive (molecular and turbulent) fluxes are approximated by 'Central Differencing Scheme' (CDS). Source and sink terms are assumed to be constant over the control volume considered.

With all the relations considered between volume face points and nodal variables, the algebraic equation for Φ at node P becomes:

$$\left(\sum_{nb} A_{nb}^{\Phi}\right) \cdot \Phi_P = \sum_{nb} A_{nb}^{\Phi} \cdot \Phi_{nb} + b_P^{\Phi} \tag{6.20}$$

, resulting, for a computational grid containing n nodes, in a system of n algebraic equations. In (6.20) nb refers to neighbours of node P. Φ represents any advected and/or diffused variable, including components of velocity u,v and w, energy, turbulent kinetic energy and its dissipation, and other transport scalars.

The inclusion of time-dependent flows is similarly undertaken by integrating the time derivative term from time t_0 to $t = t_0 + \Delta t$.

Solution of Discrete Equations

The linear equation sets are usually too large to solve economically by direct solution methods, so iterative methods are used.

Many CFD codes for incompressible flows generate and solve the discrete equations for each variable in isolation. Since this does not account for the strong coupling between variables, for example through Coriolis terms, boundary conditions, or pressure/velocity coupling, the sequence of linear solutions

often converges slowly to the non-linear solution. In TASCflow, the important inter-variable couplings are represented in the linear equations. A block iteration methods, the block-line Gauss-Seidel, is used to simultaneously update the variables of the momentum and mass conservation equations. These block iteration methods of solving the coupled equations greatly improve the reliability of the convergence of the linear equations. They require, however, a large number of local iterations when the problem becomes large, or has highly anisotropic coefficient ratios, such as those that occur when the cell aspect ratio is large. In TASCflow two strategies are used to address these issues:

1. The Additive Correction Multigrid method [116] is used to accelerate the solution. This is a fully coupled, conservative, linear multigrid implementation that ensures that calculation times can be achieved which increase only linearly with the number of grid nodes.

2. Another variant of this accelerator, called Block Correction, is also implemented to address the coefficient ratio problem.

The turbulence equations are solved separately and successively. Details of the solution procedure are described in [113].

6.3 Numerical Simulation of the Flow Within the Isoflow ^{TM} Centrifugal Blood Pump

6.3.1 Introduction

As stated previously, the Isoflow ^{TM} pump (Aries Medical) was selected to demonstrate the numerical analysis of flow conditions within a centrifugal blood pump with complex geometry and to determine the mechanical loading of blood constituents passing through the pump.

A centrifugal pump delivers kinetic energy to the fluid by the rotating motion of its impeller and as a consequence generates two distinct relative motions of

the fluid: to the stationary part (casing) and to the rotating part (rotor). The existence of these relative motions is recognised in this study by the separate calculation of the impeller flow relative to the rotating impeller with inclusion of inflow through the inflow port, and of the flow relative to the stationary outlet system. Geometrical modelling, determination of boundary conditions, details of the numerical procedure and results are presented for both cases in the following sections.

In the numerical analysis undertaken in the frame of this work the approximation of steady flow within the impeller and outlet domain was assumed. However, with respect to a comprehensive blood damage assessment, a spatial model should be as close to reality as possible and a 3D-analysis is therefore necessary. Thus, all regions where high stresses are anticipated may be examined. In particular, the gap between blades and casing, the rear of the impeller disc as well as inflow and outflow domains are of great interest in a flow and stress analysis.

6.3.2 Simulation of the Inlet/Impeller Flow

Geometrical Model

The Isoflow ^{TM} pump is a centrifugal impeller pump. The impeller disc consists of an inner and outer segment separated by an annular gap (Fig 6.4). The segments are rigidly connected by four long curved vanes tapering in height towards the disc periphery. Similarly-shaped short vanes extending over the outer segment only are located between the long vanes. The impeller shaft rotates in a bearing in a polycarbonate casing which incorporates axial inflow and tangential outflow ports. Rotating fluid seals are avoided by magnetically coupling the impeller to an external drive motor. A schematic drawing of the pump is shown in Fig 6.4, its main dimensions are given in Appendix C.

Because of the periodicity of the geometry, it is sufficient to examine a 90^0 sector of the impeller plane. Using a boundary fitted grid of hexahedral elements, a long blade-to-long blade section containing one small blade was chosen

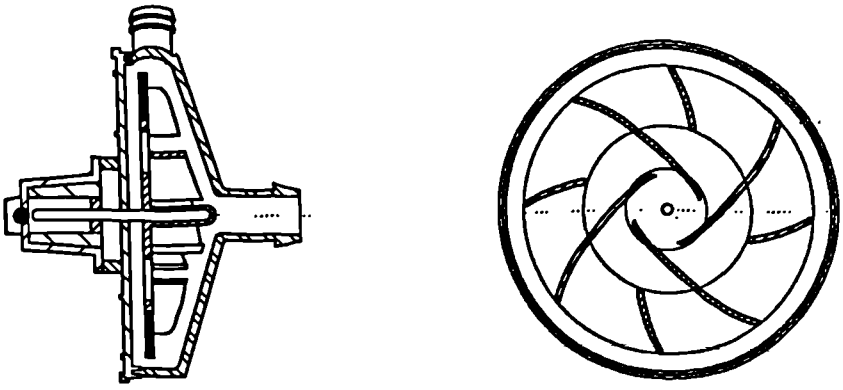

Figure 6.4: Schematic drawing of the Isoflow ^{TM} centrifugal blood pump.

for the pump analysis. Differences in the geometrical profile of suction and pressure sides of the long blade were neglected and the camber line was taken as representative for the long blade's geometry. Small blade, disc and shaft are modelled by block-off volumes. The stator inflow port was modelled separately and attached to the main grid. Grid refinements were placed in the vicinity of the edges of blades, casing walls, disc and shaft, i.e. areas where high velocity gradients are anticipated.

The grid modelling of the complete interior of the Isoflow ^{TM} pump is presented in Fig 6.5. The grid contains approx. 35,000 finite-volume elements.

In order to demonstrate the suitability and effectiveness of a numerical flow analysis for design parameter studies, the gap size between the blades and the front casing was varied. This geometrical parameter was altered in order to compare the predicted blood damage with an experimental investigation of the dependency of blood destruction on the gap size in a centrifugal blood pump reported by [117]. The original pump geometry (gap size linearly increasing with increasing radius from 3 mm at the leading edge to 5 mm at the trailing edge) and a gap size reduced by factor two (ranging from 1.5 mm to 2.5 mm) were analysed.

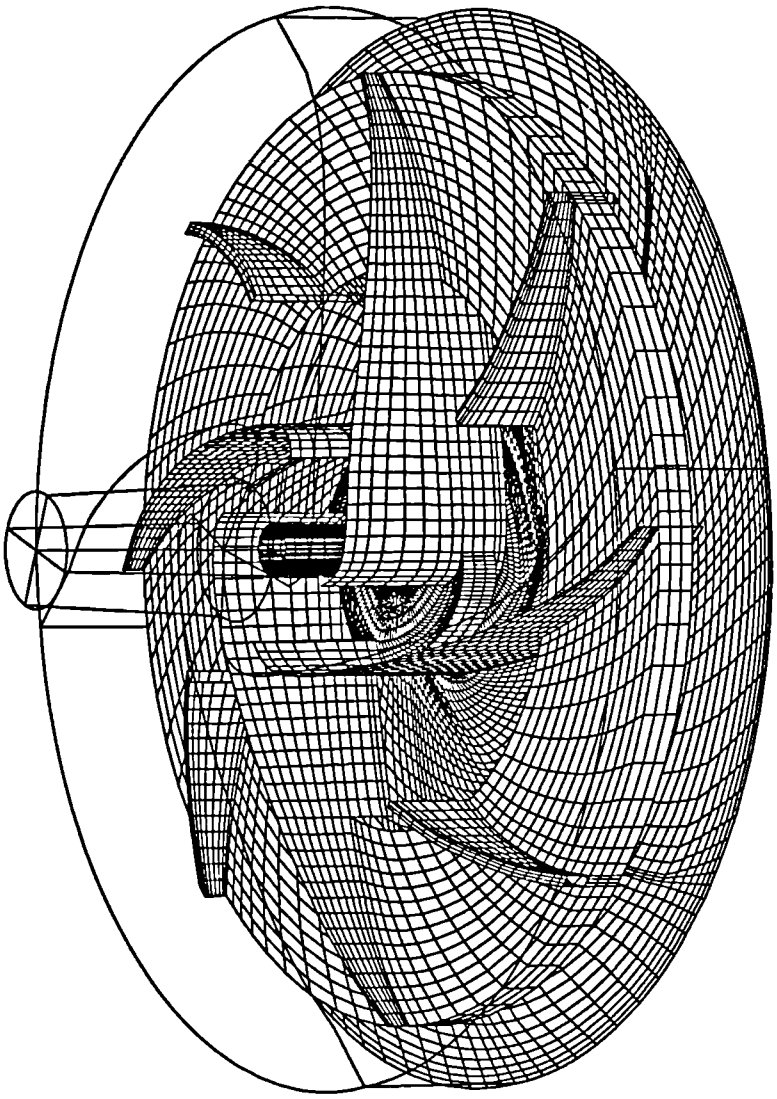

Figure 6.5: Numerical grid for entire inlet/impeller domain.

Boundary Conditions

The boundary condition at the inlet is a uniform axial flow in the absolute frame of reference calculated from a given mass flow rate. The CFD code performs an automatic conversion into the relative (rotating) frame of reference. Five rotational speed/flow rate combinations were investigated. Input parameters for rotational speed and flow rate were chosen as listed in Table 6.1 together with the related Reynolds numbers at the inlet for each operating condition:

n (rpm)	Q (l/min)	Re
500	1	785
1000	3	2,350
1500	5	3,925
2000	7	5,500
2000	10	7,850

Table 6.1: Input parameters for rotational speed and flow rate and Reynolds numbers at inlet.

Values for the turbulent kinetic energy k and its dissipation ϵ at the inflow boundary were set according to the following relations [113]:

$$k = \frac{3}{2}(Tu * v)^2 \quad ; \quad \epsilon = \frac{k^{1.5}}{L}$$

where

Tu – *Turbulence intensity, which is assumed to be* 2% ($Tu = 0.02$)

L – *Eddy length scale, is assumed to be approximately* 10% *of a characteristic length (tube diameter)* ($L = 0.001\ m$)

v – *Mean velocity.*

A $k-\epsilon$ model was included in all rotational speed/flow rate combinations despite partially low Reynolds numbers suggesting laminar or transitional flow in the inflow tube, since turbulent flow was expected to occur in the impeller region.

A reference pressure value of 0 Pa was specified at an arbitrary node of the outflow region. A direction for the velocity at the outlet had to be set in order

to prevent convergence problems. Values for k and ϵ at the ouflow boundary were obtained by a first-order extrapolation. The outflow region corresponding to the cross-sectional area of the actual outlet port was located in the centre of the outer circumference, according to Fig 6.6. Since the flow was modelled in

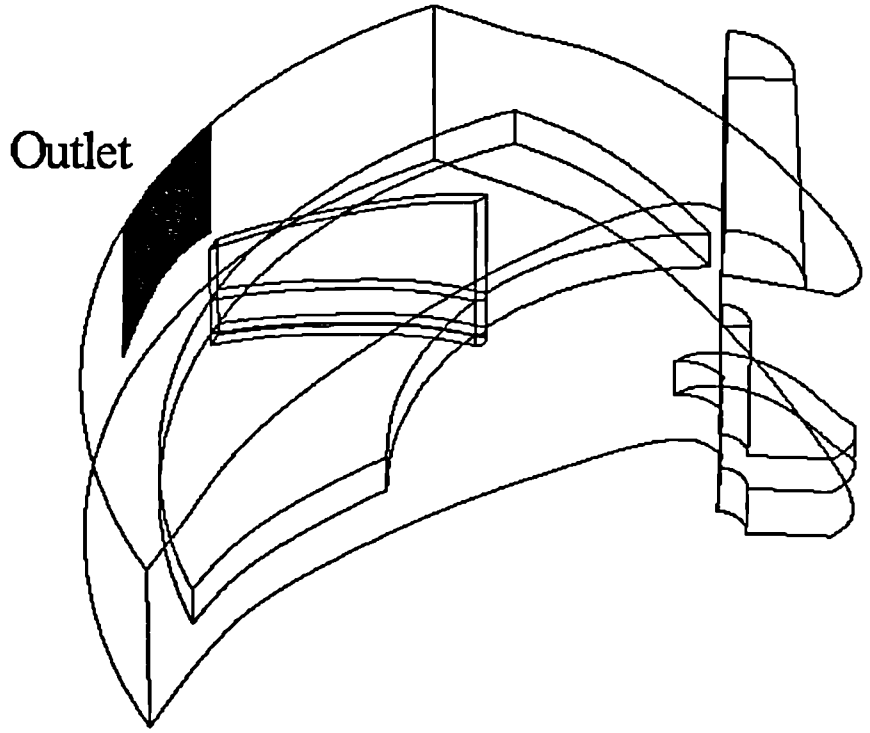

Figure 6.6: Definition of outflow domain for inlet/impeller flow simulation.

a rotating frame of reference, a stationary wall boundary condition was applied to all parts of the rotor (disc, blades, shaft), whereas the casing was defined as counterrotating walls. Near wall regions are modelled using 'wall functions'. A qualitative diagram of this region for a general turbulent flow is shown in Fig 6.7. The region consists of three distinctive zones whose depths are related to

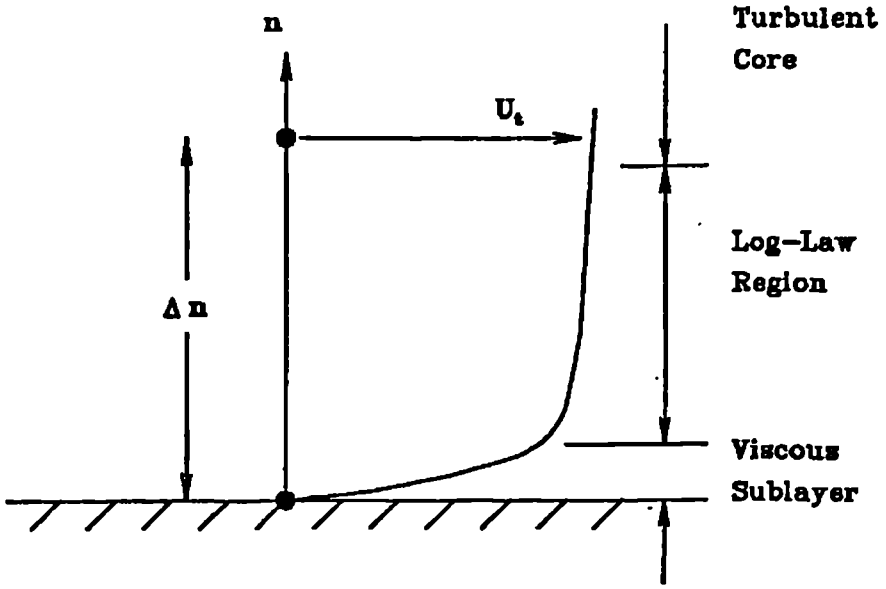

Figure 6.7: Near wall region.

the dimensionless distance function n^+. n^+ is defined as

$$n^+ = \frac{\varrho \cdot \Delta n \cdot u_\tau}{\mu} \tag{6.21}$$

where

$$u_\tau = \left(\frac{\tau_w}{\varrho}\right)^{\frac{1}{2}}$$

with

$$\tau_w \; - wall\ shear\ stress \;\; ; \;\; \Delta n - distance\ wall - node.$$

The three distinctive layers are in TASCflow ^{TM} related to n^+ as

$$\begin{aligned} n^+ \leq 30 \quad & viscous\ sublayer\ (constant\ \tau_w) \; + \; buffer\ layer \\ 30 < n^+ \leq 500 \quad & log - law\ region \\ n^+ > 500 \quad & turbulent\ core\ . \end{aligned} \tag{6.22}$$

For a cyclic blade-to-blade analysis periodic boundary conditions were specified above and below the long blade. The values for density and kinematic viscosity of the medium were taken to be 1000 kg/m^3 and $3{\cdot}10^{-6}$ m^2/s, respectively, to approximate blood properties under normal temperature and haematocrit conditions.

Numerical Calculation

The numerical solution of the discretized Reynolds-averaged Navier-Stokes equations for the rotating frame of reference was performed for all rotational speed/ flow rate combinations and for the reduced gap variant at n=2000 rpm/Q=7 l/min. Advective fluxes were discretized applying the MWS method, having a

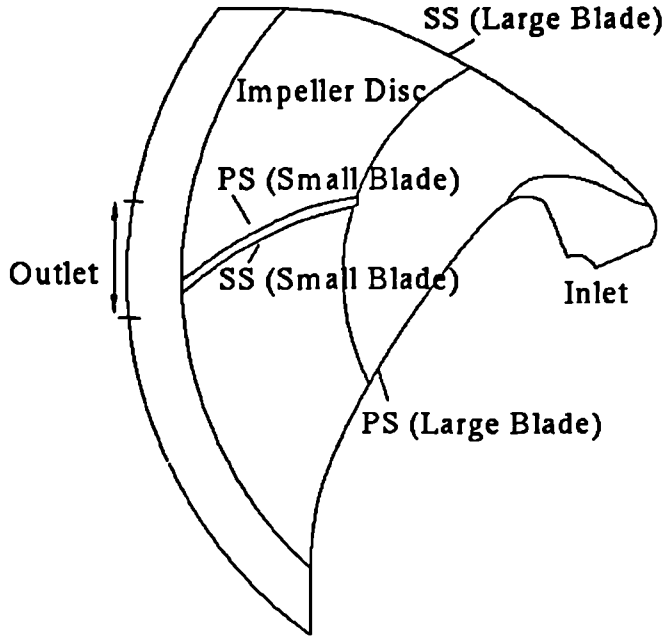

Figure 6.8: Geometric notations in blade-to-blade plane.

spatial truncation error of first order, and by the LPS method combined with PAC, having a spatial truncation error of second order. The Cartesian components of the relative velocity vector, static pressure, turbulent kinetic energy and its dissipation, turbulent viscosity, the Reynolds stress tensor and viscous wall shear stresses were calculated.

The solution was considered convergent when the maximum normalized residual fell below a value of 1×10^{-3}. The convergency criteria was reached after a maximum of 200 iterations which corresponds to a computational time of approximately 3 hours on an IBM RS 6000/53 H workstation.

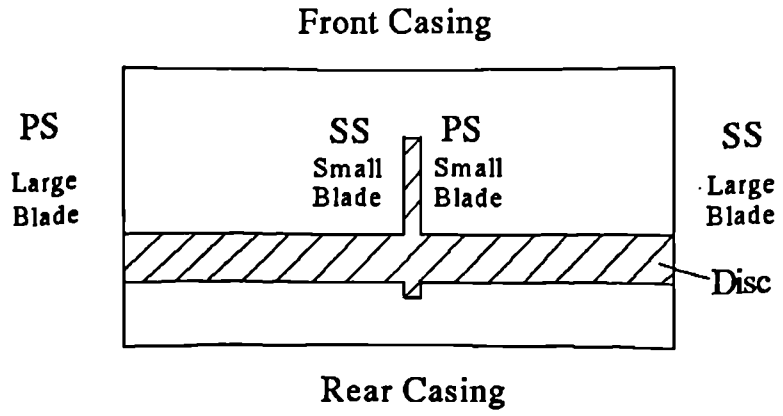

Figure 6.9: Geometric notations in impeller-channel plane.

Results

Because of the numerous flow parameters calculated for each rotational speed/ flow rate combination as well as for the reduced gap variant, a comprehensive presentation of all results would not be practicable. It was therefore decided to put emphasis on the discussion of computed flow characteristics for the case of n=2000 rpm/Q=7 l/min. The effect of variation of rotational speed (and flow rate), flow rate (at constant rotational speed) and the gap size between blades and front casing on the flow parameters is presented as a comparison with this case. Geometrical notations for the three characteristic planes , blade-to-blade plane, impeller-channel plane and meridional plane, which are used in the consequent graphical presentations are given in Figs 6.8, 6.9 and 6.10, respectively.

Speed/flow rate combination, n=2000 rpm/Q=7 l/min

Figs 6.11 to 6.14 show plots of velocity vectors projected on an intrinsic blade-to-blade plane, a blade-to-blade plane coinciding with the impeller disc and two impeller channel planes (upstream and downstream of the small-blade leading edge), respectively. Flow disturbances, stagnation areas and recirculation zones are clearly recognizable and can be assigned to their particular location. Velocity plots in the meridional plane coinciding with pressure and suction sides of the

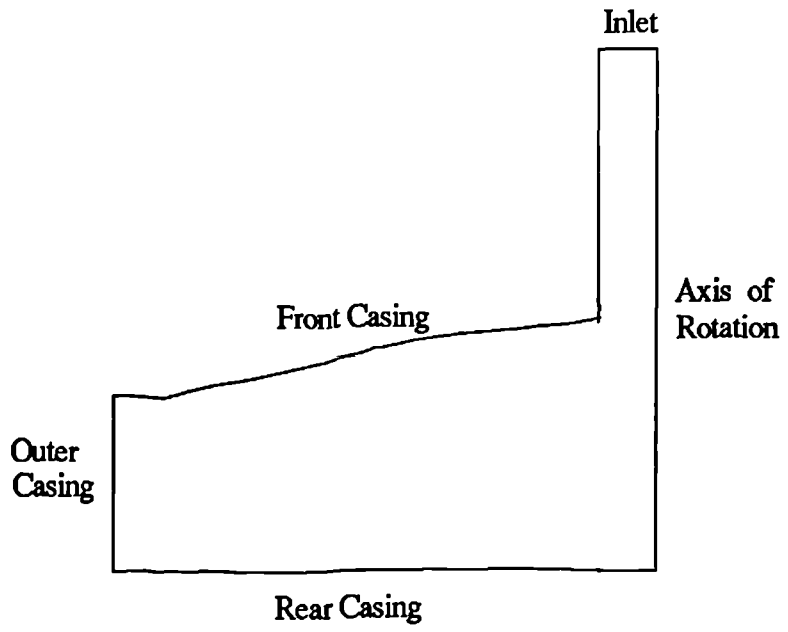

Figure 6.10: Geometric notations in meridional plane.

large and small blades allow a more spatial imaging of flow processes (Figs 6.15 to 6.18). Secondary flow phenomena are especially significant in the vicinity of the small blade and at the suction side of the large blade. Velocity distributions in planes which represent the gap between blades and front casing, and between the disc and the rear casing (Figs 6.19 and 6.20) indicate of the disturbing effects of flow redirection (from axial to radial), pressure- driven backflow, boundary layers and impeller disc. Secondary flows in form of vortices and counterrotating flow are apparent and occur mainly in the inner-radial zone.

A contour plot of the static pressure difference distribution in the blade-to-blade plane (Fig 6.21) reveals the approximate linear rise of the static pressure with radius (an exact linear dependency is only valid for a solid body rotation) and differences between pressure and suction sides of the blades. The continuity of the static pressure distribution in an axial gap plane in vicinity of the front casing (Fig 6.22) validates the periodic boundary condition. Irregularities resulting from the overflow of the blades can be observed.

The turbulent viscosity as a measure of friction in the fluid due to turbulent

Figure 6.11: Velocity distribution in blade-to-blade plane (n=2000rpm/ Q=7 l/min).

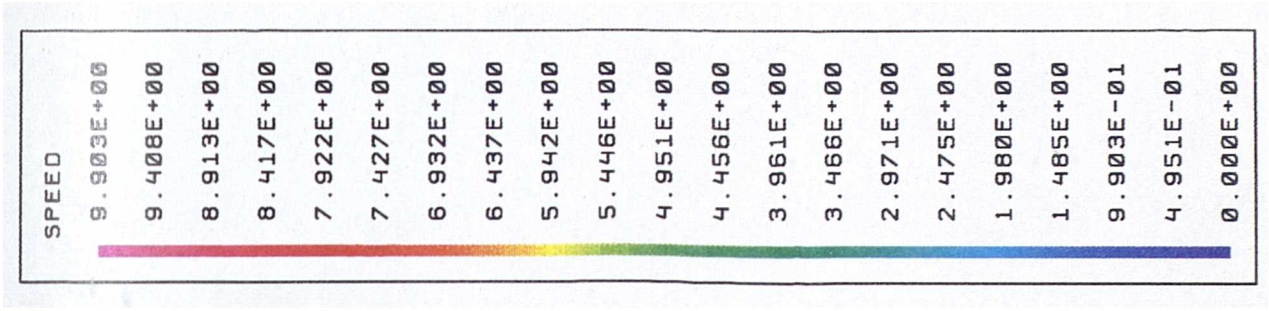

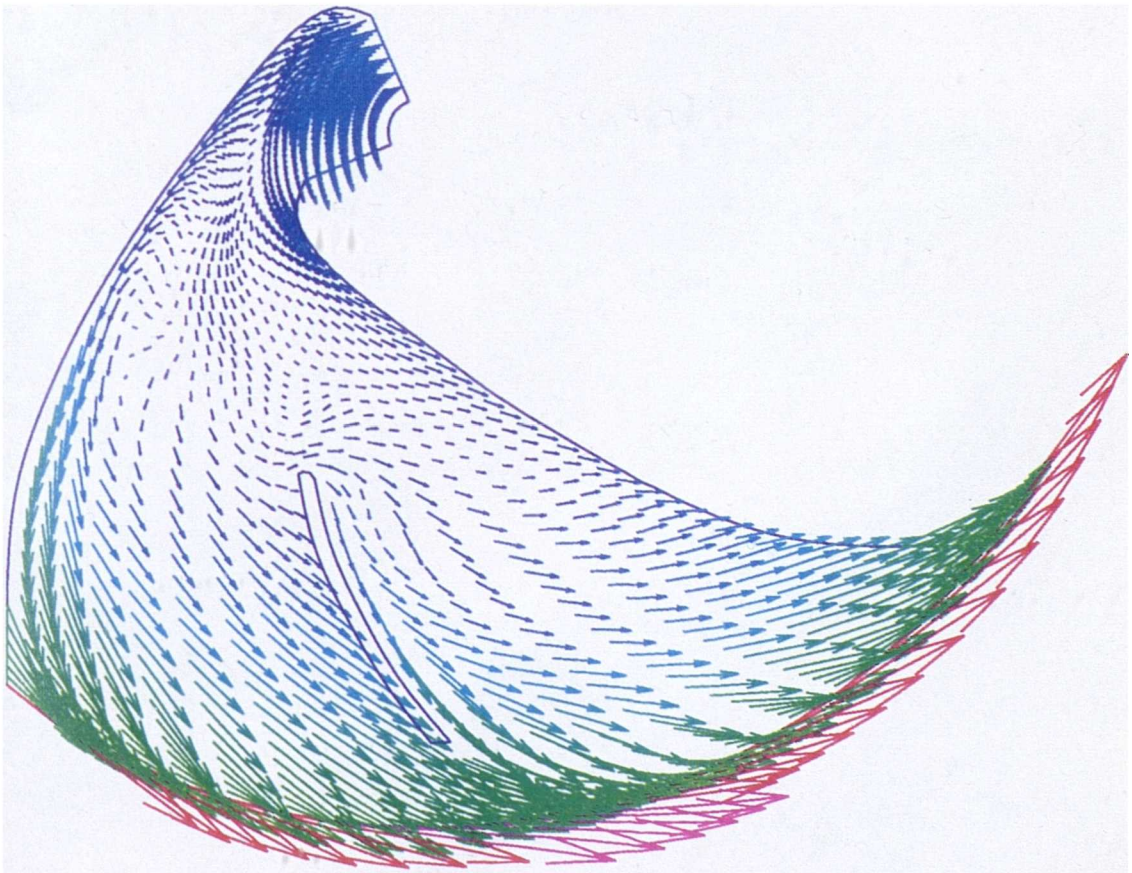

Figure 6.12: Velocity distribution in blade-to-blade plane coinciding with impeller disc (n=2000rpm/ Q=7l/min).

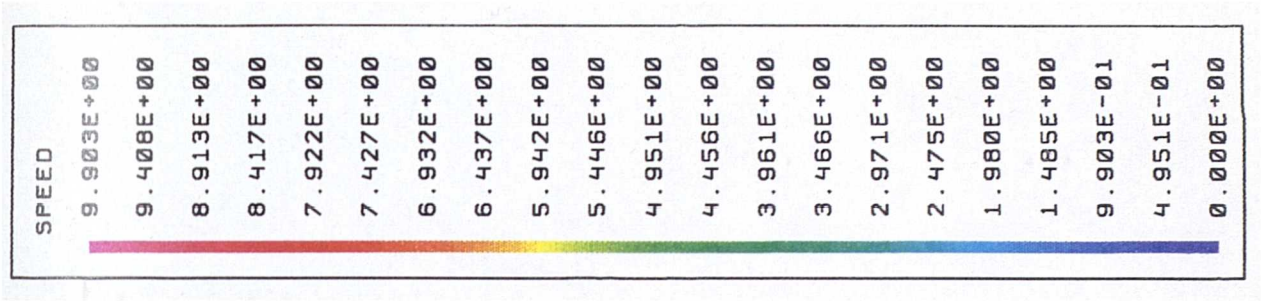

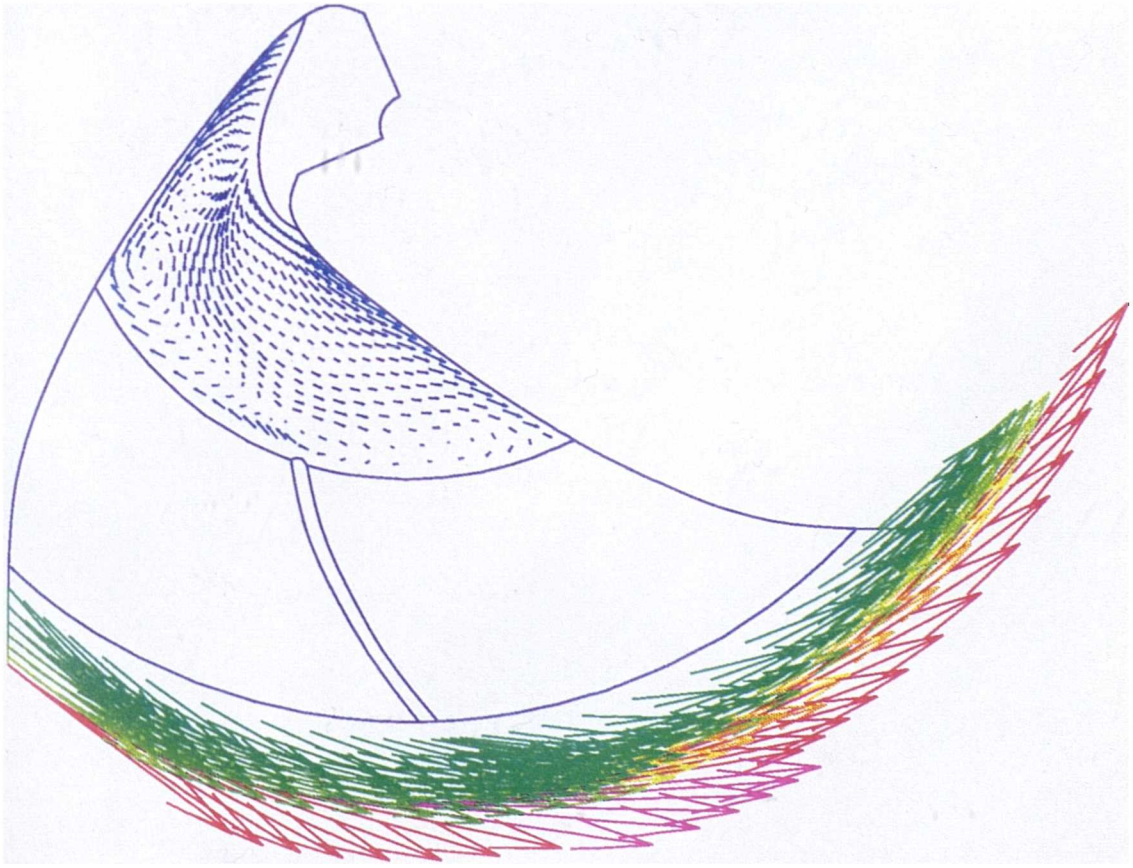

F gure 6.13: Velocity distribution in impeller-channel plane upstream of leading edge of small blade (n=2000rpm/ Q=7l/min).

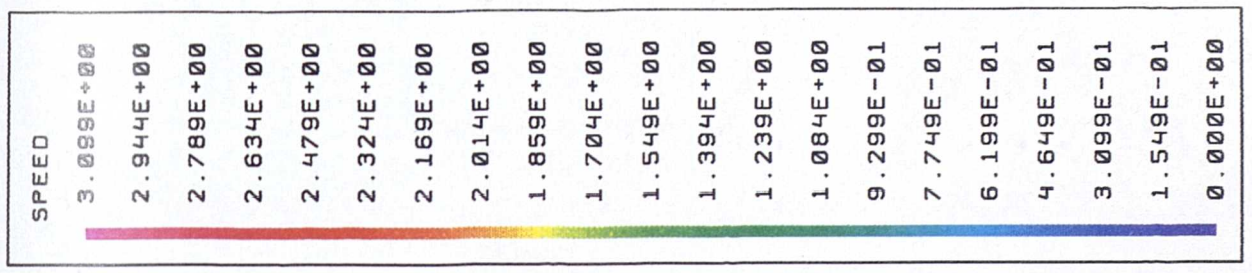

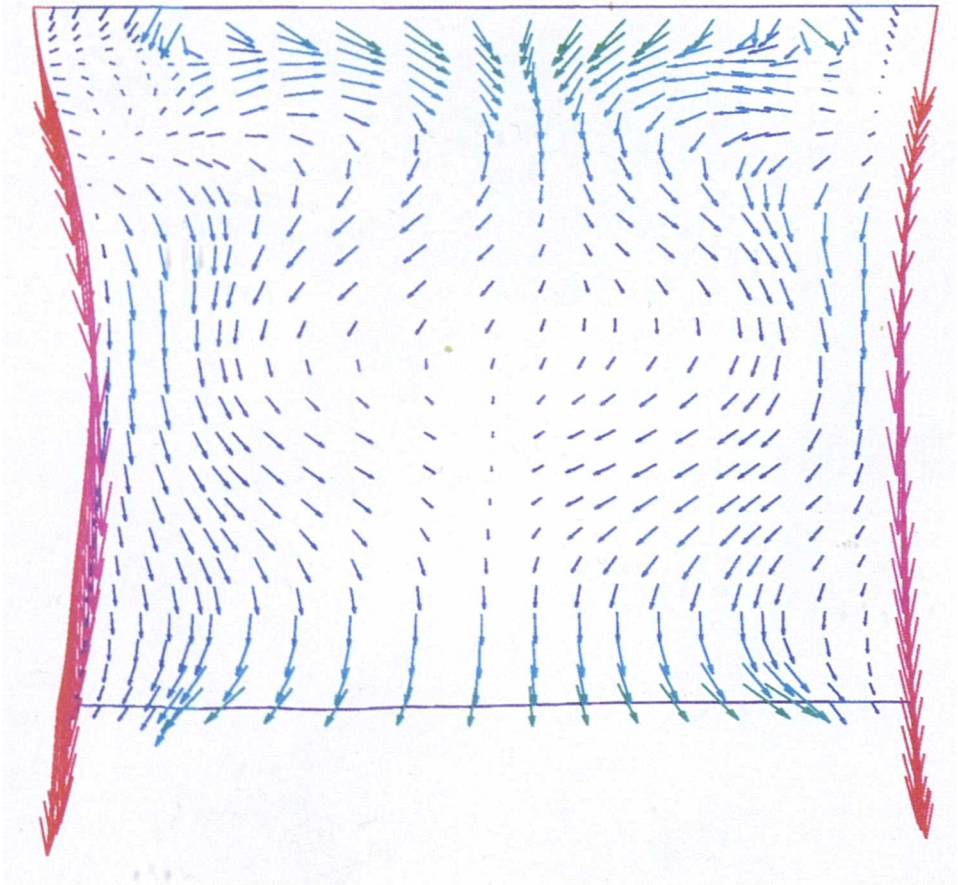

Figure 6.14: Velocity distribution in impeller-channel plane downstream of leading edge of small blade (n=2000rpm/ Q=7l/min).

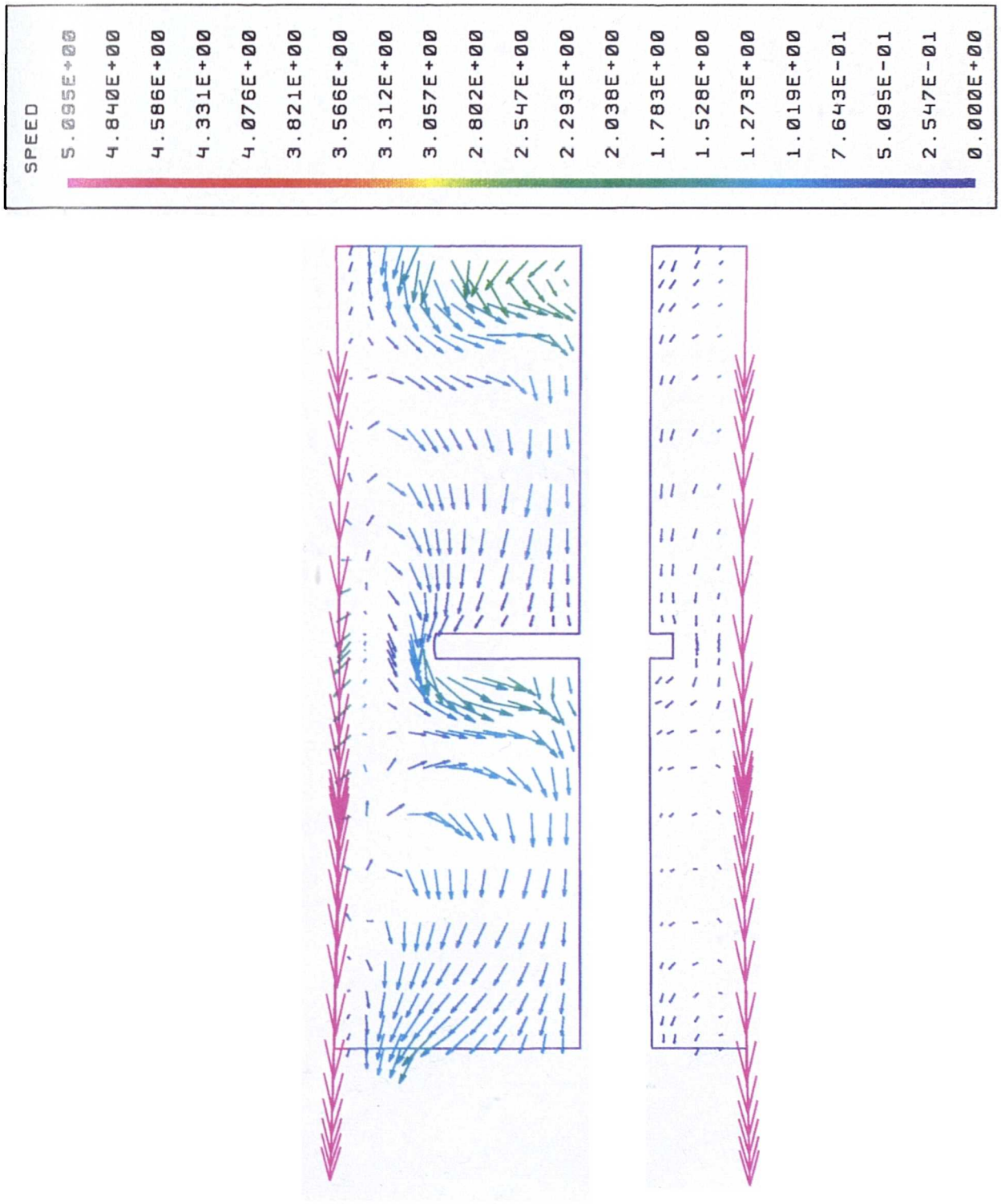

Figure 6.15: Velocity distribution in meridional plane at pressure side of large bl de (n=2000rpm/ Q=7l/min).

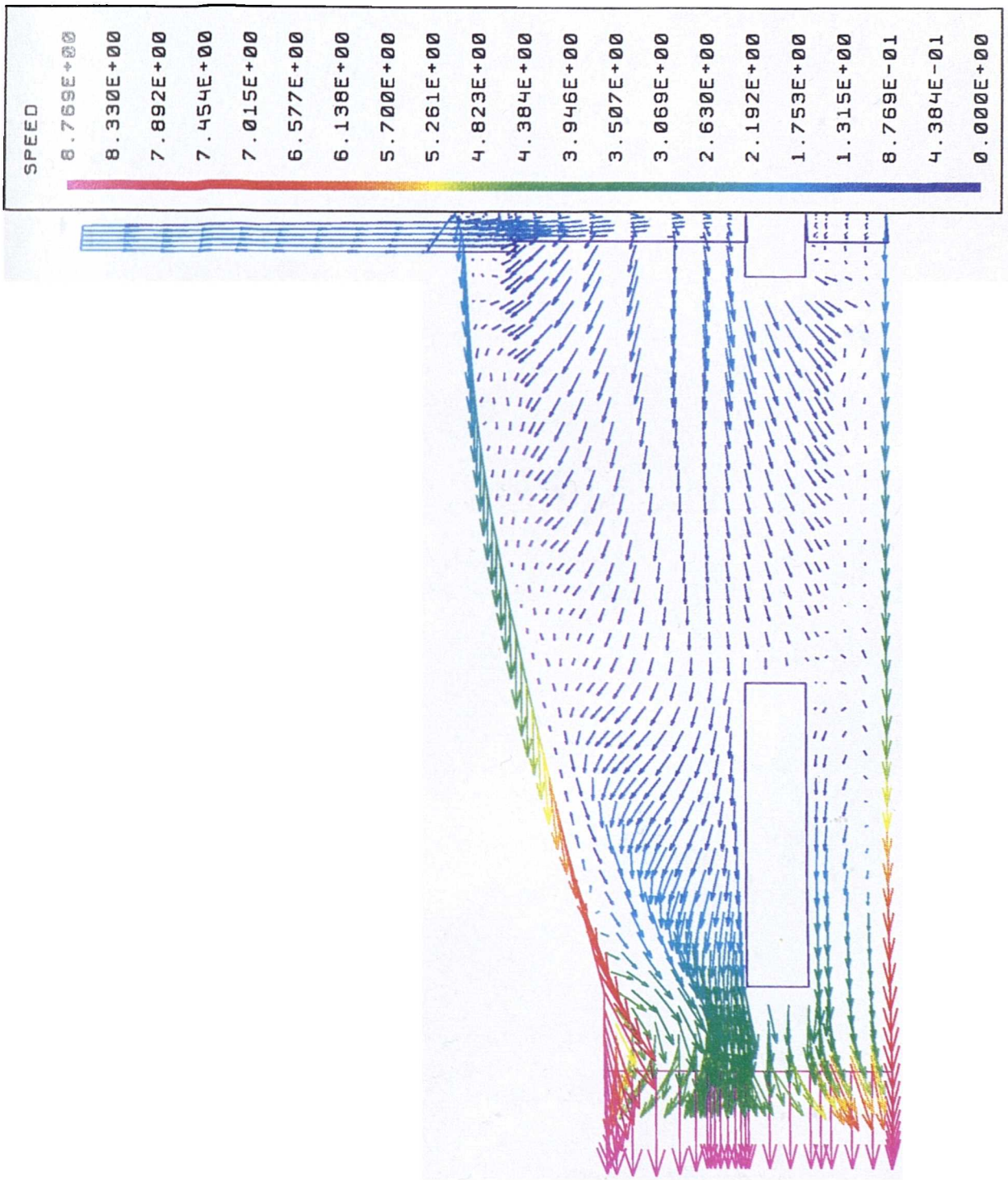

Figure 6.16: Velocity distribution in meridional plane at suction side of large blade (n=2000rpm/ Q=7l/min).

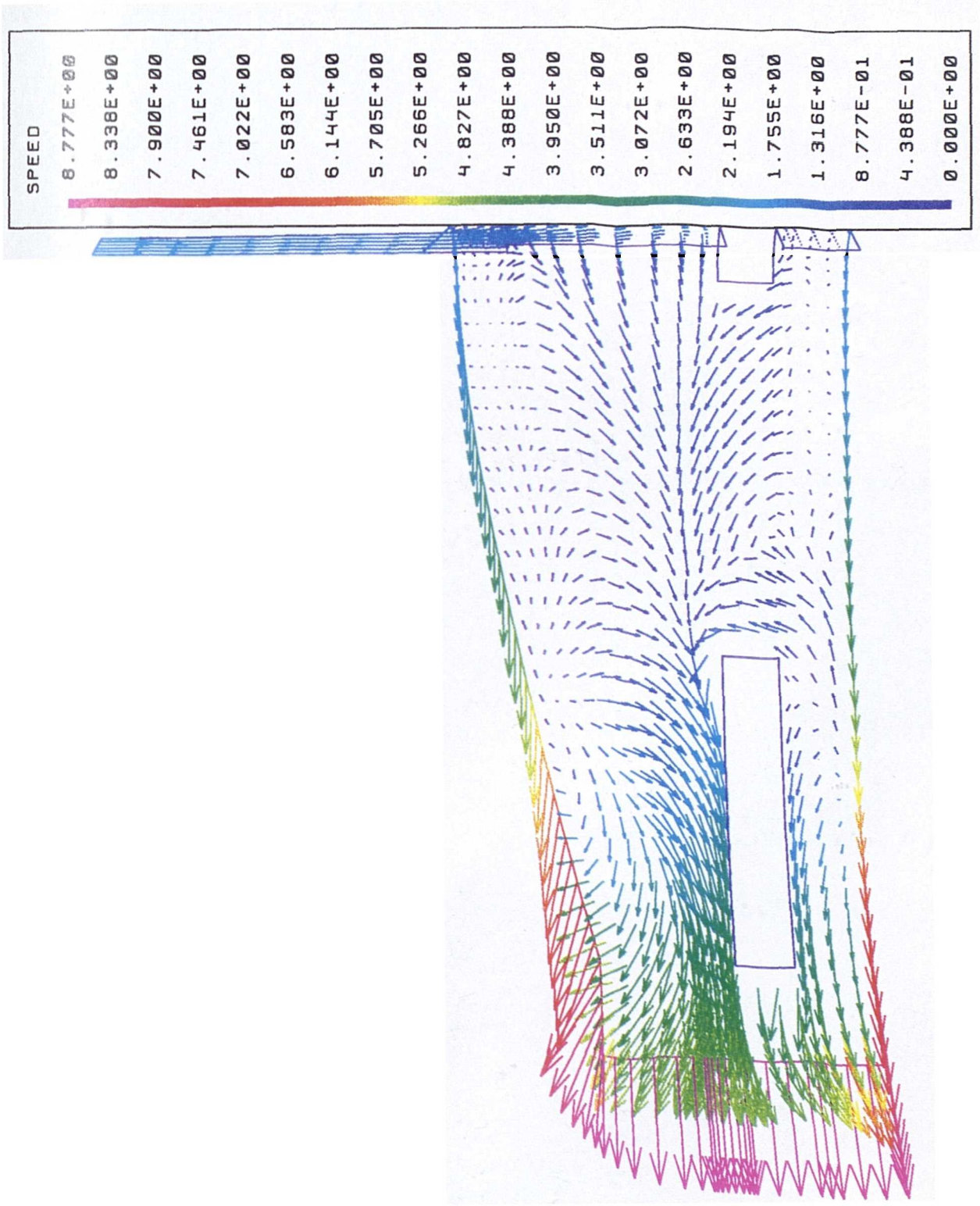

Figure 6.17: Velocity distribution in meridional plane at pressure side of small blade (n=2000rpm/ Q=7l/min).

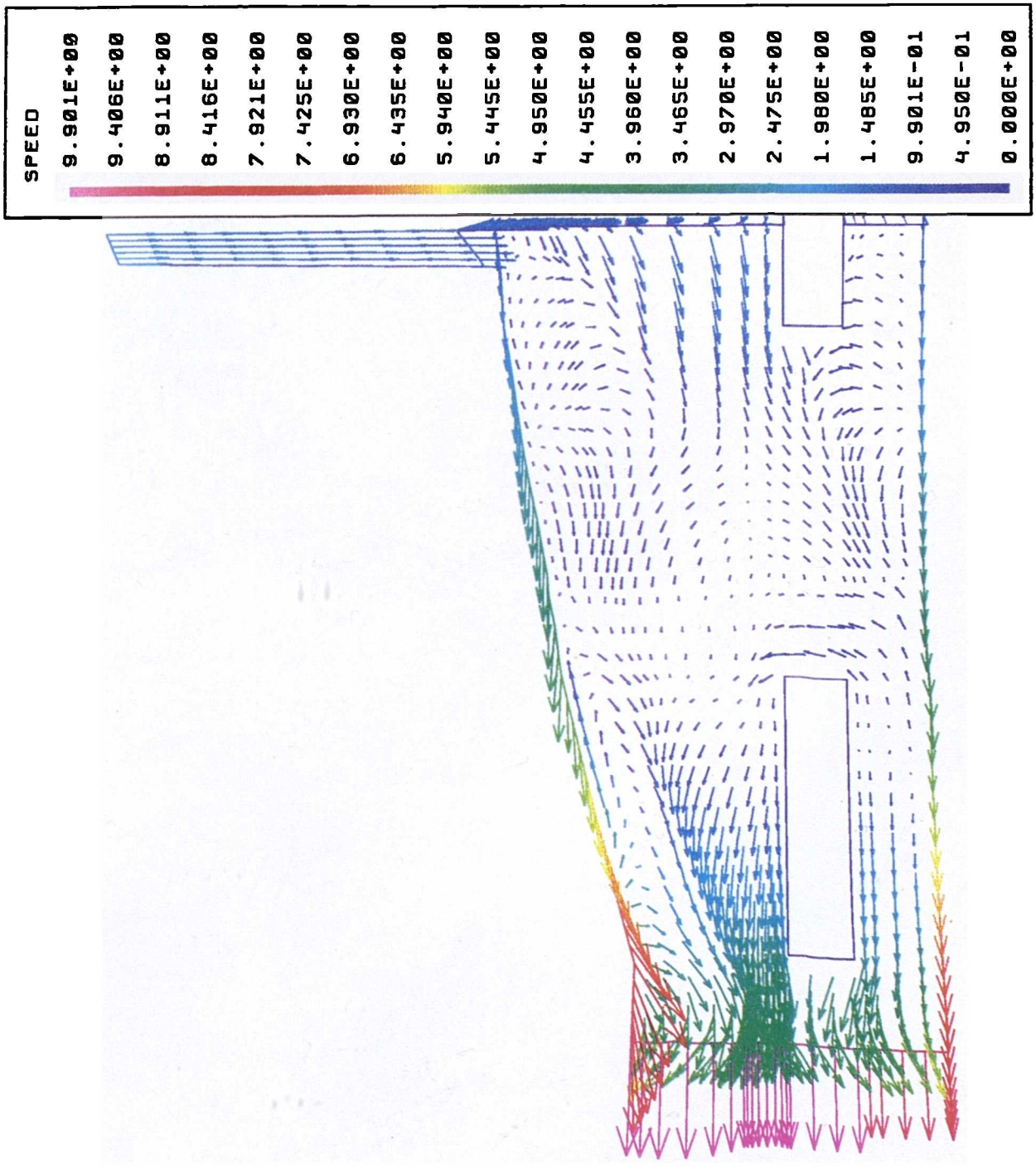

F'gure 6.18: Velocity distribution in meridional plane at suction side of small blade (n=2000rpm/ Q=7l/min).

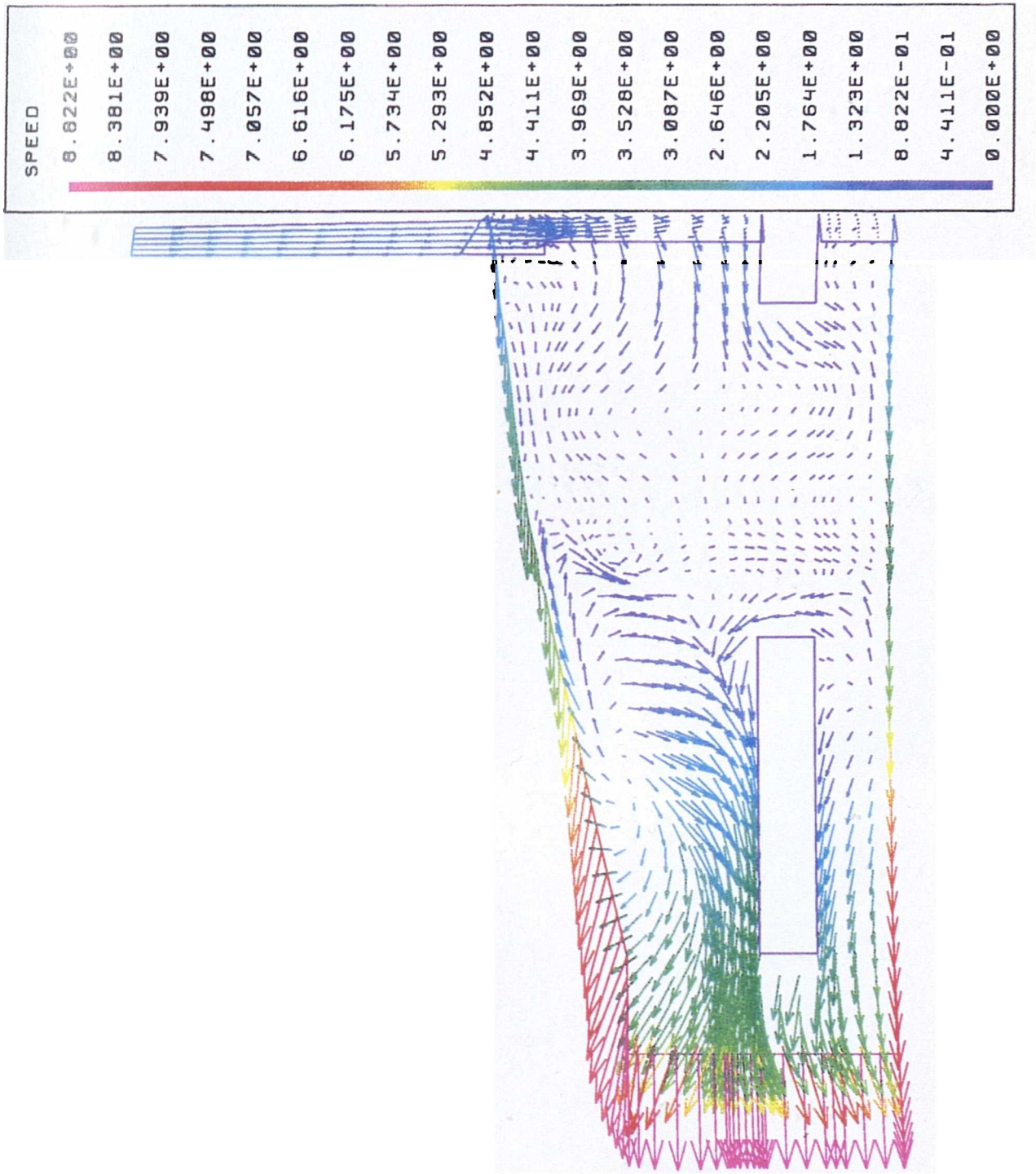

Figure 6.19: Velocity distribution in axial gap plane between blades and front casing (n=2000rpm/ Q=7l/min).

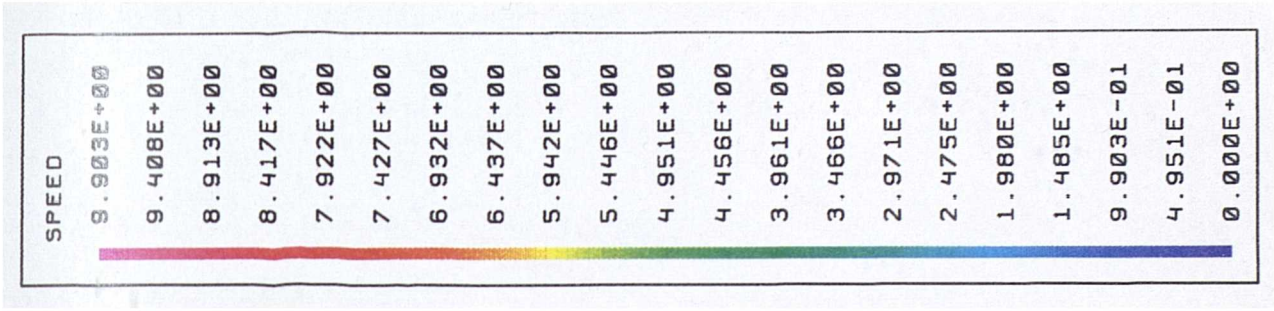

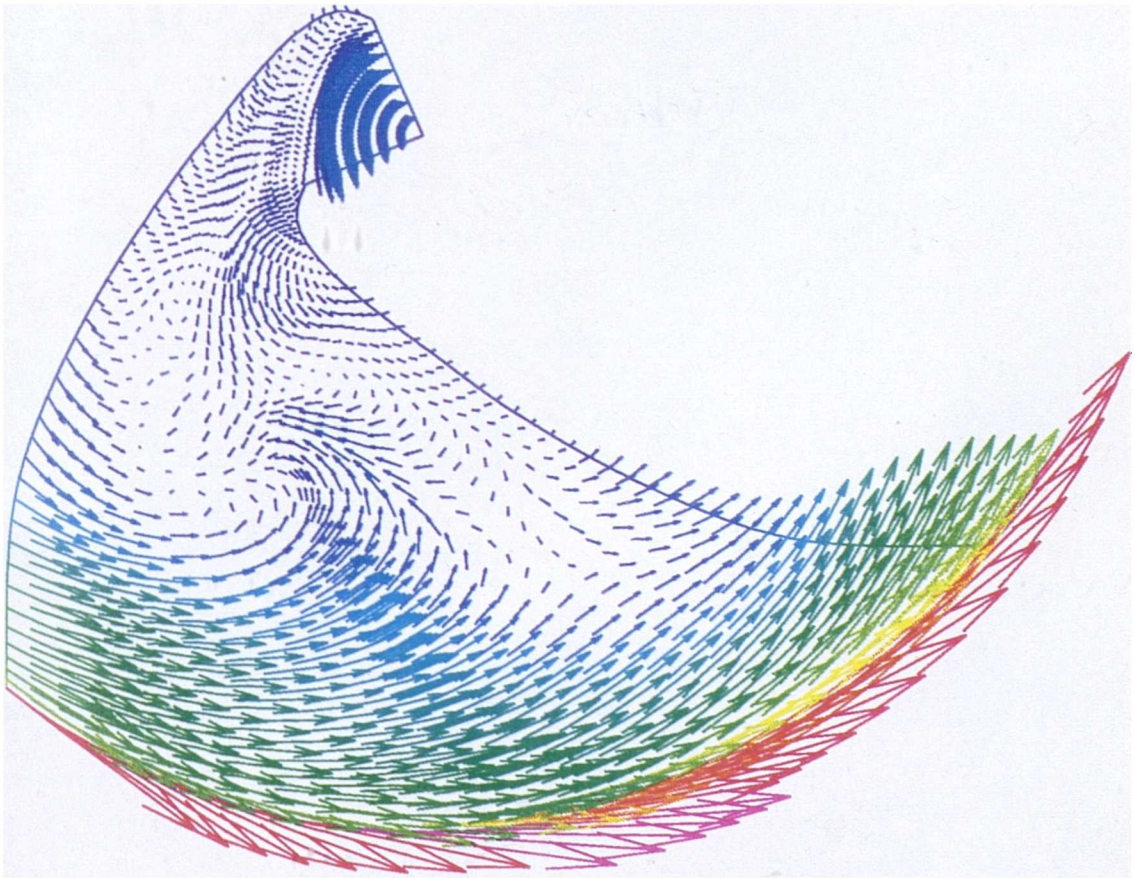

Figure 6.20: Velocity distribution in axial gap plane between impeller disc and rear casing (n=2000rpm/ Q=7l/min).

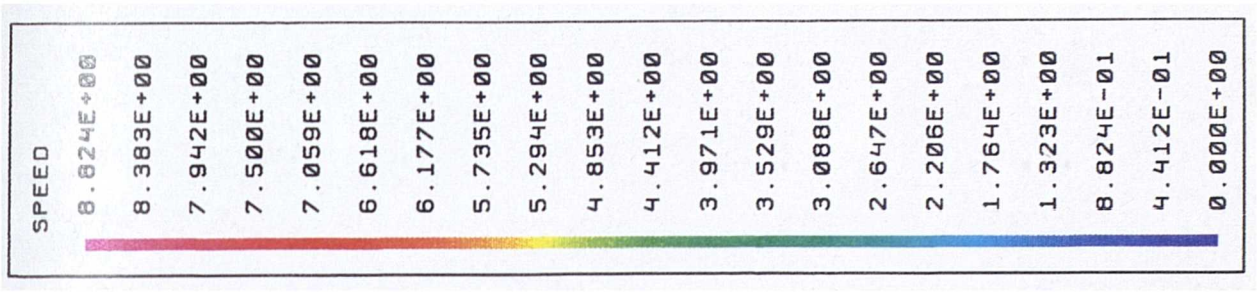

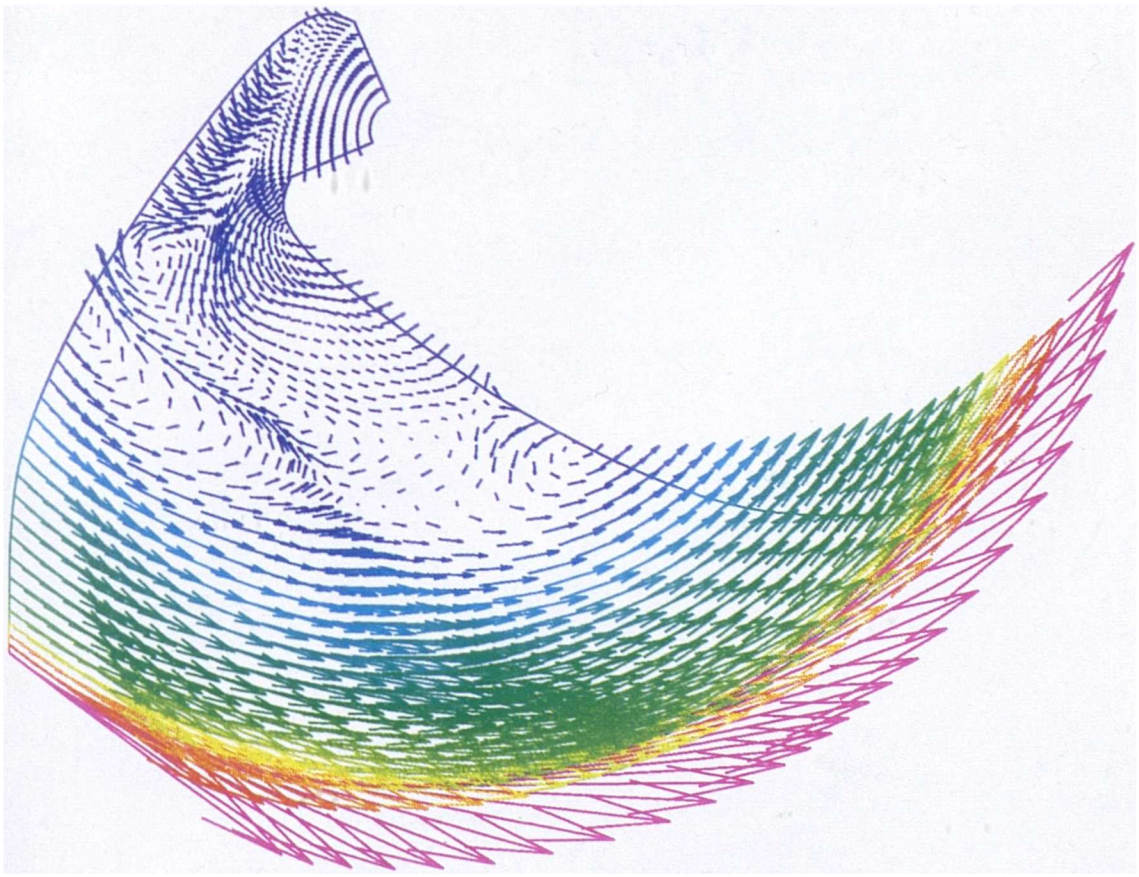

Figure 6.21: Static pressure differences in blade-to-blade plane (n=2000rpm/ Q=7l/min).

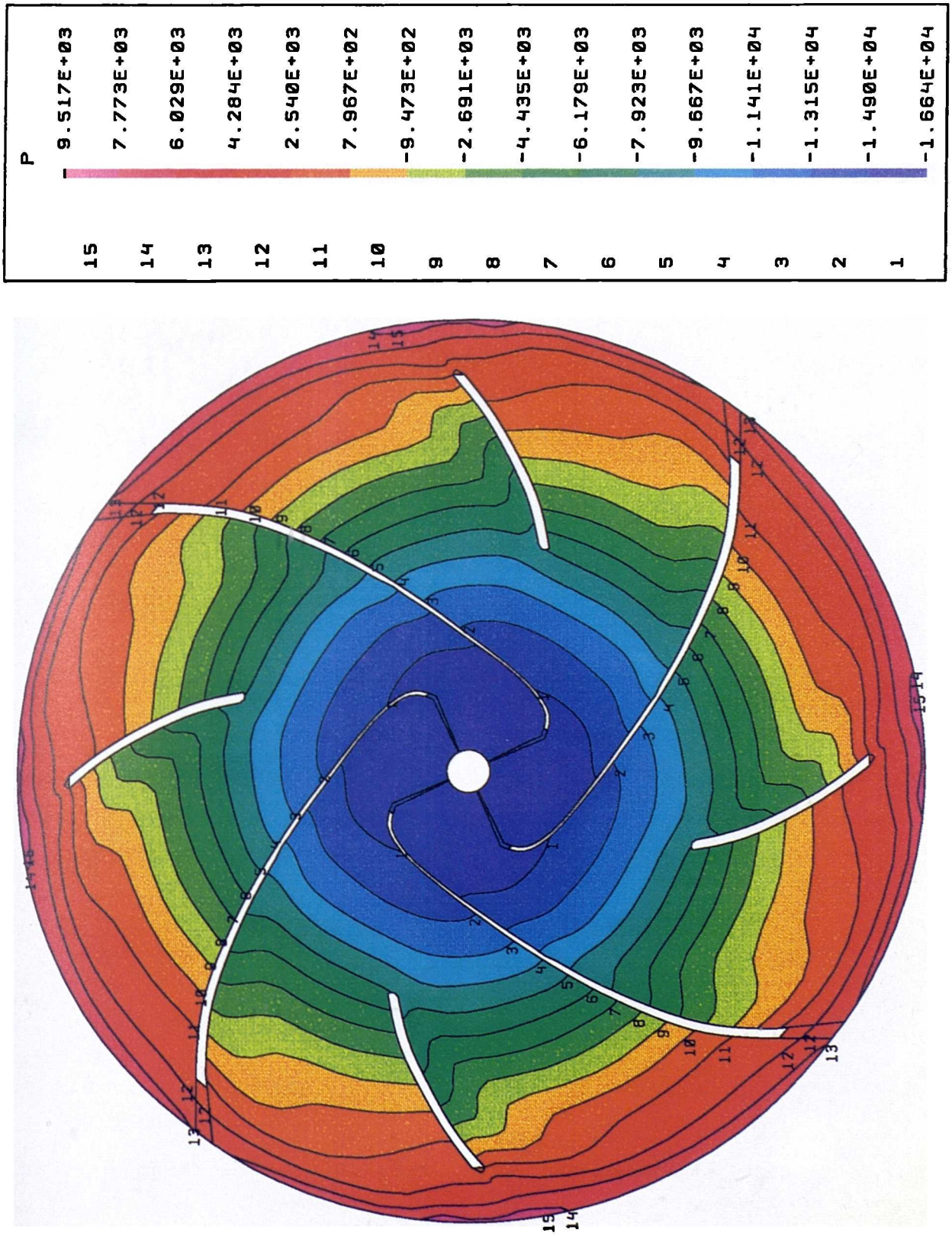

Figure 6.22: Static pressure differences in axial gap plane between blades and front casing (n=2000rpm/ Q=7l/min).

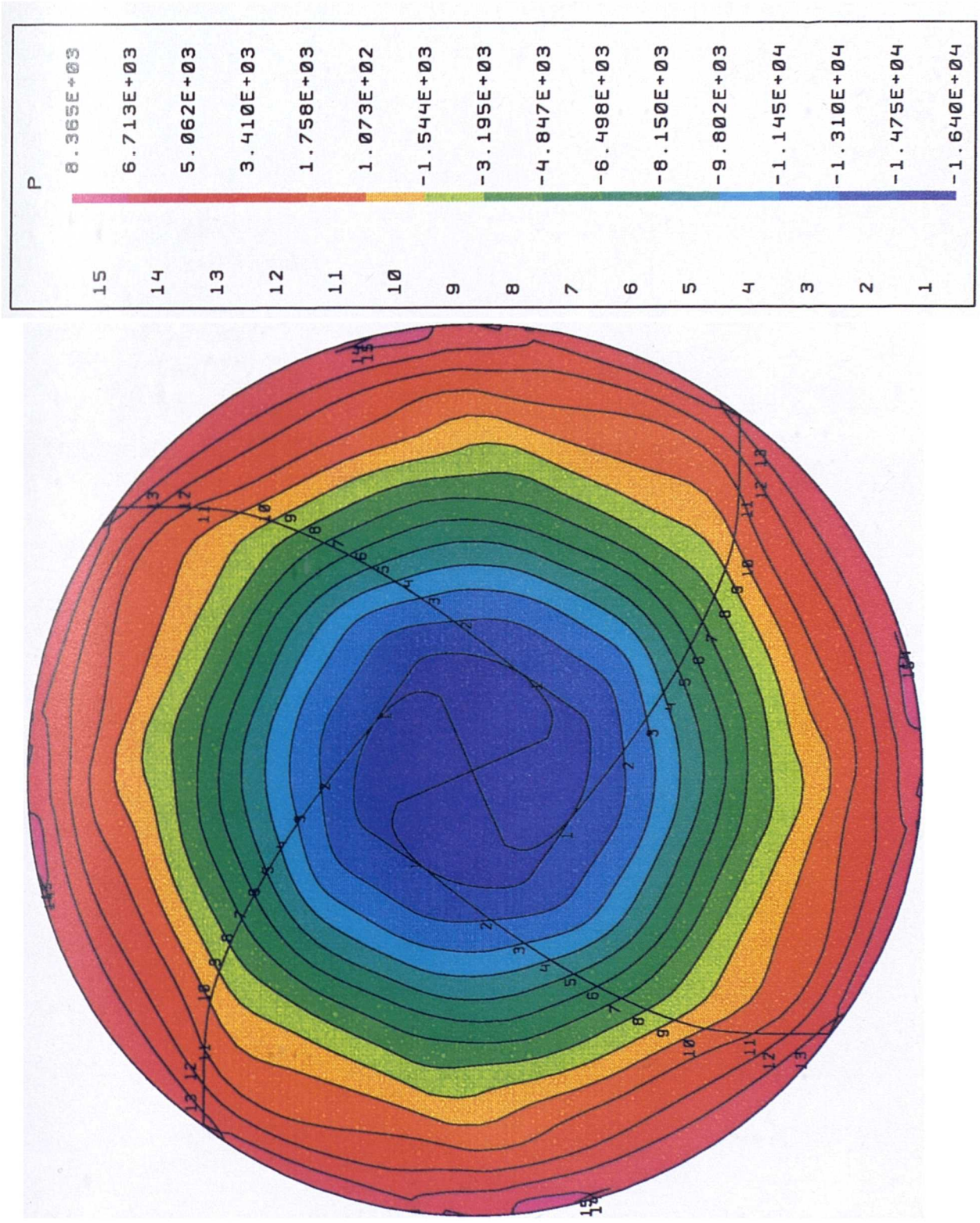

eddies has been normalised with respect to the molecular viscosity which is a constant fluid property by

$$visc\_ratio = \frac{\mu_t}{\mu} .$$

Contour plots of this ratio are shown in Figs 6.23 to 6.26. Highest values of approximately 60 were recorded near to the outlet area (Fig 6.23). Areas of considerable high turbulent viscosity are found at the large blade's suction side at an location upstream of the small blade (Figs 6.24, 6.25) and further downstream at the rear casing (Fig 6.26). The viscosity ratio in many areas of the flow is an expression for dominating eddy transport over molecular transport within this kind of centrifugal pump. It underlines the necessity to incorporate a turbulence model into the analysis, especially with respect to a comprehensive spatial stress analysis.

The distribution of viscous wall shear stresses for representative parts of the stator and rotor are given in Figs 6.27 to 6.29. Maximal values were recorded at the outer radius of the impeller disc. Values at the blade and casing surfaces were comparatively low on the global scale and showed local maxima on the front and outer part of the casing (Figs 6.28, 6.29).

For the assessment of the mechanical loading of blood particles when passing a centrifugal pump, an appropriate parameter must be chosen. For this purpose it was suggested that a scalar stress value be determined on the basis of the comparative stress theory presented in Chapter 4.3. Values for the scalar stress for each nodal point were obtained by applying Eqn. (4.8). The components of the stress tensor itself contained viscous and turbulent stresses. At stationary walls the scalar stress value equals the magnitude of the wall shear stress. Contours of the scalar stress in different planes of the flow domain are shown in Figs 6.30 to 6.36. The highest values by far ($\approx$ 1 kPa) are found in the near outlet region (Fig 6.30). Viscous and turbulent kinetic energy have their global maxima in this part of the impeller flow and therefore support this observation. However, the influence of the imposed directed outflow condition on these results is not entirely clear. Figs 6.31 to 6.34 display, respectively, local scalar stress values in an impeller-channel plane, a blade-to-blade plane, a meridional plane coinciding

Figure 6.23: Turbulent to molecular viscosity ratio in near-outlet plane (n= 2000rpm/ Q=7l/min).

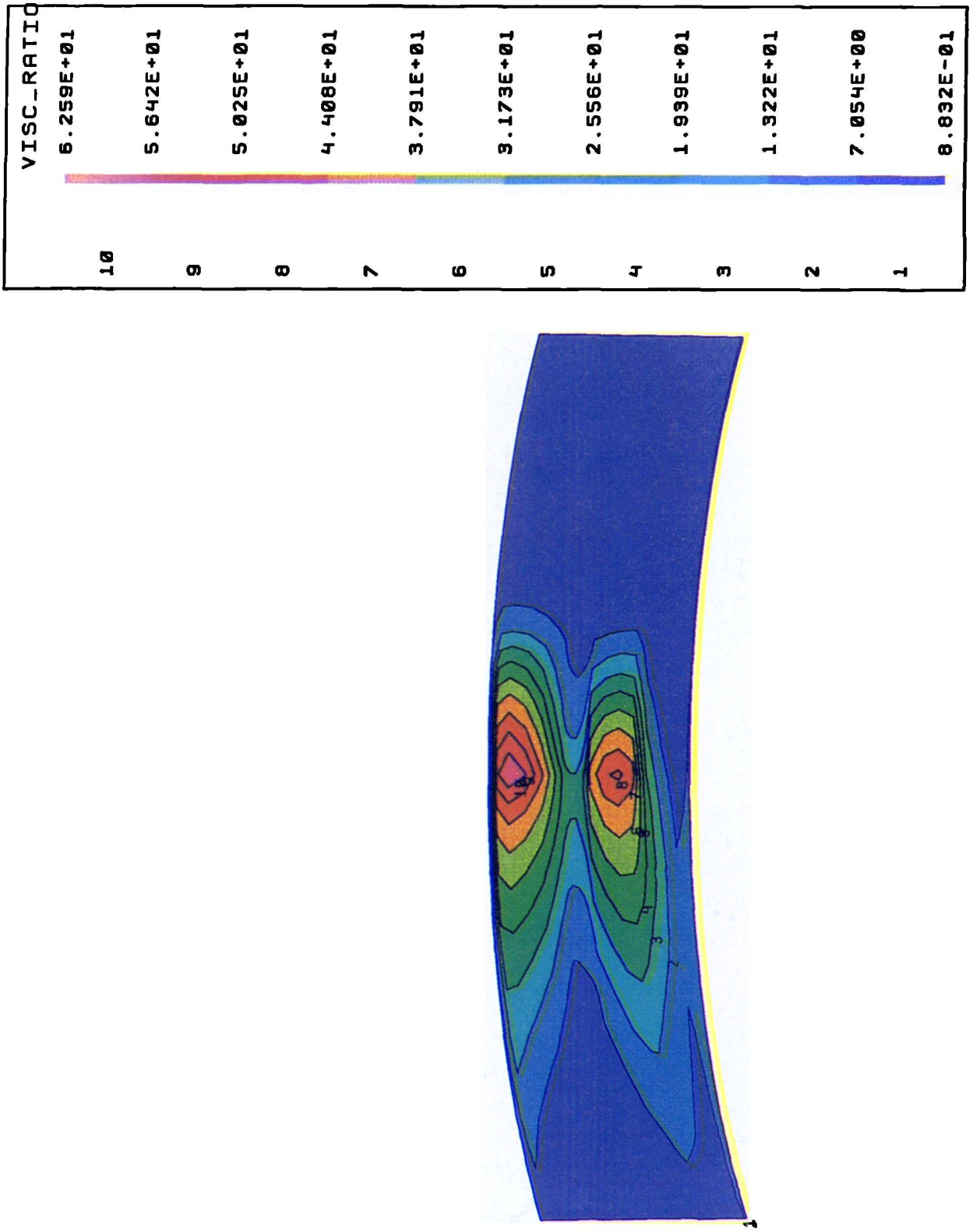

F gure 6.24: Turbulent to molecular viscosity ratio in impeller-channel plane upstream of leading edge of small blade (n=2000rpm/ Q=7 l/min).

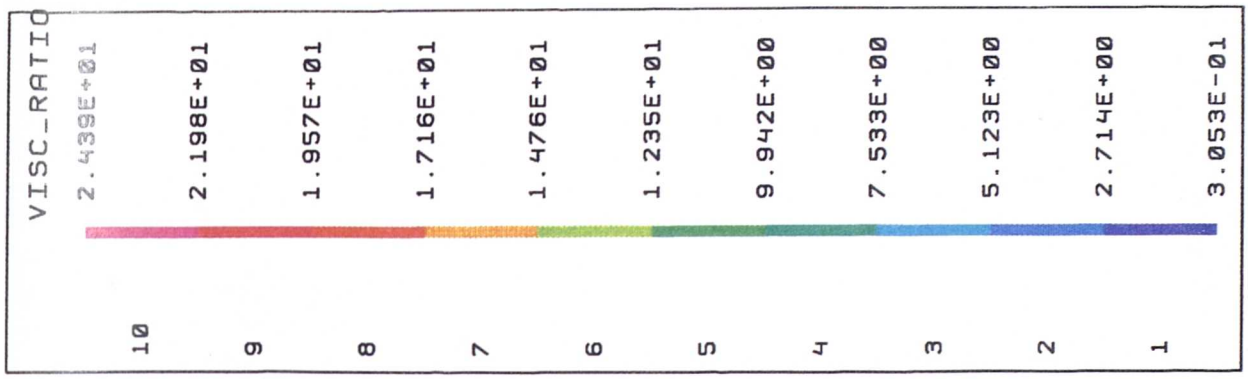

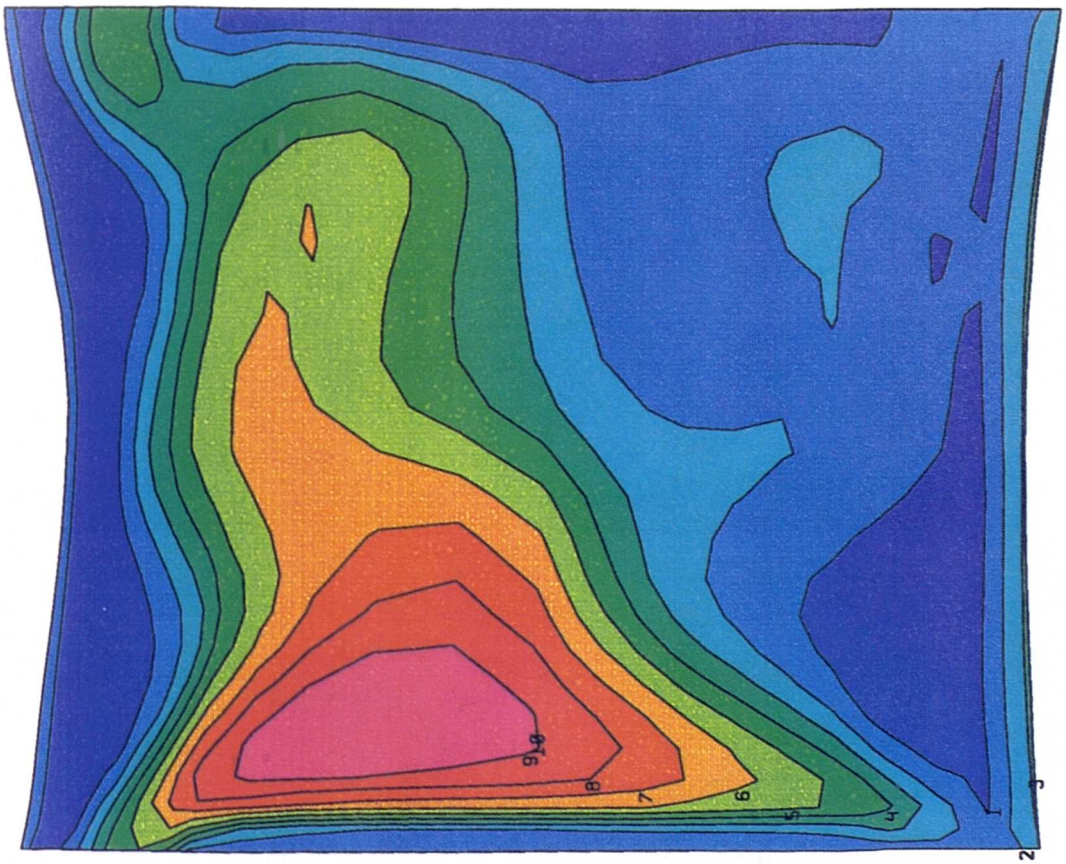

Figure 6.25: Turbulent to molecular viscosity ratio in blade-to-blade plane (n=2000rpm/ Q=7l/min).

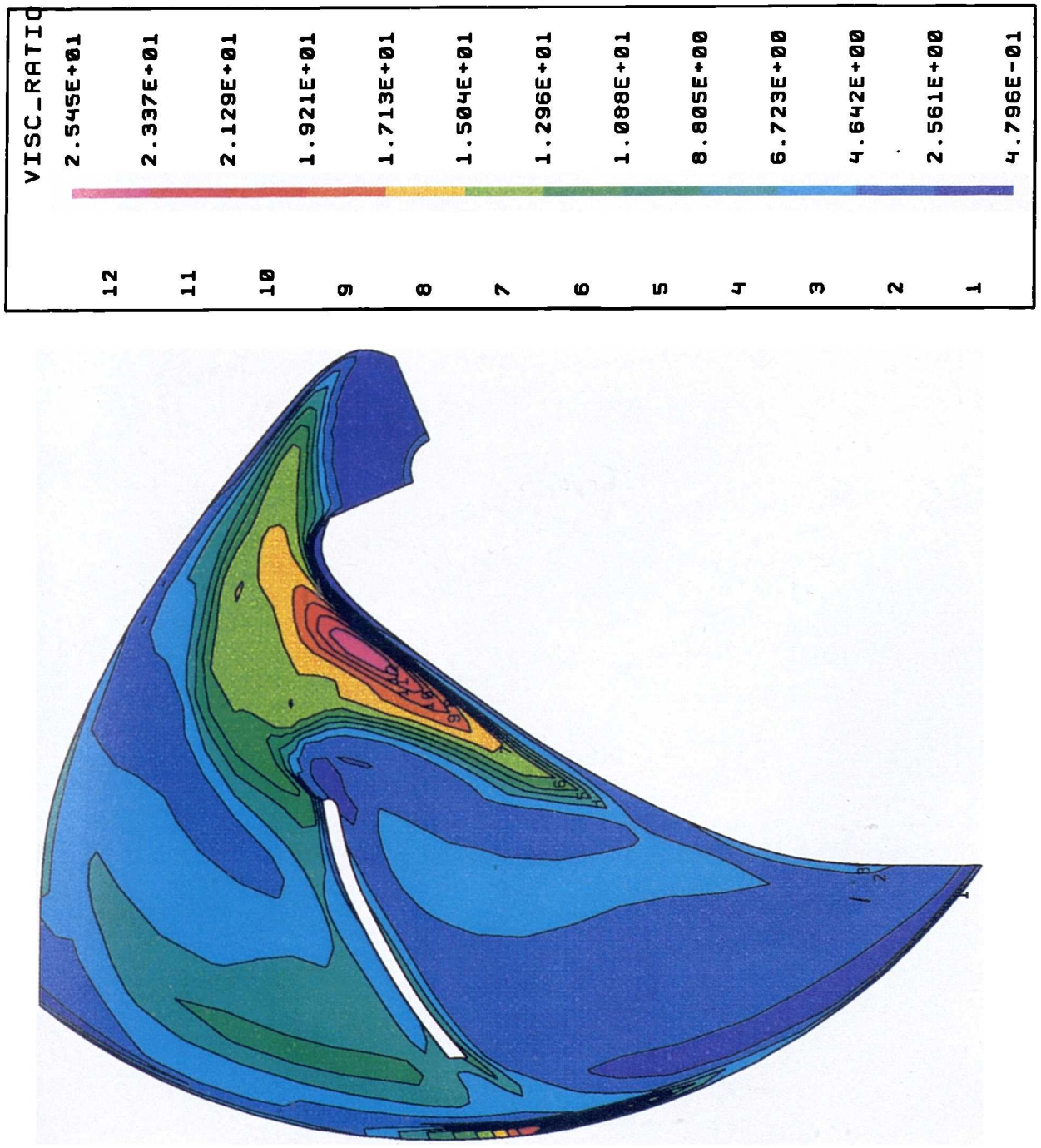

Figure 6.26: Turbulent to molecular viscosity ratio in impeller-channel plane downstream of leading edge of small blade (n=2000rpm/ Q=7 l/min).

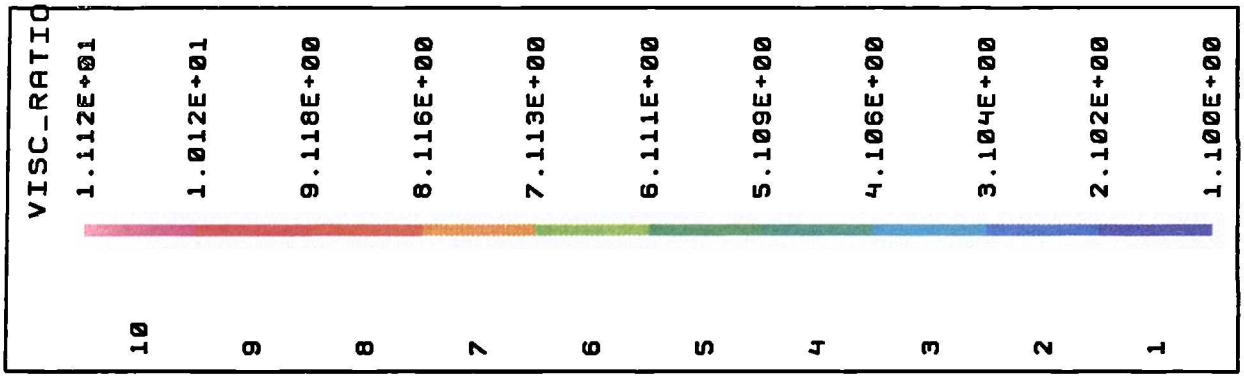

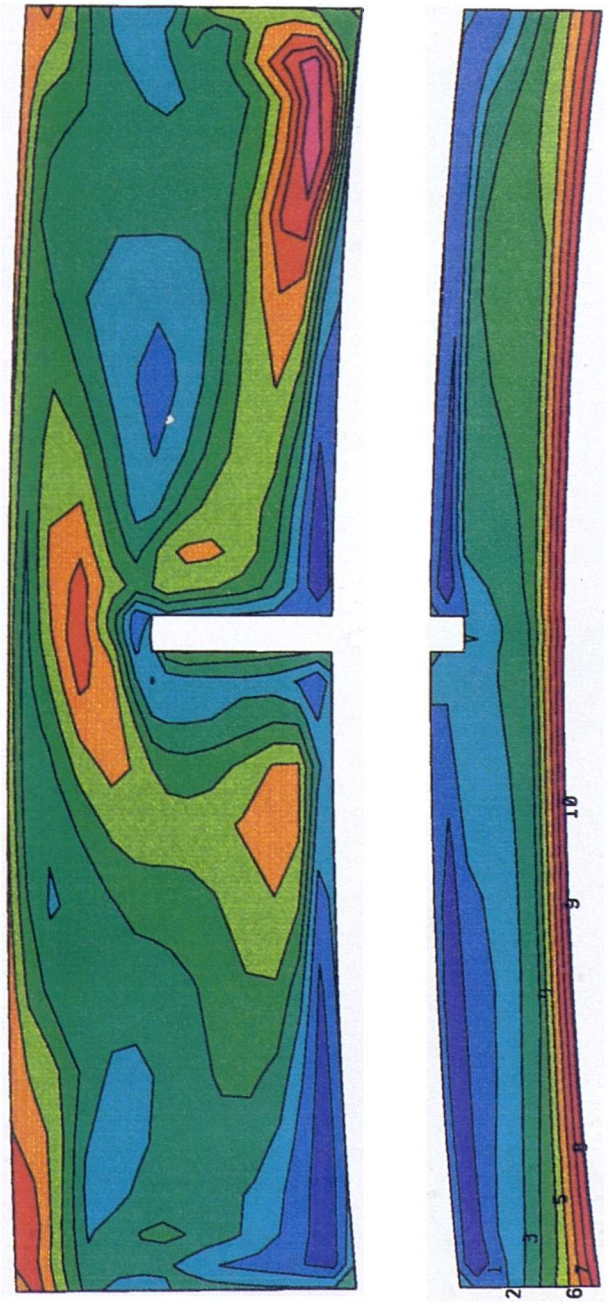

Figure 6.27: Wall shear stress on impeller disc (n=2000rpm/ Q=7l/min).

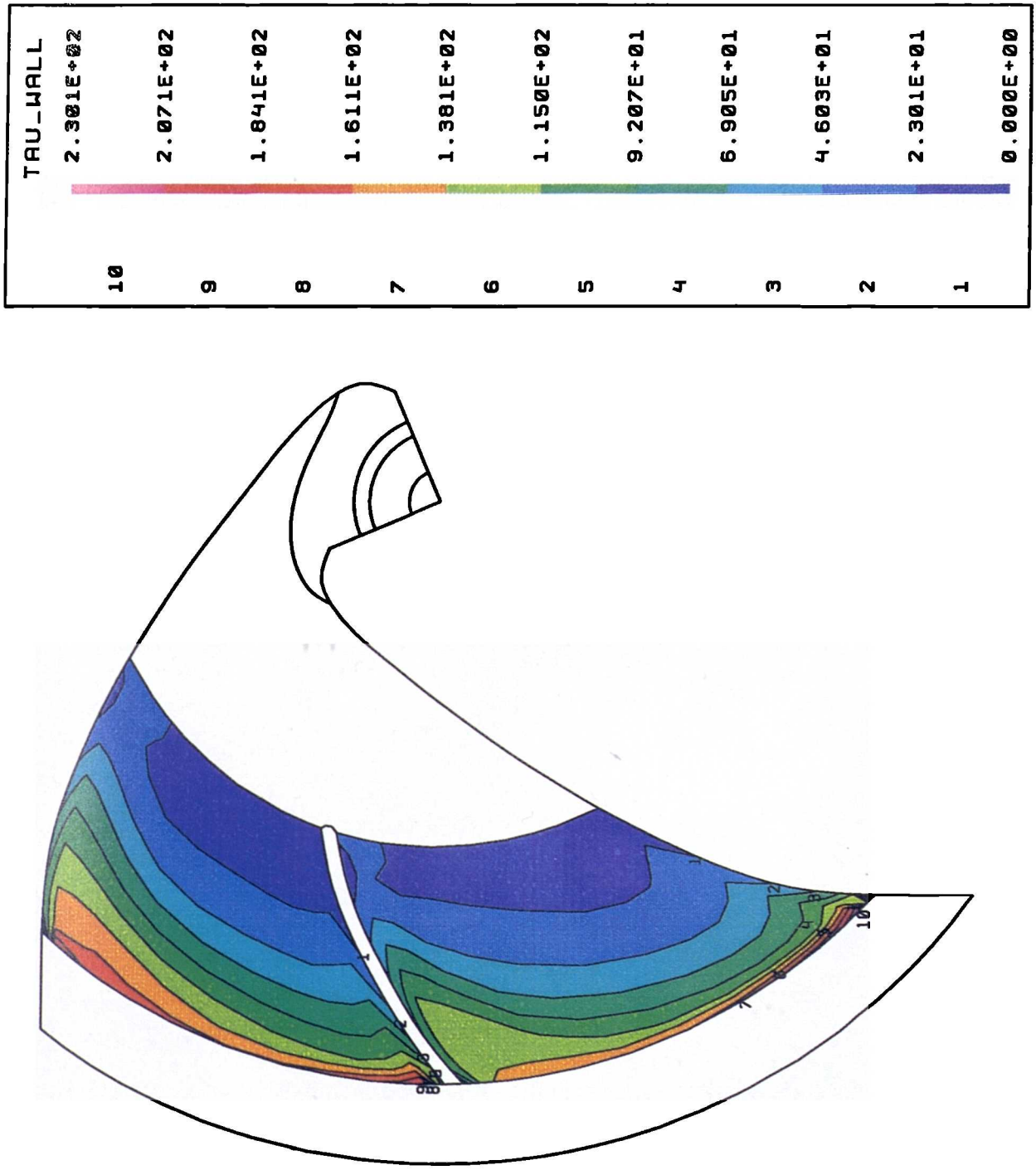

Figure 6.28: Wall shear stress on blade surfaces and rear casing (n=2000rpm/ Q=7l/min).

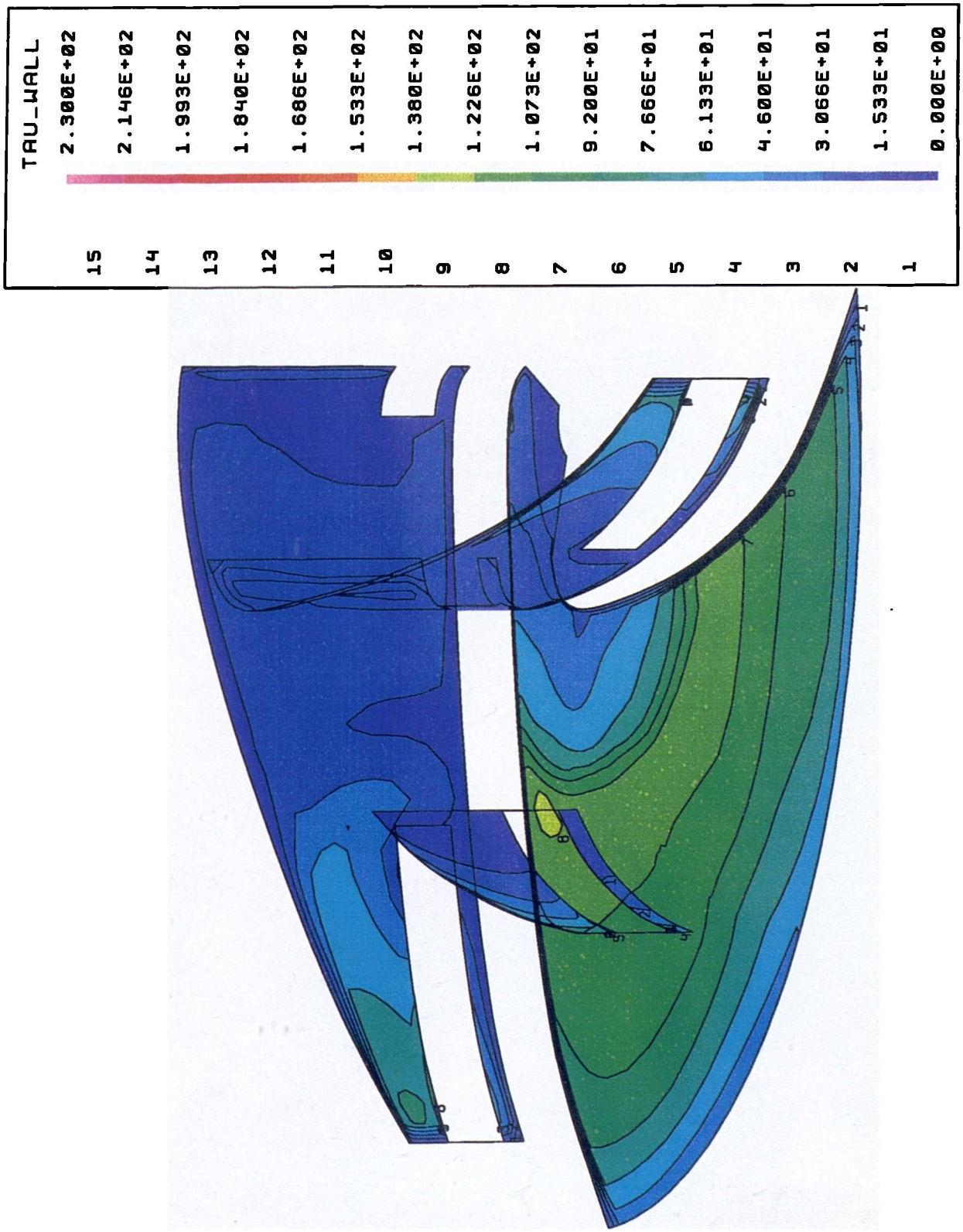

Figure 6.29: Wall shear stress on inlet port, front and outer casing (n=2000 rpm/ Q=7l/min).

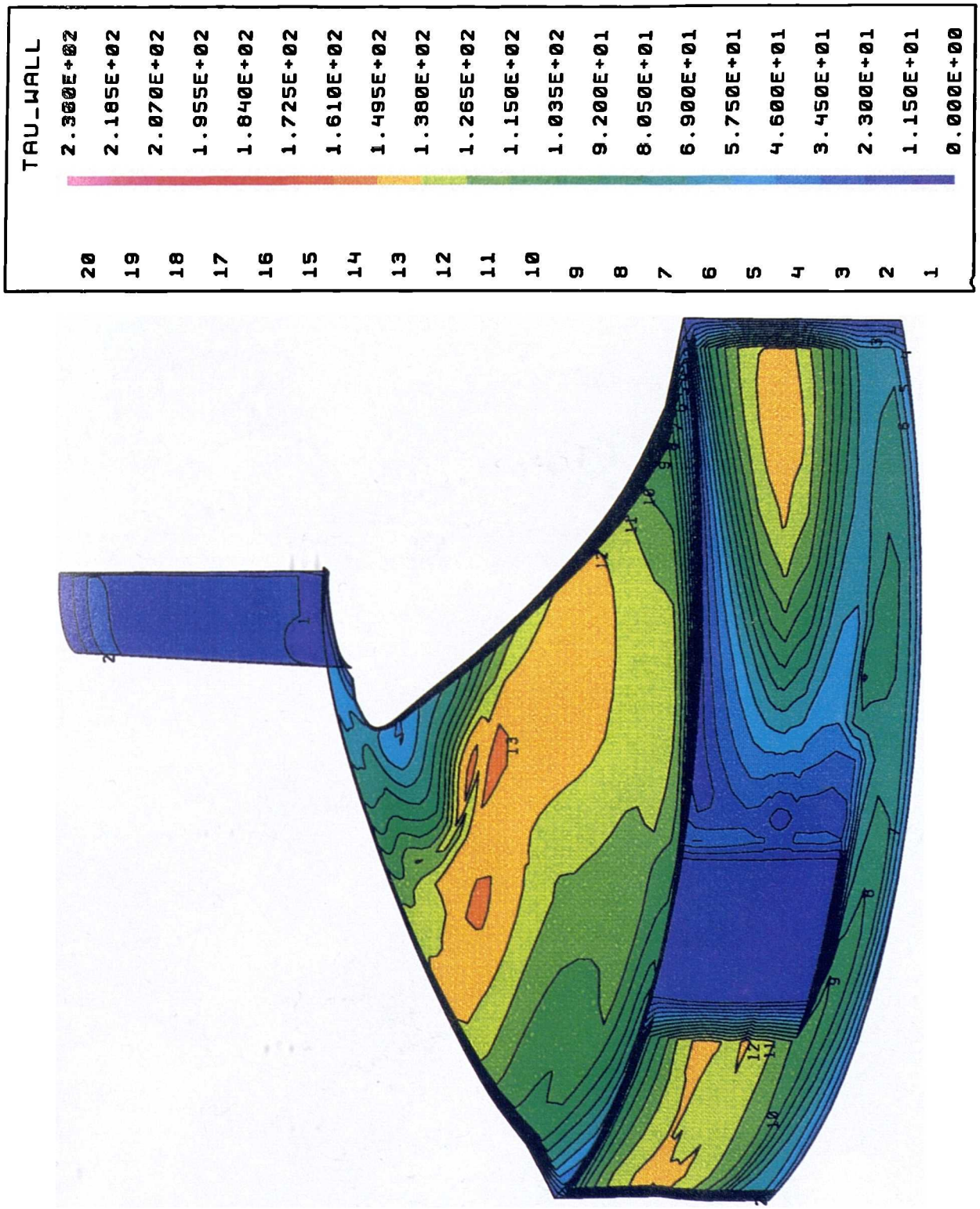

Figure 6.30: Scalar stress in near-outlet plane (n=2000rpm/ Q=7l/min).

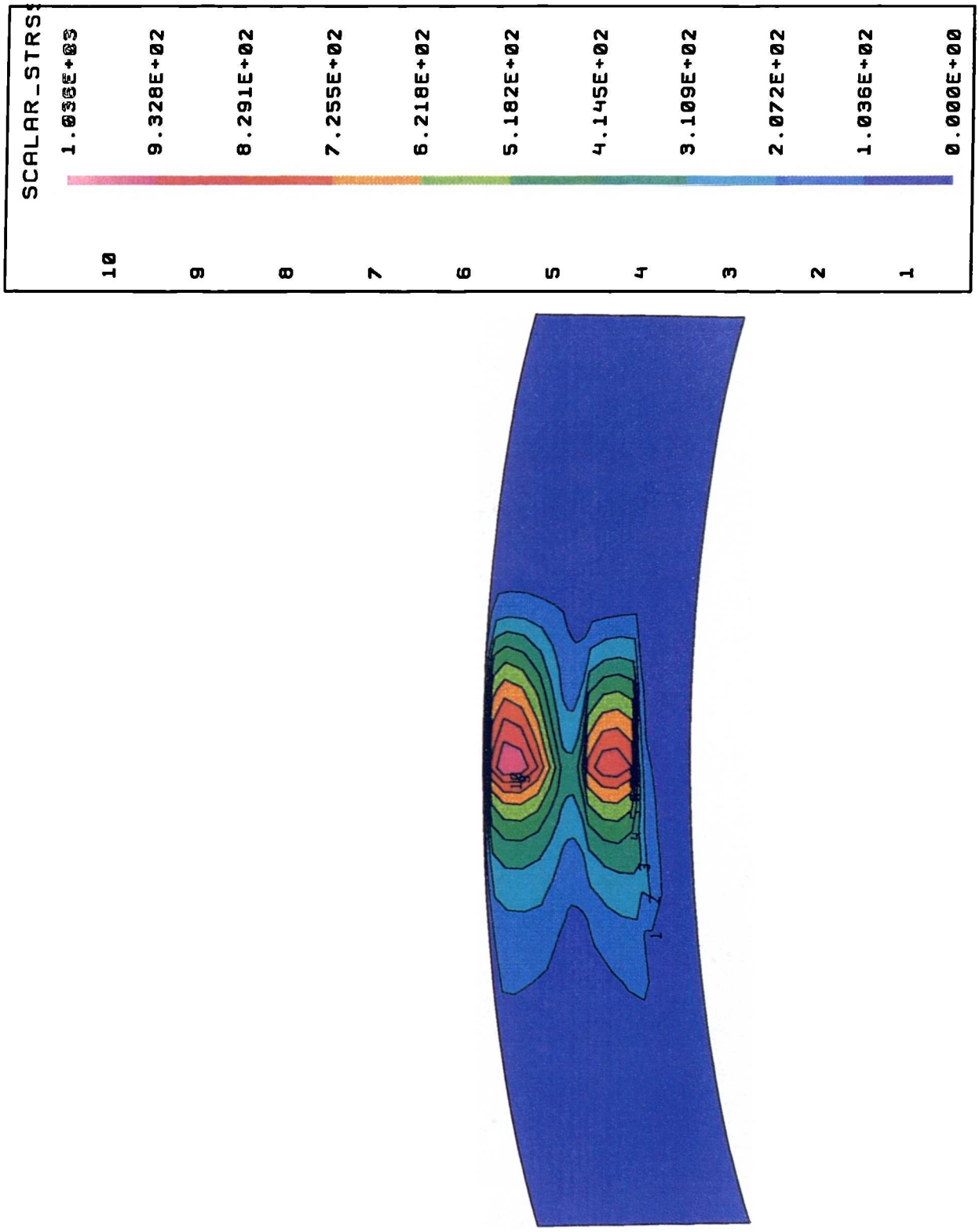

Figure 6.31: Scalar stress in impeller-channel plane (n=2000rpm/ Q=7l/min).

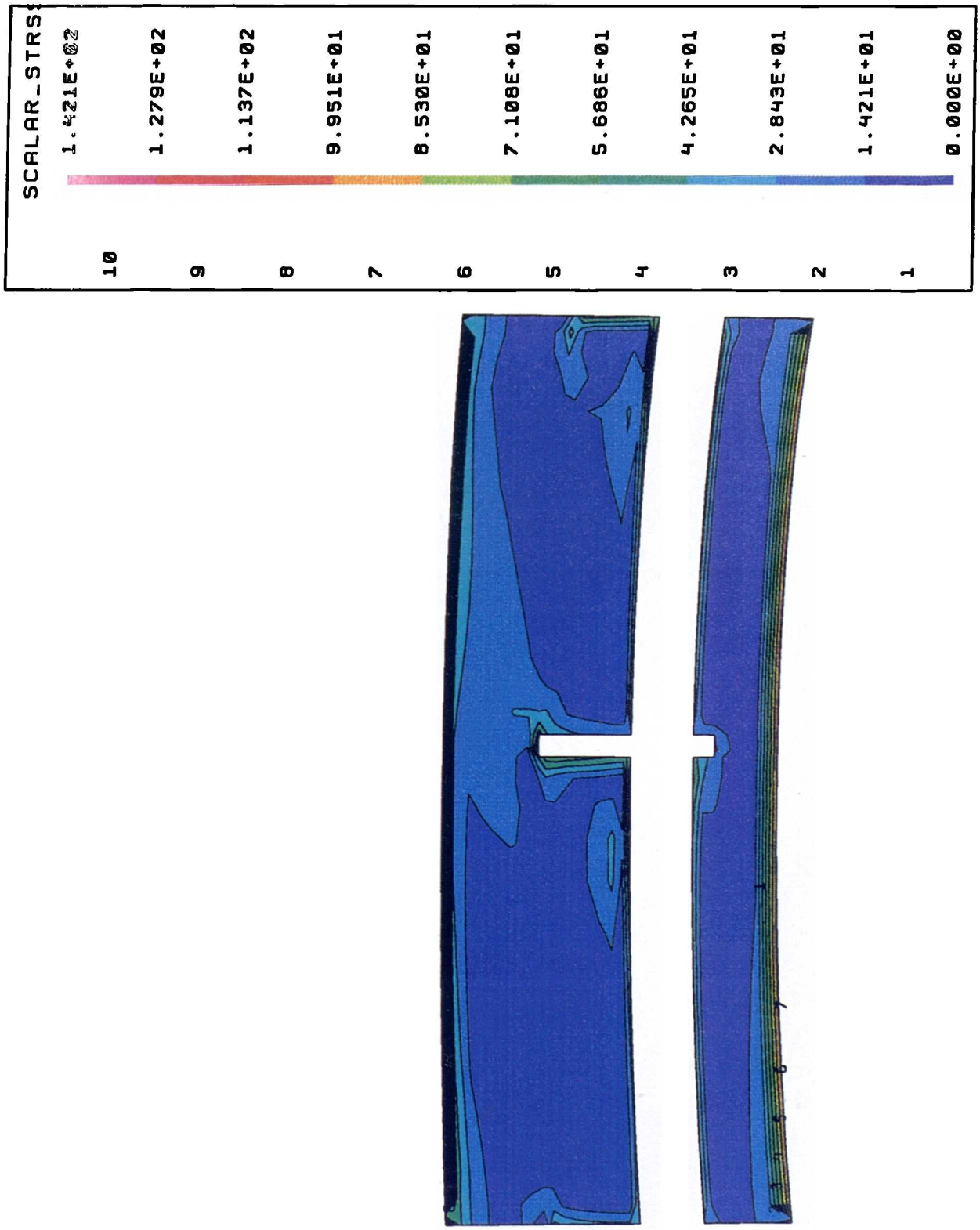

Figure 6.32: Scalar stress in blade-to-blade plane (n=2000rpm/ Q=7l/min).

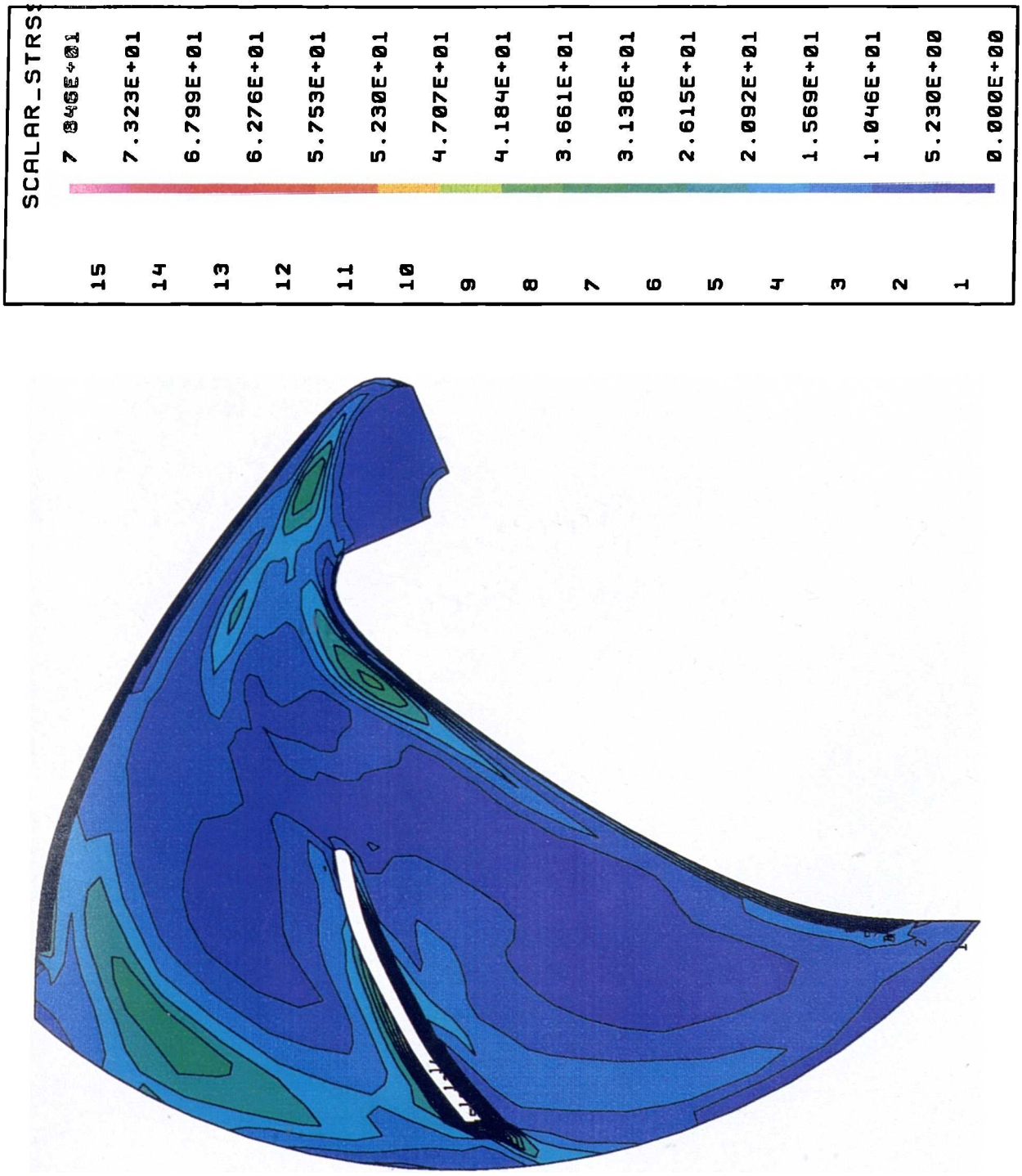

Figure 6.33: Scalar stress in meridional plane coinciding with large blade surface (n=2000rpm/ Q=7l/min).

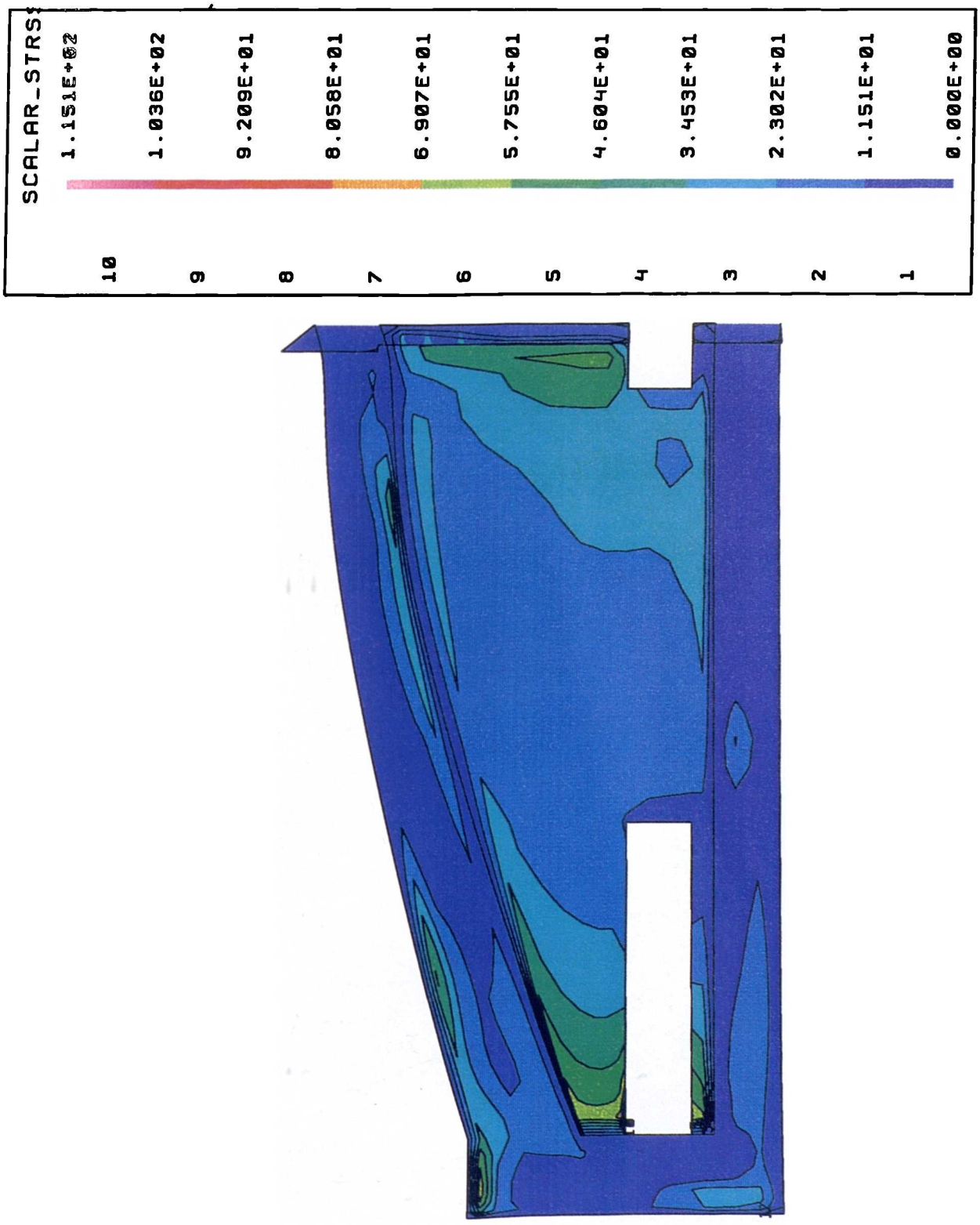

Figure 6.34: Scalar stress in plane meridionally cutting small blade (n= 2000 rp n/ Q=7l/min).

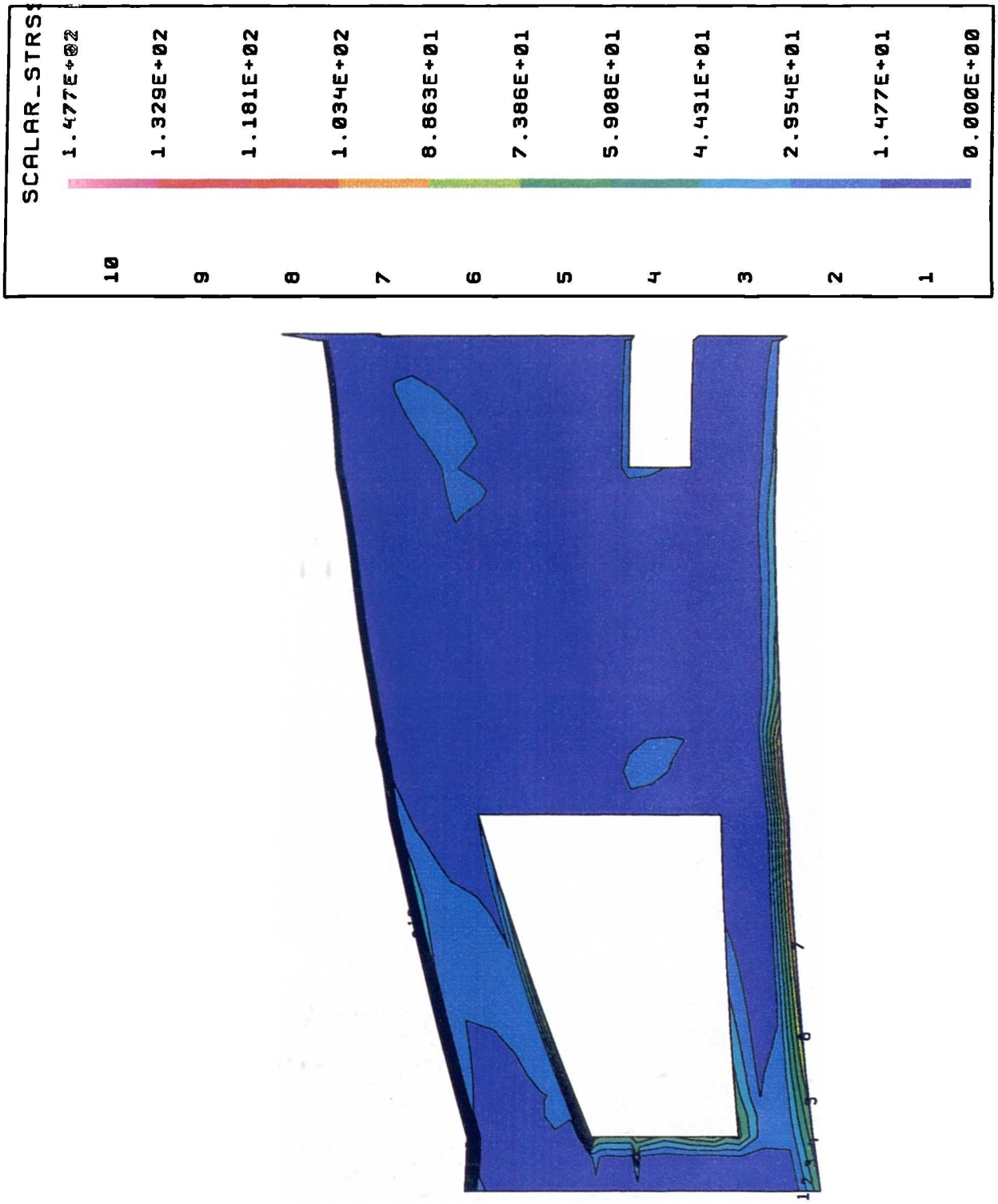

Figure 6.35: Scalar stress in axial gap plane between blades and front casing (n=2000rpm/ Q=7l/min).

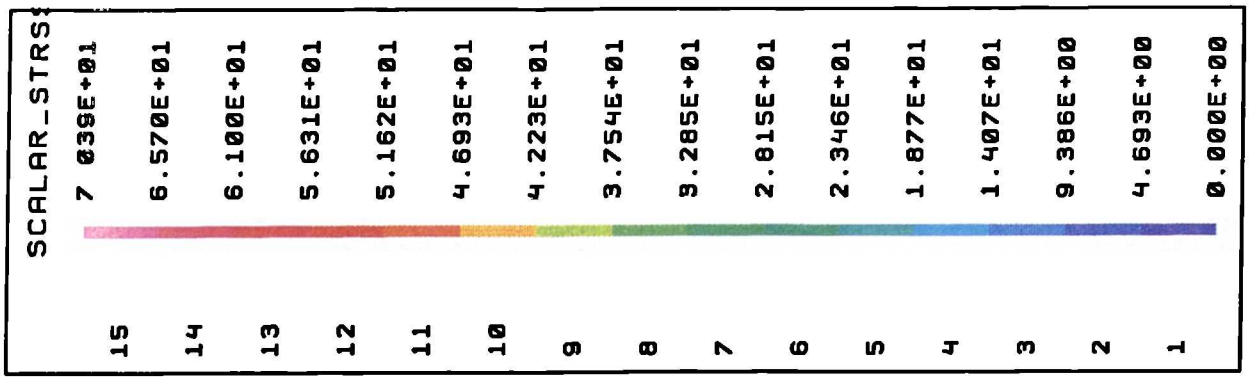

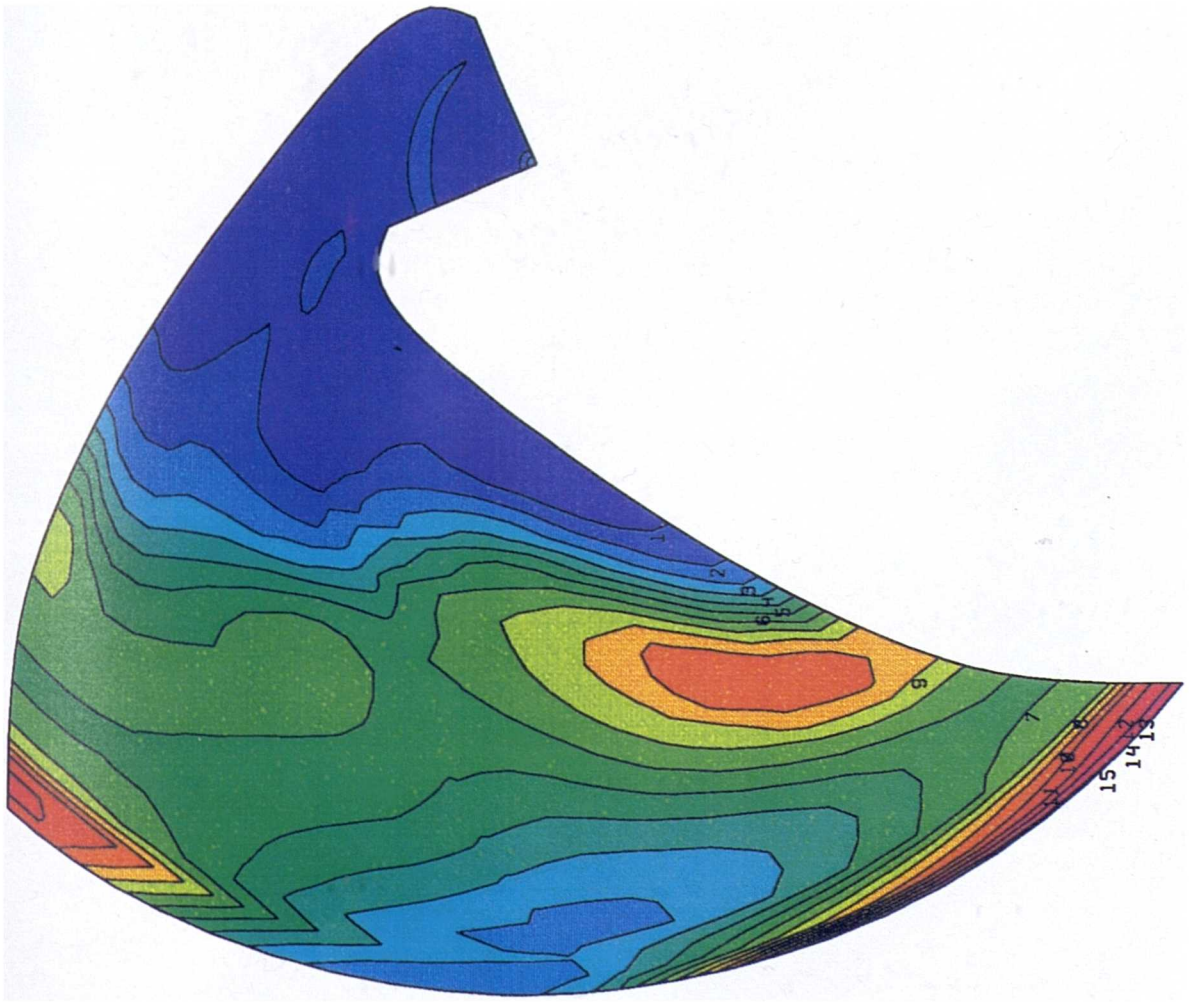

Figure 6.36: Scalar stress in axial gap plane between impeller disc and rear casing (n=2000rpm/ Q=7l/min).

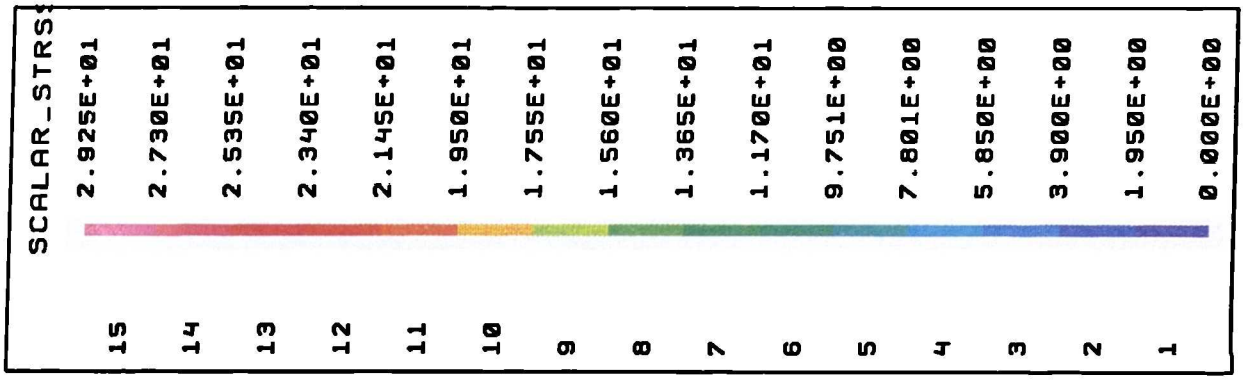

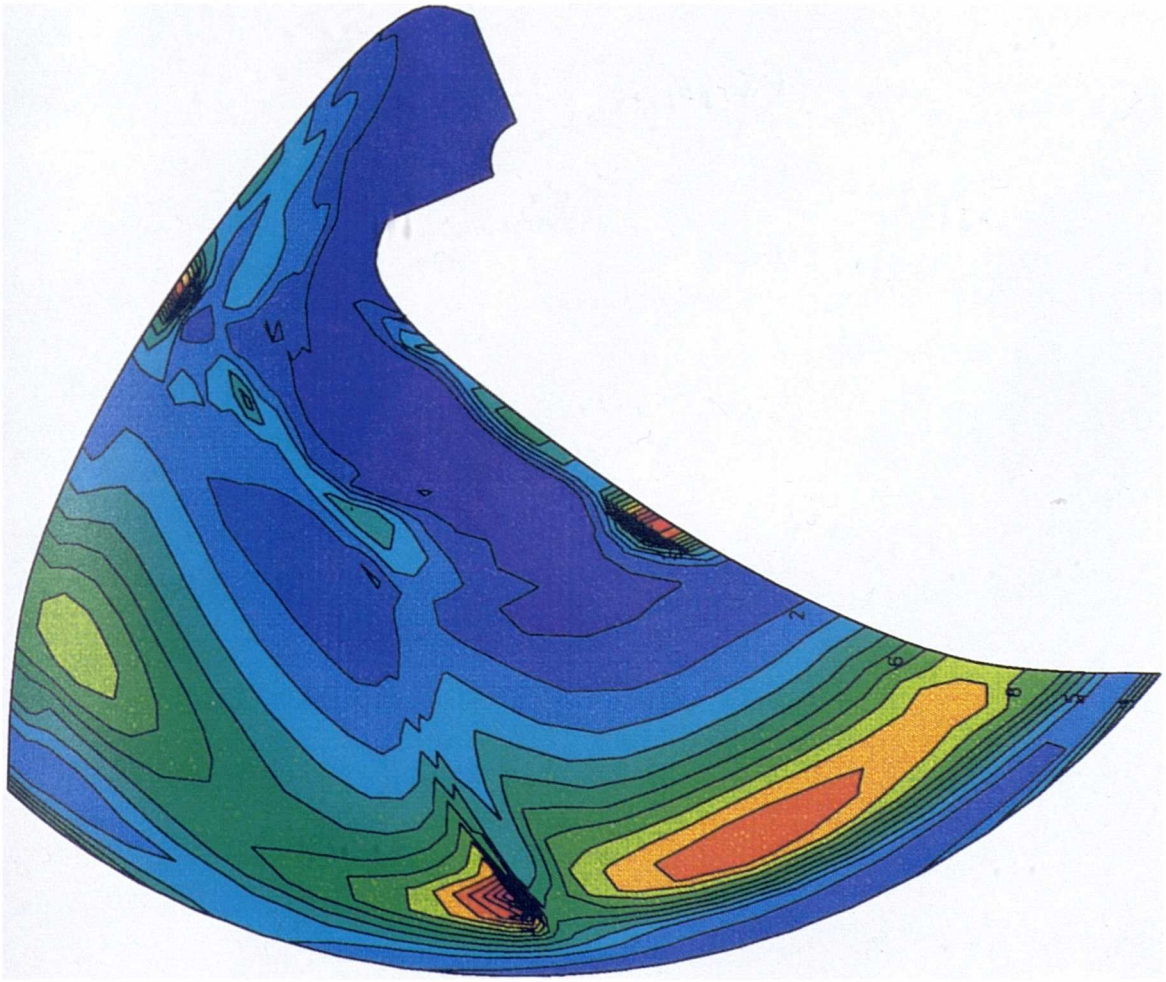

with the large blade surface and a plane which meridionally cuts the small blade. All reveal maxima in the wall regions decreasing with a high gradient to a fairly homogeneous value in the remaining flow domain. The outlet region was excluded in these plots to allow a more detailed presentation of the remaining regions. Impeller flow planes containing no solid boundaries, i.e. the gap planes at the front and rear casing (with the outlet region excluded), showed a more radially structured increase of scalar stress values (Figs 6.35, 6.36).

Other speed/flow rate combinations

An increase in flow rate (Q=10 l/min) at the same rotational speed as above (n=2000rpm) revealed no remarkable differences in flow parameters, as shown by the static pressure difference distribution in an axial plane, Fig 6.37 (compare with Fig 6.21) and by the scalar stress field in the gap plane to the front casing, Fig 6.38 (compare with Fig 6.35). A reduction of rotational speed and flow rate (n=500 rpm, Q=1 l/min) showed only minimal changes in the qualitative flow pattern, for instance for the velocity vector plots in Figs 6.39 to 6.41 (compare with Figs 6.11, and 6.16). Kinetic energy, viscous as well as turbulent, is, however, largely reduced. An indicator for the degree of turbulence, the viscosity ratio, has its highest values of 12 in the outflow area (Fig 6.42). Large turbulent fluctuations in the bulk flow do not occur, see Fig 6.43. Maxima of scalar stresses of approximately 55 Pa are reduced by an order of two (Fig 6.44) with a further polarization of local maxima to the near wall regions (Fig 6.45).

Table 6.2 lists calculated pressure heads and maximum scalar stress values for all n/Q combinations analysed showing an expected proportional dependency of maximal stress values on the rotational speed.

Reduced gap size

The effect of decreasing the gap size between blades and front casing at n=2000 rpm/Q=7 l/min is assessed by comparing flow parameters with the original design variant.

Velocity profiles showed, for the reduced gap, distinct secondary flow vortex structure in the blade-to-blade plane (Fig 6.46). Stronger backflow and

Figure 6.37: Static pressure differences in blade-to-blade plane (n=2000rpm/ Q=10 l/min).

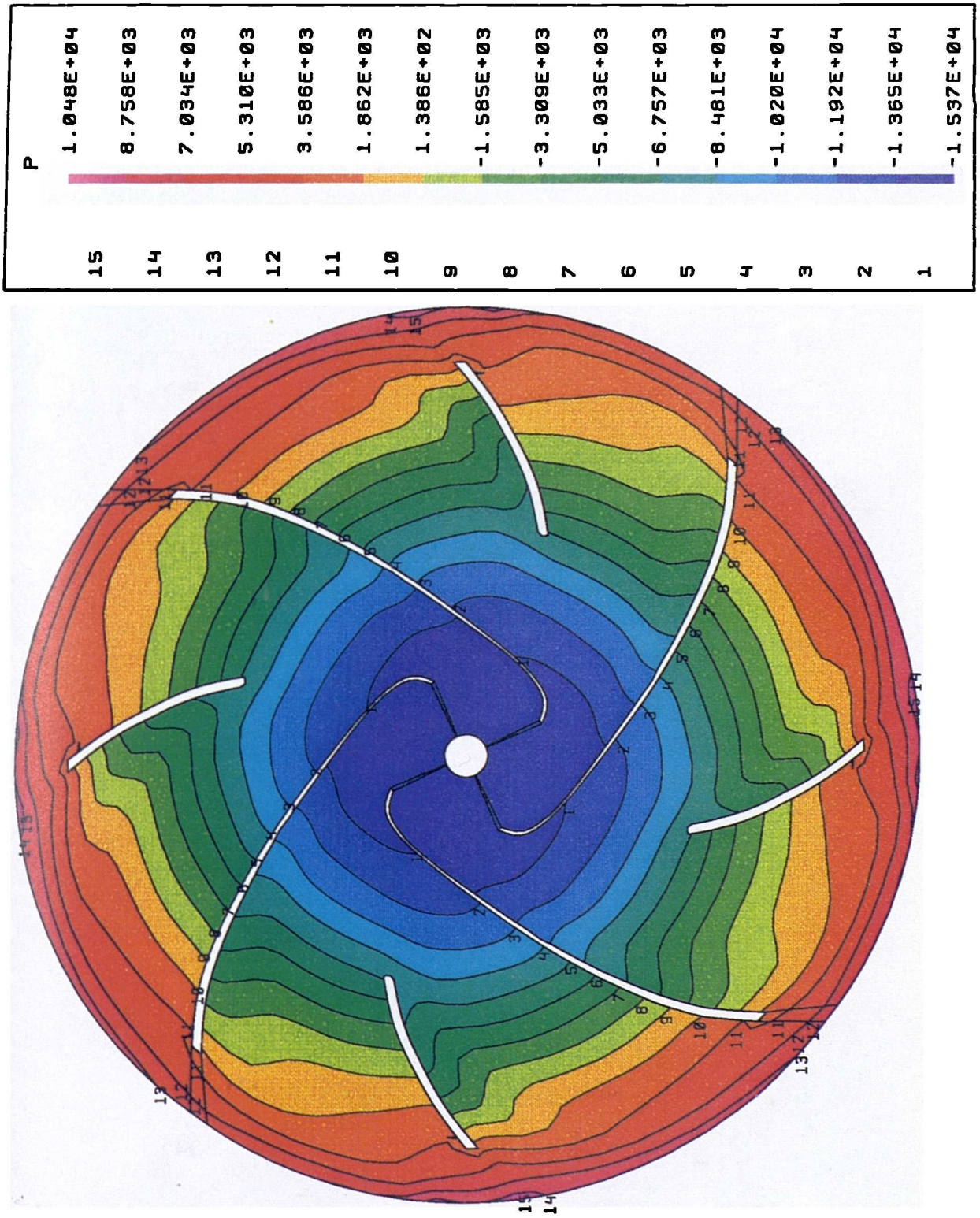

F'gure 6.38: Scalar stress in axial gap plane between blades and front casing (n=2000rpm/ Q=10l/min).

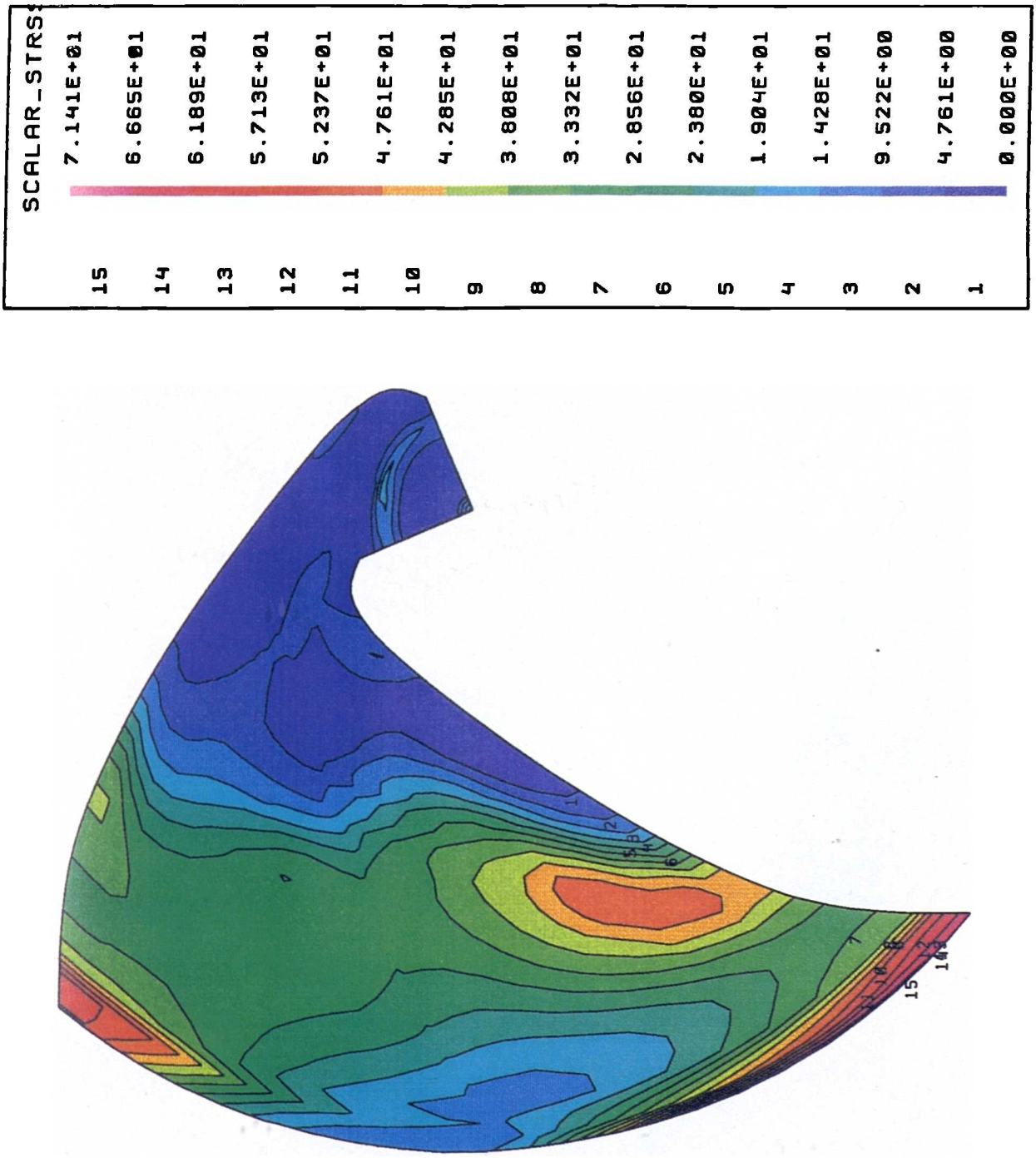

Figure 6.39: Velocity distribution in blade-to-blade plane (n=500 rpm / Q=1 l/min).

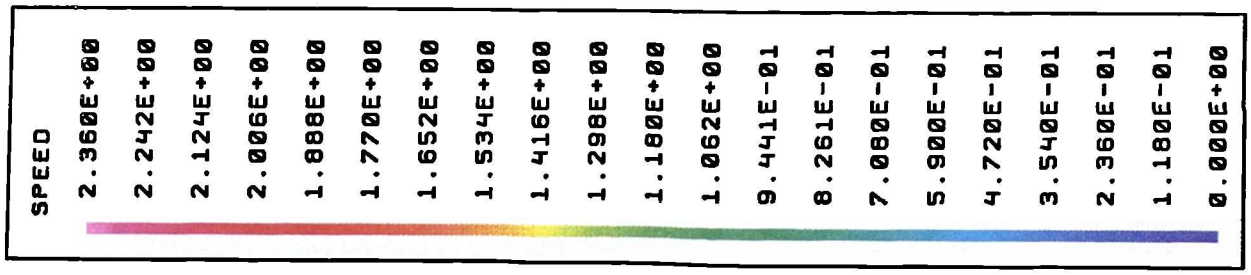

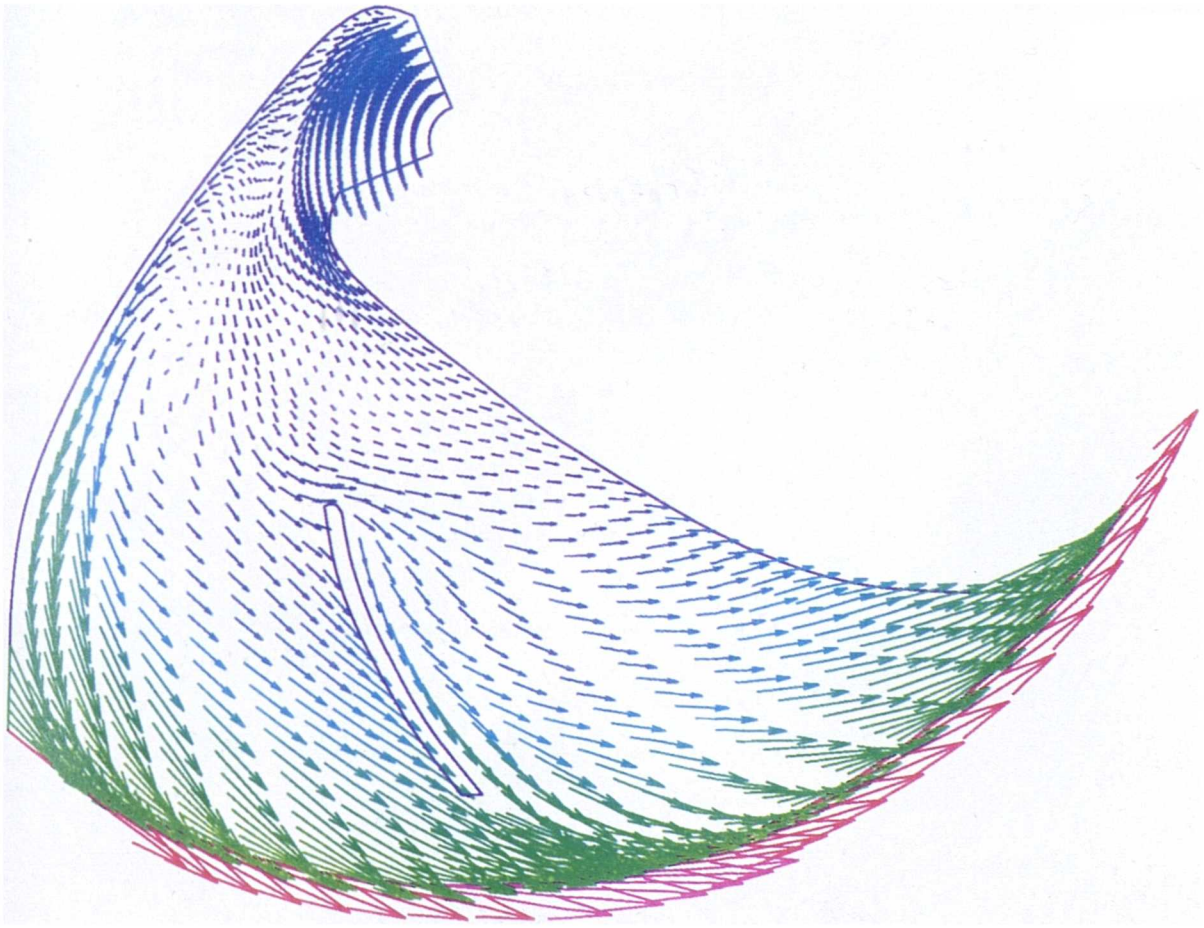

Figure 6.40: Velocity distribution in impeller-channel plane (n=500rpm/ Q=1 l/min).

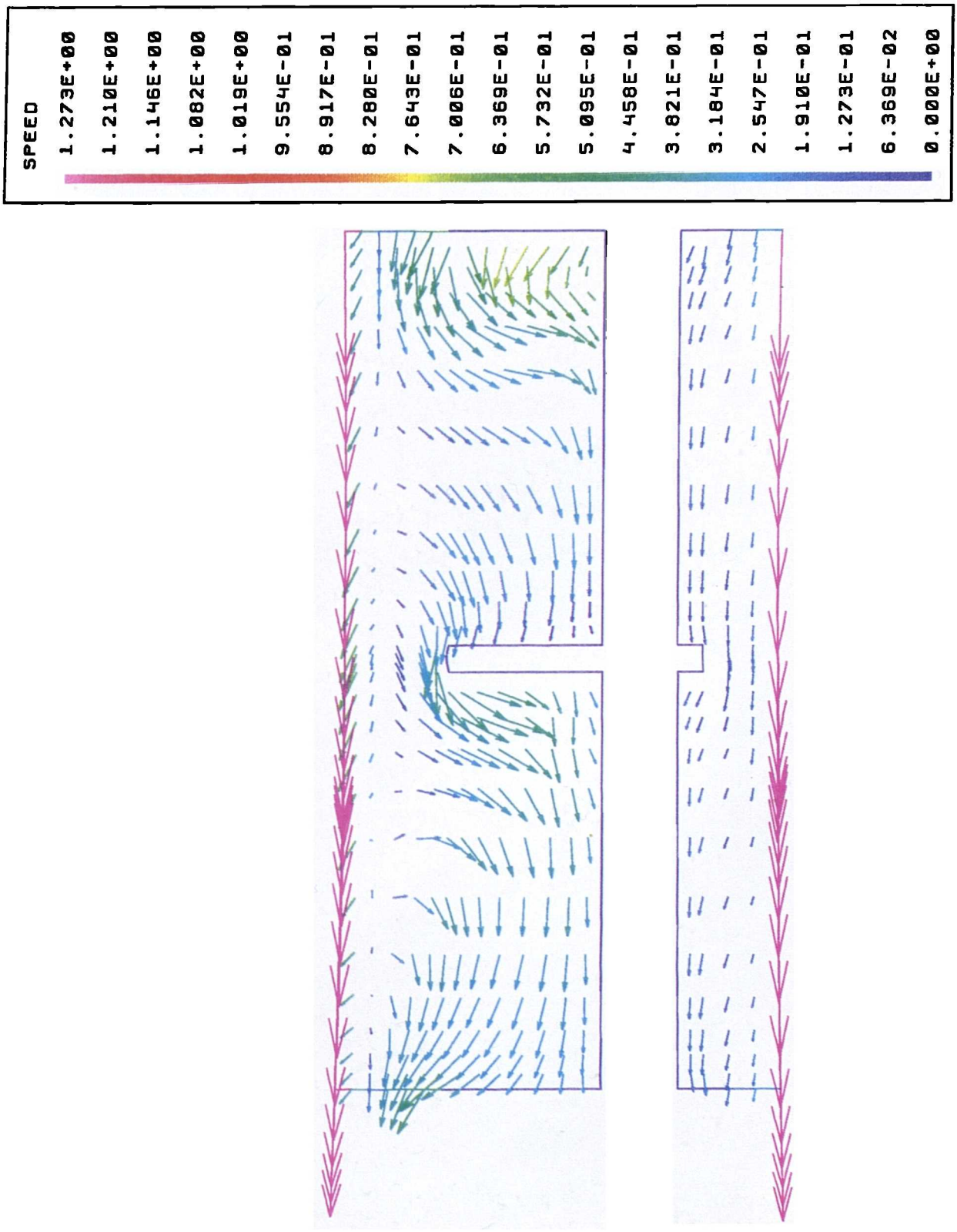

Figure 6.41: Velocity distribution in meridional plane at suction side of large blade (n=500rpm/ Q=1l/min).

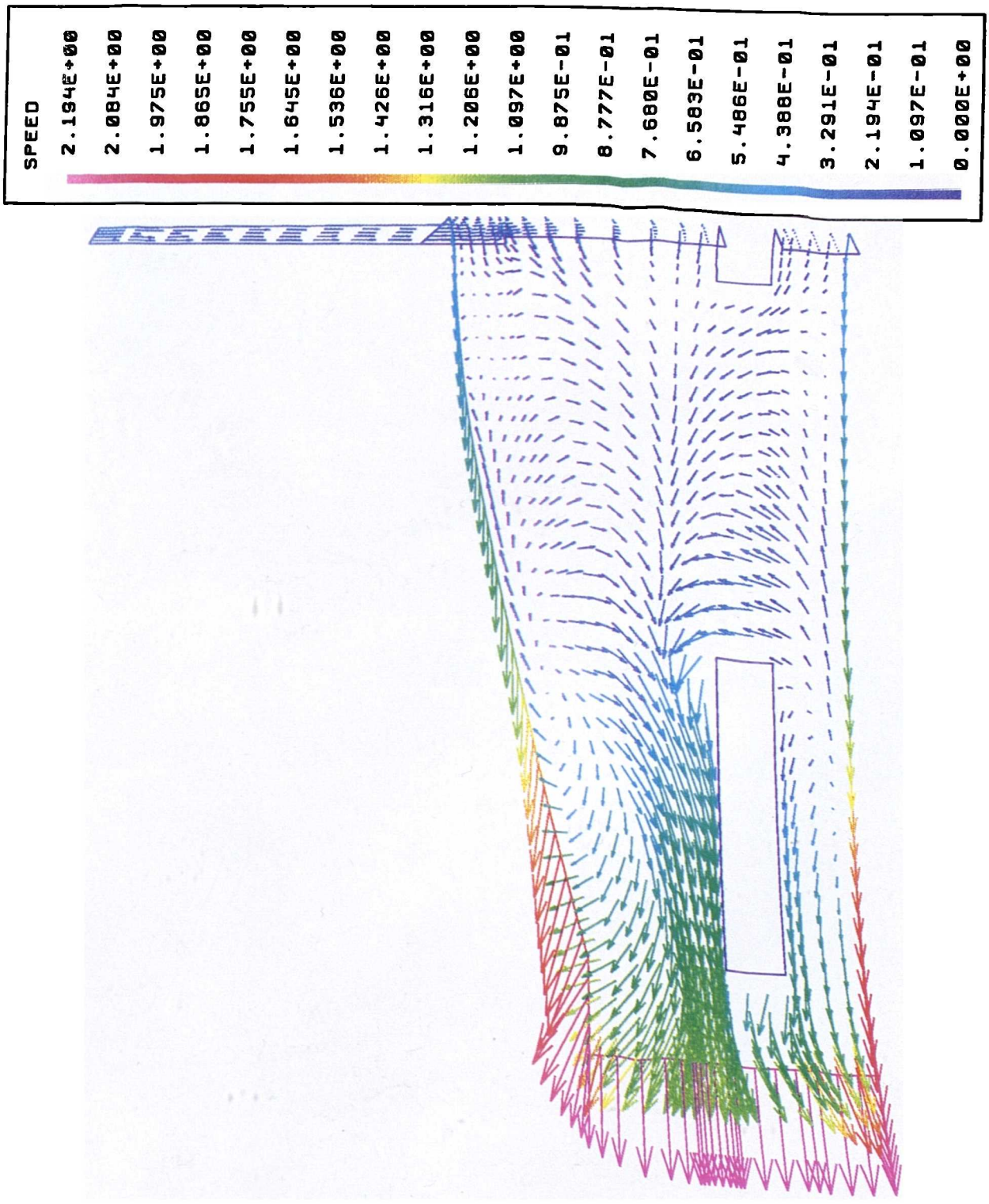

Figure 6.42: Turbulent to molecular viscosity ratio in near-outlet plane (n=500 rpm/ Q=1l/min).

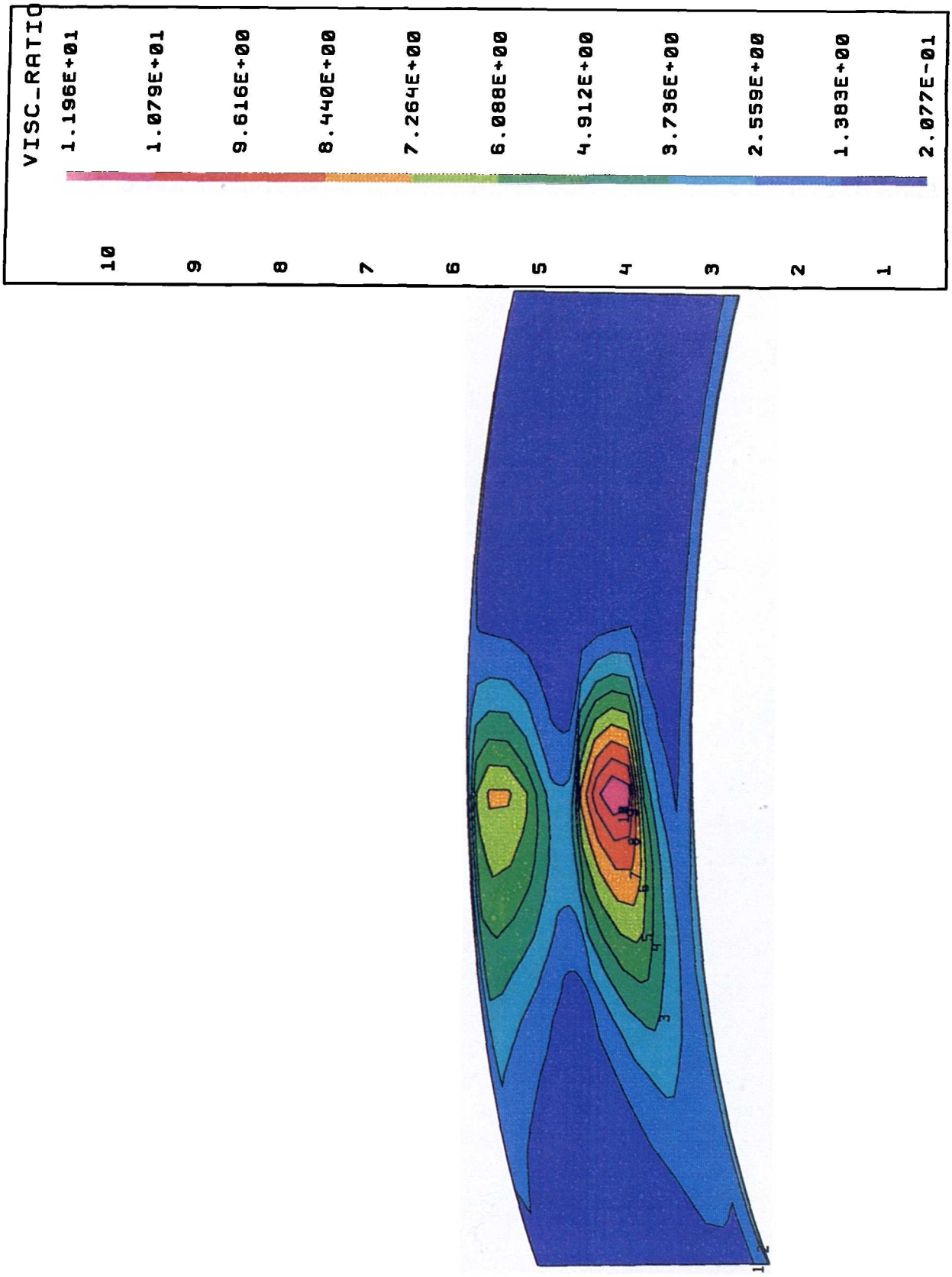

Figure 6.43: Turbulent to molecular viscosity ratio in blade-to-blade plane (n=500rpm/ Q=1l/min).

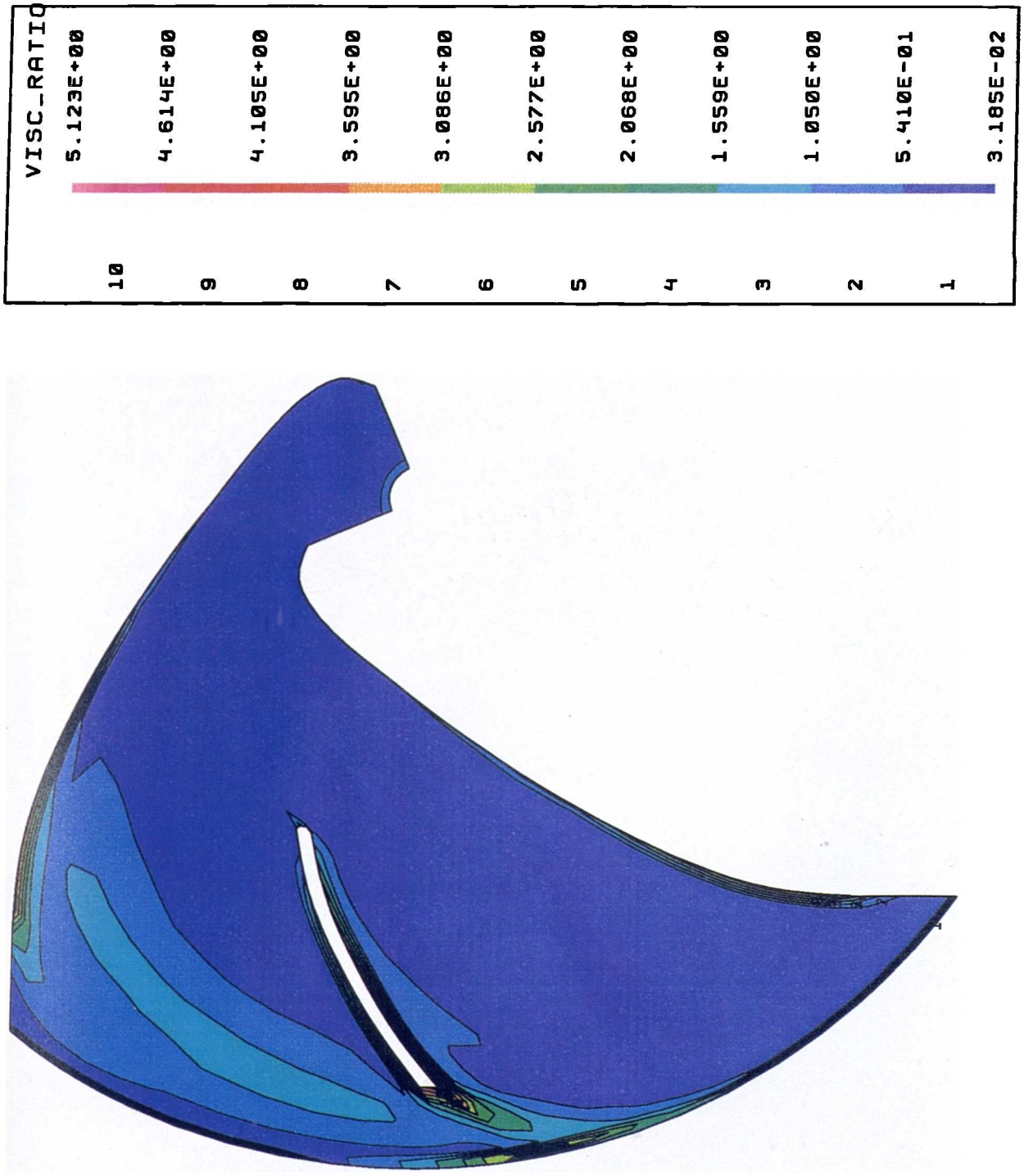

Figure 6.44: Scalar stress in near outlet-plane (n=500rpm/ Q=1l/min).

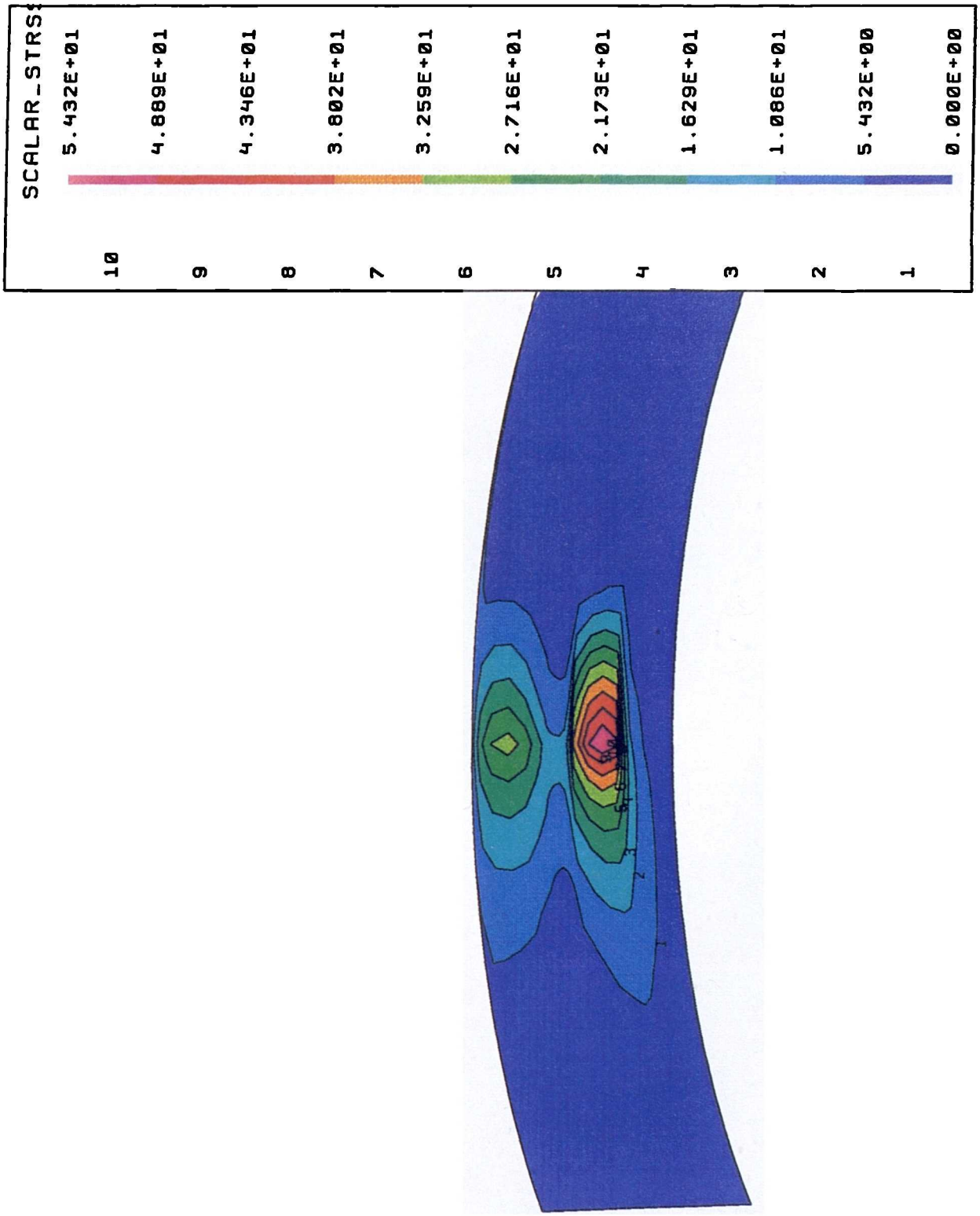

Figure 6.45: Scalar stress in impeller-channel plane (n=500rpm/ Q=1l/min).

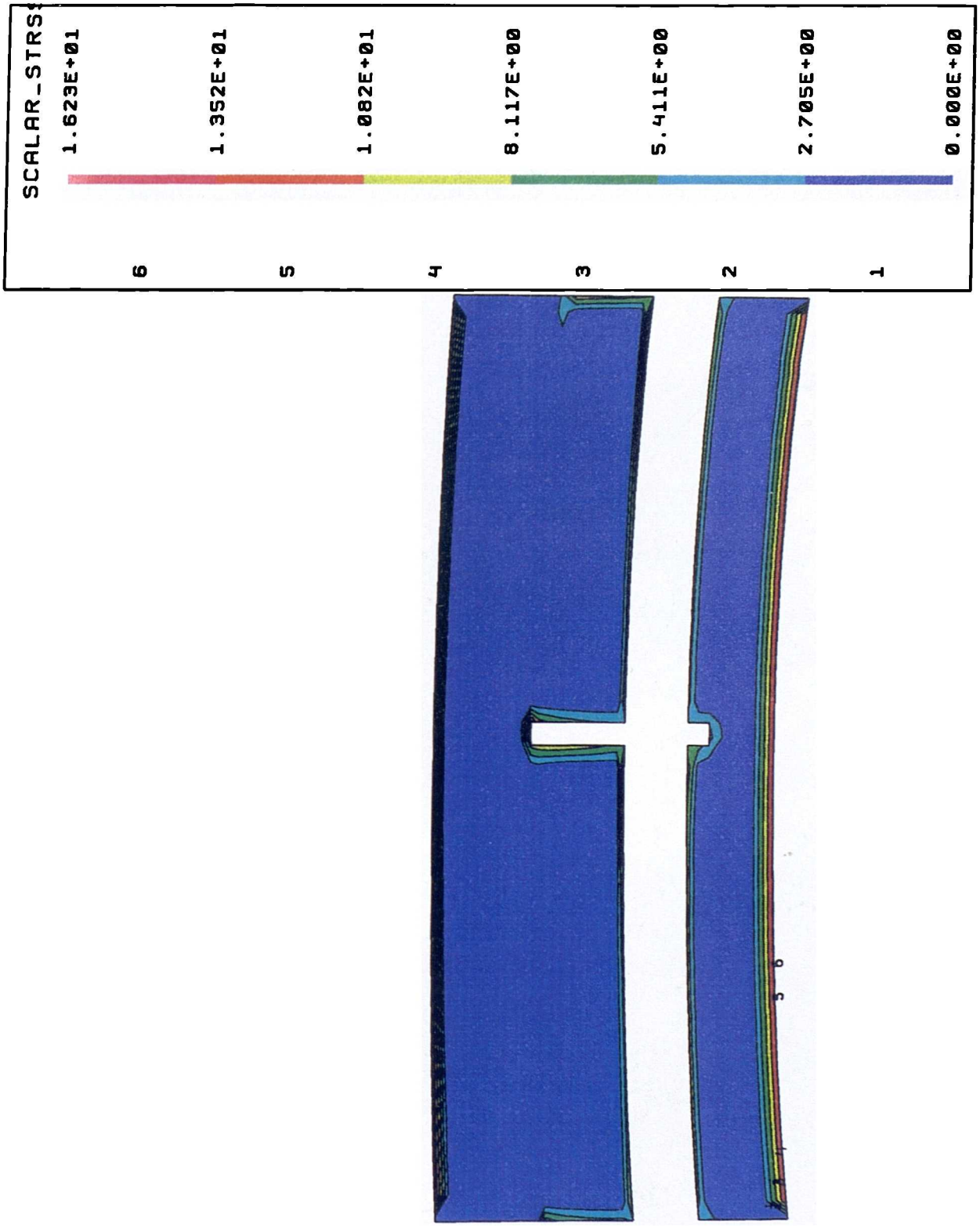

Figure 6.46: Velocity distribution in blade-to-blade plane (n=2000 rpm/ Q=7 l/min -reduced gap).

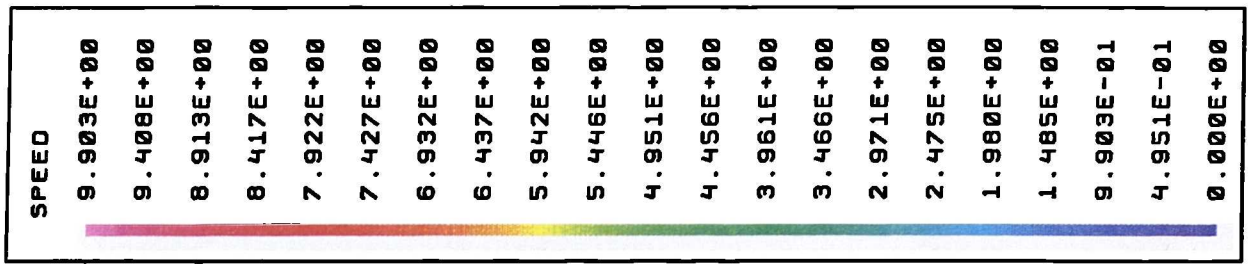

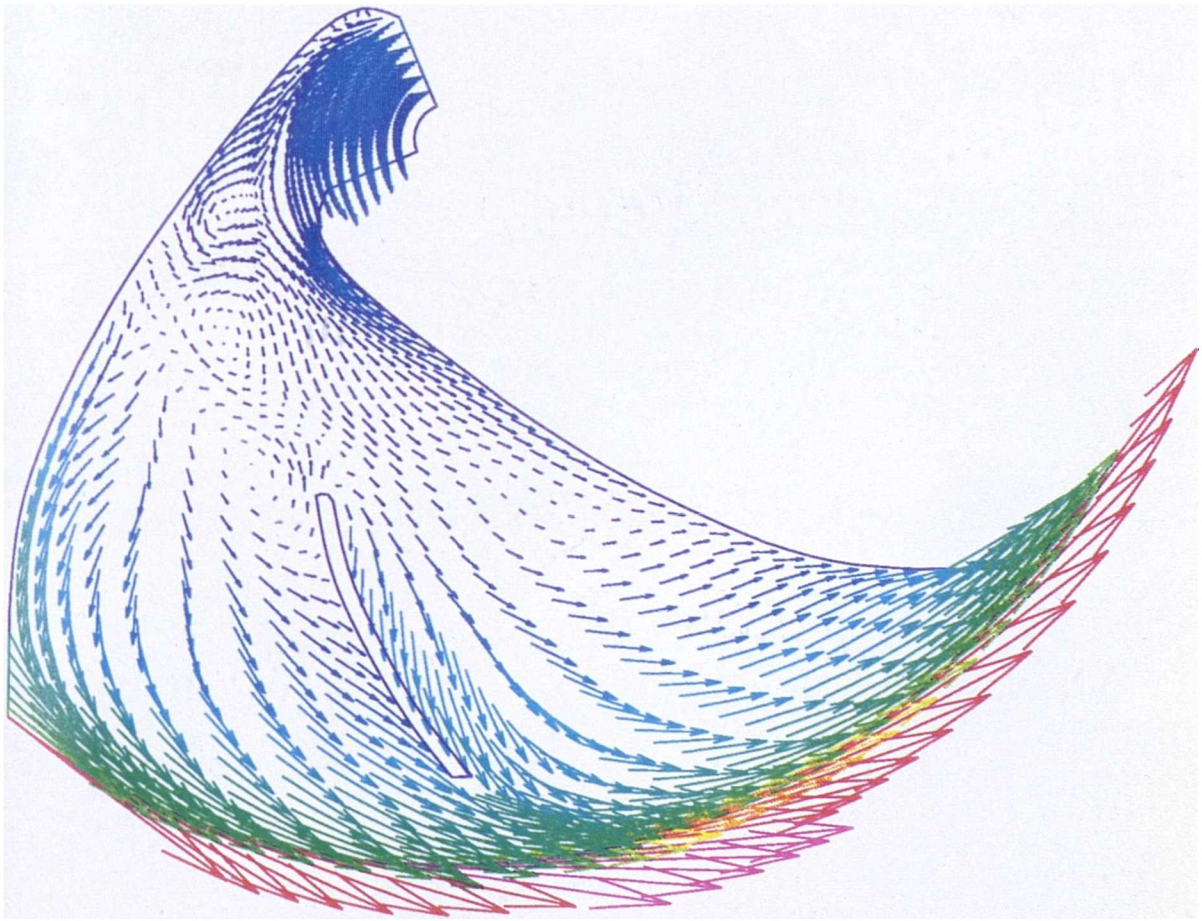

Figure 6.47: Velocity distribution in impeller-channel plane (n=2000rpm/ Q= 7 l/min -reduced gap).

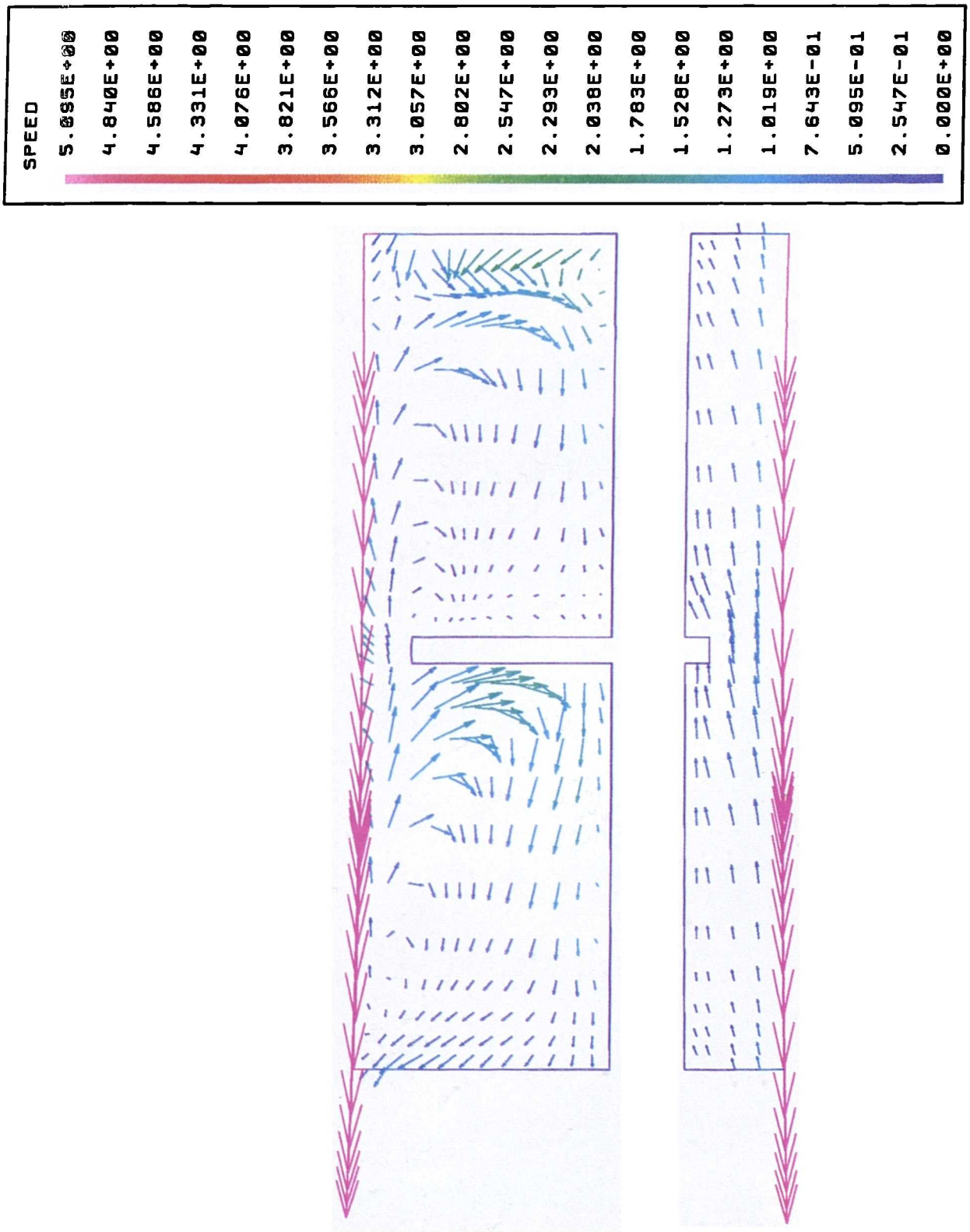

Figure 6.48: Velocity distribution in axial gap plane between blades and front casing (n=2000rpm/ Q=7l/min -reduced gap).

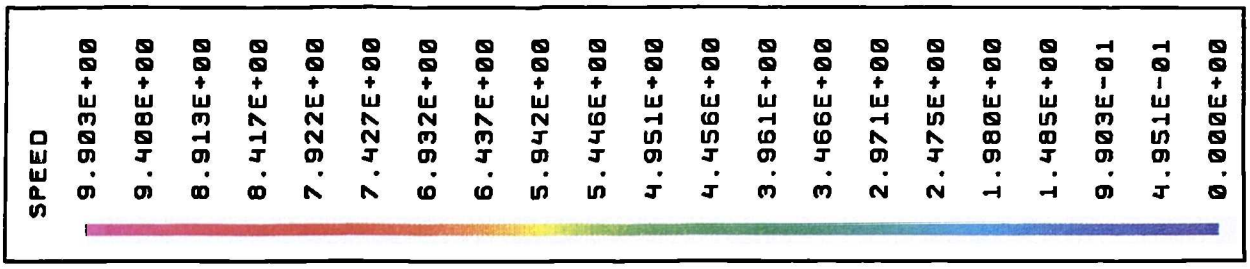

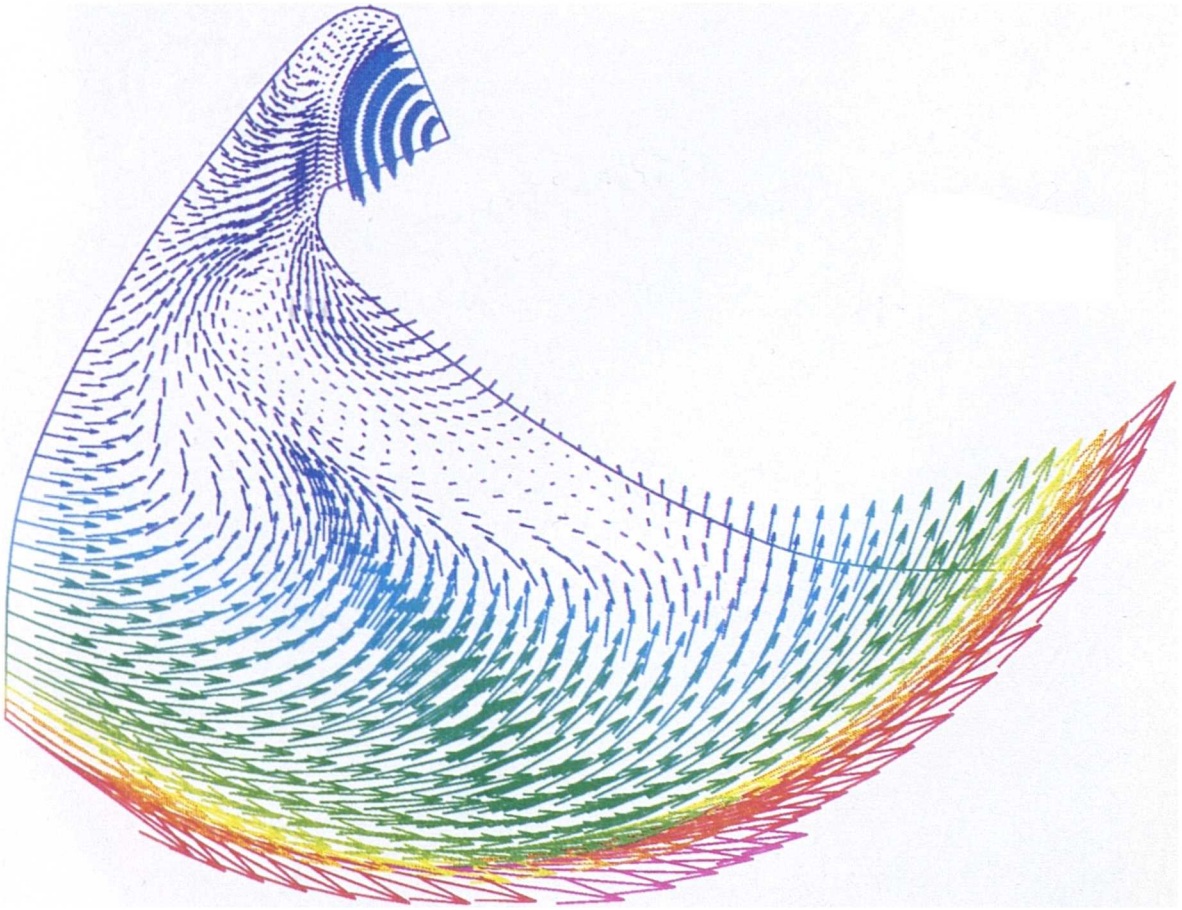

Figure 6.49: Static pressure differences in axial gap plane between blades and front casing (n=2000rpm/ Q=7l/min -reduced gap).

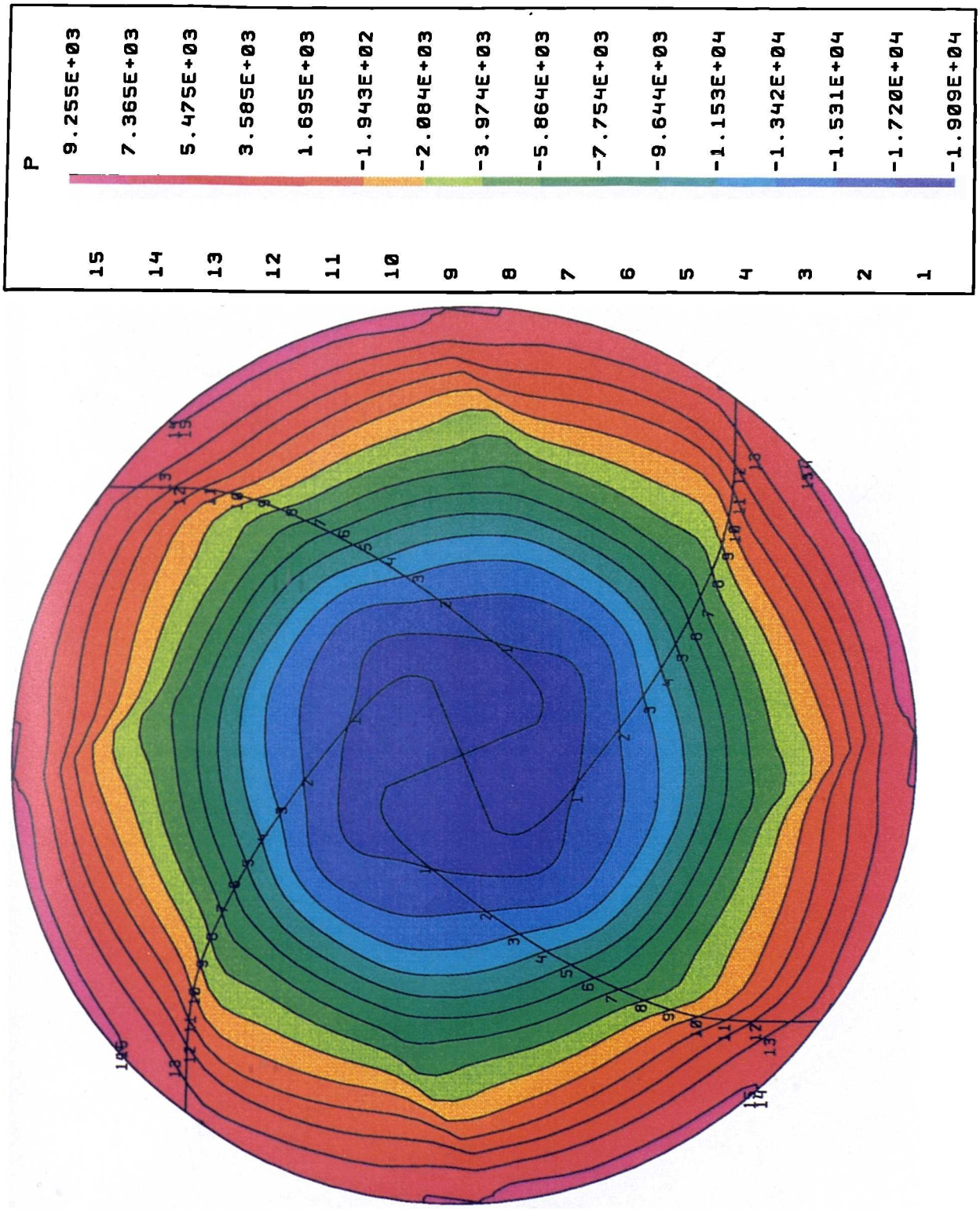

Figure 6.50: Turbulent to molecular viscosity ratio in blade-to-blade plane (n=2000rpm/ Q=7l/min -reduced gap).

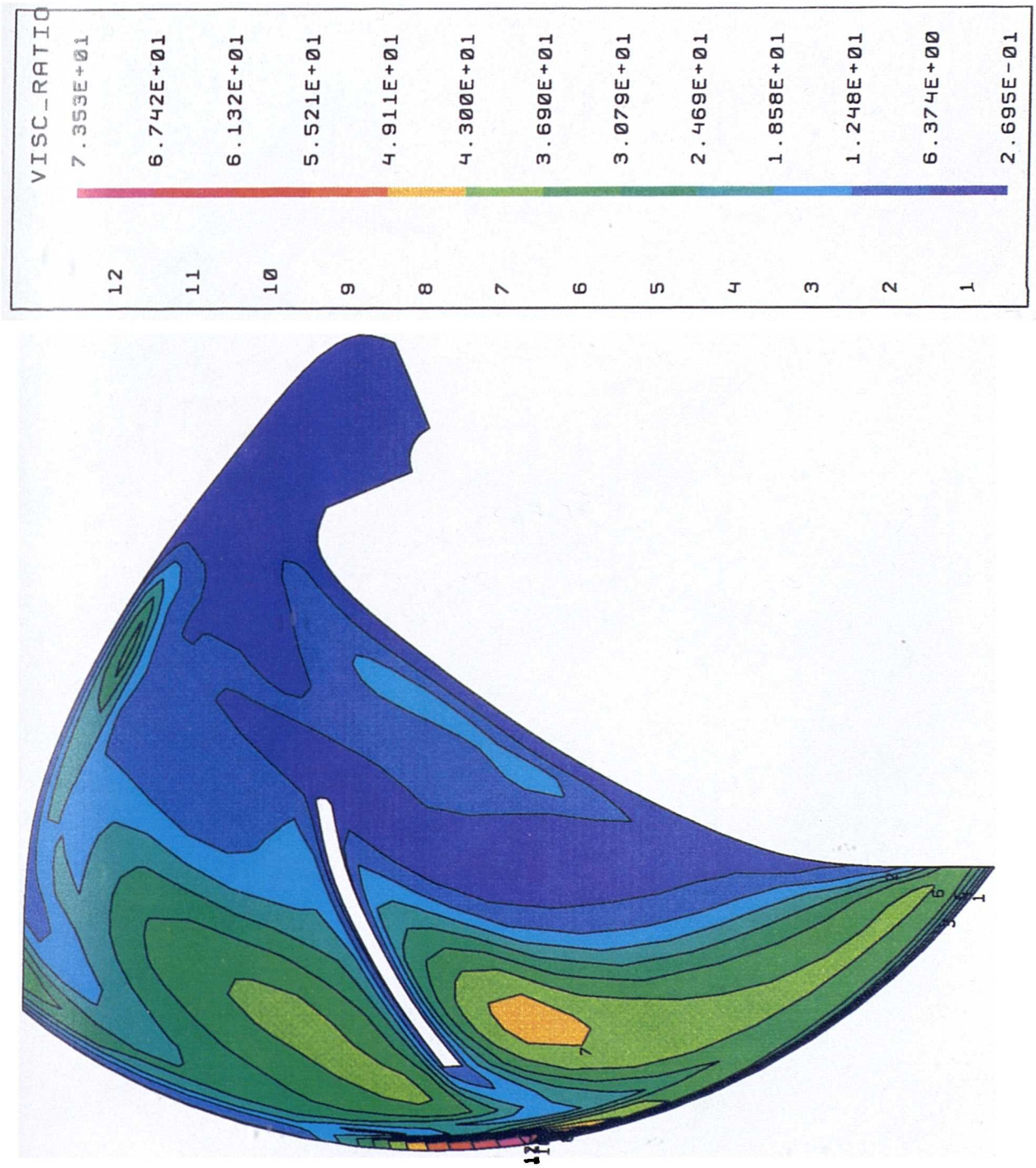

Figure 6.51: Turbulent to molecular viscosity ratio in impeller-channel plane (n=2000rpm/ Q=7l/min -reduced gap).

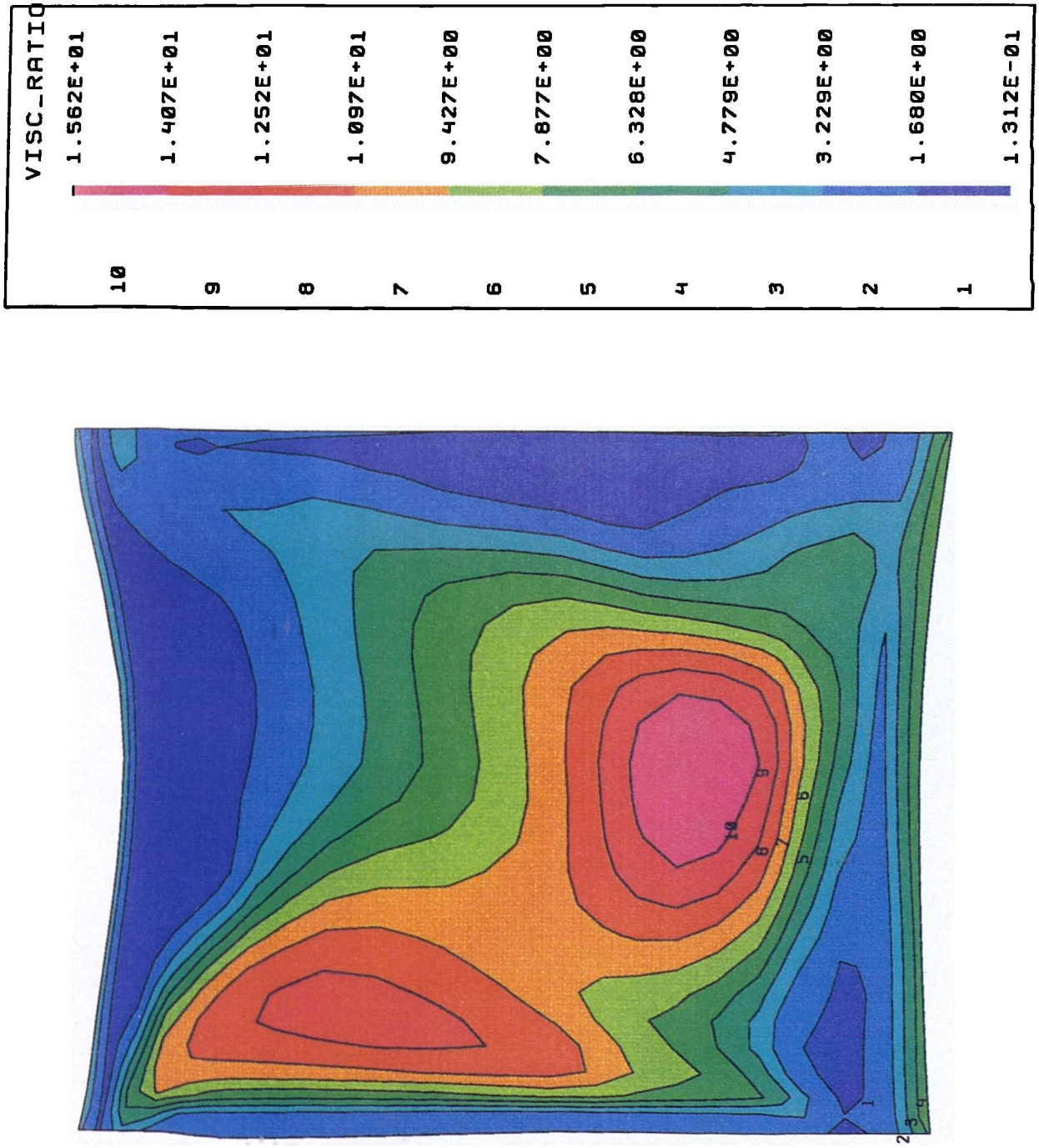

Figure 6.52: Wall shear stress on inlet port, front and outer casing (n=2000rpm/ Q=7l/min -reduced gap).

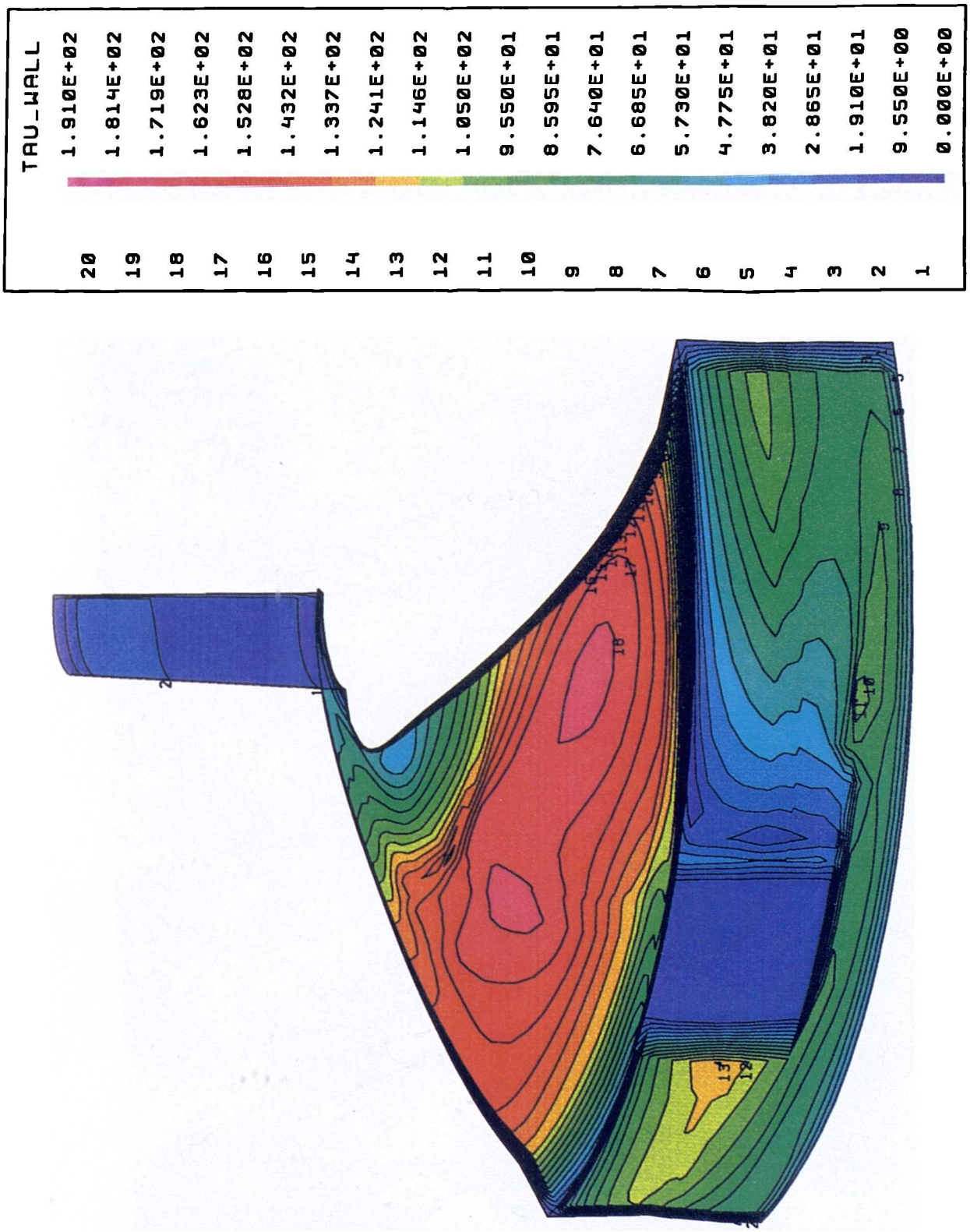

Figure 6.53: Wall shear stress on blades and rear casing (n=2000rpm/ Q=7 l/min -reduced gap).

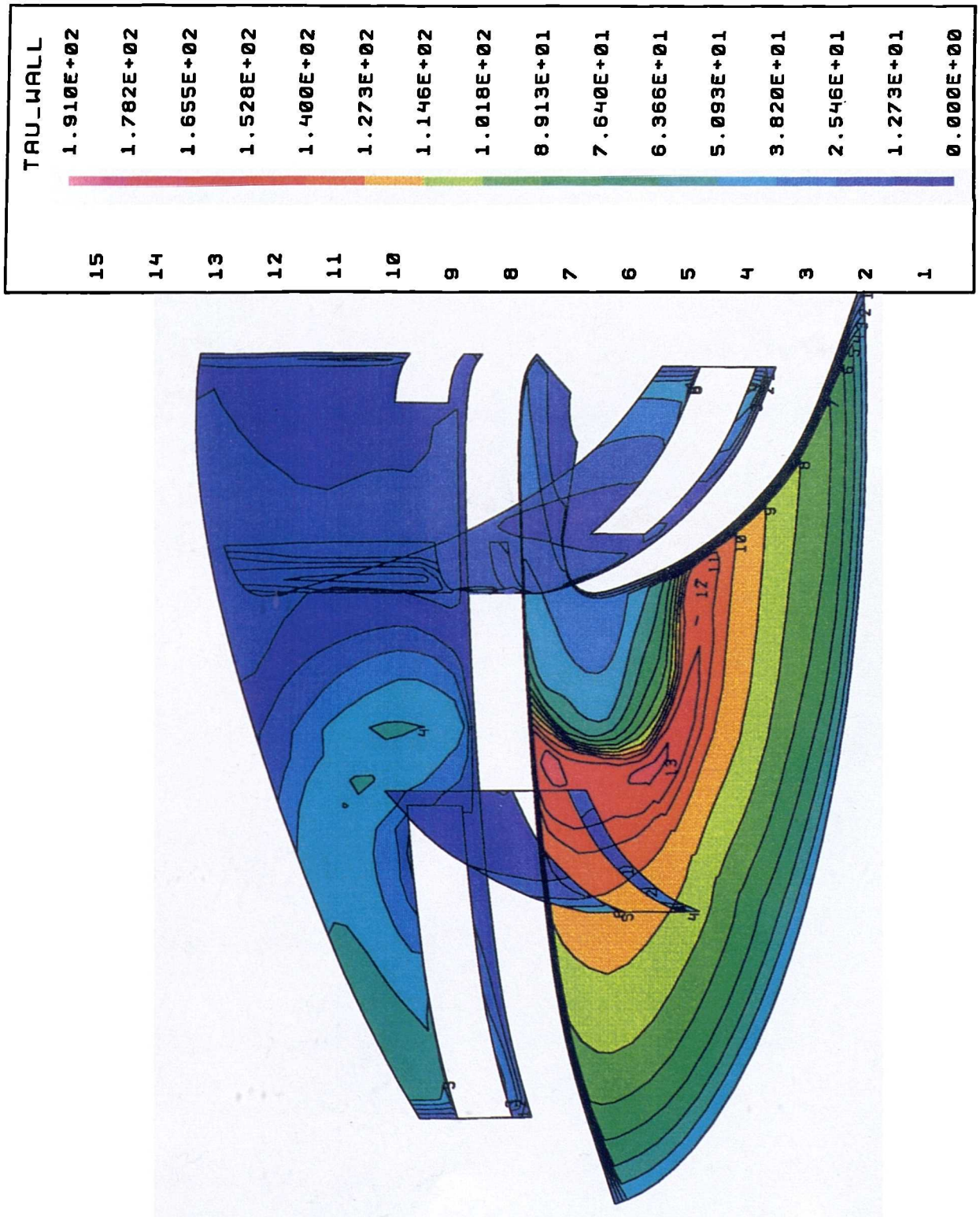

Figure 6.54: Scalar stress in near-outlet plane (n=2000 rpm/ Q=7 l/min - reduced gap).

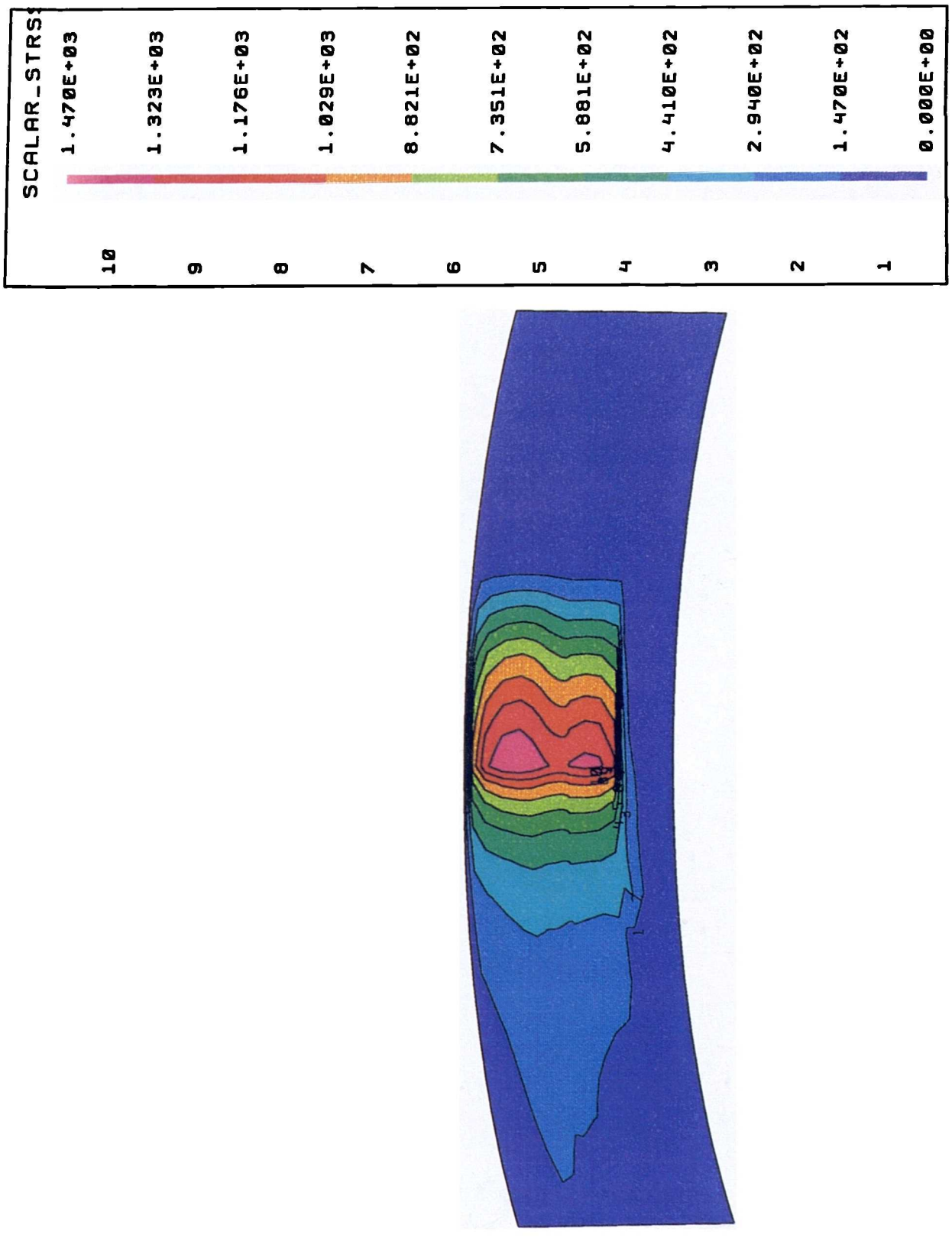

Figure 6.55: Scalar stress in blade-to-blade plane (n=2000rpm/ Q=7l/min - reduced gap).

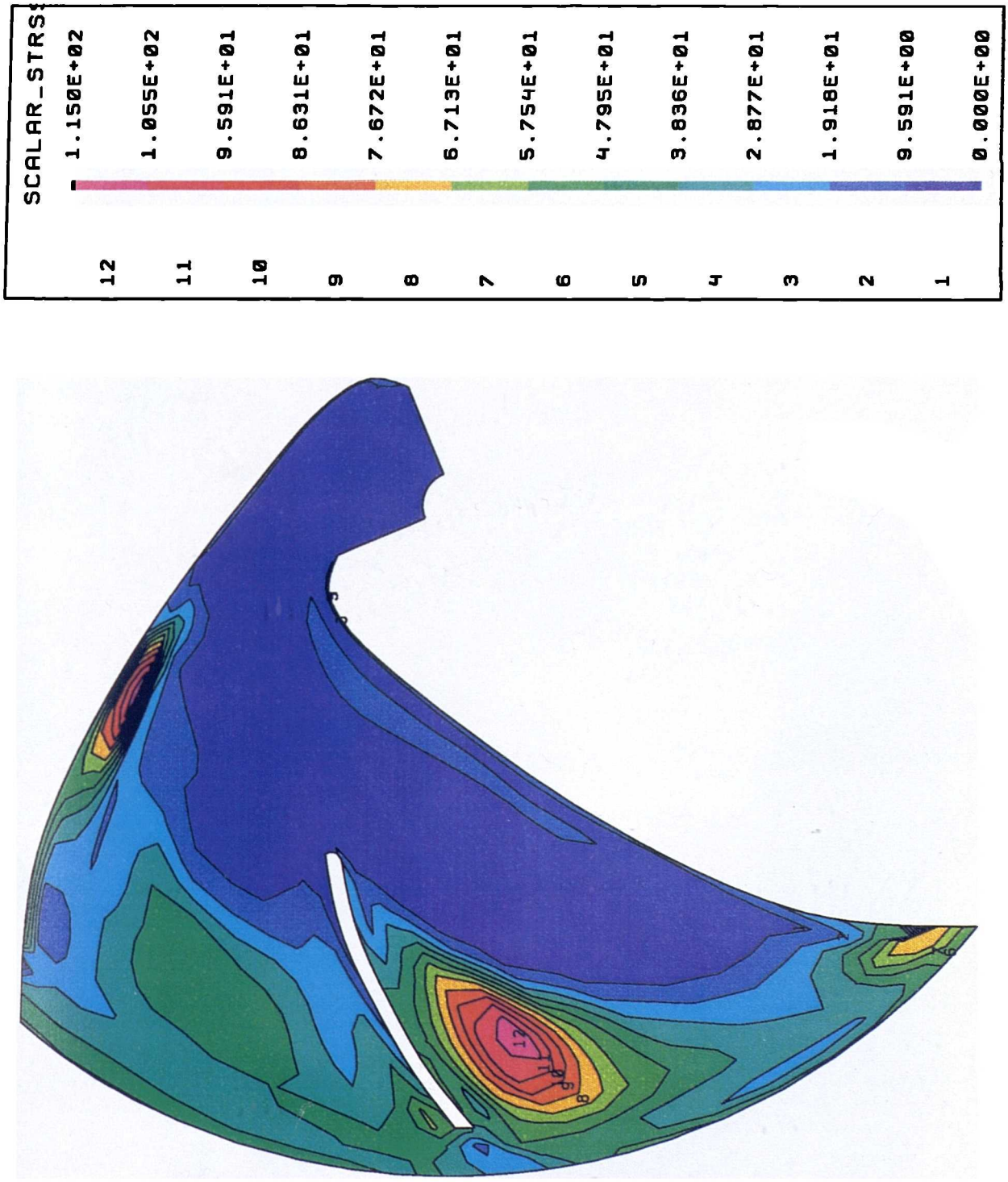

Figure 6.56: Scalar stress in impeller-channel plane (n=2000rpm/ Q=7l/min -reduced gap).

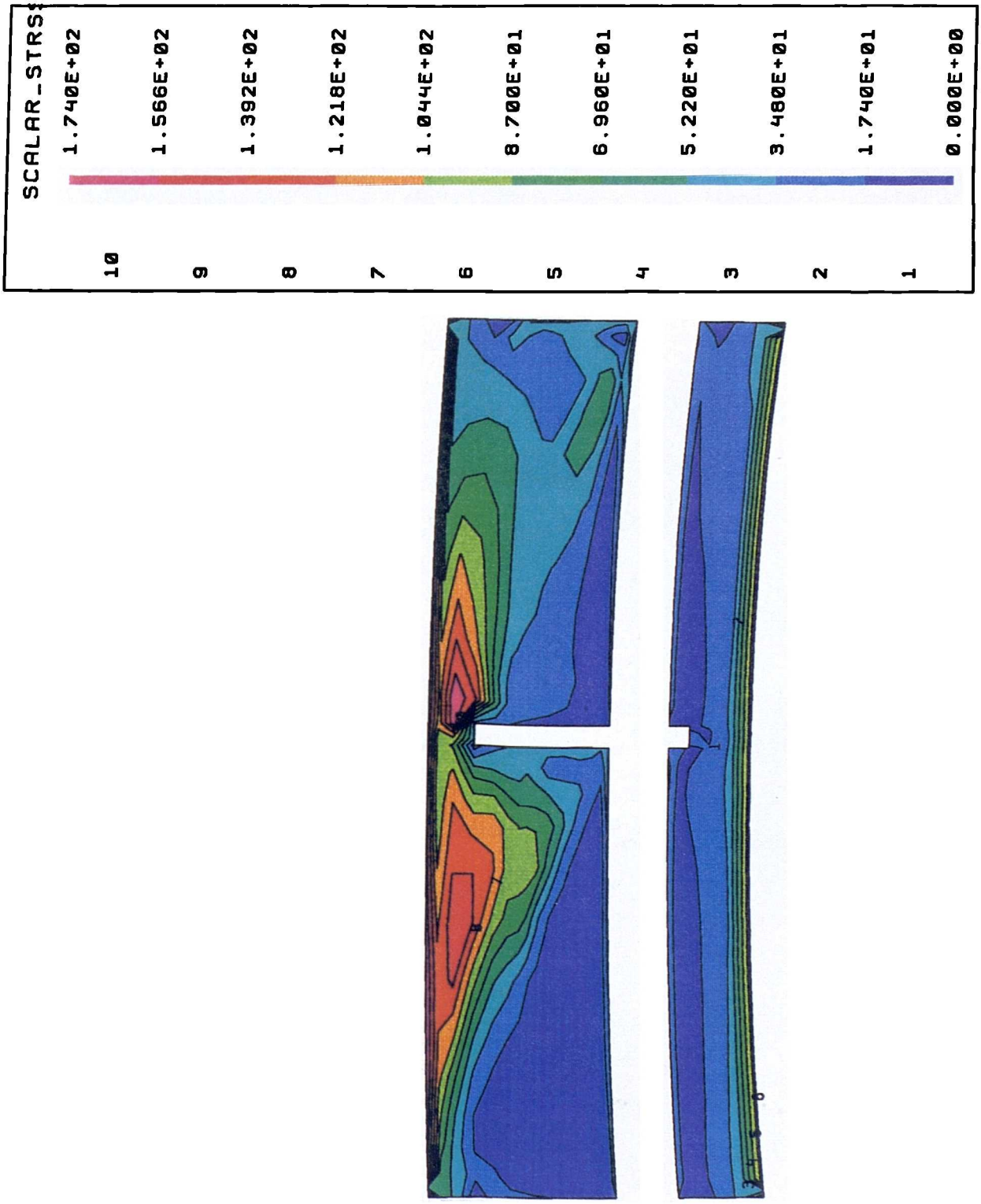

Figure 6.57: Scalar stress in axial gap plane between blades and front casing (n=2000rpm/ Q=7l/min -reduced gap).

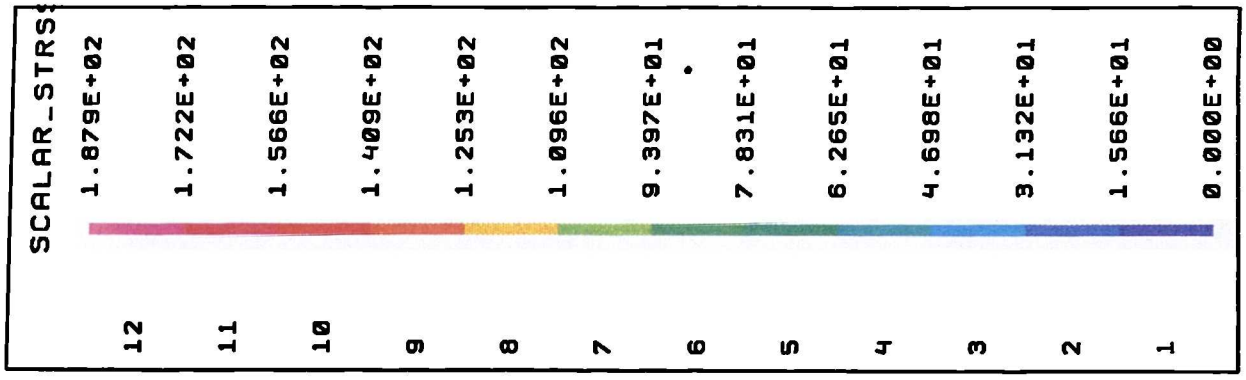

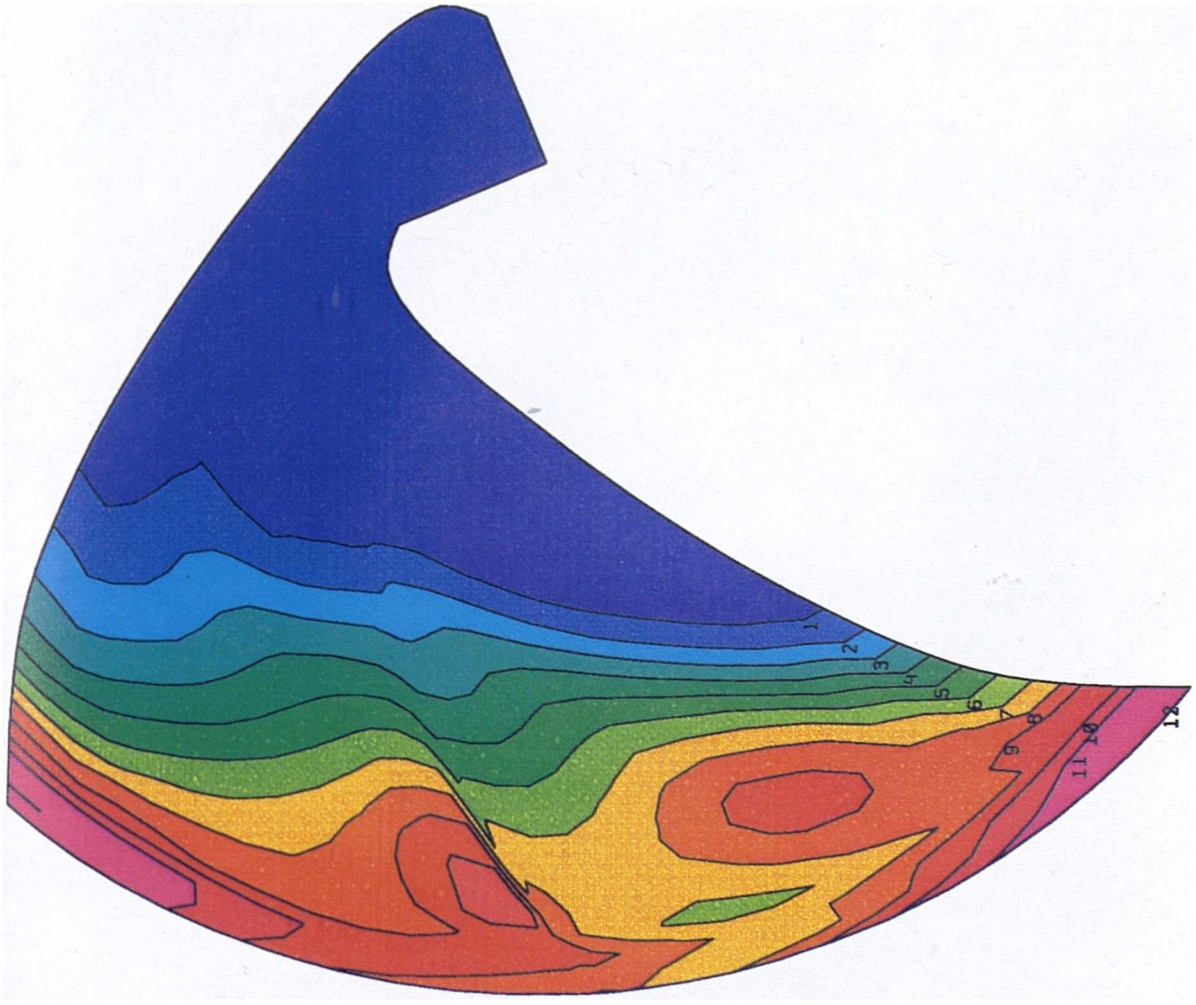

counterrotating flow in the impeller-channel plane (Fig 6.47) and in the gap plane itself (Fig 6.48) were also recorded. An increase of the hydraulic performance can is obtained through a higher static pressure head, as shown for the gap plane in Fig 6.49. Stronger irregularities due to the altered gap flow conditions can also be observed. A shift of the areas of higher turbulence to the outer radius occurs, see Figs 6.50 and 6.51. The reduction in gap size showed important effects on the distribution of viscous wall shear stresses. Maxima are, not unexpectedly, found at the front casing, but also at the rear casing (Figs 6.52, 6.53). Distributions on the blade surfaces, however, remained similar. A general increase in the level of scalar stress values as a consequence of the geometrical change is obtained. While the global maxima of approximately 1,5 kPa is also found in the near outlet region (Fig 6.54), significant qualitative changes can be observed in other areas. Local maxima are sited in the bulk flow rather than in near wall regions and show a strong proportionality to the radius (Figs 6.55 to 6.57).

n [rpm] / Q [l/min]	H_{calc} [kPa]	$\sigma_{scalar_{max}}$ [Pa]
500 / 1	1.4	55
1000 / 3	5.5	225
1500 / 5	14.0	525
2000 / 7	24.5	1040
2000 / 7 (reduced gap)	28.0	1470
2000 / 10	25.1	1200

Table 6.2: Static pressure head and maximum scalar stress calculated for various input parameters.

Particle stress-time predictions

In order to relate the stress conditions within the pump to the actual mechanical loading experienced by blood elements on their passage through the pump, the ability of TASCflow ^{TM} to determine streaklines in a 3D flow was utilised. Streaklines of particles starting at every nodal position (i,j) of the inflow area, see Appendix D, were calculated to achieve a high statistical significance,

and locations were stored in form of nearest nodal points. A time-dependent stress loading function for each of these particle streaklines was obtained by assigning scalar stress values at the particular nodal position and determining passage times by knowledge of the spatial location and the velocity field. As a result a diversity of stress-time functions of fluid particles passing the pump were obtained which showed differences in transit time as well as in distribution and frequency of stress maxima. A few examples of these functions are shown for the operating condition of n=2000rpm/Q=7l/min (original gap size) in Figs 6.58 to 6.61. Locations of local maxima of scalar stresses within the pump domain are indicated and explained in the figure captions. From these graphs it can be deduced that fluid particles on their passage through the pump undergo a highly irregular, fluctuating stress loading. The highest values occur when particles passing the vicinity of the near outlet region (600-1000 Pa). Local maxima in the range of 50 - 200 Pa are recorded at a variety of locations especially in the vicinity of the casing according to the scalar stress distribution discussed above.

Two examples of stress-time functions for particles at a reduced rotational speed of n=500 rpm are shown in Figs 6.62 and 6.63. Here similar observations regarding the general properties of these functions can be made but with a highly reduced stress scale. Transit times in general increased for this rotational speed.

The stress-time function also provides a clear and comprehensive means of assessing the effect of geometrical changes on loading properties. Two representative graphs of stress-time functions for a pump with a reduced blade-casing gap show the increase of stress maxima compared to the design gap flow (Figs 6.64 and 6.65). The non-uniformity of the functions and order of transit times remained similar.

Numerical error estimation

An estimation of numerical errors was performed by comparing the first-order MWS with the second-order LPS discretization method. Differences of less than 0.001 % for the velocity components and of less than 5 % for the static pressure between simulations using the two methods revealed a sufficient numerical accuracy.

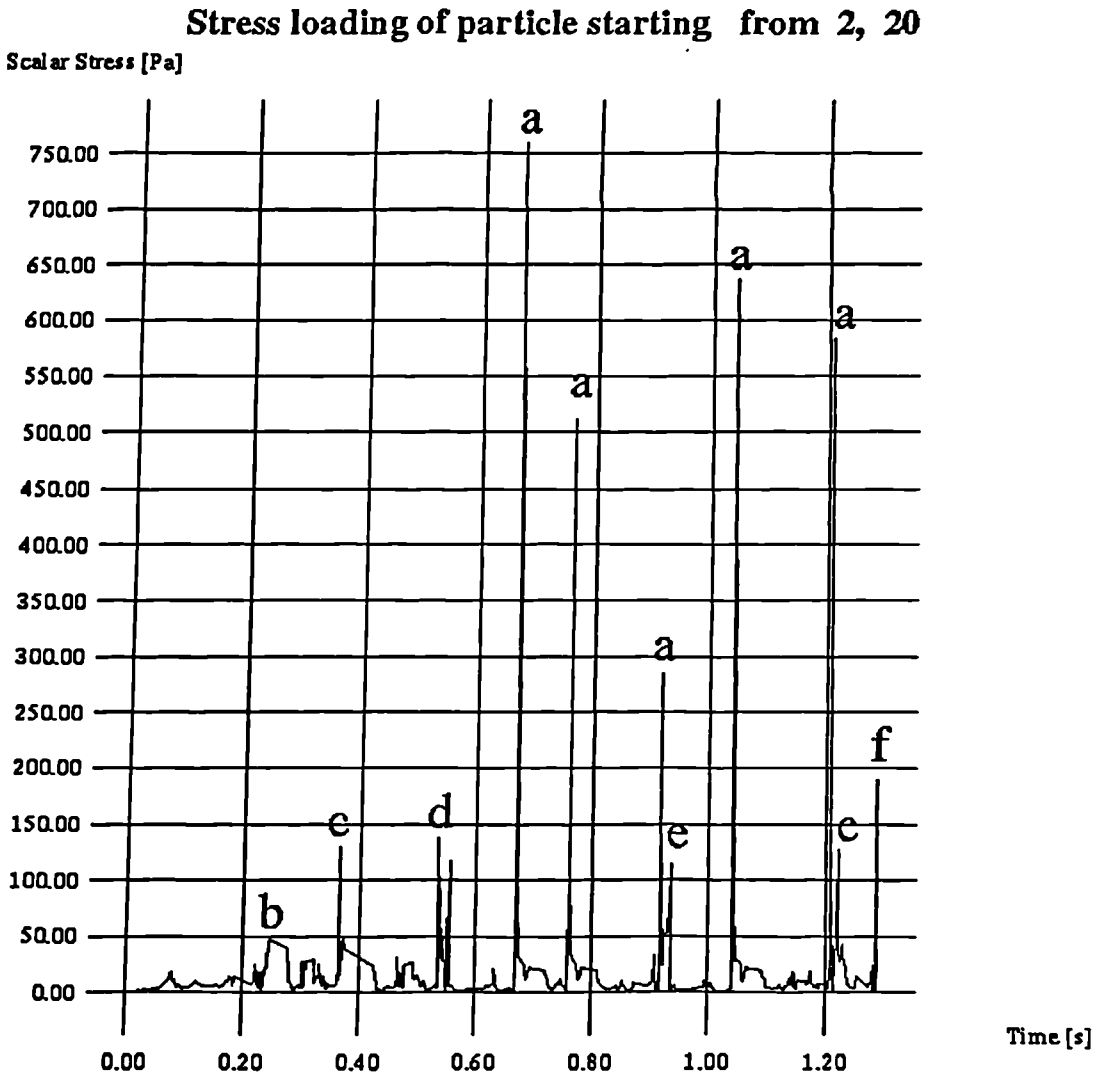

Figure 6.58: Loading-time function for n=2000rpm/Q=7l/min; Locations: a-near outlet region, b-overflow of large blade at midlength, c-front casing near trailing edge of large blade, d-outer casing near large blade, e-rear casing between blades at mid blade length, f-outlet.

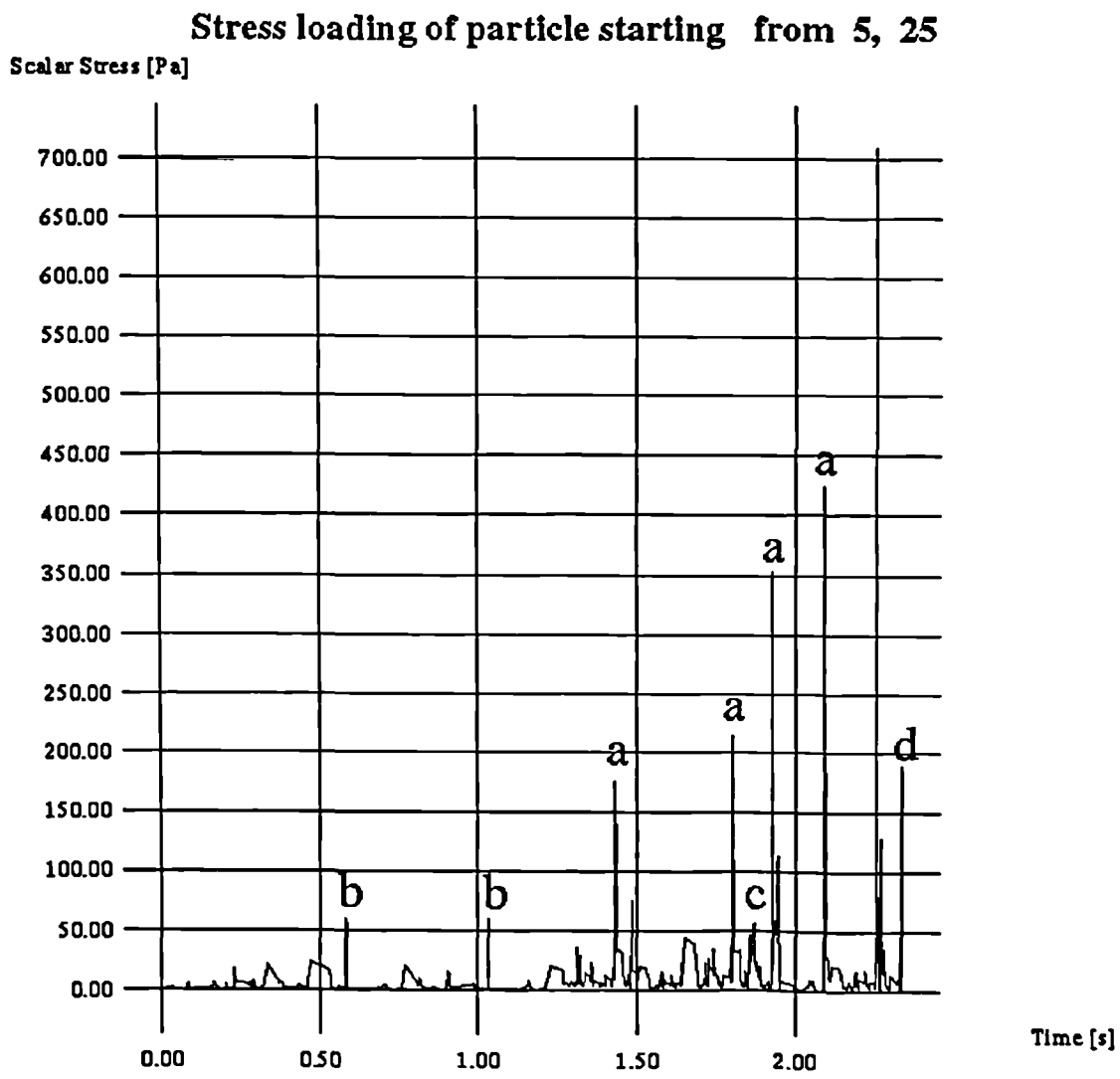

Figure 6.59: Loading-time function for n=2000rpm/Q=7l/min; Locations: a-near outlet region, b-rear casing near leading edge of small blade, c-front casing near trailing edge of large blade, d-outlet.

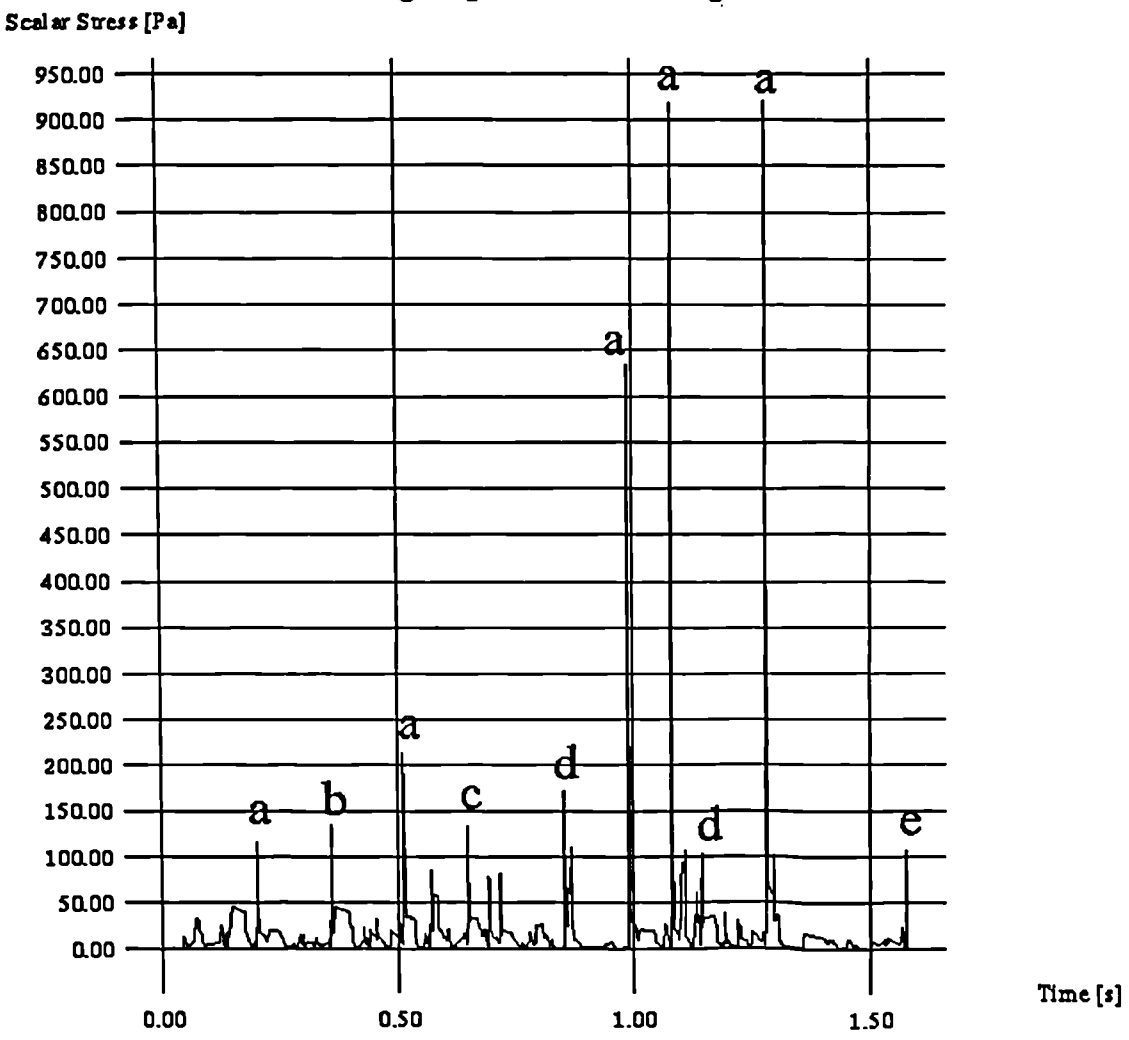

Figure 6.60: Loading-time function for n=2000rpm/Q=7l/min; Locations: a-near outlet region, b-front casing near trailing edge of small blade, c-rear casing at mid blade-to-blade distance near leading edge, d-rear casing near large blade at mid length, e-outlet.

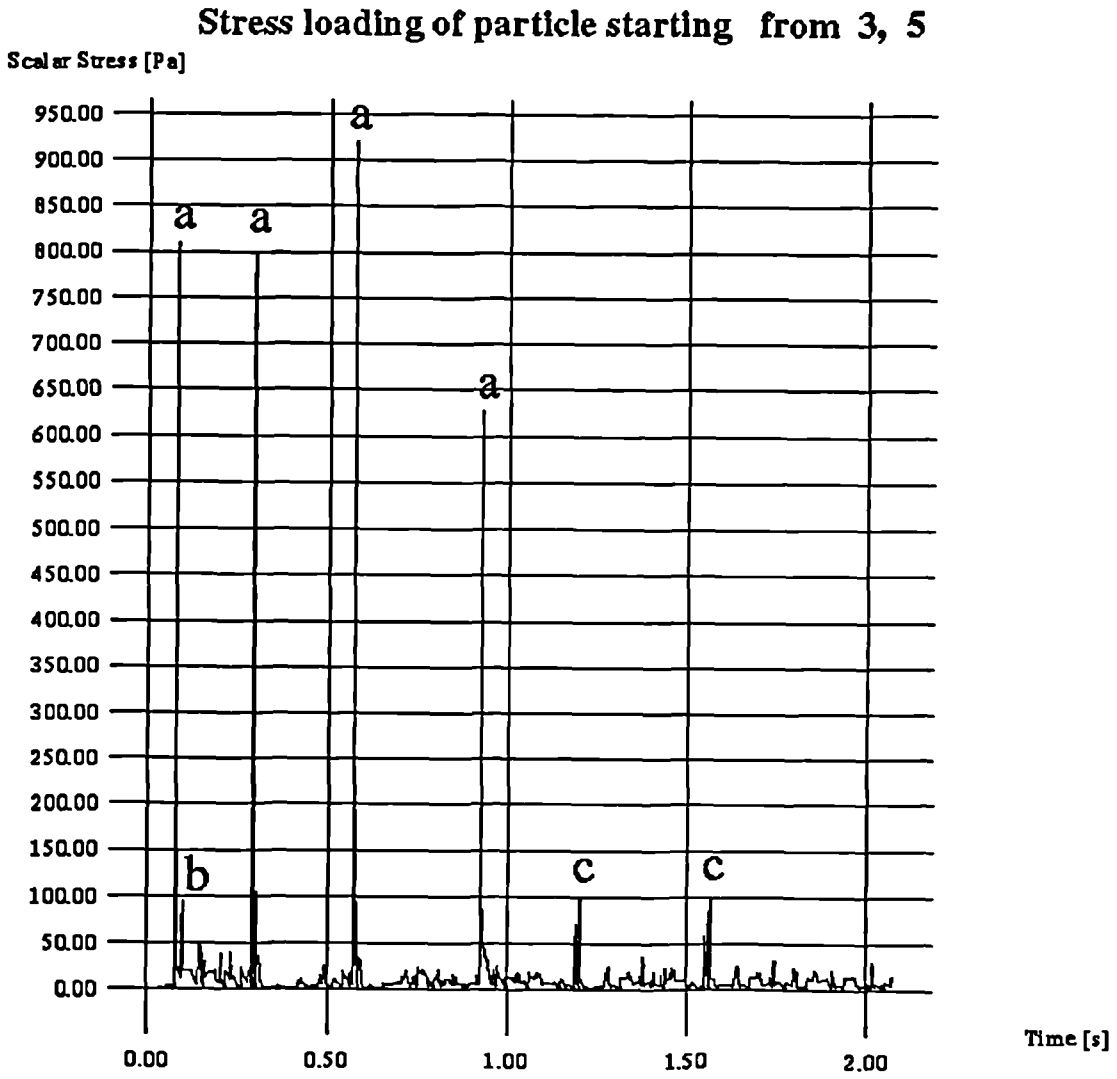

Figure 6.61: Loading-time function for n=2000rpm/Q=7l/min; Locations: a-near outlet region, b-rear casing near large blade at midlength (PS), c-rear casing near small blade at midlength.

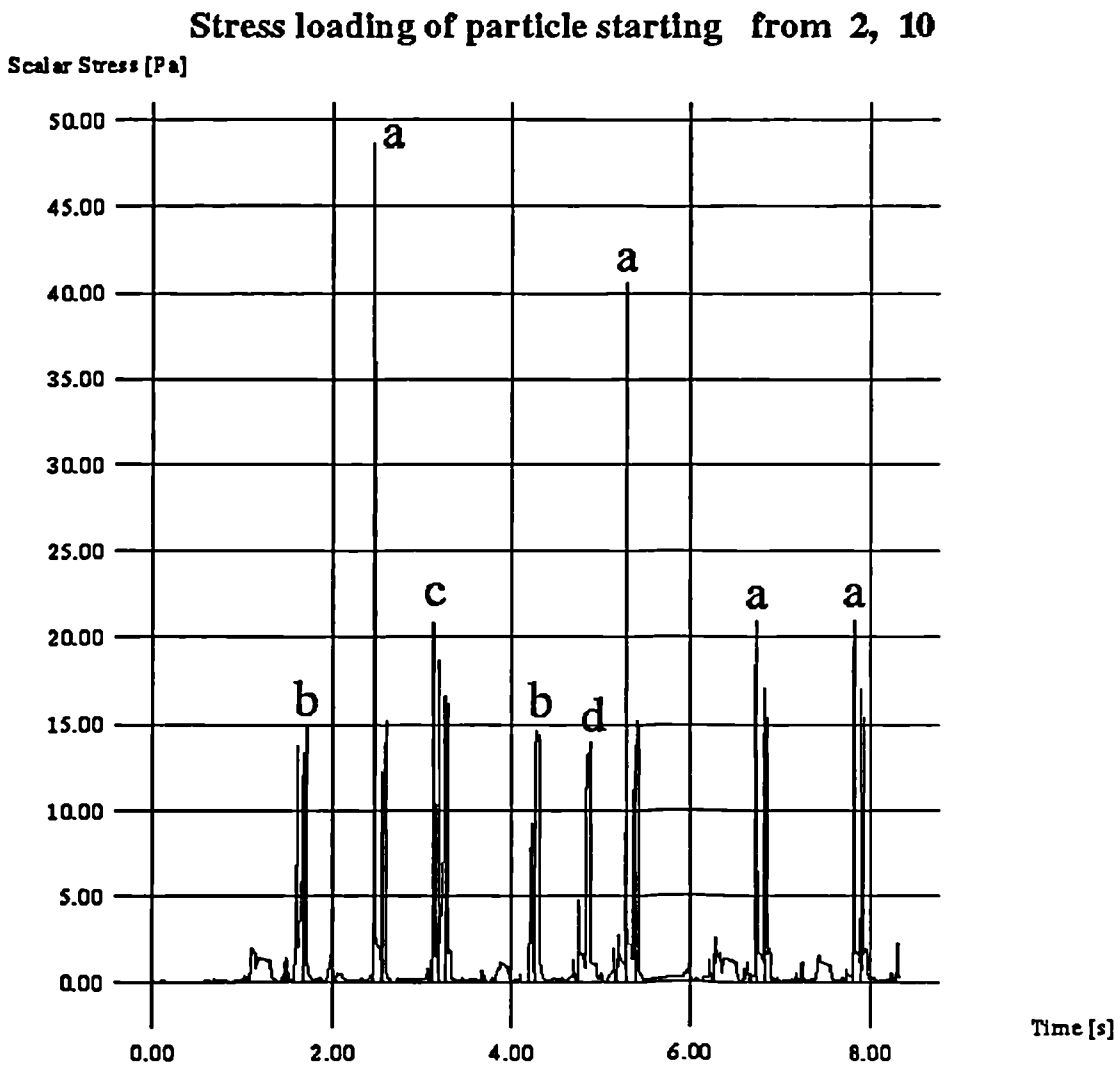

Figure 6.62: Loading-time function for n=500rpm/Q=1l/min; Locations: a-near outlet region, b-rear casing near leading edge of small blade, c-outer casing near large blade (PS), d-rear casing near large blade at midlength.

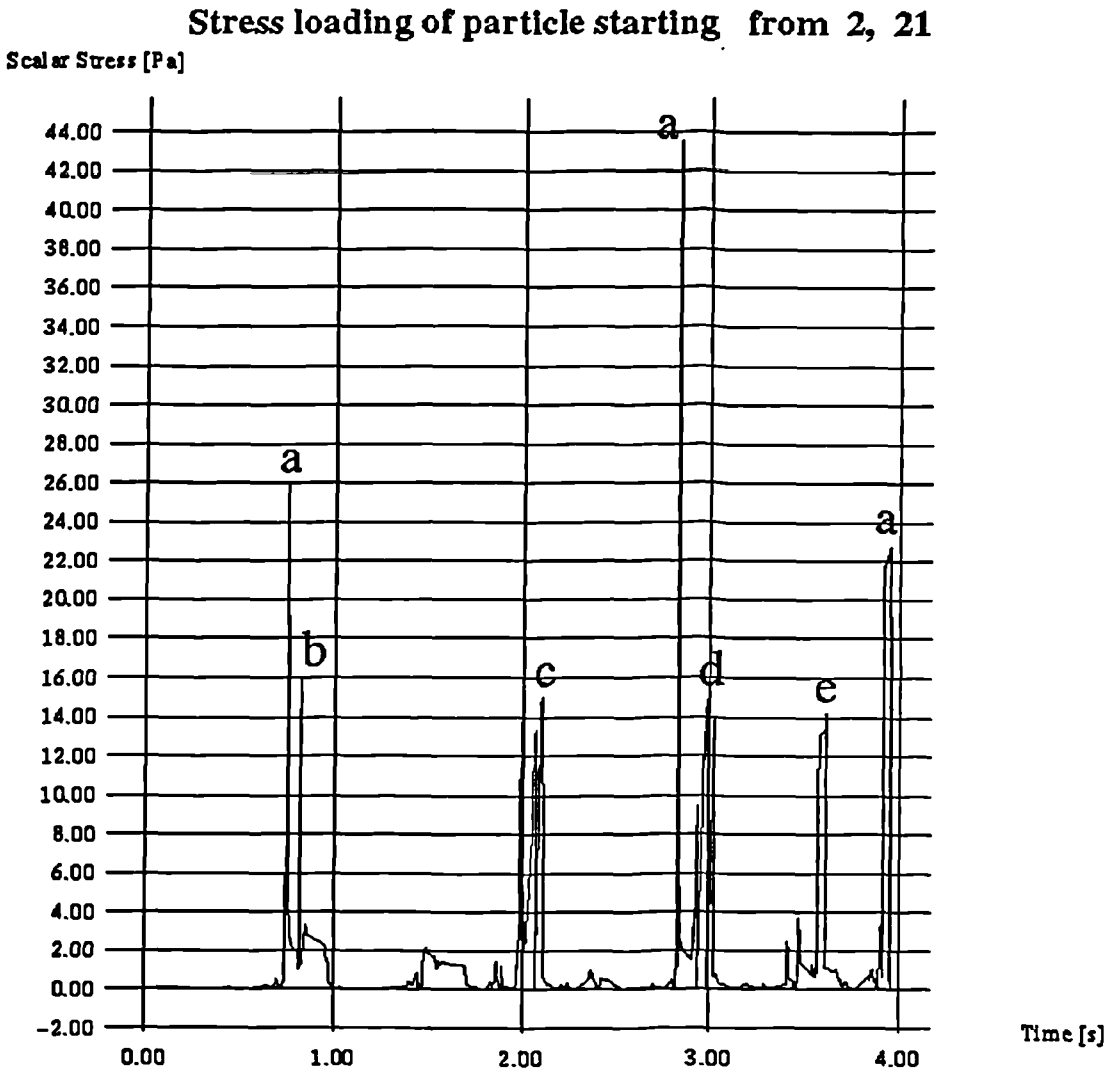

Figure 6.63: Loading-time function for n=500rpm/Q=11/min; Locations: a-near outlet region, b-front casing near trailing edge of large blade, c-rear casing near leading edge of small blade (PS), d-rear casing near leading edge of small blade (SS), e-rear casing near large blade (SS) at midlength.

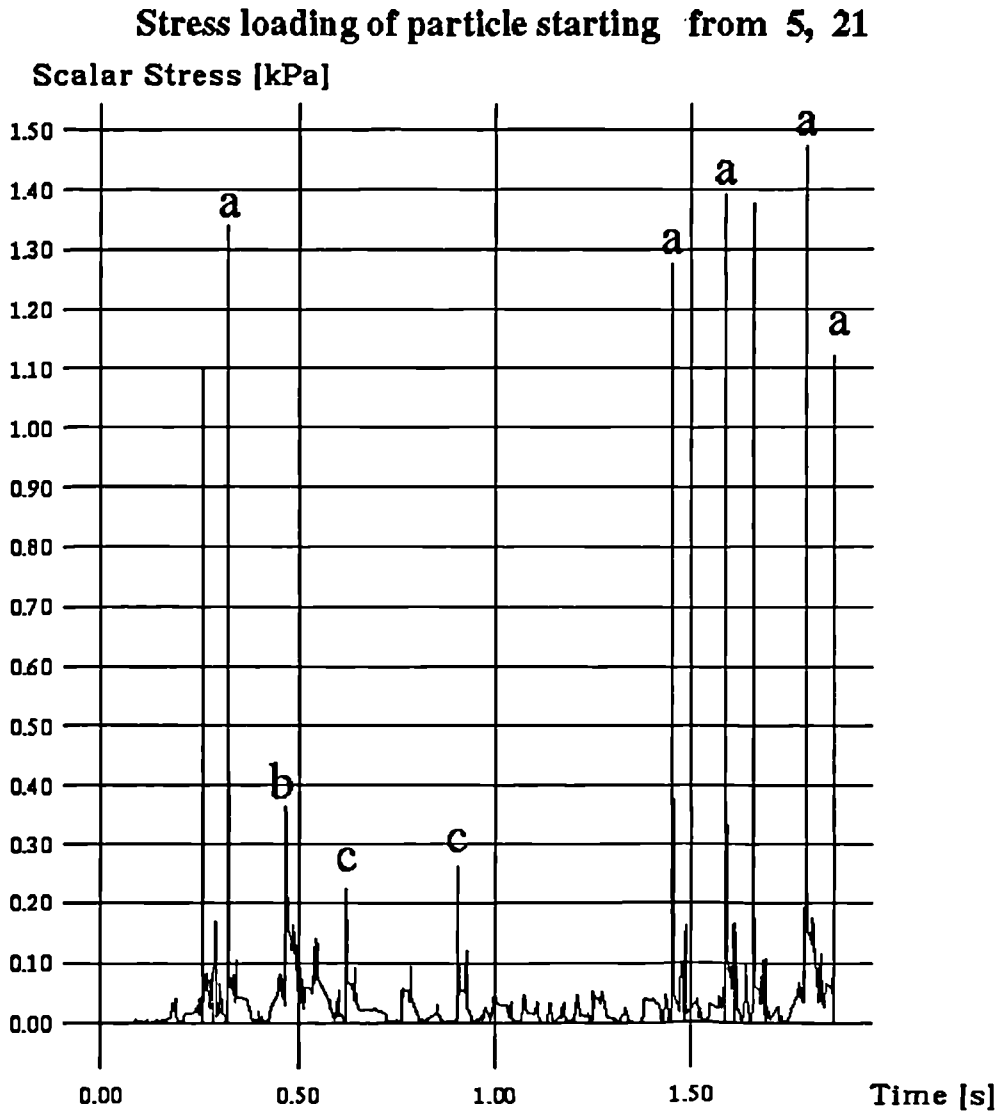

Figure 6.64: Loading-time function for n=2000rpm/Q=7l/min (reduced gap); Locations: a-near outlet region, b-outer casing near large blade, c-tip flow around small blade.

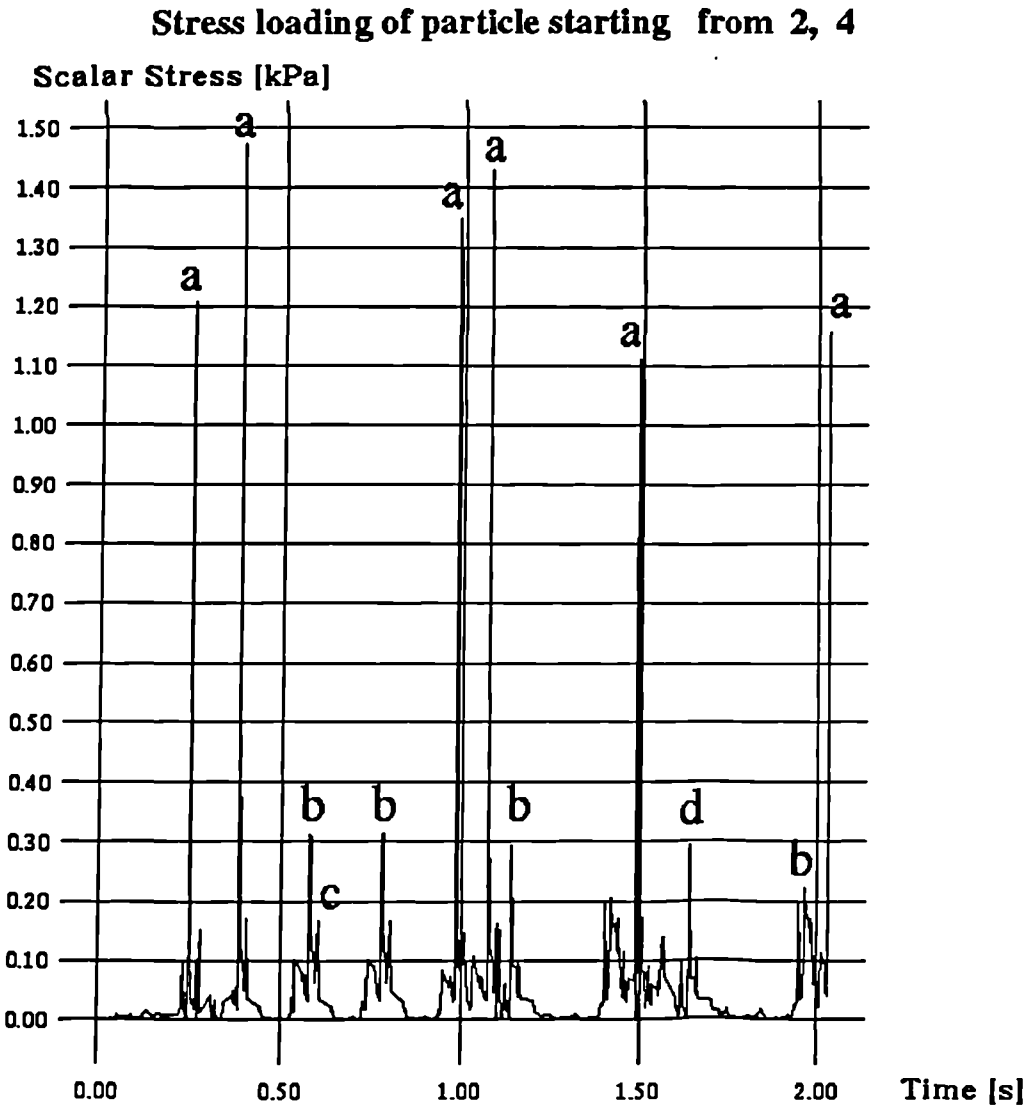

Figure 6.65: Loading-time function for n=2000rpm/Q=7l/min (reduced gap); Locations: a-near outlet region, b-tip flow around small blade, c-front casing near trailing edge of large blade (SS), d-flow around impeller disc near trailing edge of small blade.

n	$H_{meas}[kPa]$	$H_{calc}[kPa]$	$\frac{H_{calc}}{H_{meas}}$
500	1.1	1.4	1.27
1000	4.5	5.5	1.22
1500	11.5	14.0	1.22
2000	19.5	24.5	1.25

Table 6.3: Comparison of static pressure head calculated and measured.

Predicted vs. measured pressure heads

Since velocity measurements within the pump are not available, the validity of the CFD analysis has been examined by comparison of the predicted static pressure head with that measured experimentally (see Table 6.3). The pump performance was obtained with a water/glycerol solution ($\nu = 3{\cdot}10^{-6}$ m^2/s) and is given in Fig 6.66.

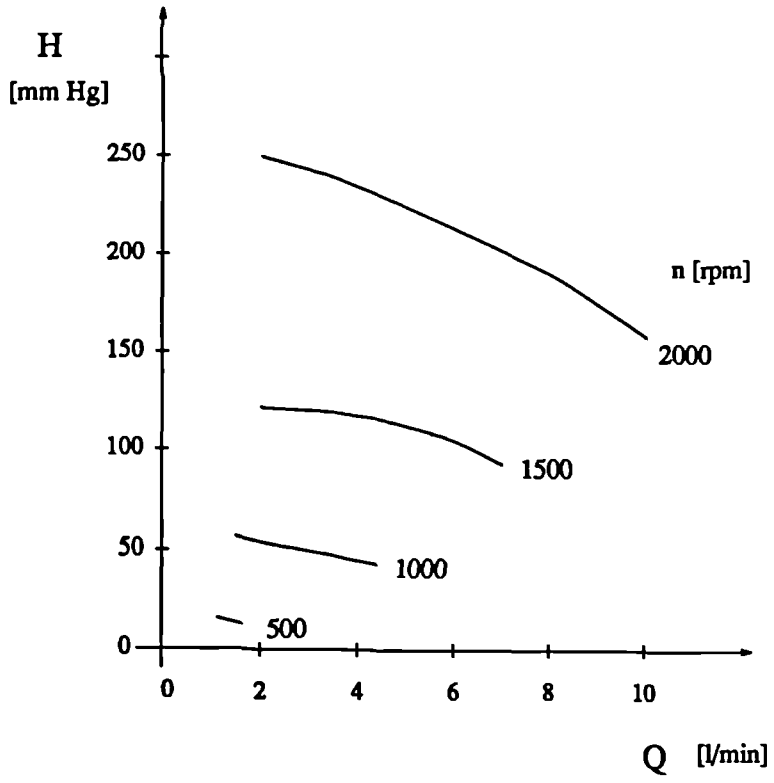

Figure 6.66: Performance curve of Isoflow ^{TM} centrifugal pump for a water / glycerol solution ($\nu = 3{\cdot}10^{-6}$ m^2/s).

The measured pressure head was corrected for tube friction loss since pres-

sure taps for the measurements were located at a distance of 30 cm upstream and downstream of inlet and outlet ports, respectively. Values obtained by numerical calculation were approximately 20% to 30% higher, which could have been caused by an unrealistic modelling of the inflow and outflow boundary conditions and of the turbulent flow conditions.

6.3.3 Simulation of the Outlet Flow

The task of the outlet system in a centrifugal pump is to collect the fluid from the impeller and to transfer kinetic energy into potential energy by reducing the flow velocity efficiently. To perform this energy transmission with losses as low as possible, the volute must be carefully designed and should match the impeller flow [14, 118]. From consideration of an ideal two-dimensional impeller discharge flow which can be represented by a spiral vortex, the spiral-shaped volute developing into a diffuser is the most common vaneless outlet system for industrial pumps.

The design-outlet of the Isoflow ^{TM} pump is a port of constant circular cross-section attached tangentially to the impeller casing which exhibits neither the spiral form nor a diffuser geometry. Therefore, flow in this geometry was numerically analysed and its performance compared with that of a spiral volute discharging into a diffuser.

Geometrical Model

a) Design Outlet

The original outlet system was modelled 3-dimensionally including the annular gap between impeller discharge radius and outer casing, and the outlet port, see Fig 6.67. The cross section of the outlet port at the interface to the impeller casing was assumed to be rectangular. This simplification was undertaken to match the outlet cross section of the impeller flow calculations and to avoid complicated numerical grids. A smooth, linear transition into the circular cross section at the end of the outflowing end of the outlet port was assumed. Grids for the circular and for the outlet port parts were generated separately and sub-

sequently attached to each other. Grid refinements were placed in the transition area from one subgrid into the other. The entire grid contained approximately 30,000 finite-volume elements.

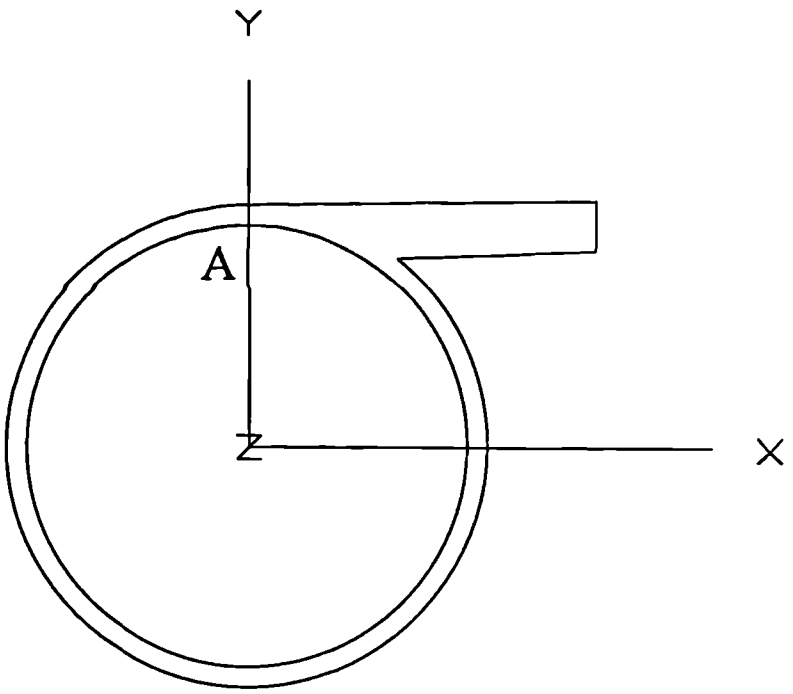

Figure 6.67: Axial cross section of design outlet.

b) Spiral Volute

An Archimedean spiral (outer radius increasing linearly with angular position) was chosen as the volute form. The angle subtended by the spiral is 360^0, where the ratio of the radii of the spiral end to the spiral beginning is 1.1 . The spiral volute extends into a diffuser with a widening angle of 2.5^0 and meets the design port diameter at its end, see Fig 6.68. The beginning cross section of the diffuser is rectangular similar to the design outlet model. Volute and diffuser grids were modelled separately and attached. Grid refinements were also placed at the transition region between both subgrids. The grid contains approximately

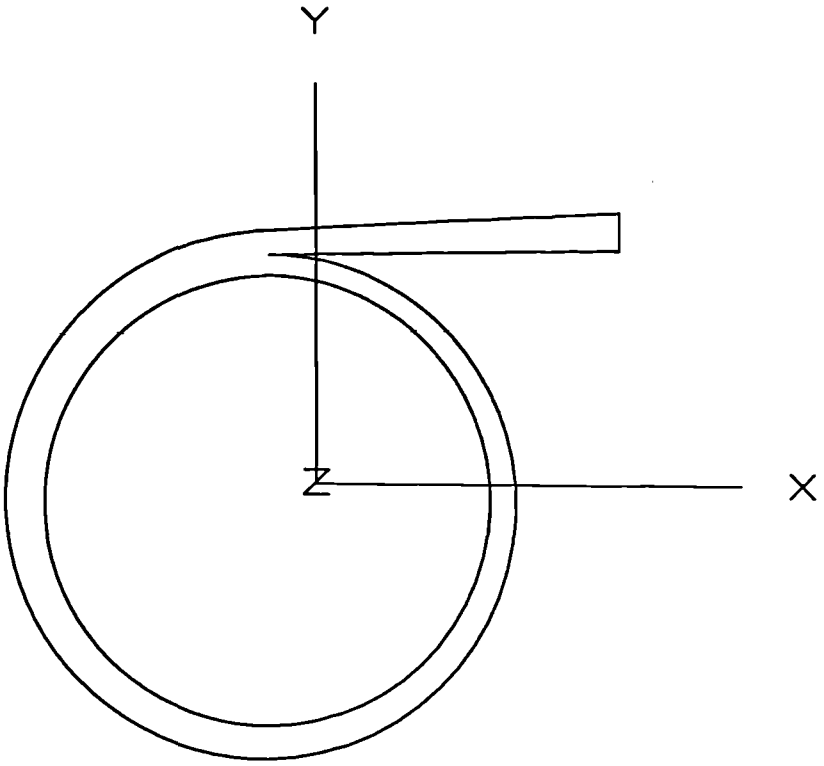

Figure 6.68: Axial cross section of spiral volute.

22,000 finite volume elements and is presented in Fig 6.69.

Boundary Conditions

The simplifying approximation of a uniform boundary condition along the circumference for the inflow was made. The velocity for each nodal point at the impeller discharge radius was defined, the radial component resulting from the flow rate and cross-sectional area and the circumferential component equalling the circumferential speed of the impeller at that radius. The axial component was set to zero. This inlet velocity assumption can be justified from the results of the impeller flow simulation which showed a small proportion of disturbances to this uniform distribution as seen in the results of the impeller flow simulation. An exception was made for the part of the inlet plane which represents

the impeller disc and was defined as a rotating wall.

Rotational speed and flow rate were chosen as n=2000 rpm and Q=7 l/min, respectively. The outlet condition satisfies mass conservation at the outlet plane

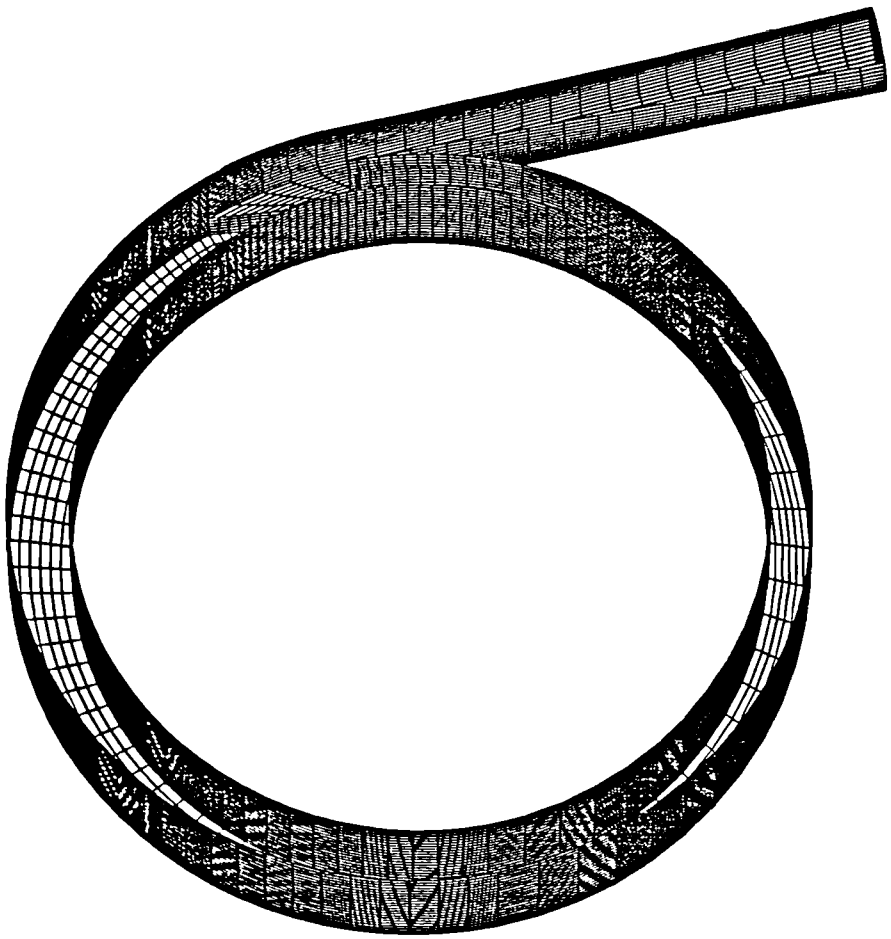

Figure 6.69: Numerical grid of spiral volute.

in relation to the inlet mass flow. Stationary wall boundary conditions were applied to all parts of the casing. Near wall regions are modelled by wall functions as represented in Chapter 6.3.2. Values for dynamic viscosity and density were

the same as in the impeller flow studies (ρ=1000kg/m^3, ν=3·10^{-6} m^2/s).

Numerical Calculation

For the outlet flow the same flow parameters were numerically determined with exception of the velocity vector which in this case is the absolute velocity.

Advective fluxes were discretized applying the MWS method.

The same convergency criteria applied as for the impeller flow calculations. Convergency was reached for the design-outlet flow after 120 iterations and for the spiral volute after 40 iterations.

Results

a) Design Outlet

Fig 6.70 depicts a plot of the velocity vector projected into an axial outlet plane at mid-height position. It shows a fairly uniform, slightly increasing velocity distribution along the impeller circumference in a direction clockwise from point A (Fig 6.67). The sudden widening of the flow domain with entrance into the outlet port leads to an abrupt decrease in velocity accompanied by strong flow disturbances. Secondary flow effects can also be seen in the velocity plot in a meridional cross section of the outlet port (Fig 6.71). The development of the velocity modulus along the outlet port in the downstream direction (Figs 6.72 to 6.74) indicates a flow pattern which is highly inconsistent and differs strongly from that for fully developed tube flow.

The velocity distribution in the outlet domain is mirrored by the static pressure field. Fig 6.75 shows a slight decrease of the static pressure along the circumference and an increase with inflow into the outlet port.

The ratio of turbulent to molecular viscosity has its highest values of approximately 200 at a position of the inflow domain (Fig 6.76) which coincides with the lowest pressure values. High values of the viscosity ratio can be found throughout the flow domain as shown in Figs 6.77 and 6.78. These results leave no doubt about the existence of turbulence in the outlet region.

Maximal viscous wall shear stresses of approximately 380 Pa are predicted

Figure 6.70: Velocity distribution in axial plane (design outlet).

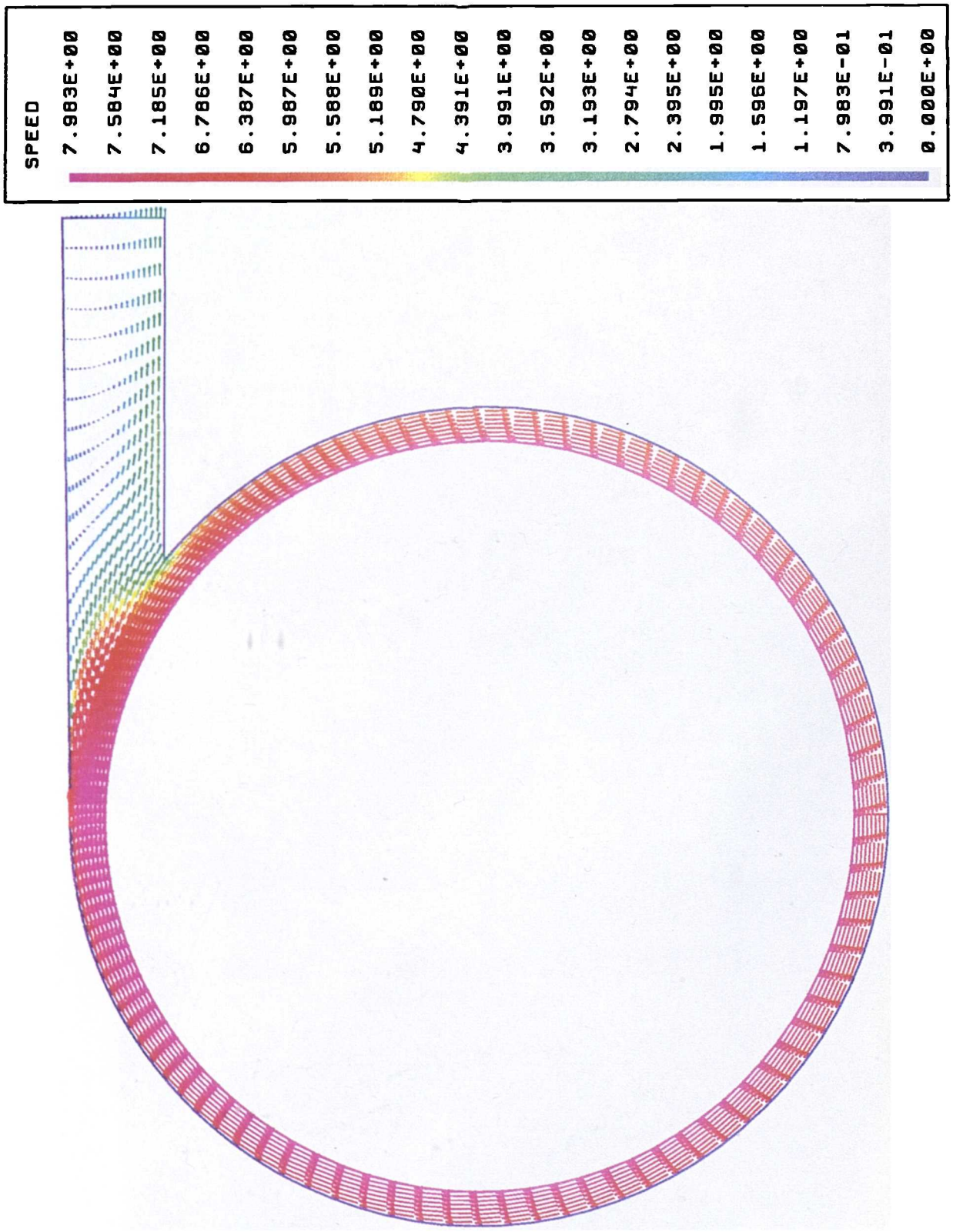

Figure 6.71: Velocity distribution in meridional plane of outlet port (design outlet).

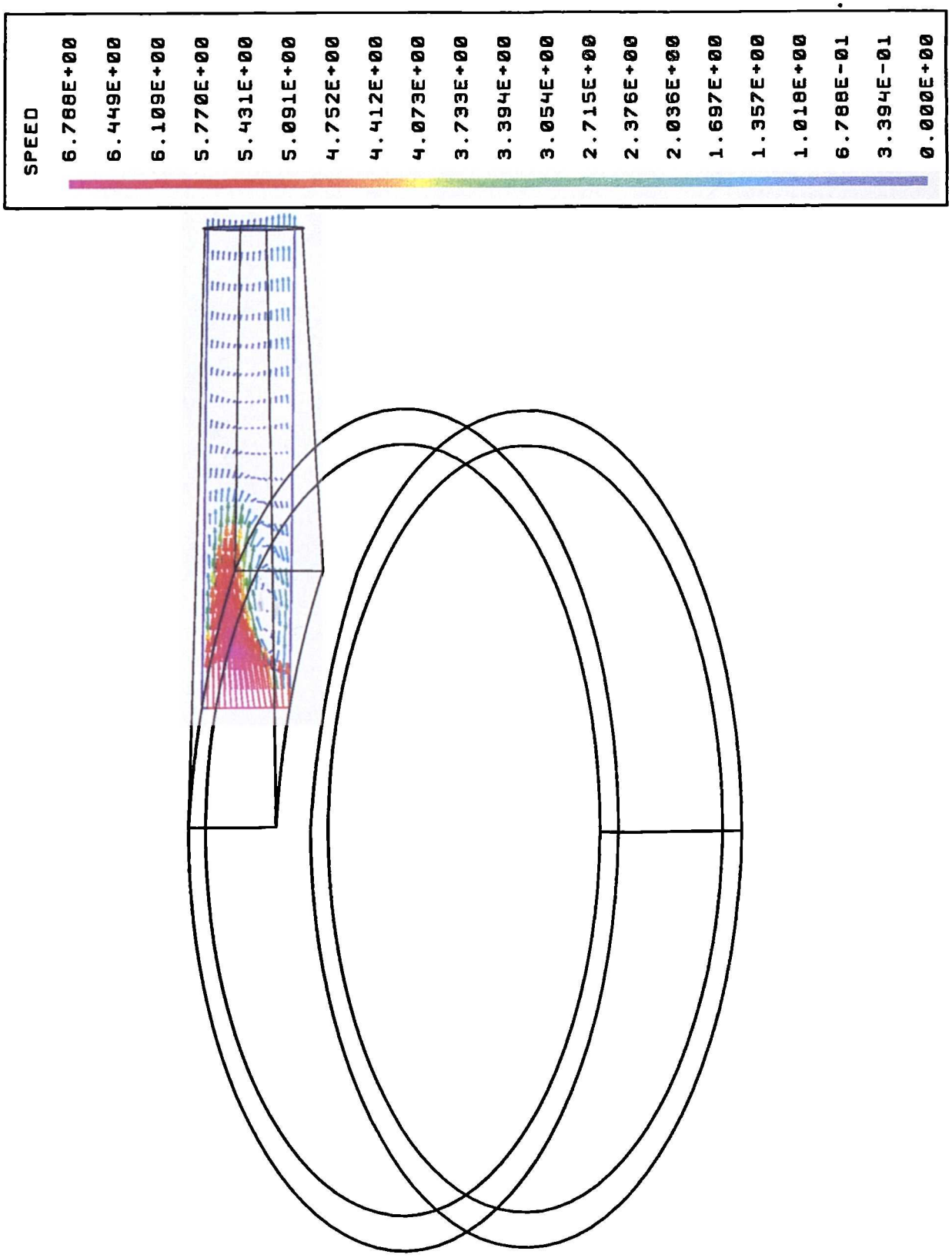

Figure 6.72: Velocity distribution in beginning cross section of outlet port (design outlet).

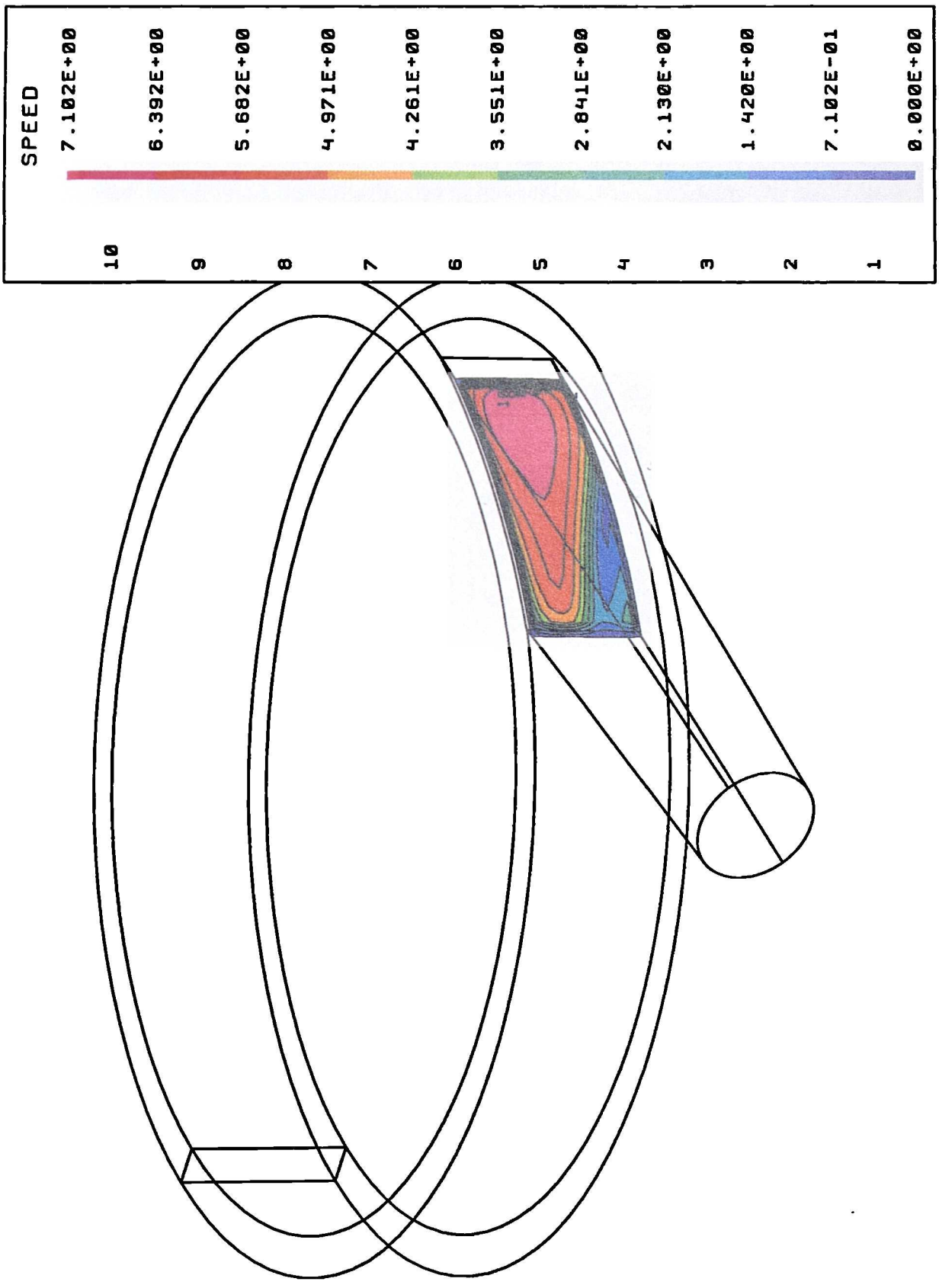

Figure 6.73: Velocity distribution in midlength cross section of outlet port (design outlet).

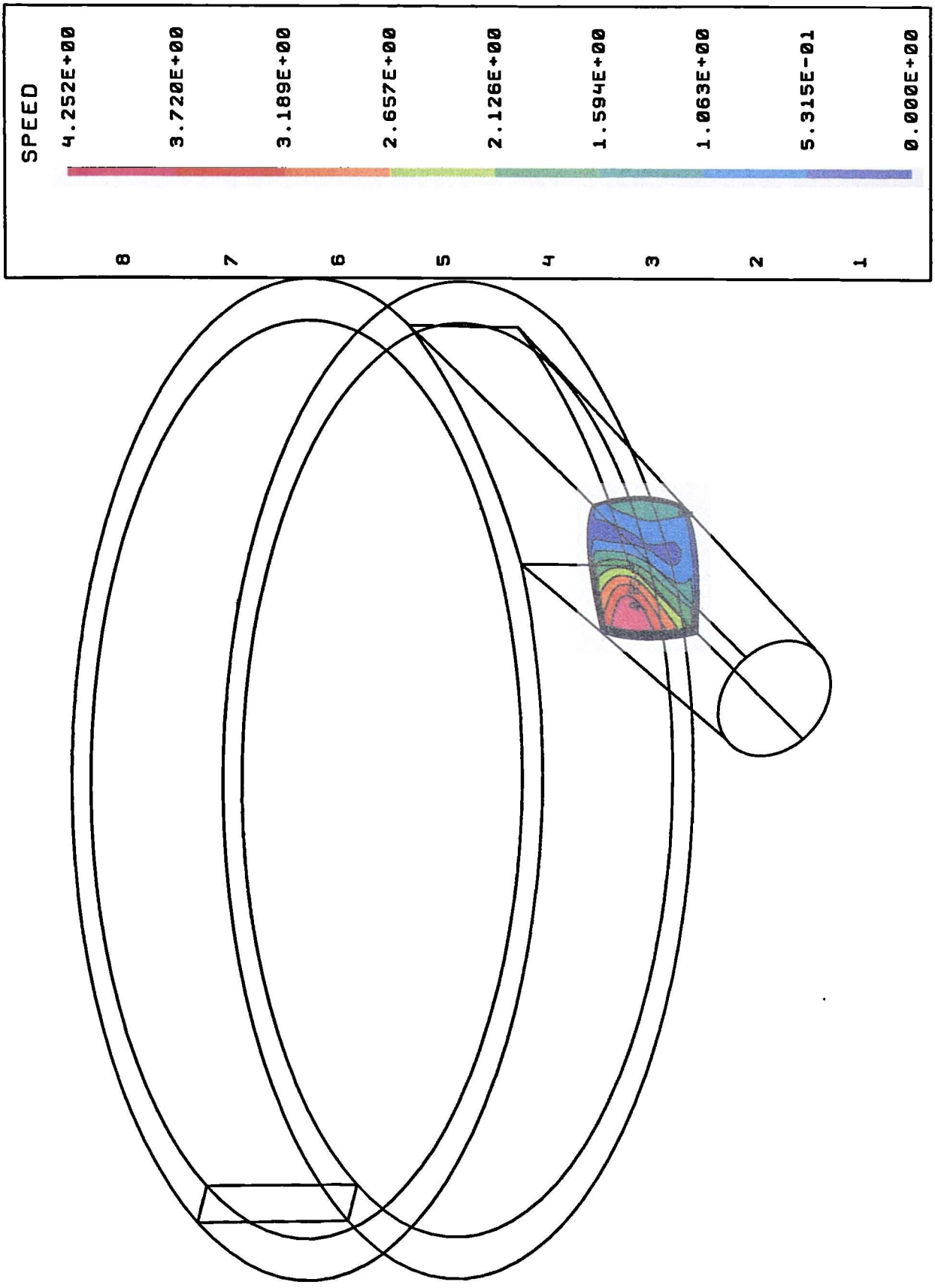

Figure 6.74: Velocity distribution in end cross section of outlet port (design outlet).

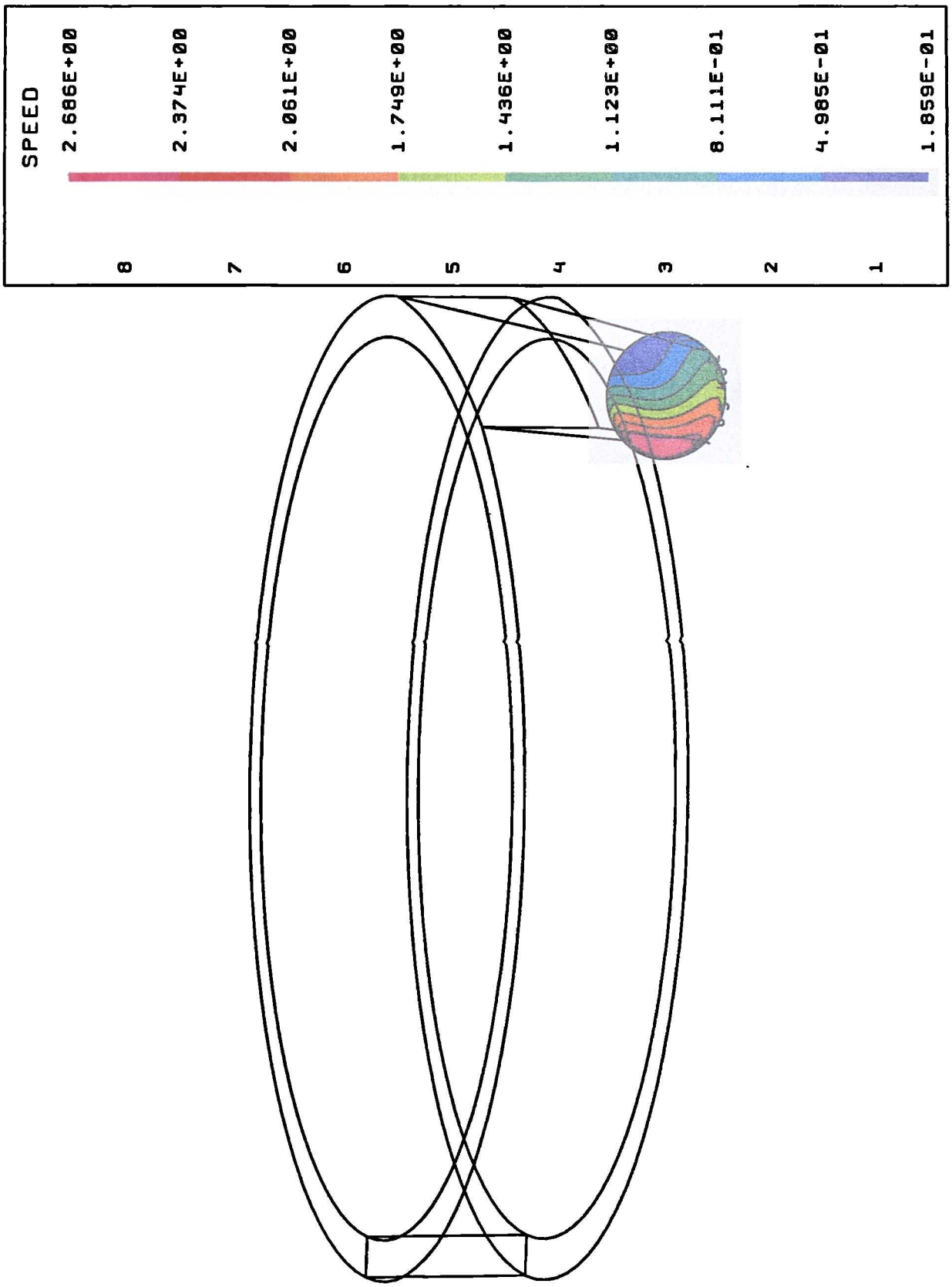

Figure 6.75: Static pressure in axial plane (design outlet).

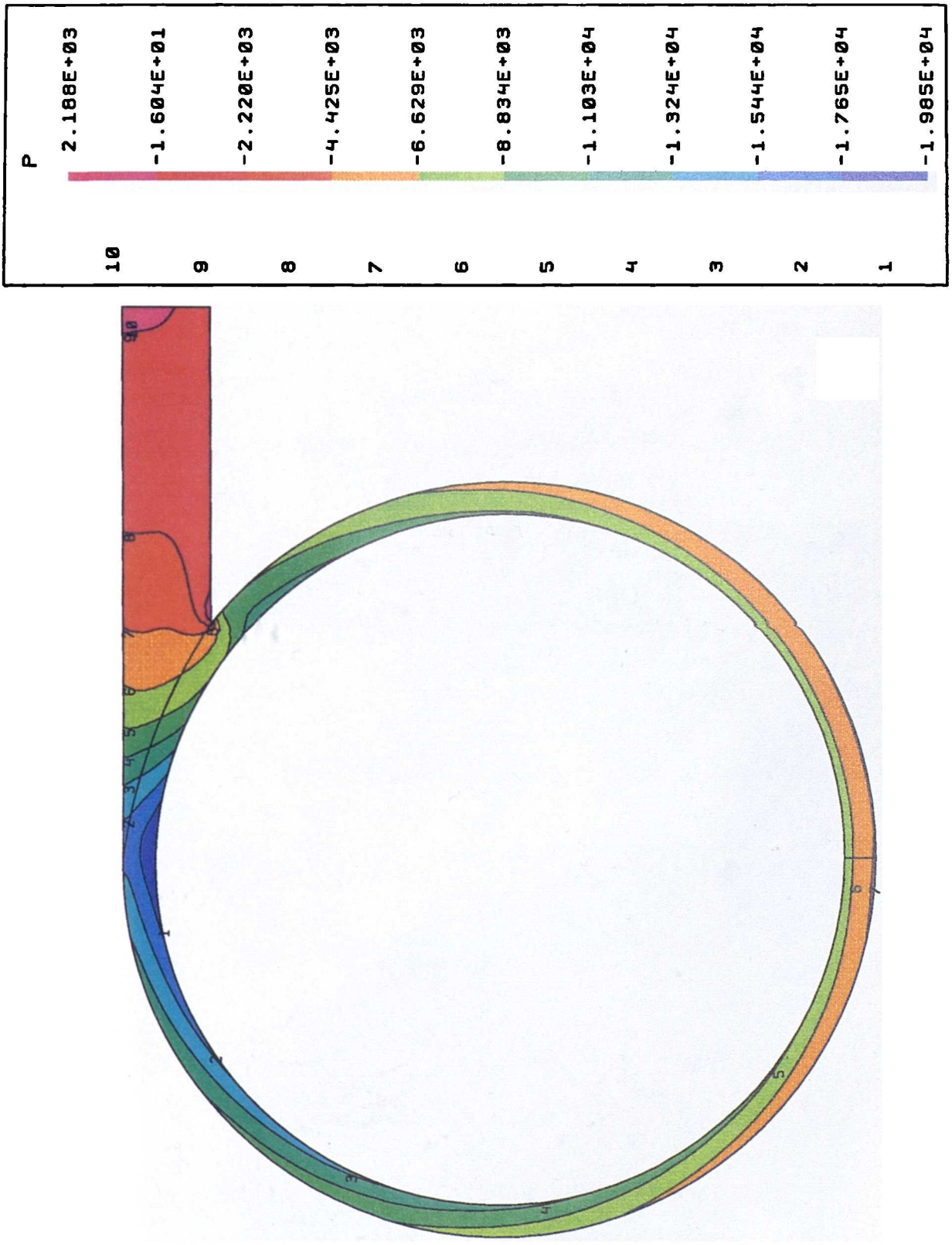

Figure 6.76: Turbulent to molecular viscosity ratio in inlet plane (design outlet).

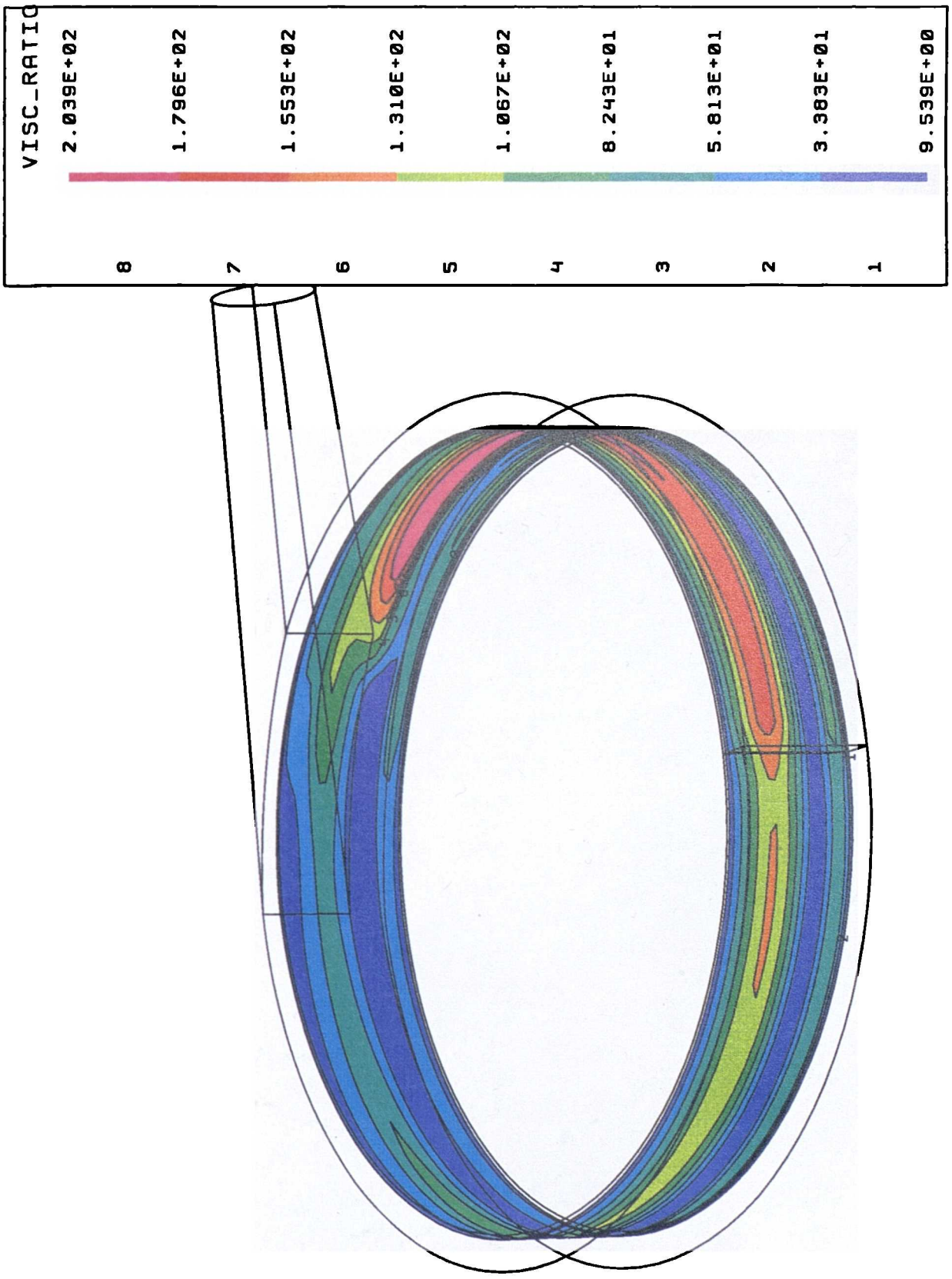

Figure 6.77: Turbulent to molecular viscosity ratio in axial plane (design outlet).

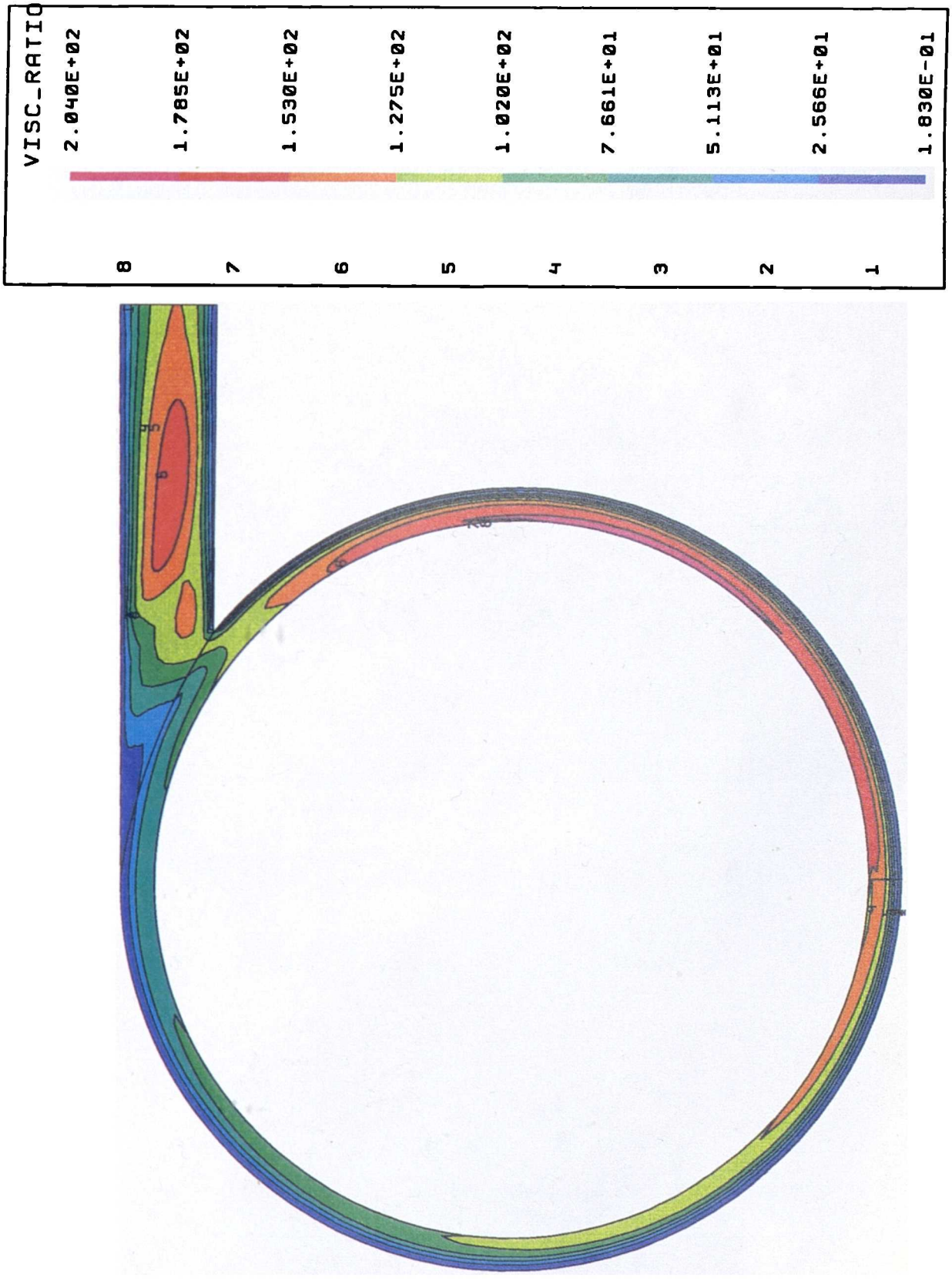

Figure 6.78: Turbulent to molecular viscosity ratio in cross section of outlet port (design outlet).

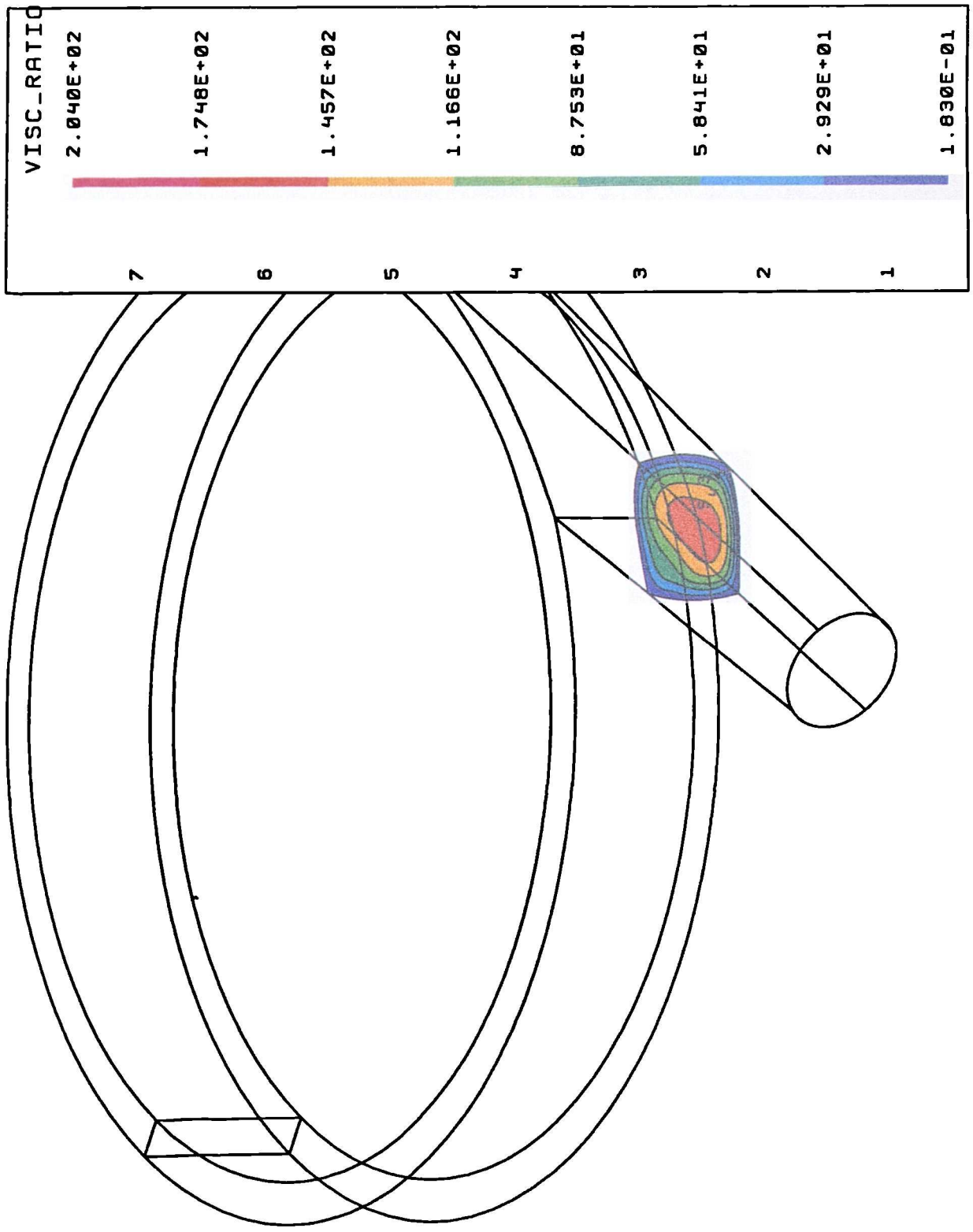

Figure 6.79: Wall shear stress on outer radius wall of outlet port (design outlet).

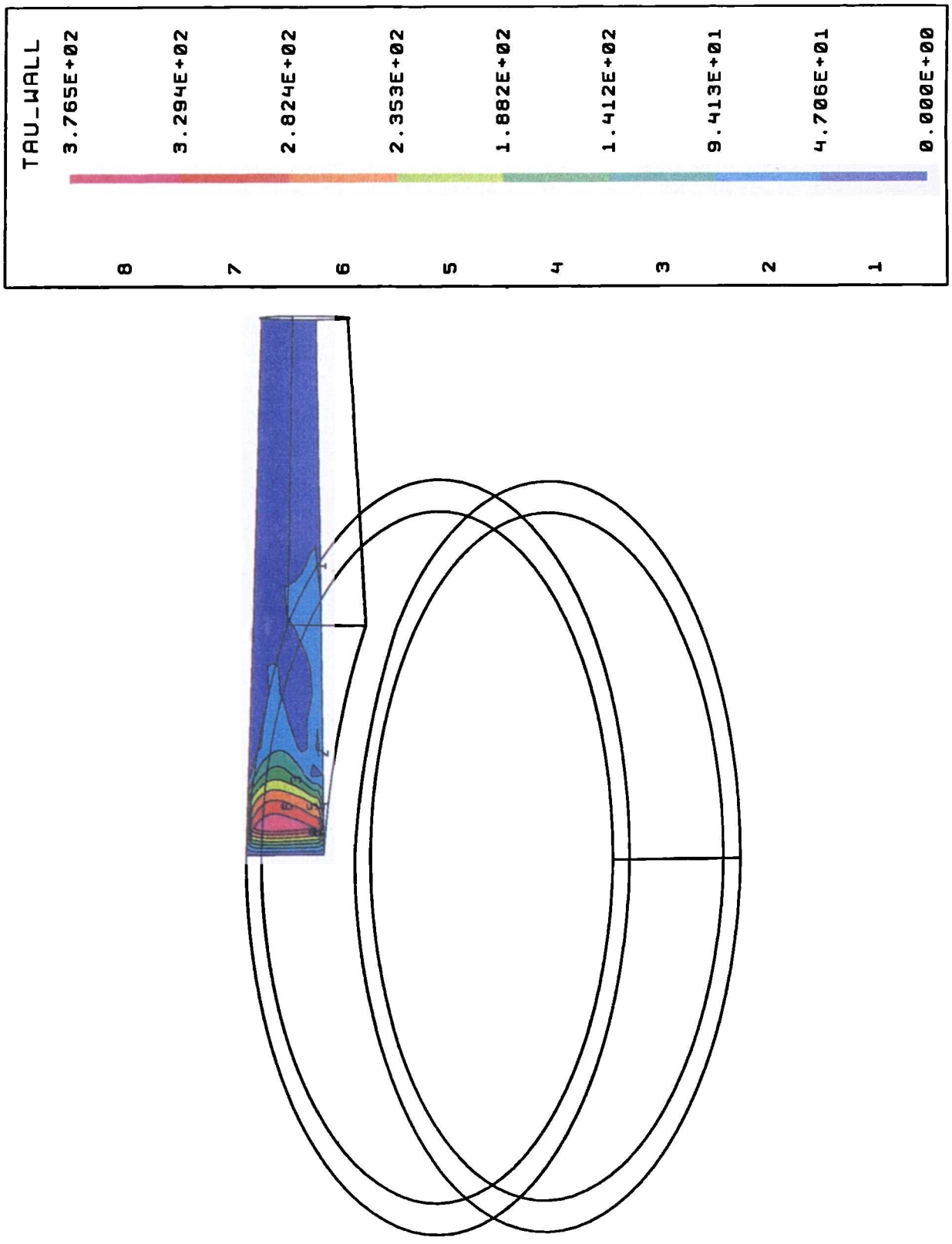

Figure 6.80: Scalar stress in inflow plane (design outlet).

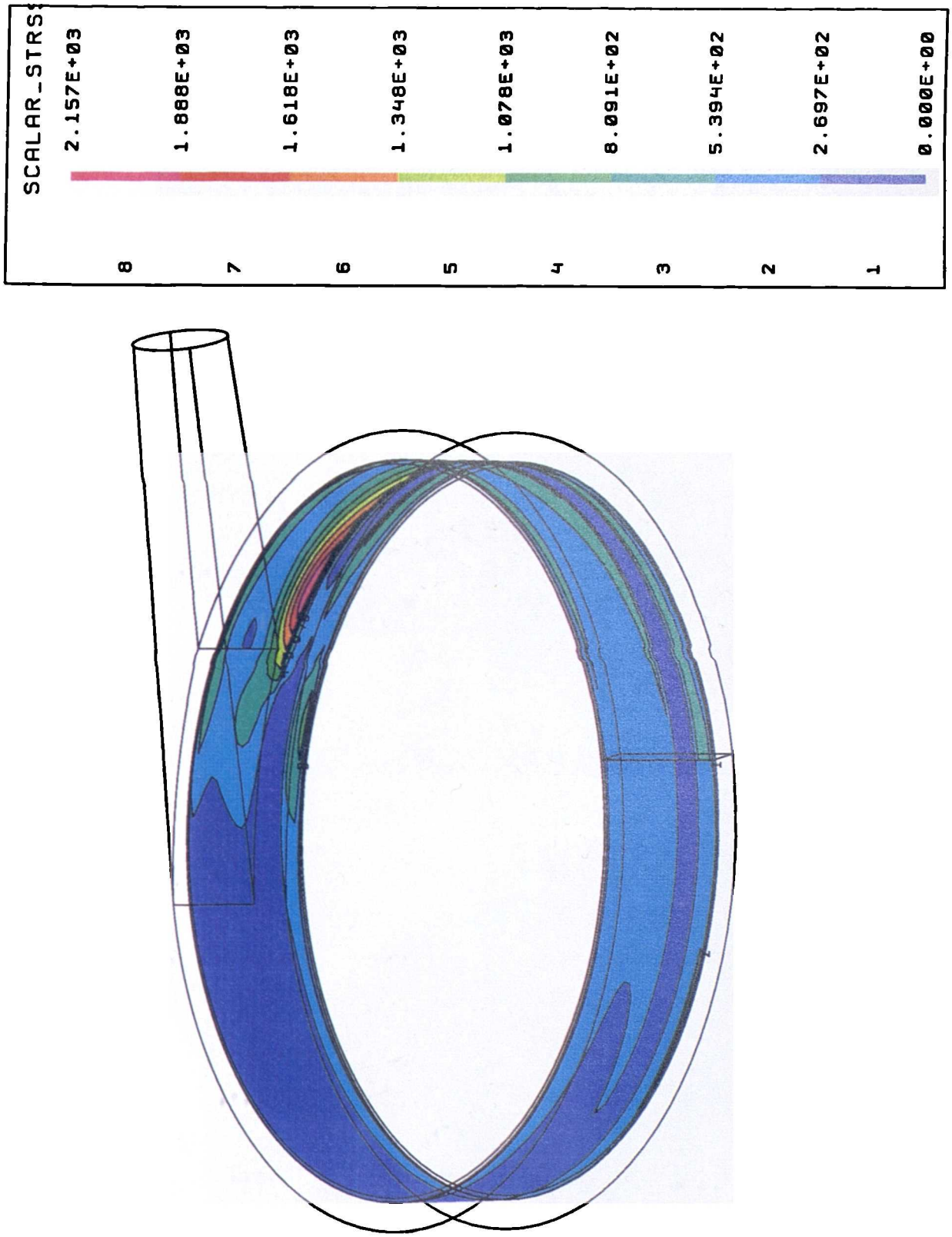

Figure 6.81: Scalar stress in axial plane (design outlet).

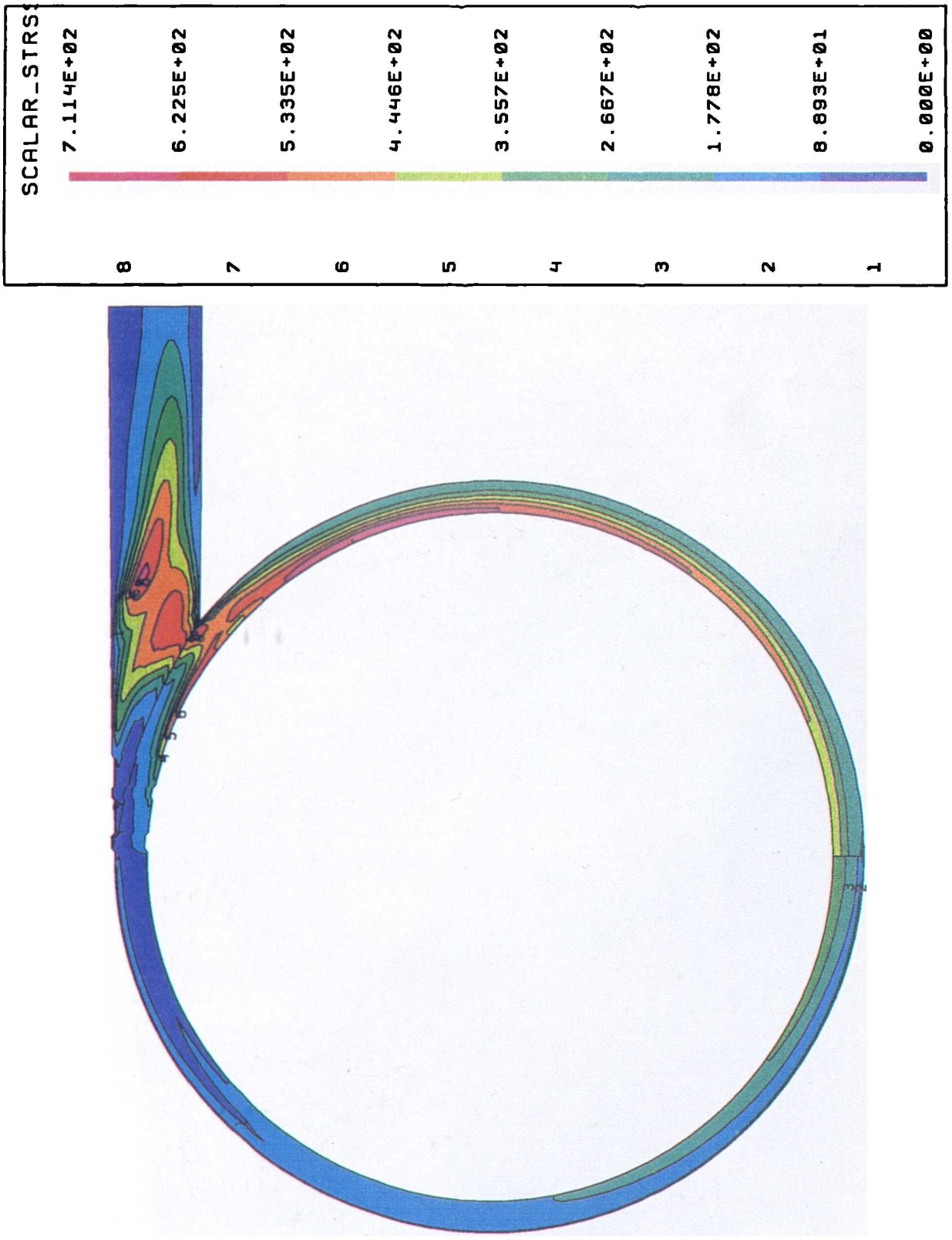

Figure 6.82: Scalar stress in meridional plane of outlet port (design outlet).

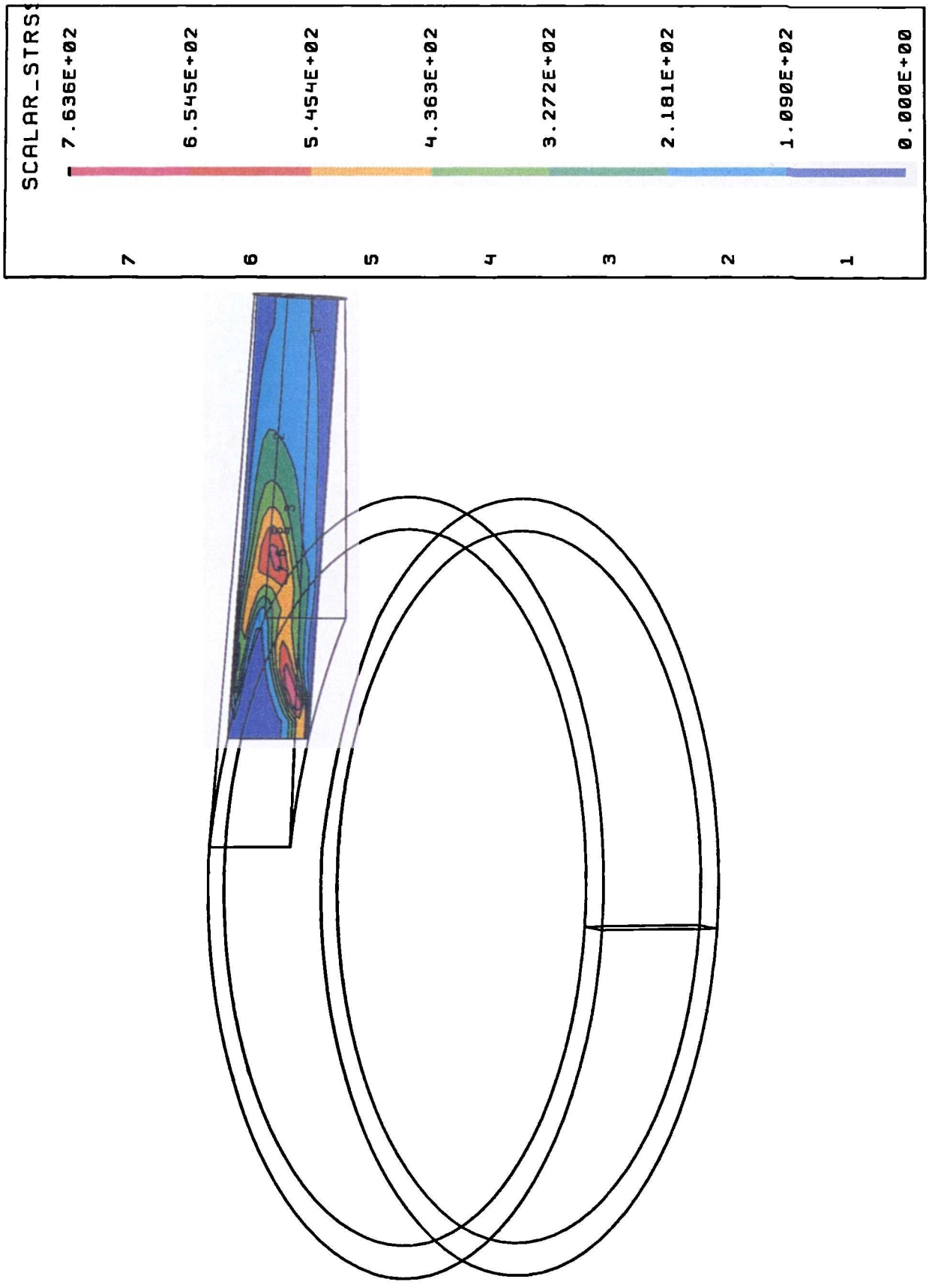

Figure 6.83: Scalar stress in cross-section of beginning outlet port (design outlet).

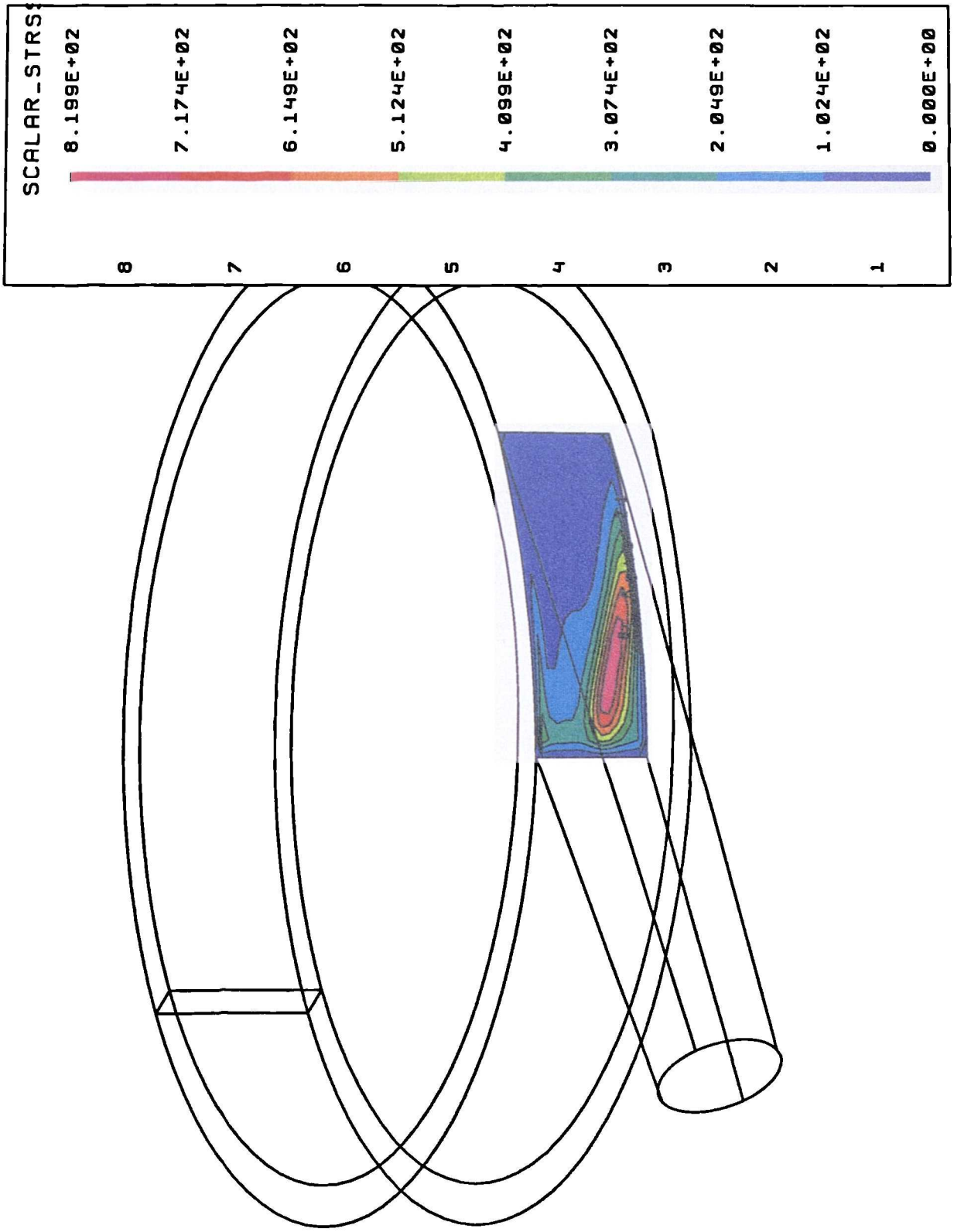

Figure 6.84: Scalar stress in midlength cross-section of outlet port (design outlet).

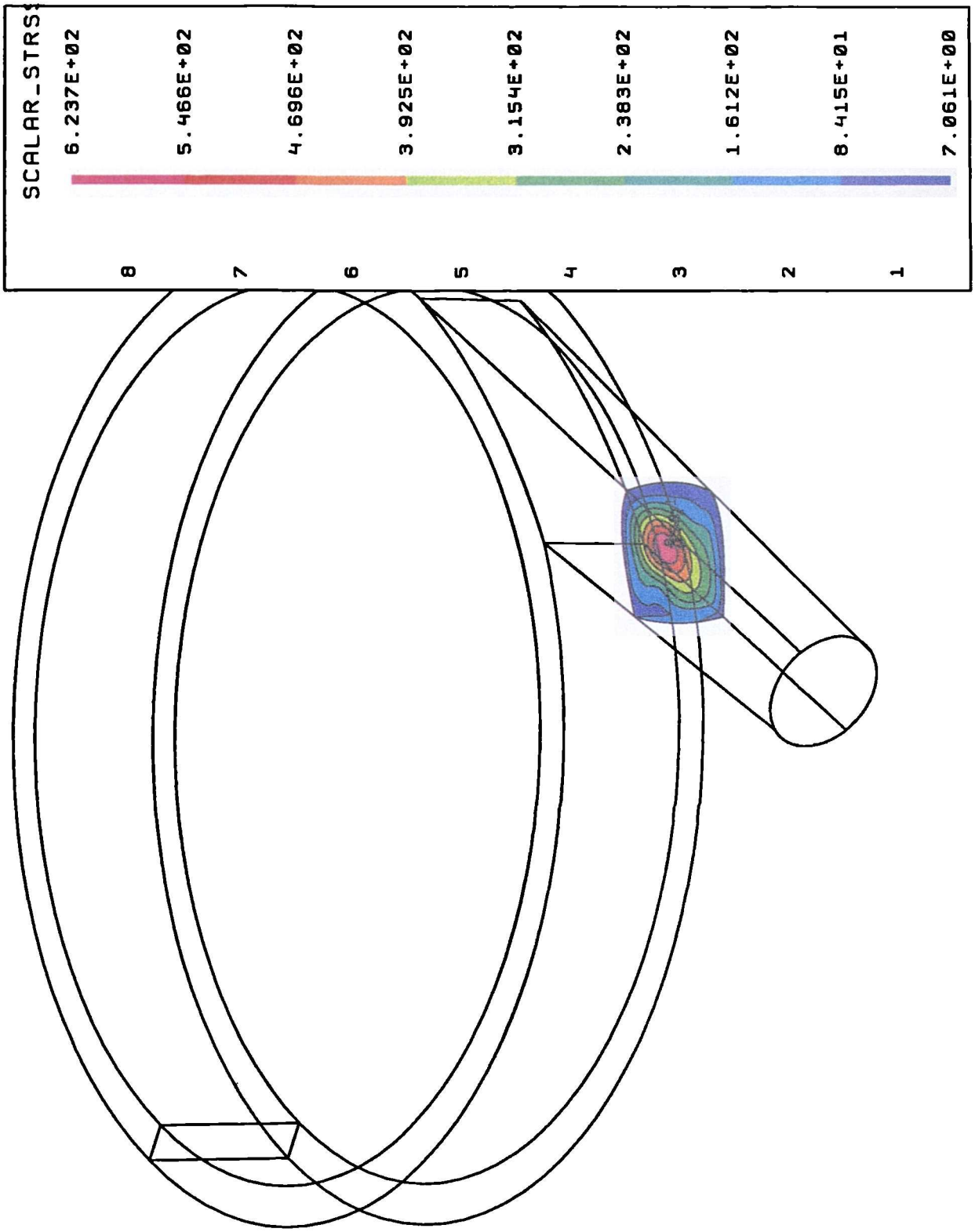

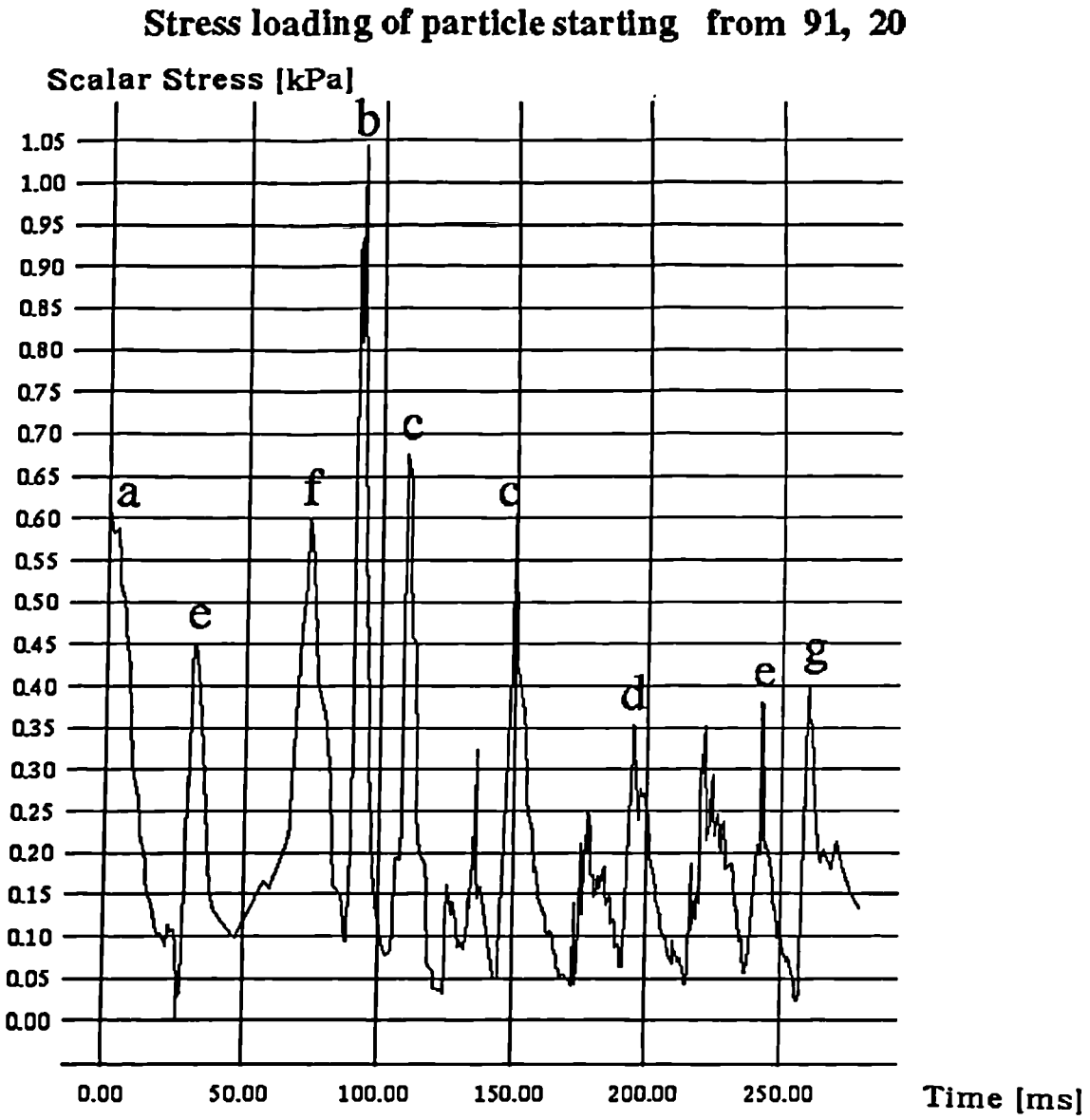

Figure 6.85: Loading-time function for design outlet; Locations: a-inlet (90^0), b-mid gap (45^0), c-near inlet (135^0), d-near inlet (60^0), e-near inlet (240^0), f-first half of outlet port, g-entrance into outlet port.

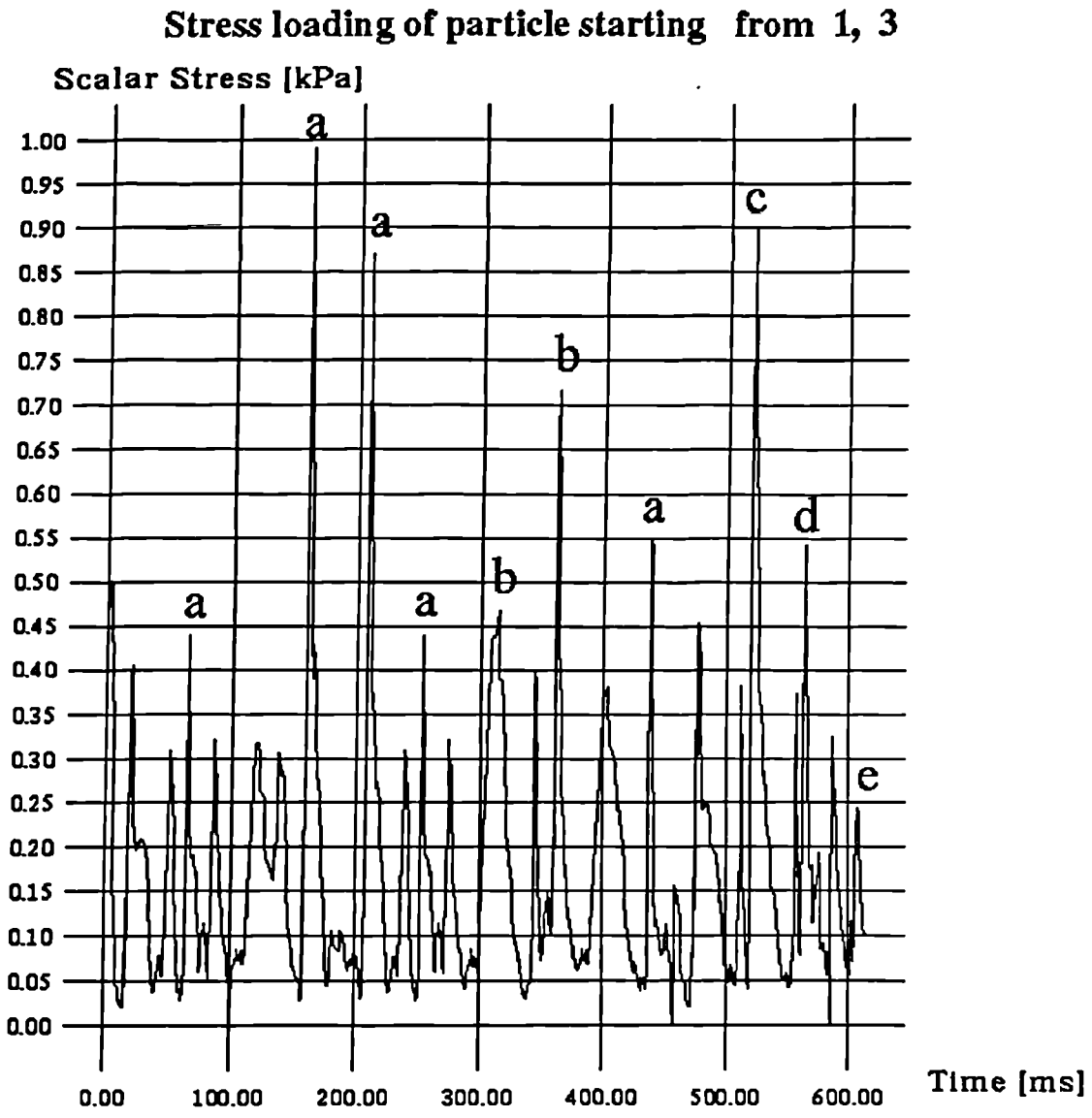

Figure 6.86: Loading-time function for design outlet; Locations: a-mid gap (45^0), b-near inlet (150^0), c-near inlet (45^0), d-near inlet (210^0), e-second half of outlet port.

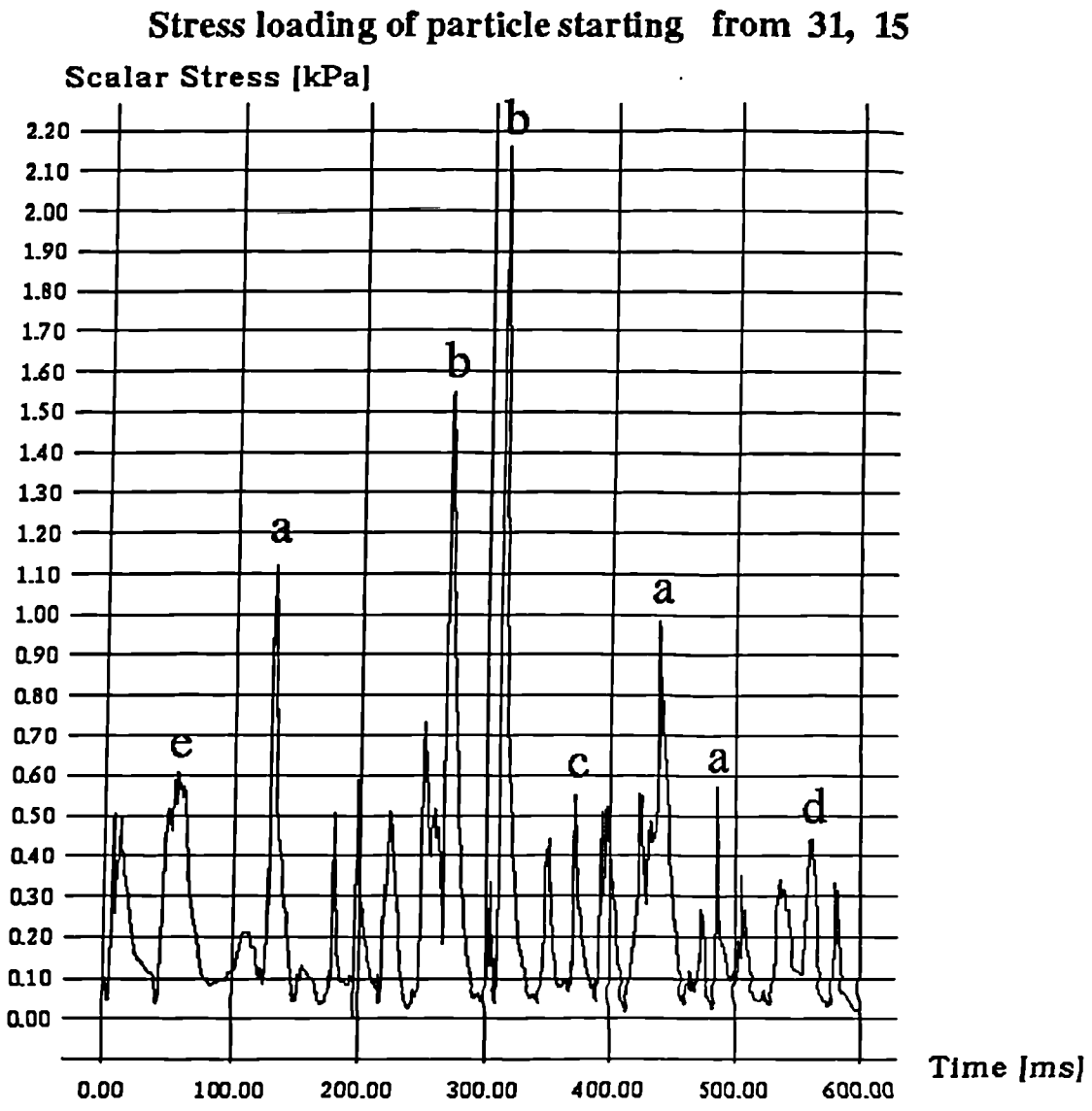

Figure 6.87: Loading-time function for design outlet; Locations: a-mid gap (45^0), b-near inlet (60^0), c-near inlet (70^0), d-near inlet (210^0), e-first half of outlet port.

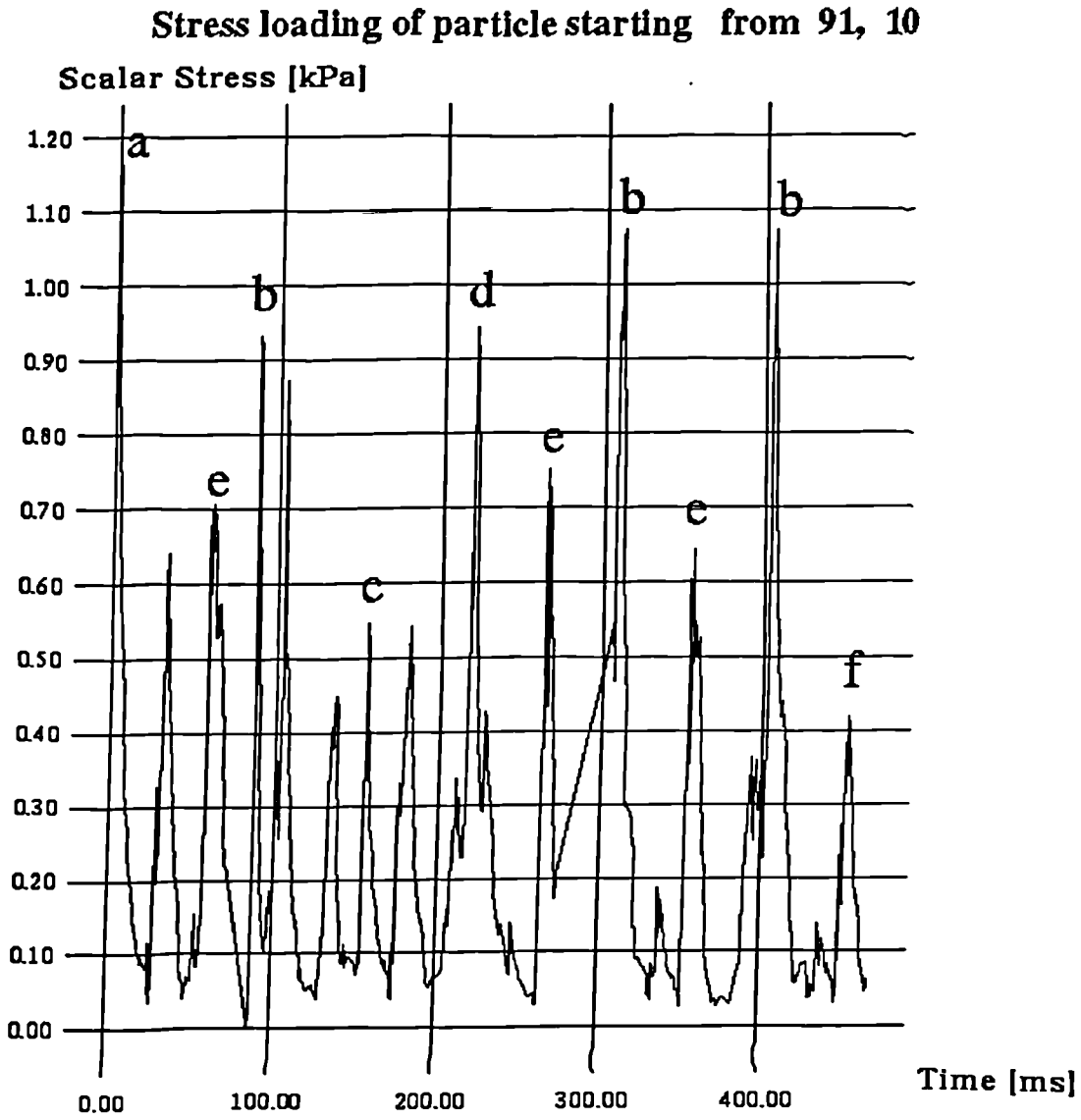

Figure 6.88: Loading-time function for design outlet; Locations: a-inlet (90^0), b-mid gap (45^0), c-near inlet (70^0), d-outer radius (45^0), e-inflow into outlet port, f-first half of outlet port.

at the transition from the annular gap to the outlet port at the outer radius (Fig 6.79). They are, however, of little significance for the comparative scalar stresses. The latter have their maximum of approximately 2.2 kPa at the inflow location where also the highest viscosity ratio was predicted (Fig 6.80). Concentrations of high scalar stresses and local maxima in the order of 700 Pa can be found in various parts of the circular outflow domain, depicted in Fig 6.81, and various cross sections of the outlet port (Figs 6.82 to 6.84).

Stress loading-time functions of fluid particles were determined on the basis of 3D-flow streaklines starting at various inlet positions similarly to those for the impeller flow calculations. Locations of maxima are given in angular position clockwise starting from the transition into the outlet port at the outer radius (x=0), see Fig 6.67. The graphs of stress functions, in Figs 6.85 to 6.88, revealed a highly fluctuating pattern. Frequent changes between maxima and minima which are both of a fairly uniform magnitude can be observed. These findings can be explained by the high velocities and a directed flow in the impeller-casing gap. Strong flow disturbances in the outlet port are predicted with backflow into the impeller-casing domain which as shown in Figs 6.85 and 6.87.

b) Spiral Volute

The velocity distribution in the spiral volute shows remarkable differences to that in the design outlet geometry. Due to the cross-sectional widening of the spiral part, the mean cross-sectional velocity slightly decreases (Fig 6.89). The flow into the diffuser occurs without a sudden velocity reduction. The diffuser geometry itself leads to a gentle decrease of speed downstream with a nearly axis-symmetric flow pattern (Figs 6.90 to 6.92).

Pressure rise and therefore hydraulic performance were drastically increased by the changed geometry. Whilst uniformity of the pressure distribution around the impeller discharge radius is desirable, this is not achieved with that particular spiral volute (Fig 6.93). A comparison of the static pressure distribution along this radius related to the overall outlet pressure head for the two geometries is shown in Fig 6.100. Considerable differences between the flow field in both

Figure 6.89: Velocity distribution in axial plane (spiral volute outlet).

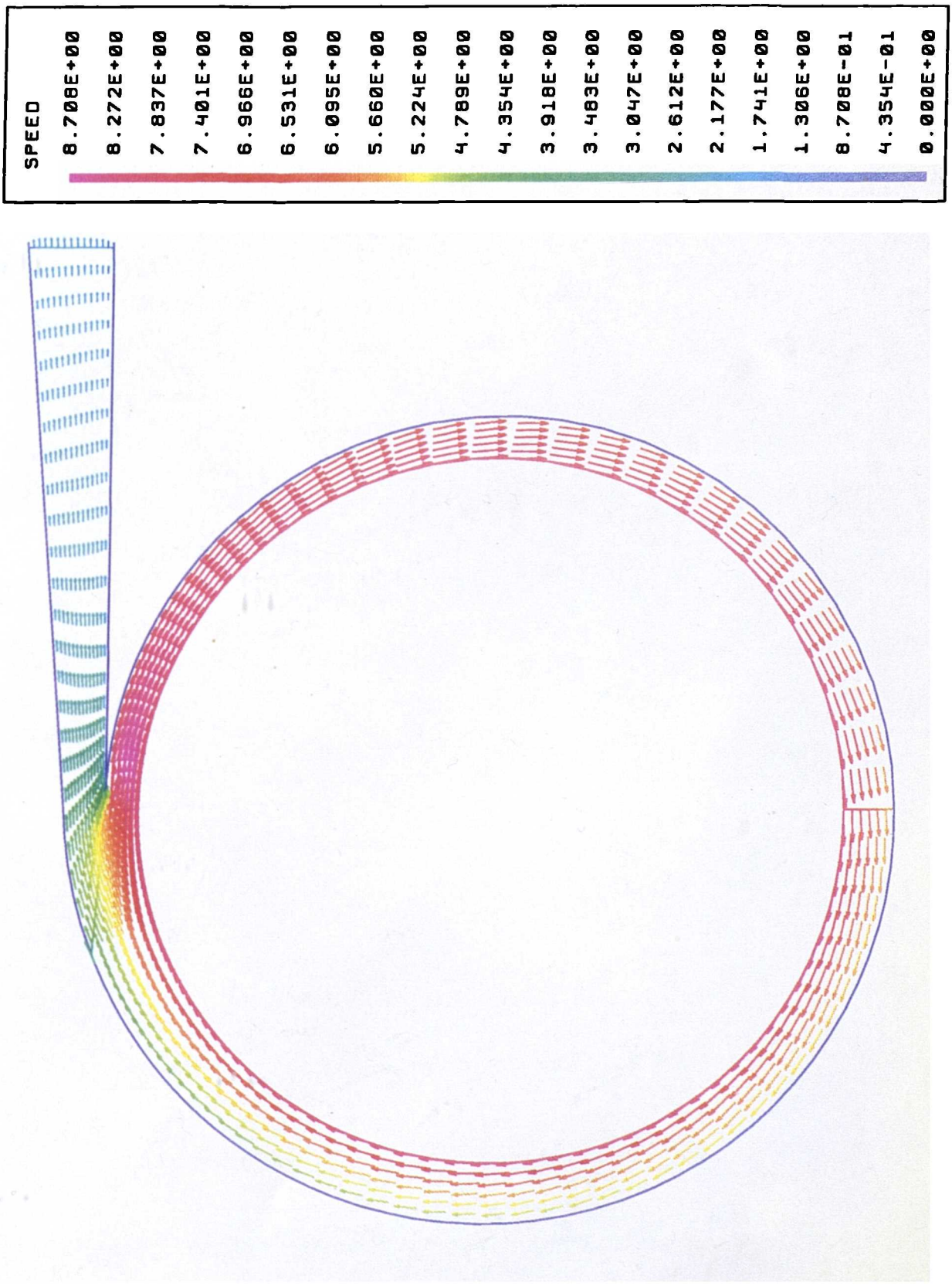

Figure 6.90: Velocity distribution in meridional plane of diffuser (spiral volute outlet).

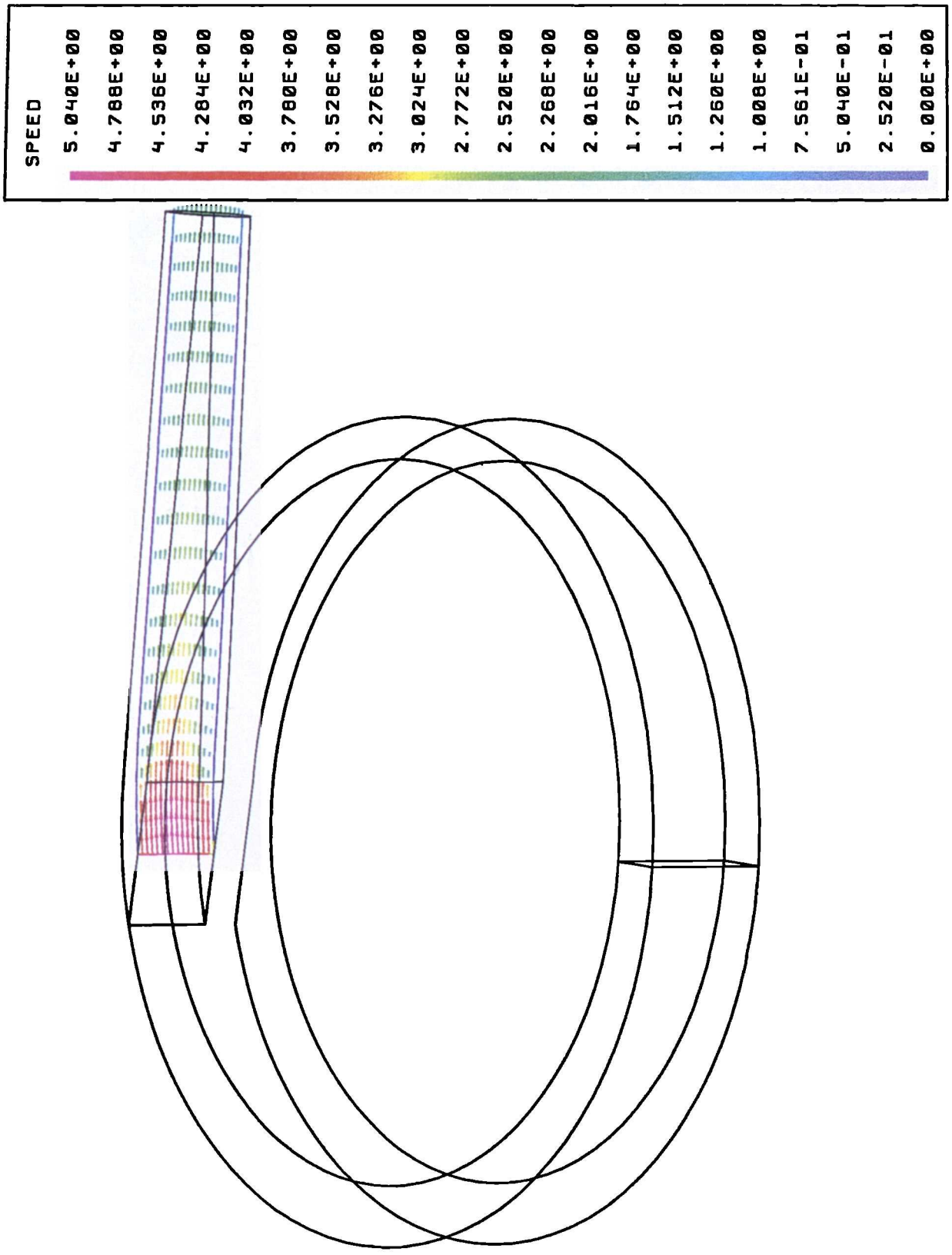

Figure 6.91: Velocity distribution in beginning cross section of diffuser (spiral volute outlet).

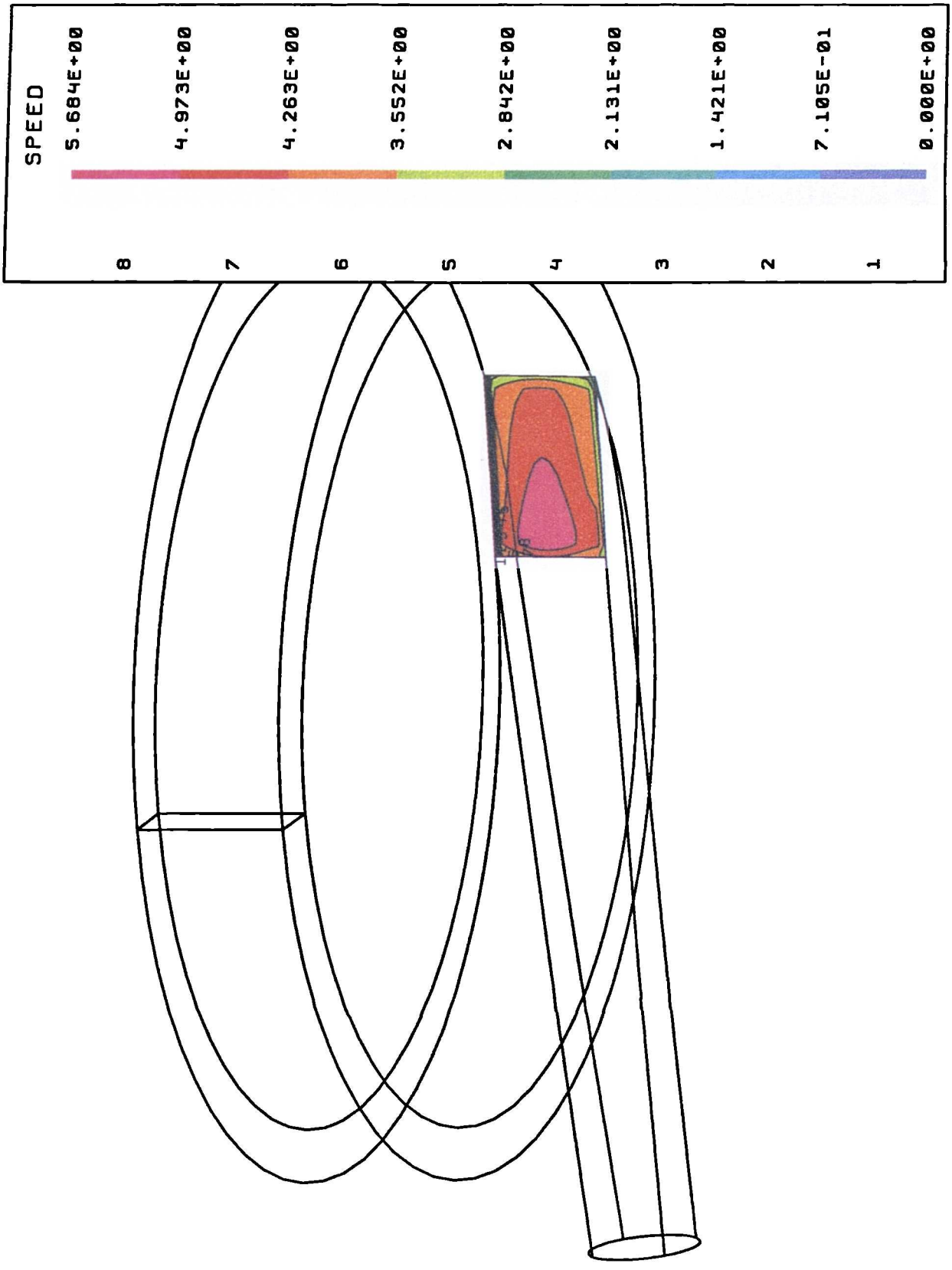

Figure 6.92: Velocity distribution in end cross section of diffuser (spiral volute outlet).

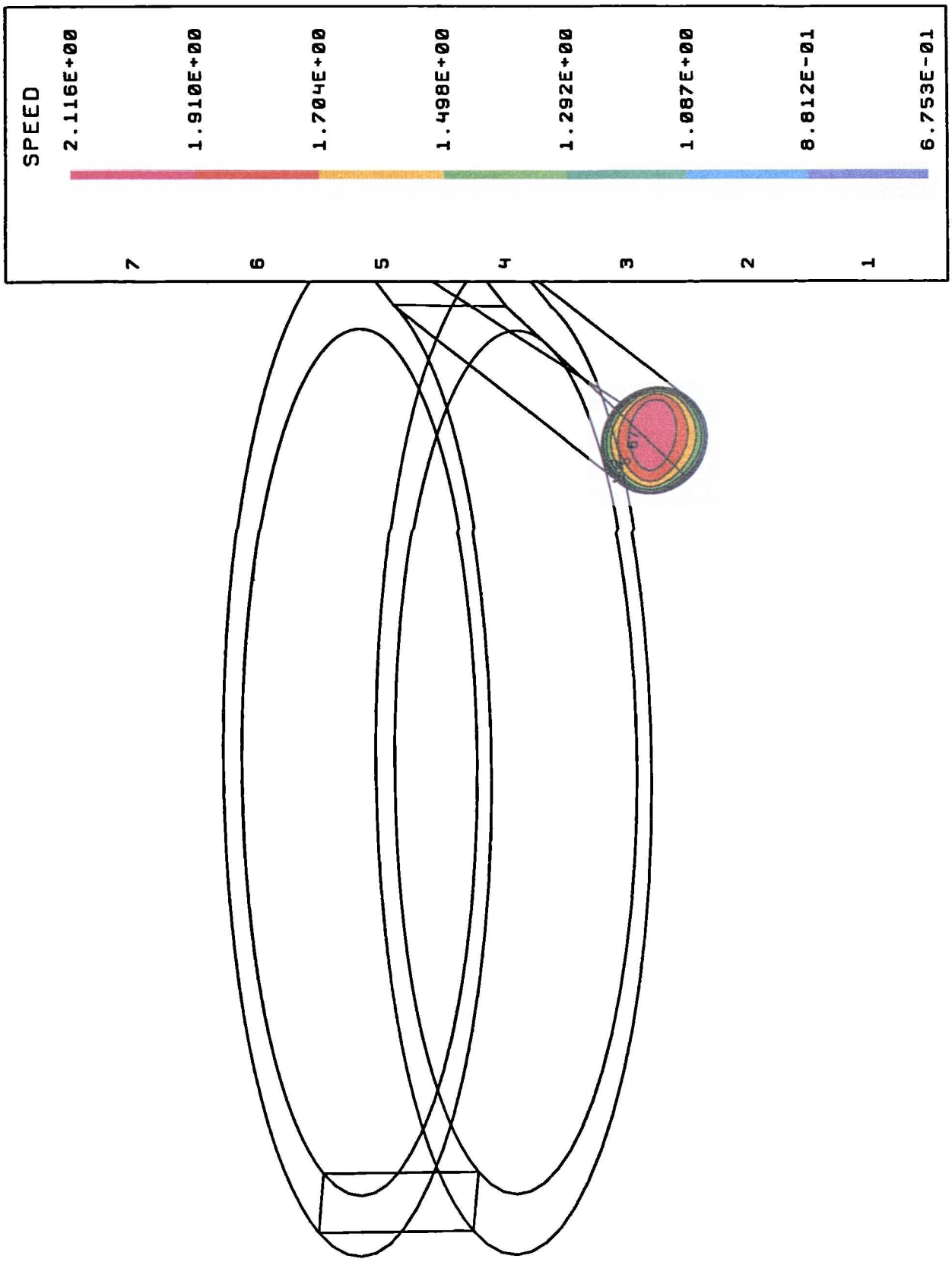

Figure 6.93: Static pressure in axial plane (spiral volute outlet).

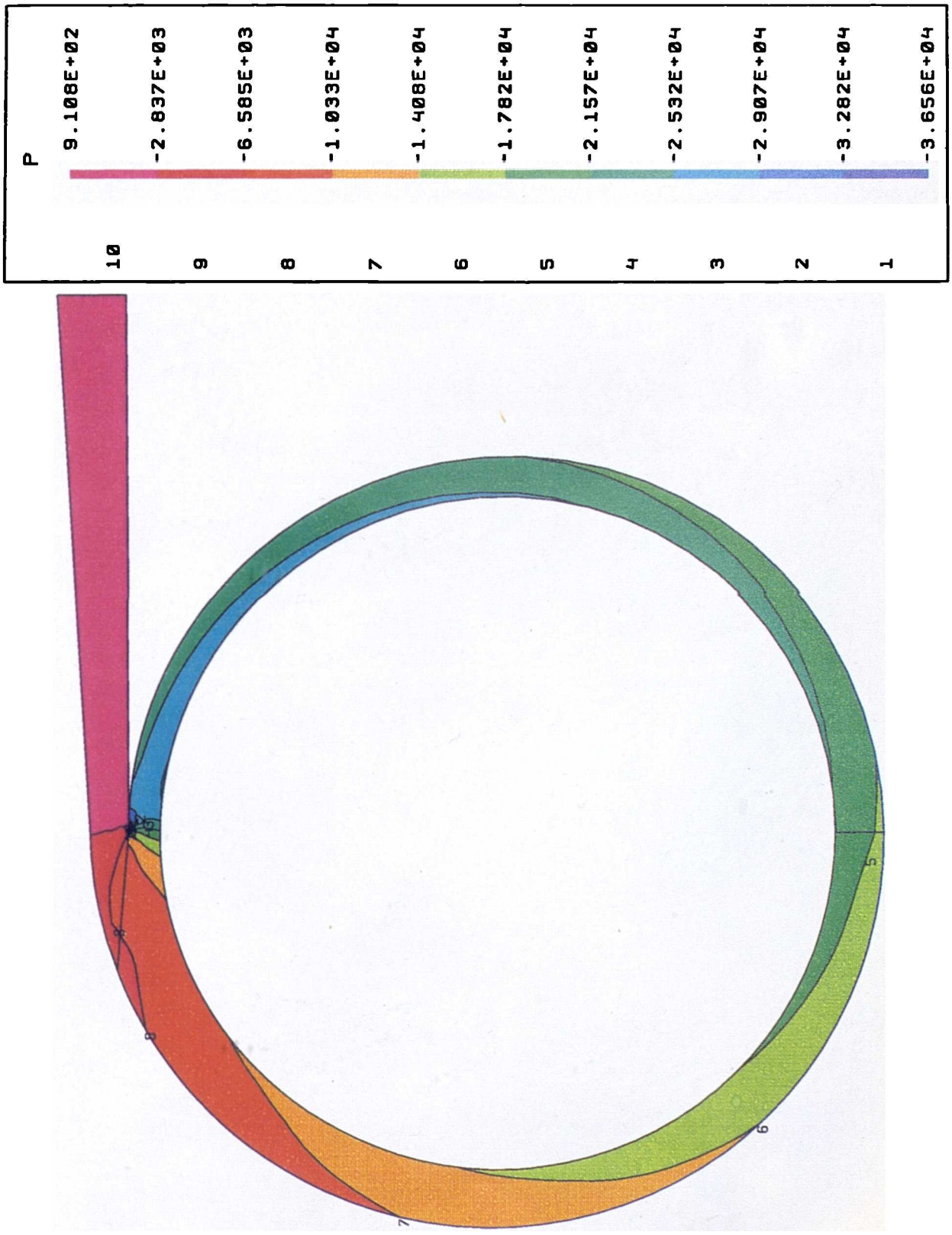

Figure 6.94: Turbulent to molecular viscosity ratio in axial plane (spiral volute outlet).

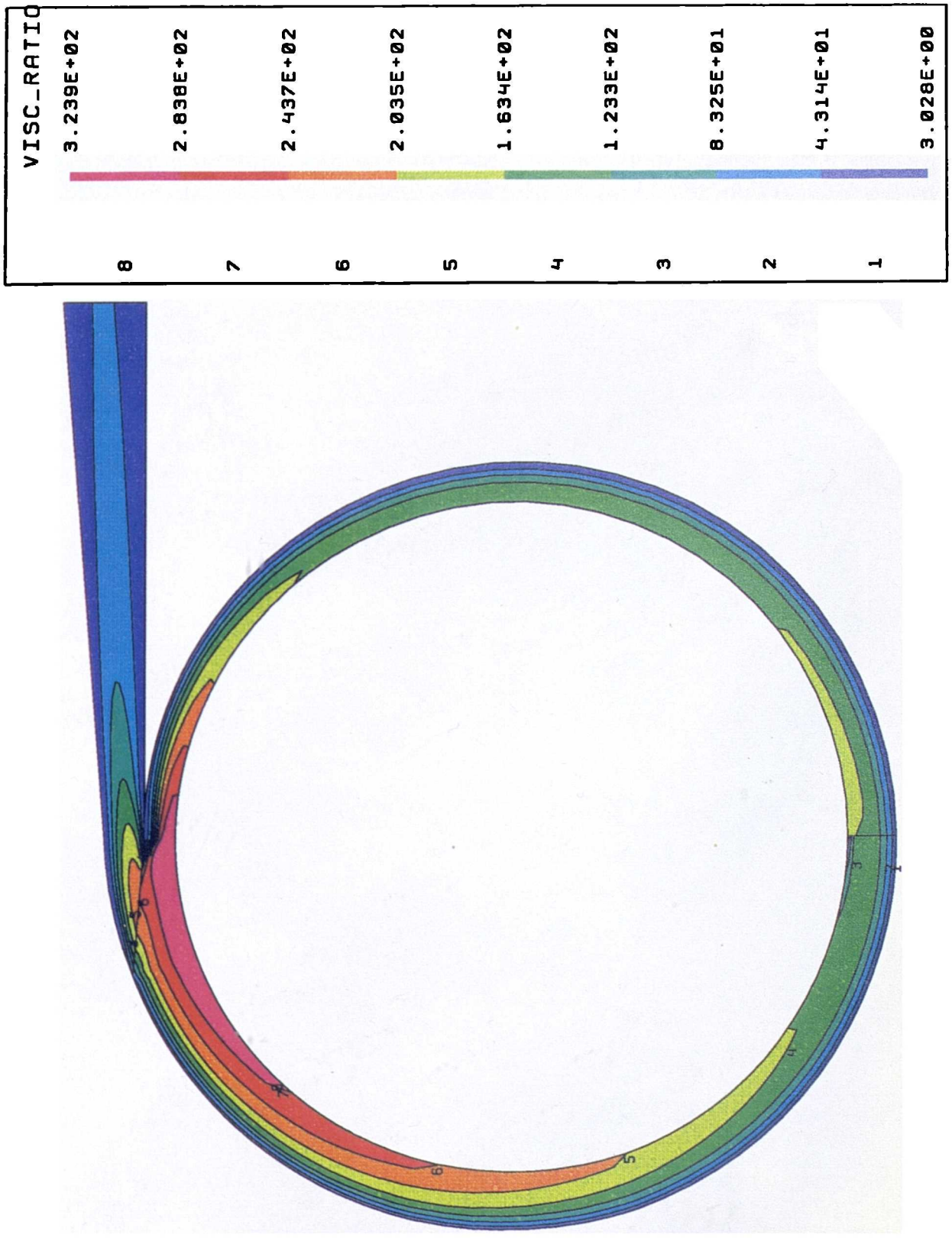

Figure 6.95: Wall shear stress at inner radius wall of diffuser (spiral volute outlet).

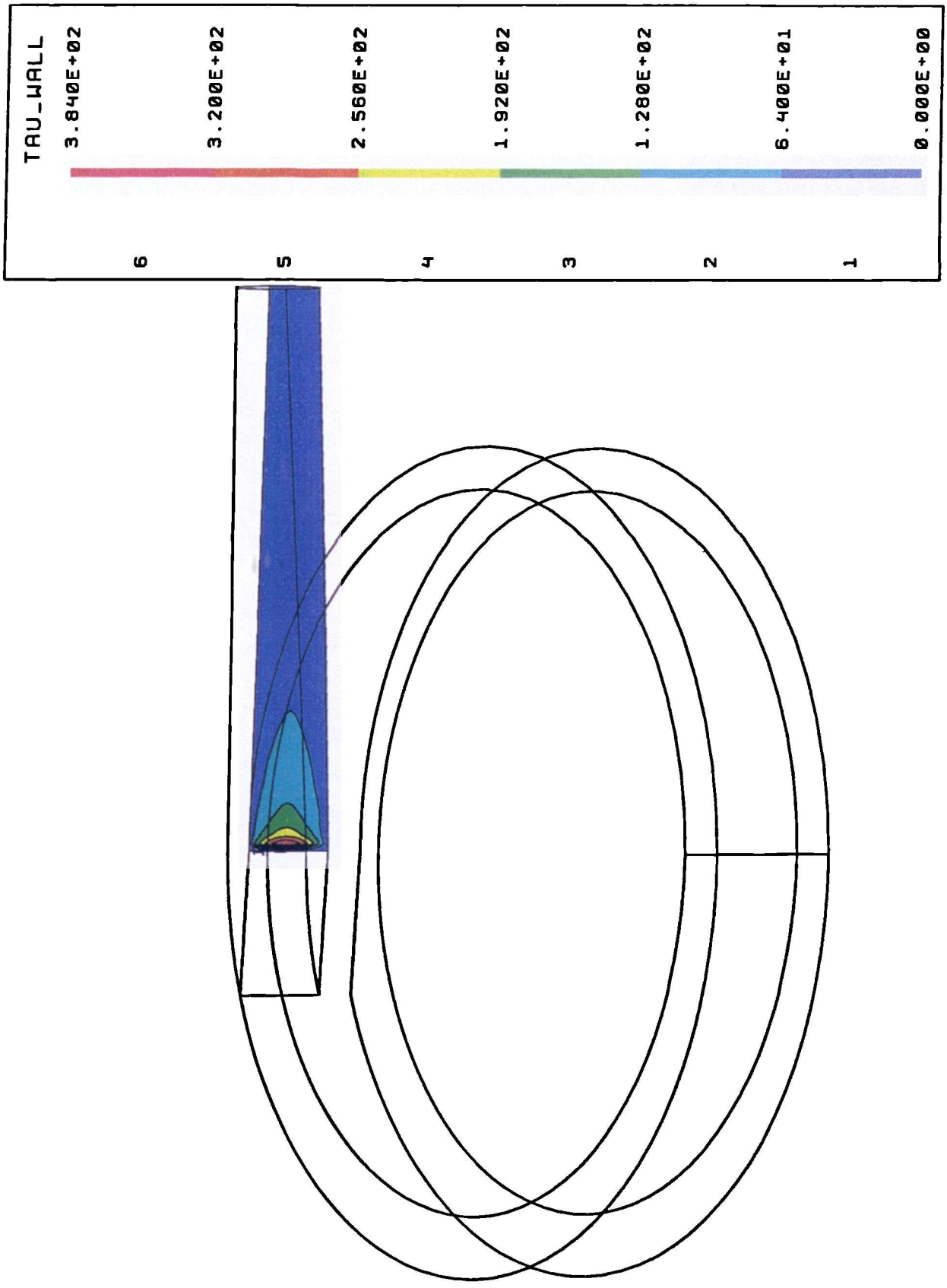

Figure 6.96: Scalar stress in inlet plane (spiral volute outlet).

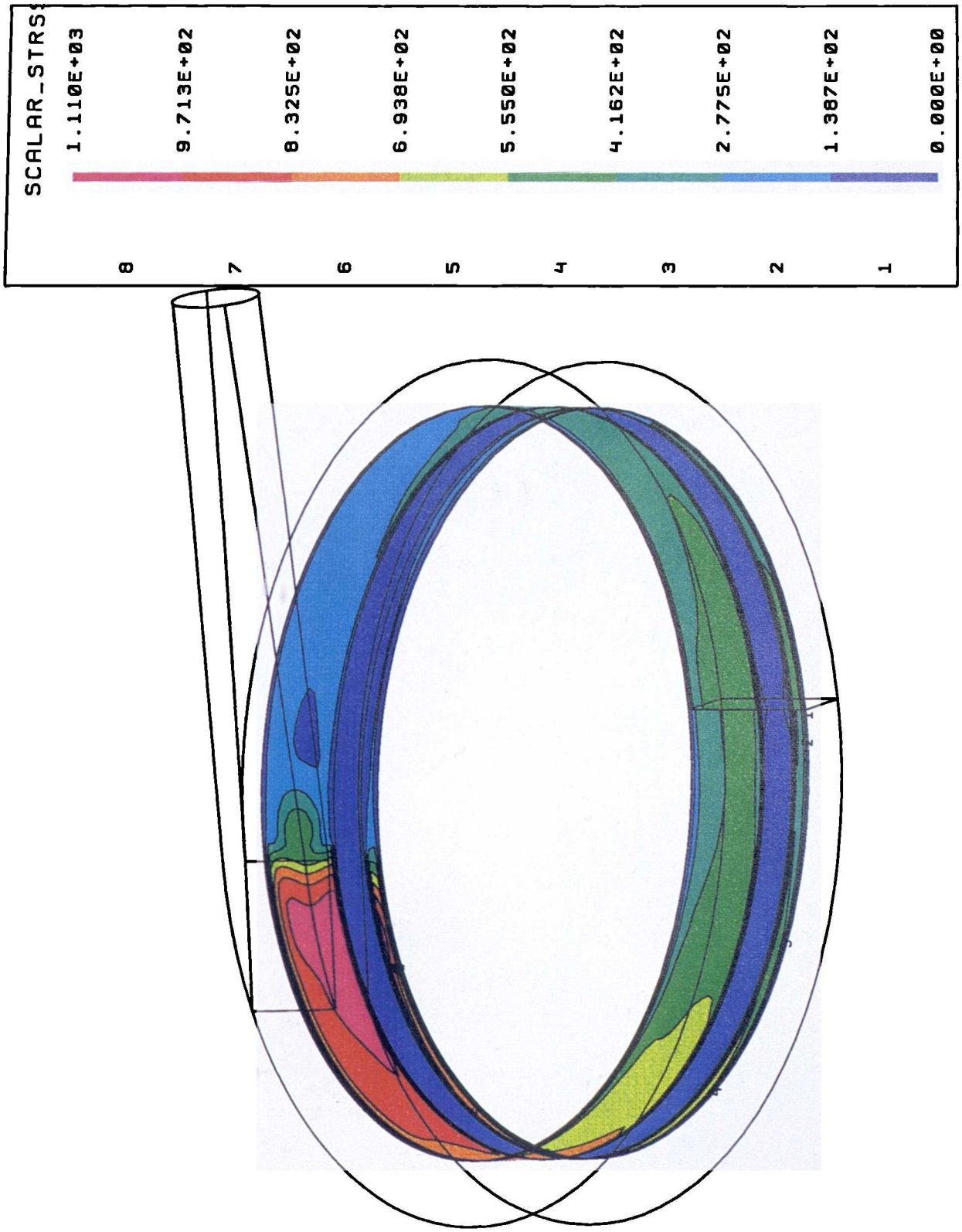

Figure 6.97: Scalar stress in axial plane (spiral volute outlet).

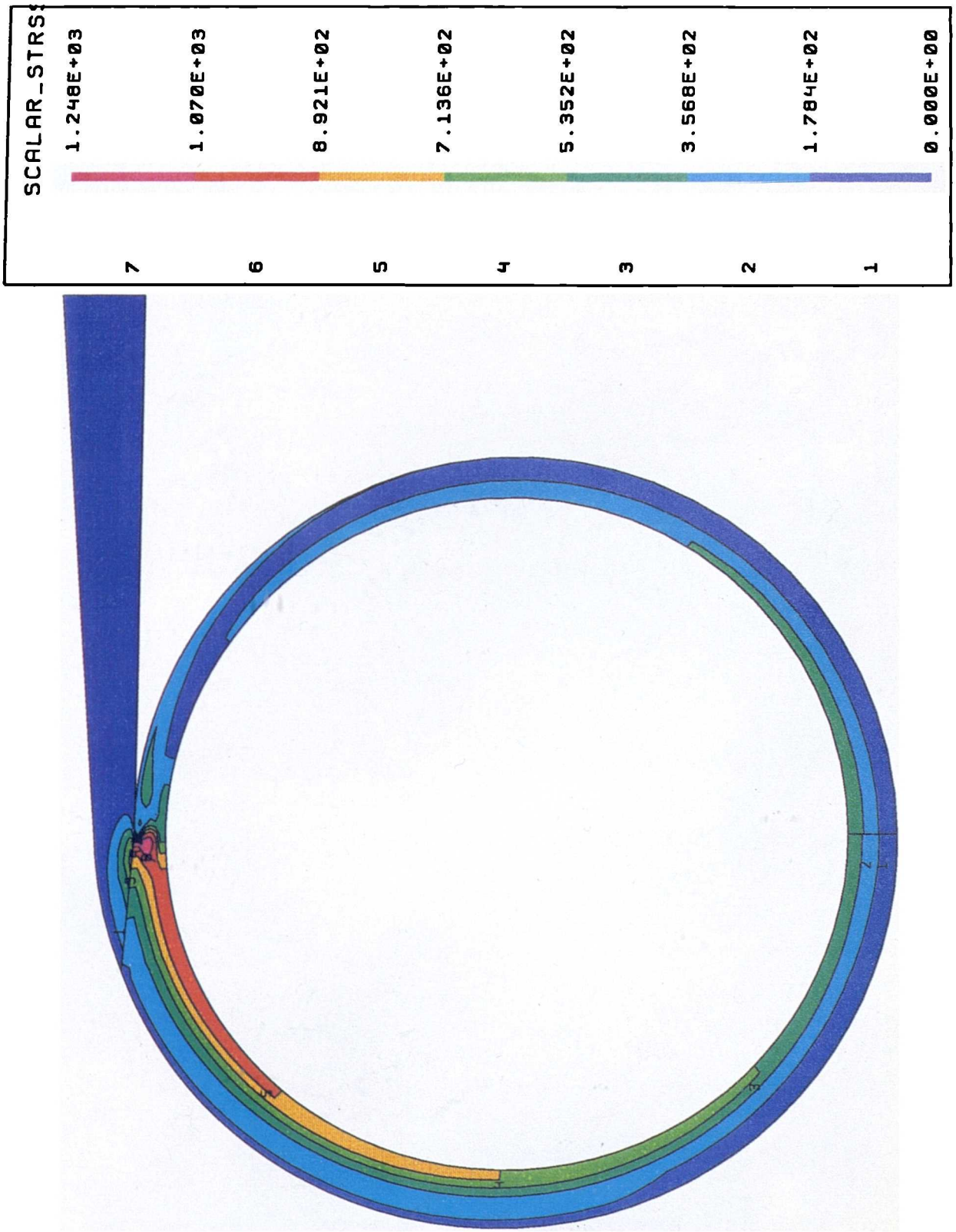

Figure 6.98: Scalar stress in meridional plane of diffuser (spiral volute outlet).

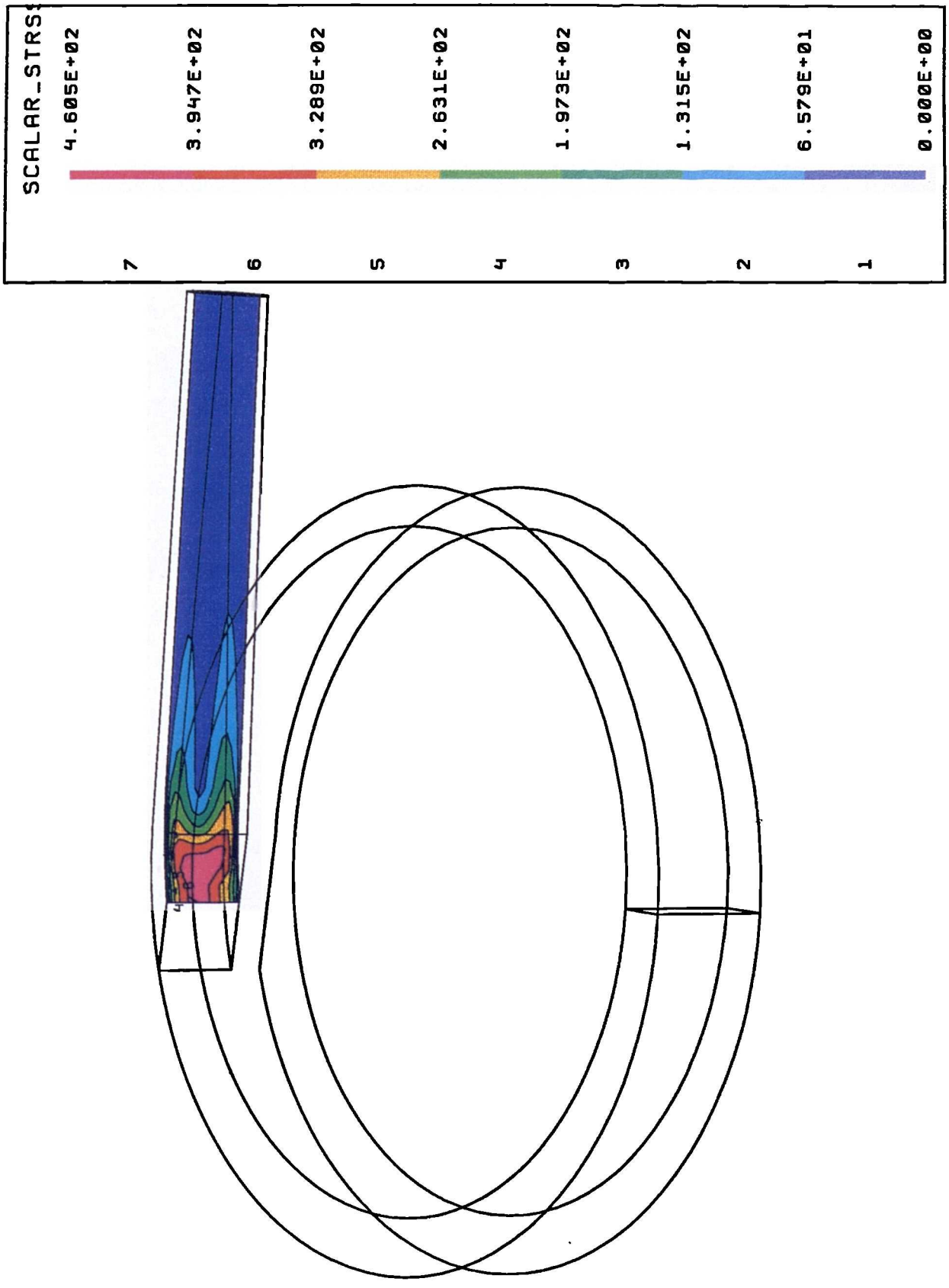

Figure 6.99: Scalar stress in midlength cross section of diffuser (spiral volute outlet).

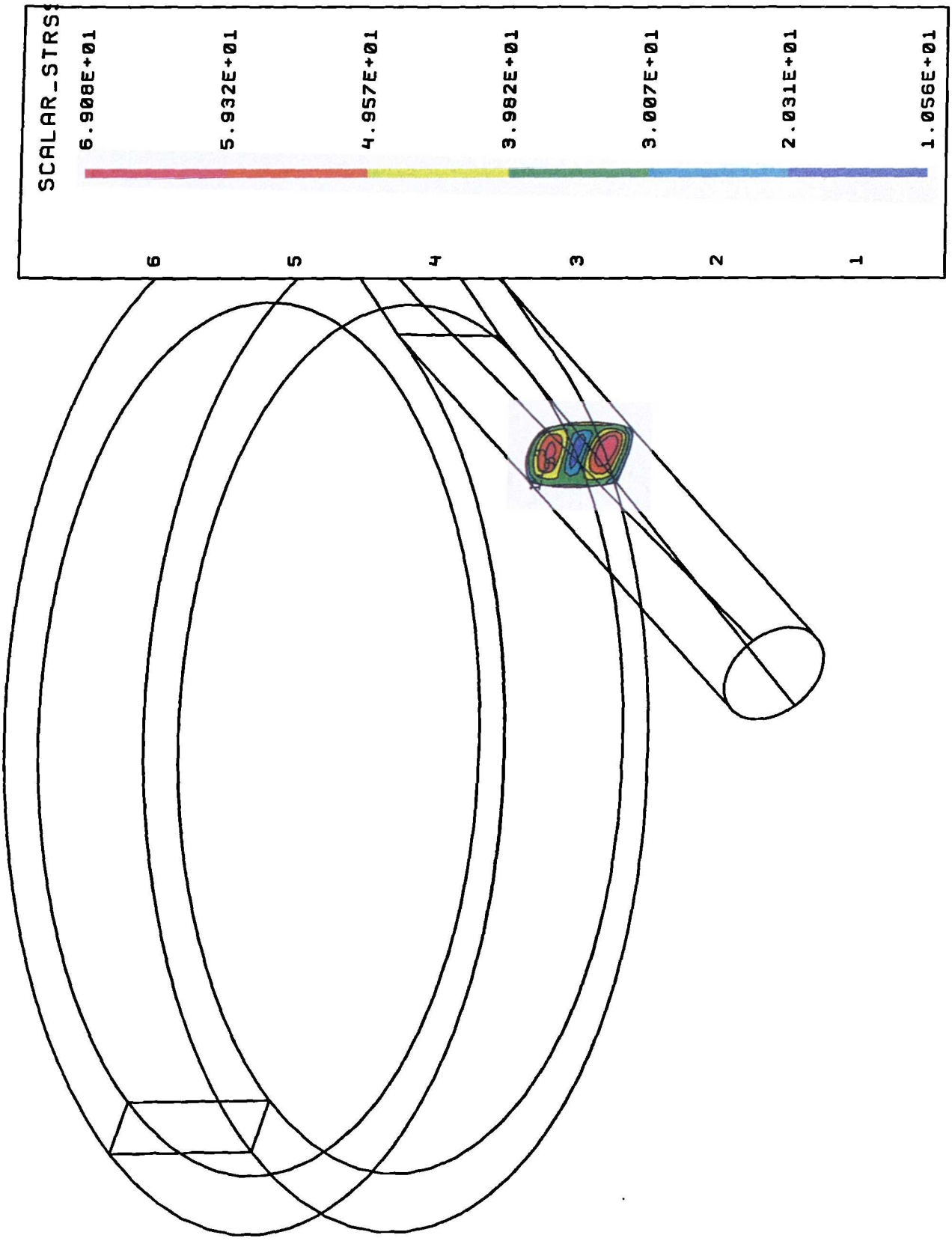

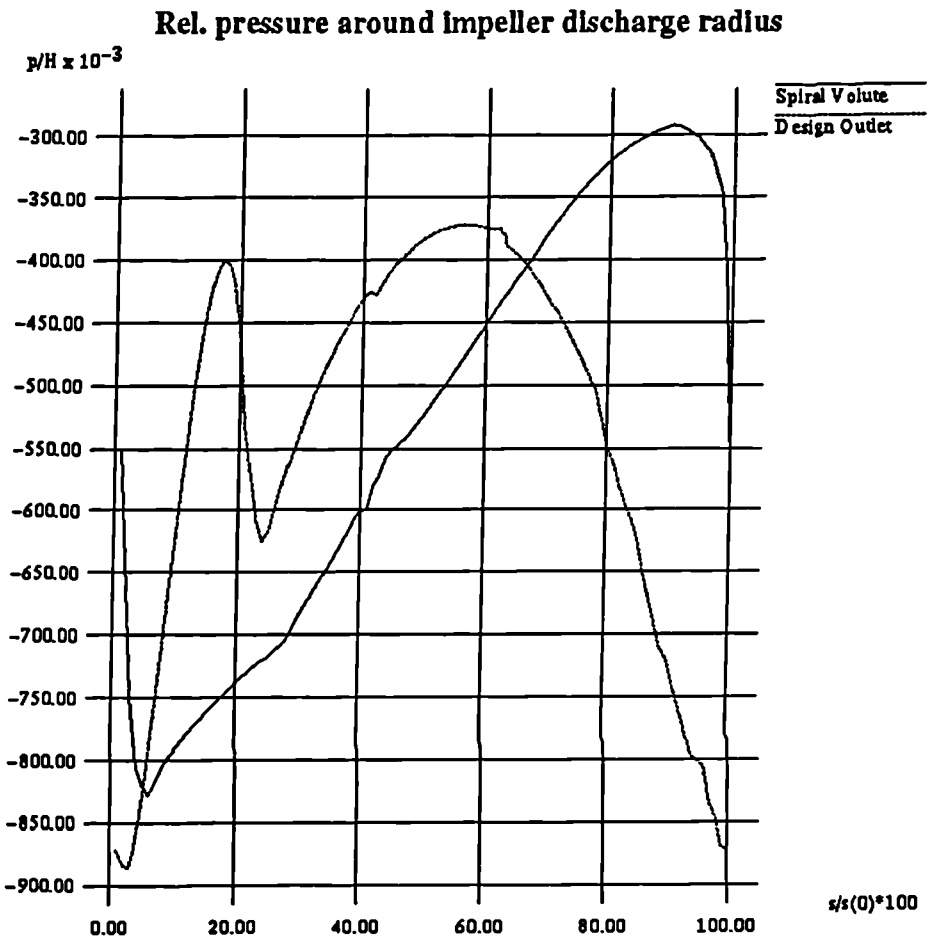

Figure 6.100: Static pressure related to the overall pressure head along the impeller discharge radius for design outlet and spiral volute.

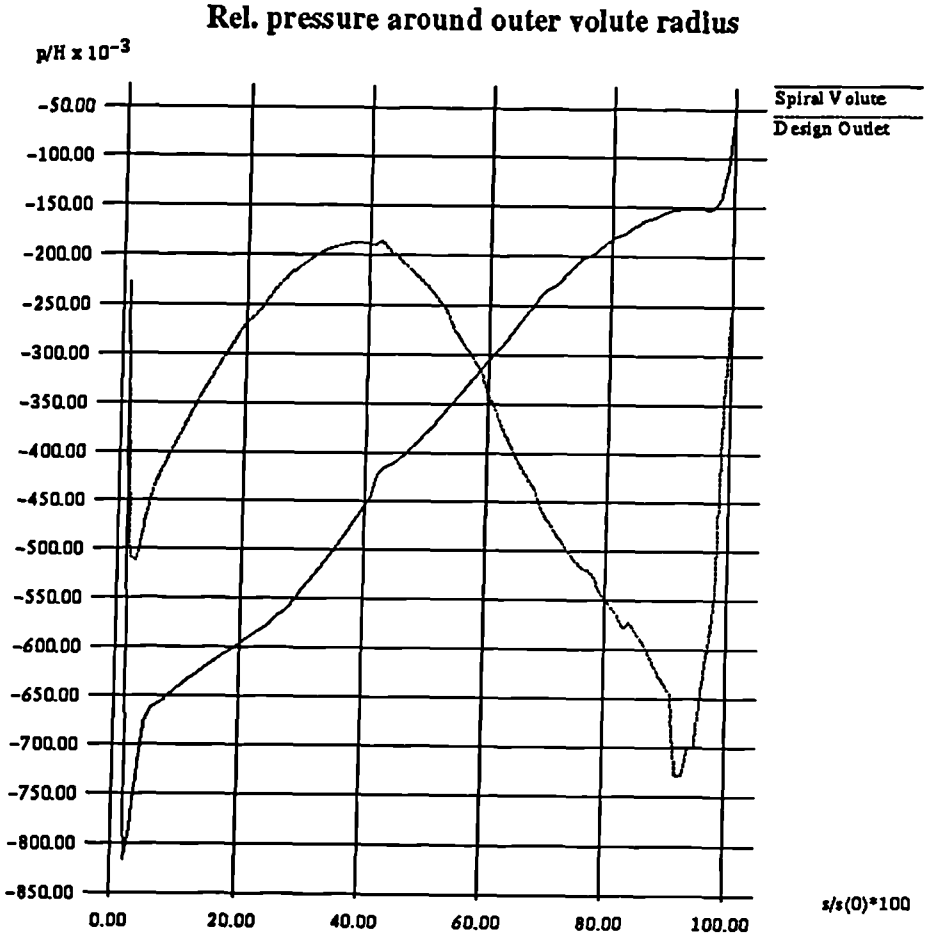

Figure 6.101: Static pressure related to the overall pressure head along the outer radius of the volute for design outlet and spiral volute.

outlet forms is revealed by the respective static pressure distributions along the outer radius of the volute in Fig 6.101.

The viscosity ratio was highest at the inlet domain where the spiral volute has its almost largest outer radius. The maximum turbulent viscosity is higher than for the design case, but turbulence is absent in the diffuser region (Fig 6.94). Wall shear stresses were highest at the diffuser tongue (Fig 6.95).

The significant parameter for mechanical loading assessment , the scalar stress, is reduced in the volute design to maximum values of approximately 1.1 kPa. These occurred at the inner radius of the end section (Figs 6.96 and 6.97). At the entrance into the diffuser scalar stresses values are in the order of 750 Pa, but decrease rapidly (Figs 6.97 to 6.99).

Stress-time functions for particles passing the spiral volute outlet (Figs 6.102 to 6.105) showed similar properties to those of the design outlet. A considerable reduction in local stress maxima could not be achieved, however, backflow from the outlet tube (diffuser) does not occur in this case.

6.4 Discussion

The determination of mechanical loading conditions of blood components within a flow device is an important part of the proposed blood damage prediction procedure. To solve the above task the application of numerical methods to calculate the flow parameters of interest presents a powerful, cost and time effective means.

Taking as an example the Aries Medical Isoflow ^{TM} pump, numerical flow simulation could be shown to provide distinct information about arbitrary and time-dependent mechanical loading characteristics. A comprehensive 3-dimensional analysis of the entire flow domain, including inlet, impeller and outlet regions was performed with separation into impeller/inlet flow relative to the rotating impeller and outlet flow relative to the stationary casing.

According to the assumption that stresses present a major traumatic parameter of blood in artificial organs, the time-dependent stress loading of fluid

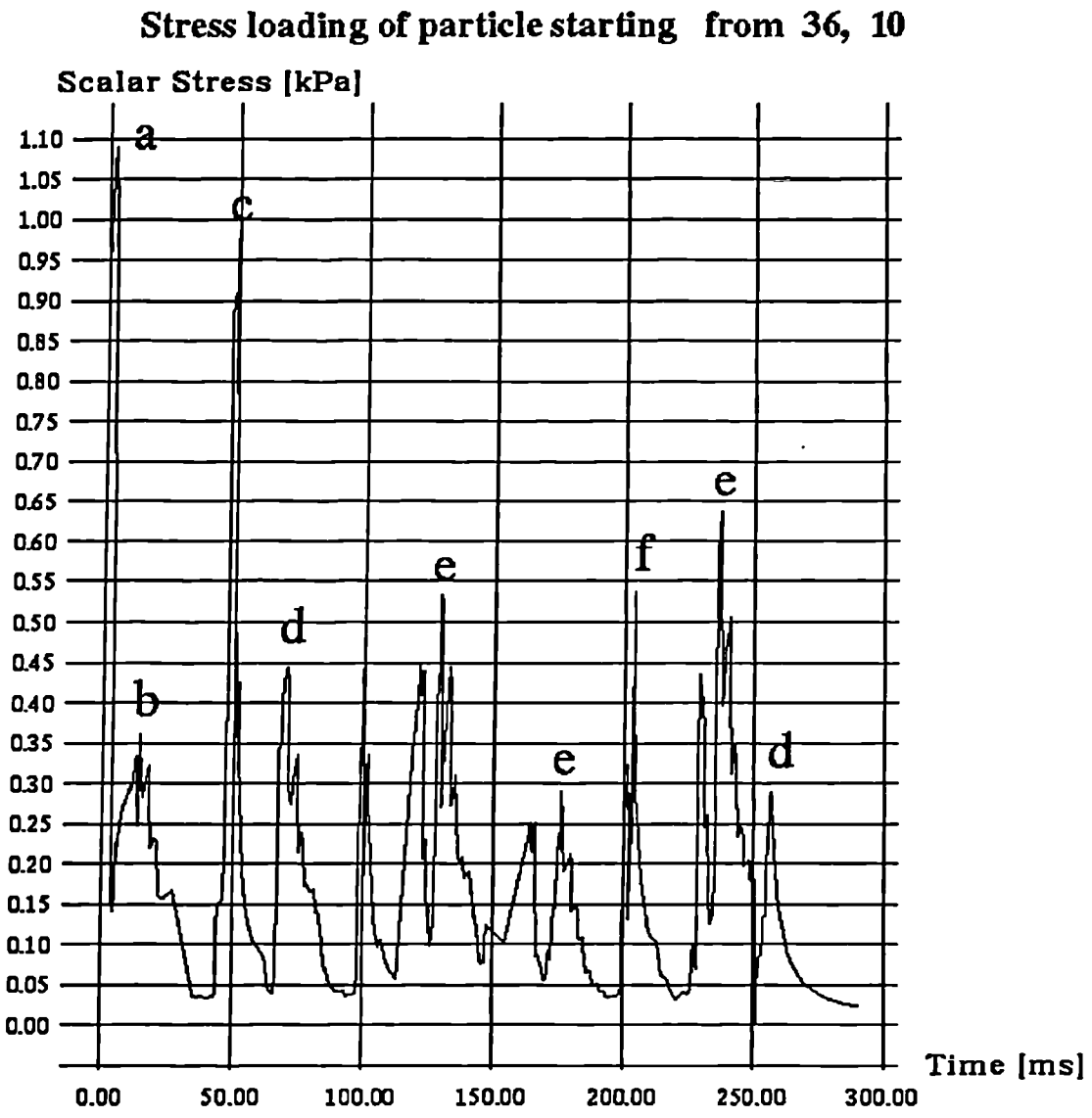

Figure 6.102: Loading-time function for spiral volute; Locations: a-inlet (340^0), b-near inlet (120^0), c-near inlet (340^0), d-near inlet (170^0), e-near inlet (240^0), f-mid gap (0^0).

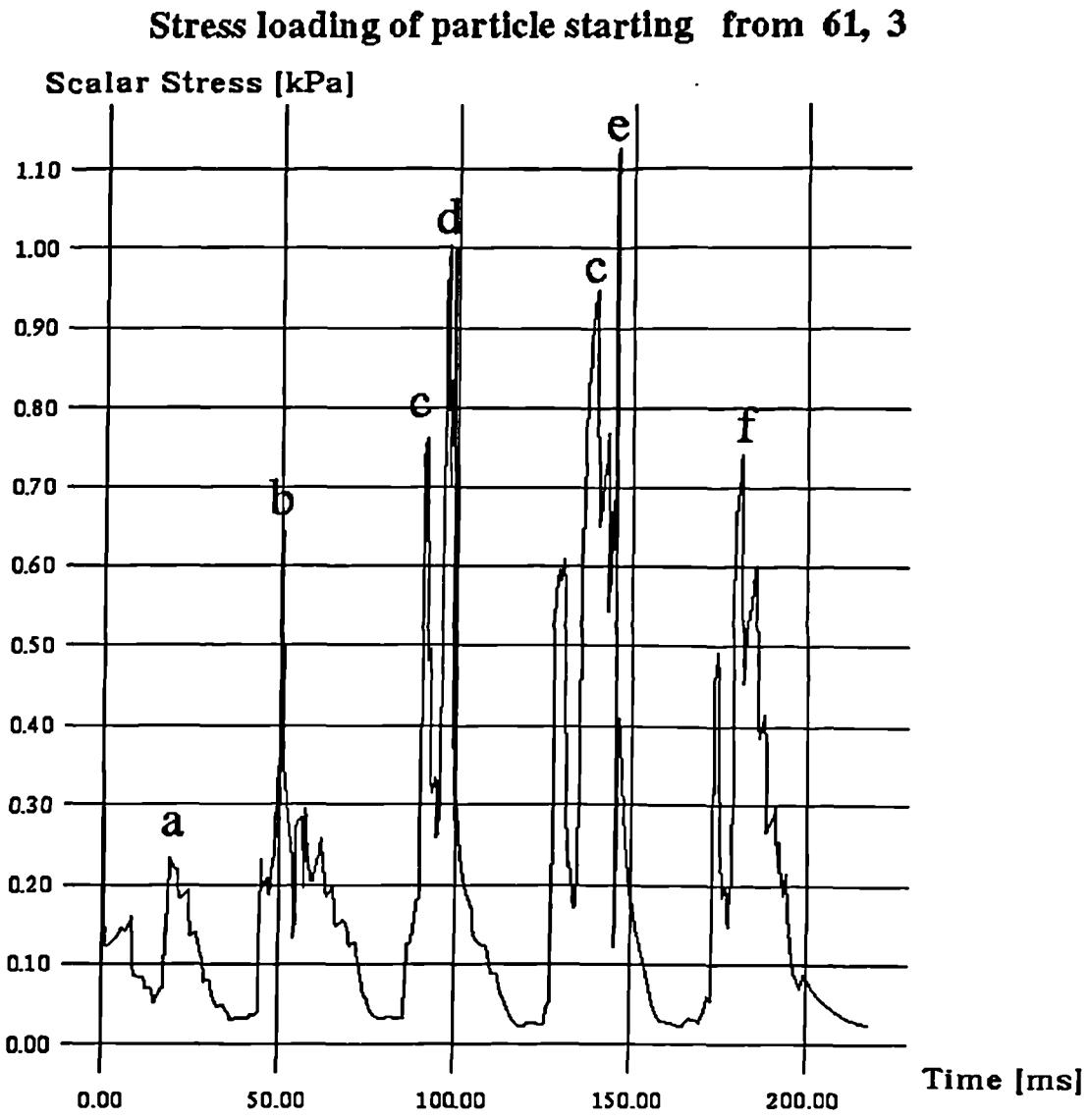

Figure 6.103: Loading-time function for spiral volute; Locations: a-mid gap (180^0), b-mid gap (340^0), c-near inlet (320^0), d-near inlet (340^0), e-outer radius (340^0), f-near inlet (270^0).

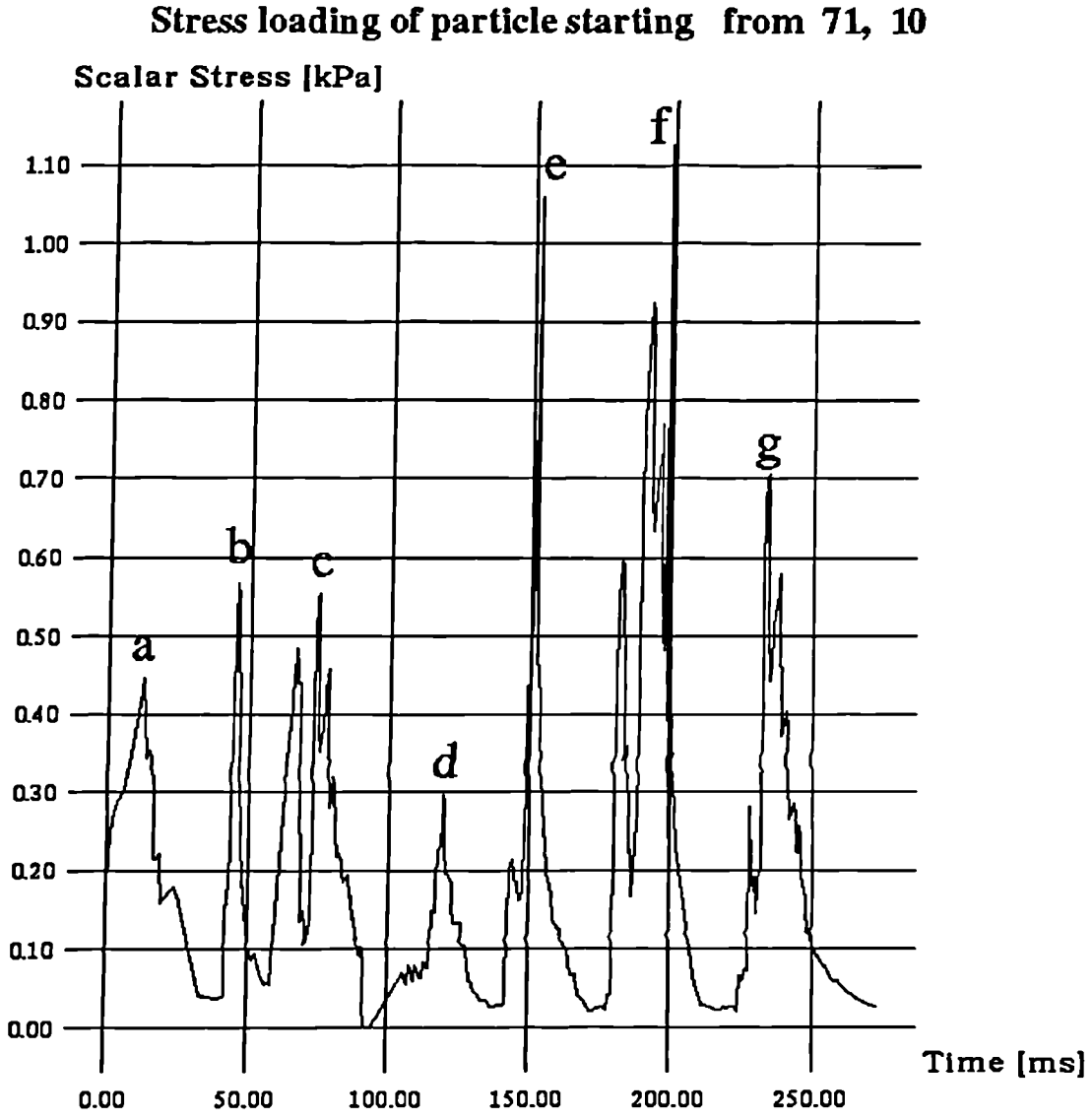

Figure 6.104: Loading-time function for spiral volute; Locations: a-near inlet (120^0), b-near inlet (340^0), c-near inlet (240^0), d-near inlet (170^0), e-mid gap (340^0), f-outer radius (340^0), g-near inlet (270^0). .

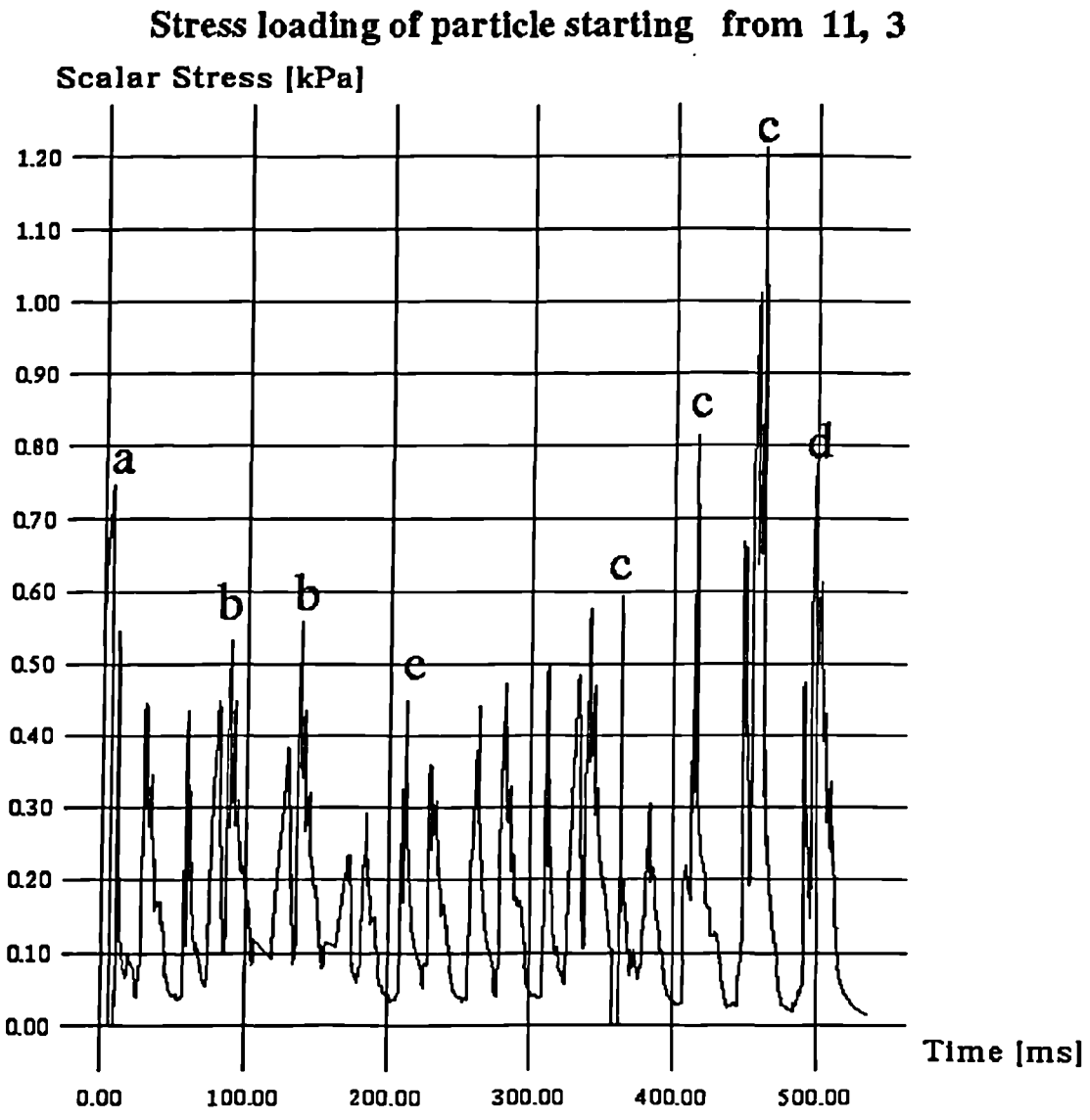

Figure 6.105: Loading-time function for spiral volute; Locations: a-inlet (300^0), b-near inlet (240^0), c-mid gap (340^0), d-near inlet (300^0).

elements passing the pump was analysed by assigning scalar stress values to particle streaklines. In analogy, pressure-time functions of blood elements passing the pump are easily obtainable. The scalar stress value resulted from both Newtonian and Reynolds stress tensor components. Thus, besides a very distinct insight into pump flow phenomena, the investigations undertaken provided for the first time a realistic picture of actual particle stress loading functions. The latter were found to be of a highly irregular, fluctuating nature. Maxima of the stress functions are observed in the near-outlet domain and to a lower degree in near-casing wall regions for the relative impeller flow and especially in the volute domain for the absolute outlet flow.

Conclusions from the results obtained can be drawn as follows:

1. The approximation of a 2-dimensional blade-to-blade analysis applied in hitherto performed centrifugal blood pump simulations is not sufficient and a 3-dimensional analysis of the entire pump domain is essential for assessing influential stress parameters.

2. A careful design and realistic analysis of the pump outflow domain deems especially important since mechanical loading of blood particles is greatest in this pump area.

3. Although the impeller domain does not present the highest stress values, its optimization must be seen under the aspect of reducing particle transit times.

4. The fact that components of the Reynolds stress tensor presented the predominant part of the overall stress values proves the existence of turbulence in these pumps under certain operating conditions and underlines the importance of incorporating a turbulence model into the analysis.

5. Numerical flow simulations with resulting comparative stress-time functions provided an excellent means to assess the effect of varying operating conditions and of geometrical changes to the design on the blood cell loading.

6. The complex, highly unsteady nature of mechanical loading of blood cells in centrifugal pumps requires the formulation and application of an appropriate general blood damage theory for a successful prediction of blood trauma.

An improvement of the numerical pump flow analysis is seen in the further liquidation of simplifying approximations, in particular, the consideration of the time dependency of the actual pump flow. Furthermore, the extension of simulating fluid-particle-suspension flow and calculating streaklines of particles with density and volume equal to that of blood cells as well as consideration of heat transfer processes present tasks of the future. A CFD code which meets the demands on such a comprehensive analysis is, for the case of flow relative to a rotating frame of reference, currently not available. Also, a considerable increase in computing time and in capacity requirements need to be taken into account with realisation of these refinements of numerical blood pump flow analysis.

The experimental prediction of the flow field is seen as important for a final validation of the numerically obtained results. In particular, because of their high significance for a stress prediction, the measurement of turbulent structures and its parameters must show if the model assumptions undertaken are satisfying. However, a complex geometry and the rotating impeller, require highly sophisticated measurement techniques and represent a challenging future task.

Chapter 7

Theoretical Trauma Prediction of Blood Within a Centrifugal Blood Pump

7.1 Data Reduction

In Chapter 6 the numerical simulation of the flow field in the entire stator-rotor configuration of a centrifugal blood pump provided stress-time loading functions of RBCs during pump transit. The time-dependent tracking of particle streastreakklines through the pump domain from the inlet to the outlet plane also enabled the spatial location of a particular load to be specified. Thus, areas with a high damage potential can be identified and selected for modification.

Since the stress-time functions are of a highly irregular nature some form of data reduction is required which enables the application of known damage criteria under defined loading conditions. This data reduction process has the task to perform a classification which selects all loading parts with an essential influence on RBC destruction. All loading parts which are not relevant for damage are excluded.

In the process of service life prediction of engineering materials and equipment, a variety of classification methods, known as counting methods, for load

data reduction are employed [119] of which the most common are:

1. One-parameter counting methods (in which only one characteristic, e.g. amplitude, is counted):

- peak counting
- mean-crossing peak counting
- range counting
- range-pair counting
- level crossing counting

2. Two-parameter counting methods (in which two characteristics, e.g. stress amplitude and order of appearance, are registered simultaneously)

- range-mean counting
- rain-flow cycle counting

Because of the initial stage of the blood damage prediction, the application of a simple reduction method is seen as appropriate, and

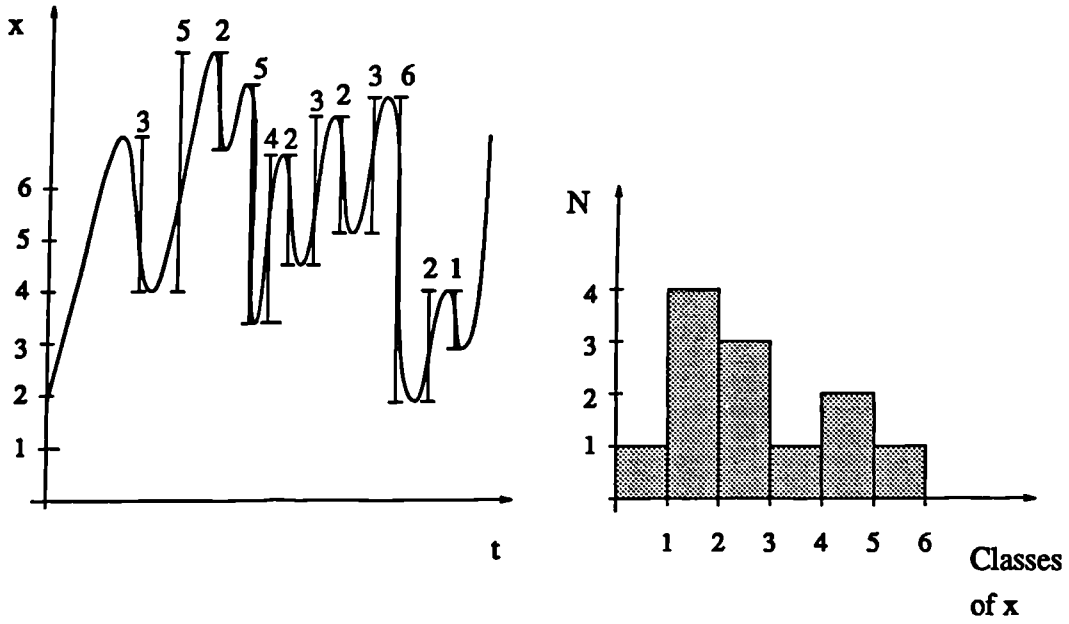

Figure 7.1: One-parameter range-counting classification method

a one-parametric classification, the range-counting method, was selected. The main principles of this classification method are displayed in Fig 7.1. A division into equally-sized ranges or classes of the loading parameter is undertaken

and maximum-minimum intervals ordered into these classes. These intervals are seen as one cycle of an oscillating function with the difference between maximum-minimum representing the double amplitude. The zero-level coincides with the mean value for each range. The number of appearances of a cycle in a specific class is counted.

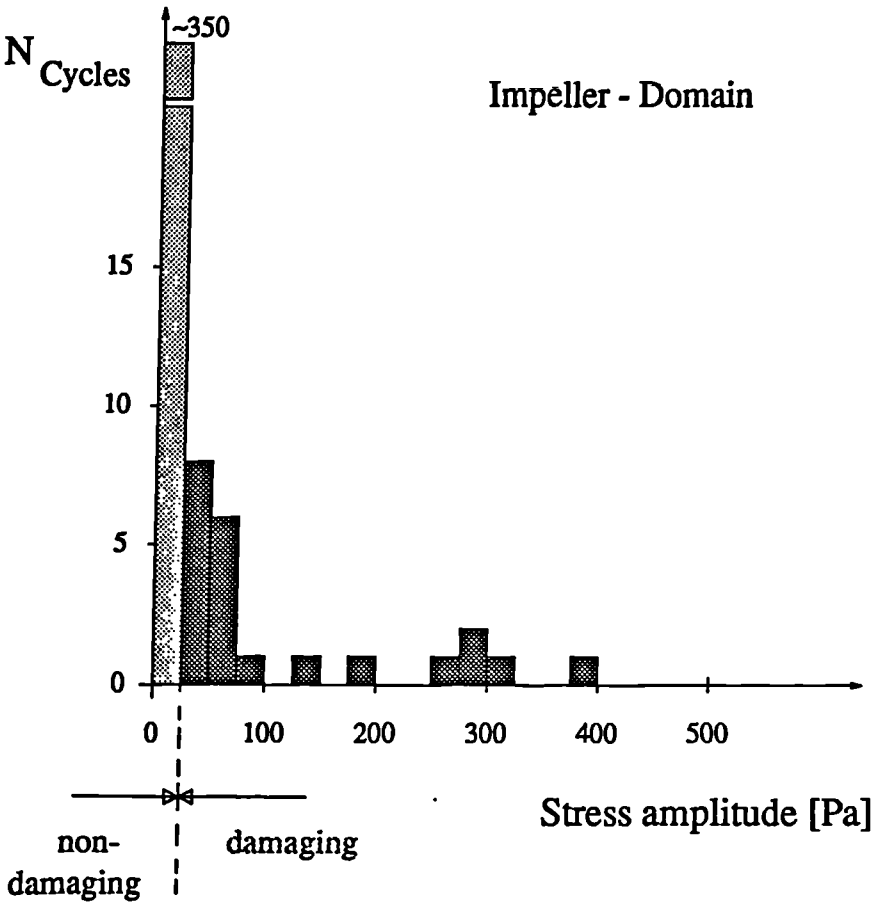

Figure 7.2: Data reduction for particle loading function 2,13 (Impeller).

The result of the data reduction into stress amplitude classes is shown for a loading function in the impeller domain (see Fig.6.60) and in the outlet domain (see Fig 6.85) in Figs 7.2 and 7.3, respectively. A classification into damaging and non-damaging stress amplitudes, i.e. those below endurance (fatigue) strength, say 25 Pa, could be undertaken as presented in Figures 7.2 and 7.3 considering the experimental investigations carried out in Chapter 5. However, stress amplitudes beyond this point have not been examined yet with regard to

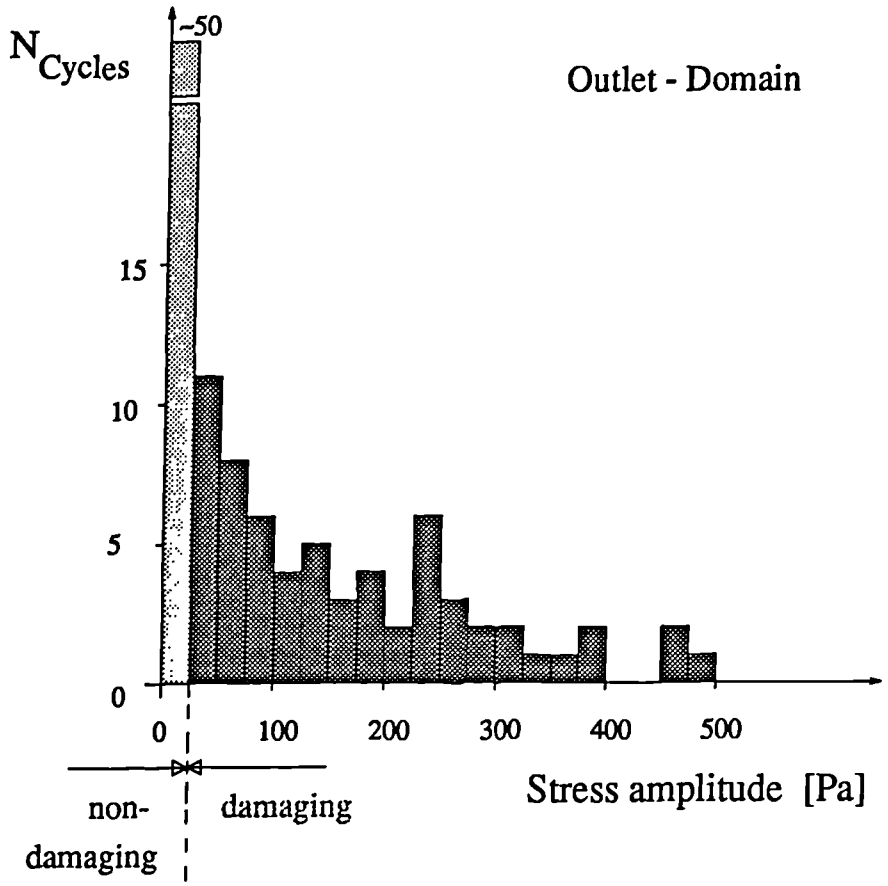

Figure 7.3: Data reduction for particle loading function 90,20 (Outlet).

their haemolytic effect, so that a higher critical threshold cannot be excluded.

Comparison of the classified cyclic loading functions between impeller and outlet domain of the pump revealed the occurence of higher amplitudes and a more dense spectrum for the outlet domain. Thus, it may be concluded that the outlet domain of the centrifugal pump exerts a dominant effect on blood damage.

7.2 Damage Accumulation and Overall Damage Prediction

The linear damage hypothesis proposed in this thesis assumes that equal mechanical loading amplitudes cause an equal increase in damage. As a conse-

quence, the damaging action of a mechanical load is independent of the sequence of the partial loads.

The application of the damage accumulation hypothesis may be demonstrated for a selected blood particle passing the Isoflow ^{TM} pump. If a volume element is marked at the entrance into the pump domain, it is possible to pursue this particle exactly on its path through the pump, as shown in Chapter 6. On its path the particle passes various areas of the pump domain in which the stress conditions can change considerably. An increase in damage of that particle is assumed if the stress level exceeds a certain value (endurance strength). In the linear damage theory these partial damage contributions along the particle path may be summed to give an overall damage. A RBC which follows the streaklines through the impeller and outlet domain, for which the data reduction of loading functions was performed in the previous section, would thus experience an overall damage of:

$$D_{Particle} = \left(\sum_{i=1}^{k} \frac{n_i}{N_i}\right)_{impeller} + \left(\sum_{j=1}^{l} \frac{n_j}{N_j}\right)_{outlet} \tag{7.1}$$

Here, the n_i and n_j denote the number of appearances of the ith or jth stress amplitude and they are set in relation to the critical cycle number. The damage is summed up over all stress amplitudes.

To predict a statistically relevant average value for the damage, e.g. haemolysis, caused to the entire blood volume passing the pump, a sufficient large number of particles starting at the inlet plane must be examined with regard to their loading conditions and subsequent damage. Each of these fluid particles represents a finite volume partion according to the geometrical division of the inlet domain by the numerical grid. It is assumed that all blood elements within this finite volume follow the same pathline through the pump and therefore experience a similar loading. For n particles, the overall damage of a blood volume can thus be expressed as

$$D_{Pump} = \frac{1}{n} \sum_{i=1}^{n} D_{i_{Particle}} \,. \tag{7.2}$$

However, an examination of damage by means of single particle pathlines is necessary to assess the most critical mechanical loading conditions.

Blood elements could experience additional mechanical trauma on their path through the entire circulatory system, e.g. passage through heart valves. This increase would also need to be considered for the damage accumulation. A repeated passage through the pump would add the same amount of damage to the blood volume, although the initial value can be influenced by additional damage sources or by removal of haemoglobin by the reticuloendothelial system.

7.3 Discussion

The method presented in this chapter to theoretically predict the damage progress in blood pumps or other blood conducting systems presents a new approach to minimisation of blood trauma in these devices. Practical application of this method for a quantitative damage prediction is hindered by the lack of blood damage data under cyclic stress loading over a sufficiently wide range of stress amplitudes.

The determination of blood loading functions by means of particle pathlines obtained from a CFD simulation has the advantage of indicating critical local loading maxima at the design phase. It therefore facilitates a directed design improvement which seeks to minimise stress loading peaks. This is desirable because of the non-linear relationship between stress amplitude and critical stress cycle number. An optimal decrease in stress amplidudes would be achieved if they fall below the endurance strength. This non-linear relation also provides the reason for the necessity of considering damage caused by different stress amplitudes accumulatively rather than performing an averaging of the stress amplitudes.

Taking the Isoflow ^{TM} pump as an example for theoretical trauma prediction, major differences between impeller and outlet domain with respect to stress levels and frequency of appearance of stress peaks could be observed classifying

the outlet region as the most critical for blood trauma. A high potential for design improvement with regard to liberalisation of loading parameters exists and studies should be concentrated on the outlet domain. The division of the pump domain performed for the numerical simulation has proven to be advantageous especially with respect to the simulation of geometrical changes in particular parts of the pump.

No consideration of hydrostatic pressure loading for the overall damage prediction has been undertaken in this study. The methods and principles of the mechanically-caused damage prediction demonstrated for stress loading may be similarly applied for a pressure load. The knowledge about blood damage resistance to particular simple constant and cyclic pressure loading functions is, however, very limited.

Changes to the design which lead to an increase in the hydraulic performance, as demonstrated with reduction of the blade-front casing gap, can have an undesirable increase of trauma-causing stress levels as a consequence. Therefore, a compromise between minimisation of trauma and pump performance might often be necessary, the decrease of the former might be achieved only with an equal or lower level of the latter.

The proposed method offers the possibility for a multi-parameter optimisation, e.g. trauma potential and performance, by means of a CFD simulation at the design stage. This ability could reduce experimental costs and labour efforts enormously because only an optimised design would need to be experimentally evaluated.

Chapter 8

Conclusions and Future Work

8.1 Conclusions

In the design and use of artificial organs consideration must be given not only to high efficiency, low specific mass and minimal material and production costs but also to biological compatibility, human acceptance, reliability and ease of handling and control.

Blood pumps also have to meet these general demands, besides the specific task of ensuring the blood perfusion of the body whilst allowing a sufficient flow rate against the circulatory resistance. The survey of existing blood pumps highlighted that the latter requirement is fulfilled. A far more difficult task is the assessment and consequent minimization of blood destruction caused by artificial pumping devices. Such trauma is an additional burden to the already severely ill patient.

Existing models which seek to correlate mechanical loading in these pumps and the amount of blood trauma are oversimplified. They are primarily based on knowledge obtained from static mechanical blood damage tests. In reality, blood particles pass through the pump along complicated paths resulting in a highly irregular loading condition for every blood volume element. In order to enable the prediction of blood damage under the action of these complex loading conditions, a general blood damage model was developed in this thesis.

This model concept comprises a combination of the information about mechanical loading-time functions of blood with the knowledge of its resistance properties to basic loading functions. A linear damage accumulation theory contributes towards the determination of partial damage events and their correlation in the overall damage process. The application of this novel blood damage prediction theory was demonstrated for blood flow through a commercial centrifugal pump, the Isoflow ^{TM} pump (Aries Medical).

A 3-dimensional numerical simulation of flow within the entire and authentic stator-rotor configuration of the pump was performed. The calculation of particle streaklines permitted the tracking of blood elements from the inlet to the outlet of the pump domain and the description of the stress-loading conditions along this path. The six component-stress tensor containing viscous and turbulent stresses was reduced to a scalar stress value by means of a comparative stress theory to enable correlation with uniaxial mechanical blood damage tests. The numerical flow simulation was shown to be an efficient tool to study the effect of a variation of operation conditions (rotational speed, flow rate) and of pump geometry (blade-casing gap, volute shape) on the mechanical blood loading.

With this approach, a new method of assessing the spatial and time-dependent mechanical loading conditions of blood cells on their transit through a pump was developed. The highly irregular stress loading-time functions could be reduced to discrete amplitude ranges of a harmonic stress function acting for a particular number of cycles by means of a one-parameter classification method.

Because of insufficient information on blood damage resistance properties under cyclic stress loading, an appropriate test setup was designed to perform haemolysis tests in a hitherto unexplored amplitude and frequency range. The principle of creating an oscillating shear stress within a blood column through its relative motion to an axially oscillating capillary was analysed and applied.

A complex dependency of haemolysis values on stress amplitude, number of stress cycles and frequency was found. Stress-cycle number damage curves for a particular frequency were derived which are indicative for the existence of an

endurance strength of red blood cells.

Finally, a method for prediction of overall haemolysis rates as a consequence of the actual mechanical loading of blood on its pump transit was methodically described.

Thus, for the first time, distinct information about the actual mechanical loading of blood within a centrifugal pump was obtained and set in relation to its traumatic effect by means of a new, general blood damage prediction theory. This theory considers the essential parameters influencing the damage process.

An effective blood pump optimization with respect to its traumatic potential and pumping performance appears plausible and possible in the design phase by application of this computer-aided approach. The proposed method would allow the designer to observe and assess the effect of changes of pump geometry and/or operating conditions on the resultant blood trauma generation. A numerical optimization technique in combination with a CFD simulation will undoubtedly be a powerful tool for this purpose. Objective functions for the optimization process will result from the mechanical loading-damage relationships described in the blood damage theory. An experimental validation would then need to concentrate only on the already optimised design.

Furthermore, suggestions for a low-damage operating regime during clinical use of the pump could be given on the basis of theoretical damage predictions for a variety of operating conditions. An objective non-experimental comparison of different pump types is also feasible.

8.2 Future Work

The application of the blood damage prediction model presented is not restricted to the particular case of centrifugal pumps. Because the theory is comprehensive and general, a similar approach to the traumatic assessment of any blood conducting system can be readily performed.

For the validation and further development of this new damage prediction concept future investigations should focus on:

1. Extension of the CFD analysis to time-dependent flows and consideration of a cell-plasma suspension flow.

2. Further examination of blood resistance properties under a cyclic mechanical loading for an extended amplitude range (up to 500 Pa).

3. Experimental validation of assumptions undertaken in the damage accumulation hypothesis by controlled multi-load or step-load tests (the development of on-line measurement methods of blood damage would prove to be advantageous for this task).

4. Investigation of similarities and differences between the cellular blood components in their response to mechanical loading.

5. Formation of a database for blood damage parameters obtained from systematic mechanical blood damage tests with chemical and biological factors also taken into account.

Appendix A

Bessel Functions

A linear differential equation of second order of the form

$$\frac{d^2y}{dx^2} + \frac{1}{x}\frac{dy}{dx} + y = 0 \tag{A.1}$$

has two distinct or linearly independent solutions.

The Bessel function of first kind of order n is defined as

$$\begin{aligned} J_n(x) &= \left(\frac{1}{2}x\right)^n \left\{ \frac{1}{n!} - \frac{(\frac{1}{2}x)^2}{1!(n+1)!} + \frac{(\frac{1}{2}x)^4}{2!(n+2)!} + \frac{(\frac{1}{2}x)^6}{3!(n+3)!} + \cdots \right\} \\ &= \sum_{r=0}^{\infty} (-1)^r \frac{(\frac{1}{2}x)^{n+2r}}{r!(n+r)!} \end{aligned} \tag{A.2}$$

which yields for the Bessel function of first kind of order zero

$$J_0 = 1 - \frac{x^2}{2^2} + \frac{x^4}{2^2 4^2} - \frac{x^6}{2^2 4^2 6^2} + \cdots = \sum_{r=0}^{\infty} (-1)^r \frac{(\frac{1}{2}x)^{2r}}{(r!)^2} . \tag{A.3}$$

It can be shown that the following relations hold:

$$\frac{dJ_0(x)}{dx} = -J_1 \quad ; \quad \frac{d}{dx}\left[x \cdot J_1(x)\right] = x \cdot J_0(x)$$

Thus $y_1 = J_0(x)$ is one solution of the differential equation (A.1). The second solution is given with the Bessel function of second kind of order zero Y_0 which is not a numerical multiple of $J_0(x)$ and is defined as follows

$$\begin{aligned} Y_0(x) &= J_0(x) \cdot log\ x + \left\{ \left(\frac{1}{2}x\right)^2 - \frac{(\frac{1}{2}x)^4}{(2!)^2}\left(1 + \frac{1}{2}\right) + \frac{(\frac{1}{2}x)^6}{(3!)^2}\left(1 + \frac{1}{2} + \frac{1}{3}\right) - \cdots \right\} \\ &= J_0(x) \cdot log\ x - \sum_{r=1}^{\infty} (-1)^r \frac{(\frac{1}{2}x)^{2r}}{(r!)^2}\left(1 + \frac{1}{2} + \frac{1}{3} + \cdots + \frac{1}{r}\right) . \end{aligned} \tag{A.4}$$

Thus, the general solution of Eqn (A.1) takes the form

$$y = A\,J_0(x) + B\,Y_0(x)\,. \tag{A.5}$$

Writing kx for x in Eqn. (A.1), with k being an unrestricted but non-zero finite constant, gives

$$\frac{d^2y}{dx^2} + \frac{1}{x}\frac{dy}{dx} + k^2y = 0, \tag{A.6}$$

so by applying (A.5), the complex solution of (A.6) is

$$y = A\,J_0(kx) + B\,Y_0(kx)\,. \tag{A.7}$$

The substitution $x = ix = \sqrt{-1}\,x$ transforms Eqn. (A.6) into:

$$\frac{d^2y}{dx^2} + \frac{1}{x}\frac{dy}{dx} - k^2y = 0\,. \tag{A.8}$$

The solution of Eqn(A.8) is

$$y = A\,I_0(kx) + B\,K_0(kx) \tag{A.9}$$

where I_0 and K_0 are the modified Bessel functions of first and second kind respectively of zero order.

I_0 is defined as

$$I_0 = 1 + \frac{x^2}{2^2} + \frac{x^4}{2^2 4^2} + \frac{x^6}{2^2 4^2 6^2} + \cdots \tag{A.10}$$

Similarly, the solution of the differential equation occurring in many engineering applications of the form

$$\frac{d^2y}{dx^2} + \frac{1}{x}\frac{dy}{dx} - ik^2y = 0\,. \tag{A.11}$$

is

$$y = AI_0(kxi^{\frac{1}{2}}) + BK_0(kxi^{\frac{1}{2}}) = AJ_0(kxi^{\frac{3}{2}}) + BK_0(kxi^{\frac{1}{2}}) \tag{A.12}$$

with

$$J_0(kxi^{\frac{3}{2}}) = 1 + i\left(\frac{1}{2}kx\right)^2 - \frac{(\frac{1}{2}kx)^4}{(2!)^2} - \frac{i(\frac{1}{2}kx)^6}{(3!)^2} + \cdots$$
$$= \left[1 - \frac{(\frac{1}{2}kx)^4}{(2!)^2} + \frac{(\frac{1}{2}kx)^8}{(4!)^2} - \cdots\right] + i\left[\left(\frac{1}{2}kx\right)^2 - \frac{(\frac{1}{2}kx)^6}{(3!)^2} + \cdots\right]. \quad \text{(A.13)}$$

According to Kelvin, the expression in the first bracket of the right hand side in (A.13) is termed as ber (kx), and that in the second bracket as bei (kx) , so that Eqn. (A.13) can be written as:

$$J_0(kxi^{\frac{3}{2}}) = \text{ber}\,(kx) + i\,\text{bei}\,(kx)\,. \quad \text{(A.14)}$$

These series and their derivatives are absolutely and uniformly convergent in any closed interval of x real. Hence, they may be differentiated and integrated term by term. The first derivative with respect to x of the real and imaginary Bessel functions ber (kx) and bei (kx) can therefore be written as

$$\frac{d\ \{ber(kx)\}}{dx} = k\left[-\frac{(kx)^3}{2^24} + \frac{(kx)^7}{2^24^26^28} - \frac{(kx)^{11}}{2^24^26^28^210^212} + \cdots\right]$$
$$\frac{d\ \{bei(kx)\}}{dx} = k\left[\frac{kx}{2} - \frac{(kx)^5}{2^24^26} + \frac{(kx)^9}{2^24^26^28^210} - \cdots\right]. \quad \text{(A.15)}$$

Appendix B

Velocity and Shear Stress Distribution in Oscillating Capillary

The radius and time dependent velocity distribution of a viscous, Newtonian fluid within a capillary tube which performs sinisoidal axial oscillations is determined applying Eqn. (5.15).

A graphical display of the radial velocity distribution during one period of oscillation is given in Fig B.1 with the following geometric and kinematic parameters:

R = 0.3 mm ; ρ = 1000 kg/m^3 ; $\eta = 3 * 10^{-3}$ Pa s ;
f = 50 Hz ; v_0 = 3.14 m/s (x_0 = 5 mm)

The distribution of the shear stress τ_{rz} over one period of oscillation for the above parameters using Eqn. (5.16) is given in Fig B.2.

The bulk shear stress graph representing a time - step related characteristic shear stress value according to Eqn. (5.17) for the above case is shown in Fig B.3.

The effect of variation of different parameters on the periodic bulk shear

stress is given in Figs B.4 to B.7 with variation of the tube radius R (Fig B.4), haematocrit leading to a kinematic viscosity according to Eqn. (5.19), (Fig B.5), frequency (Fig B.6) and displacement amplitude - related to velocity amplitude by relations (5.18), (Fig B.7). The corresponding constant parameters are chosen as in the above case.

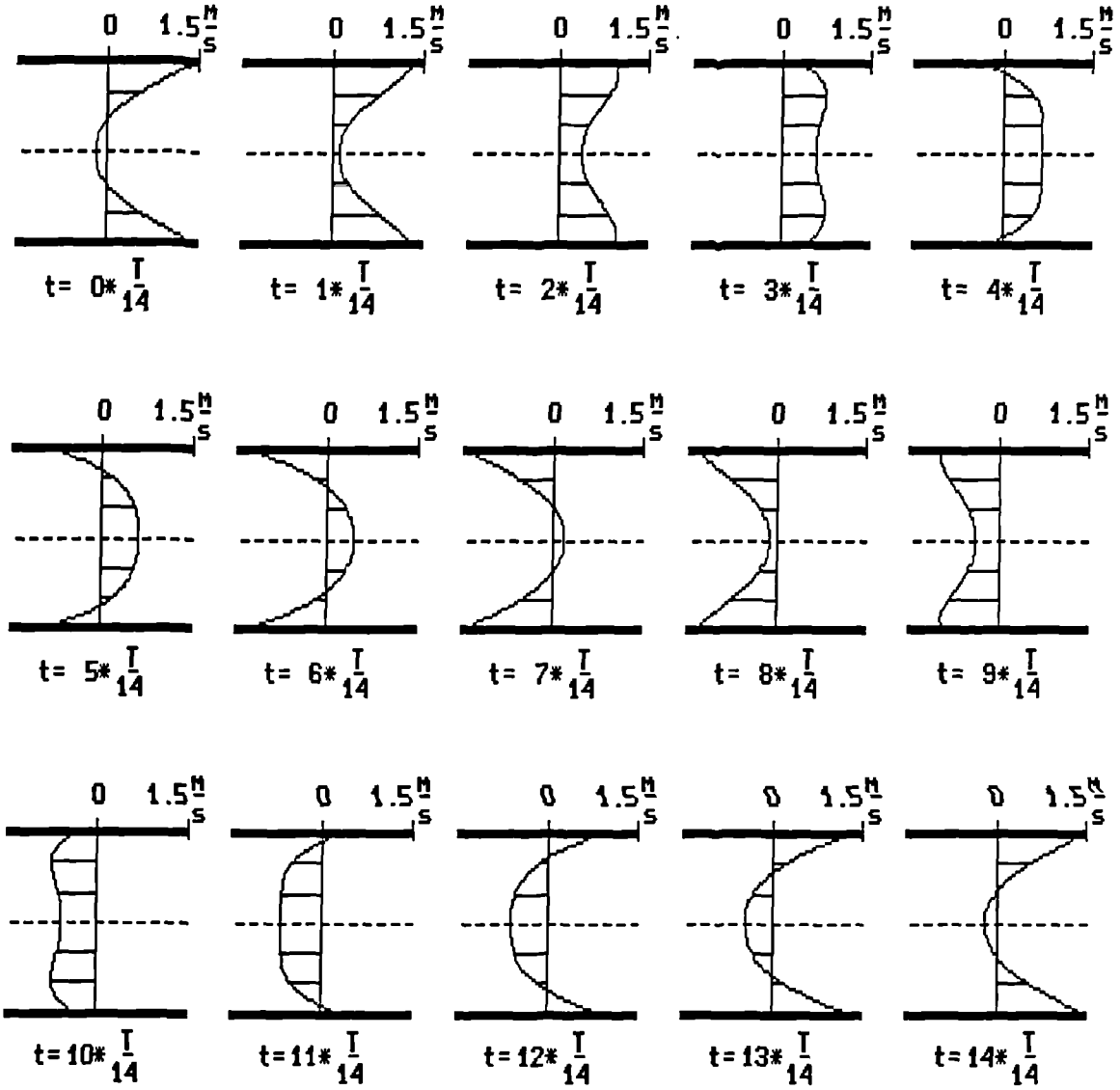

Figure B.1: Velocity distribution within oscillating capillary for one period (μ=3 mPa; $\rho = 1000\ kg/m^3$; f=50 Hz; R=0.3 mm; v_0=3.14 m/s)

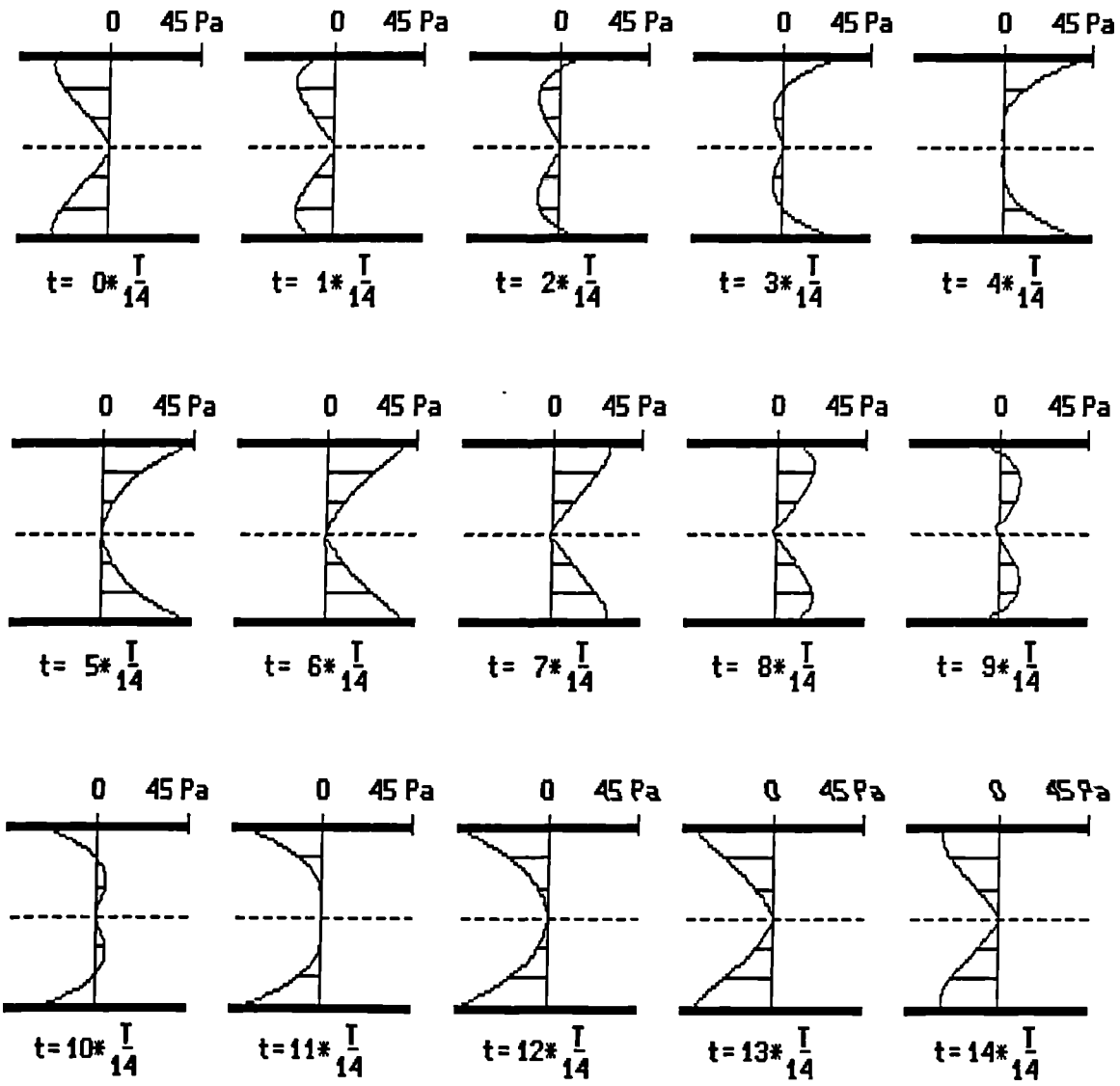

Figure B.2: Shear stress distribution within oscillating capillary for one period (μ=3 mPa; $\rho = 1000\ kg/m^3$; f=50 Hz; R=0.3 mm; v_0=3.14 m/s)

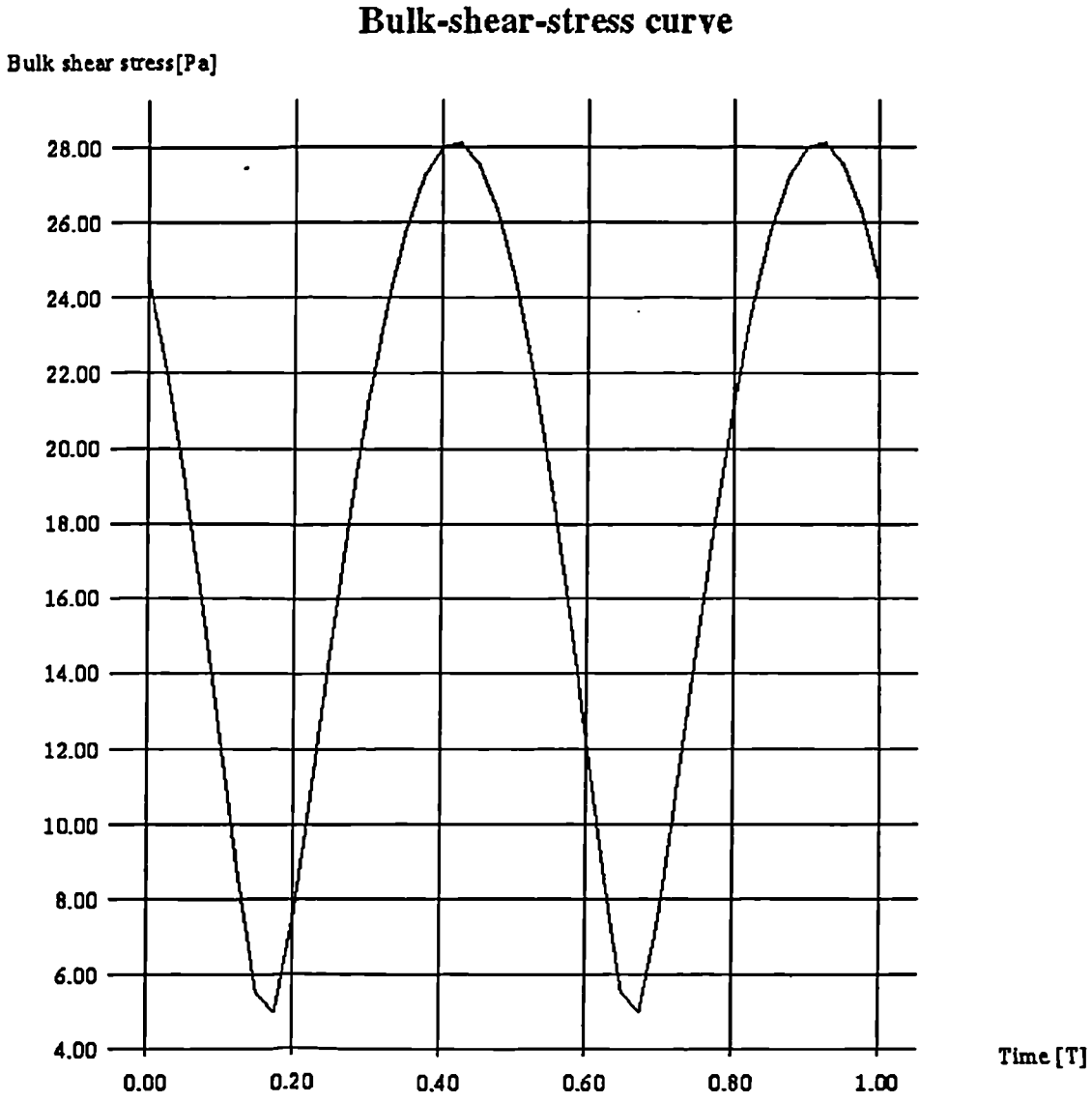

Figure B.3: Bulk shear stress curve for the shear stress distribution presented in Fig B.2 for one time period

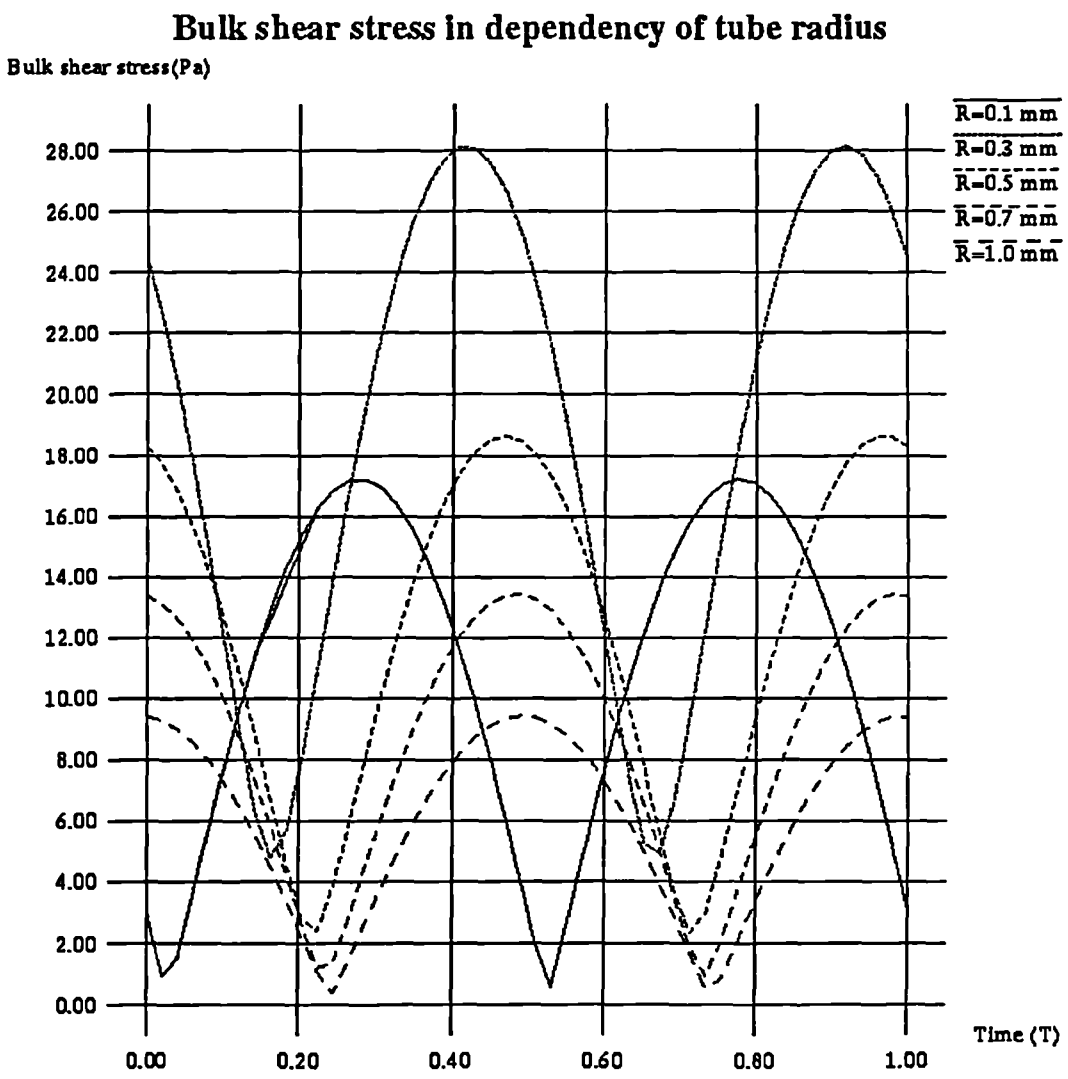

Figure B.4: Dependency of bulk shear stress amplitude on the tube's inner radius

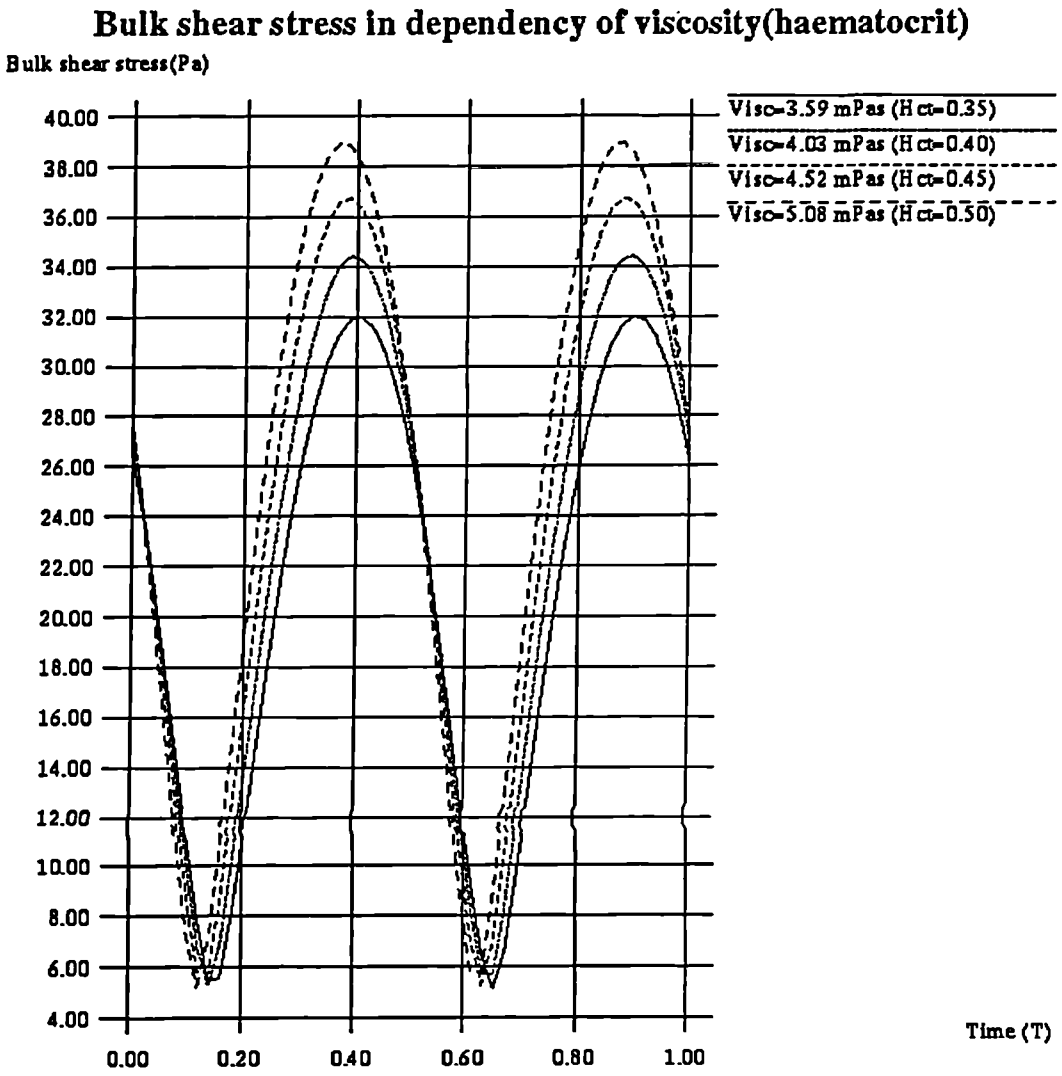

Figure B.5: Dependency of bulk shear stress amplitude on the viscosity via haemotocrit

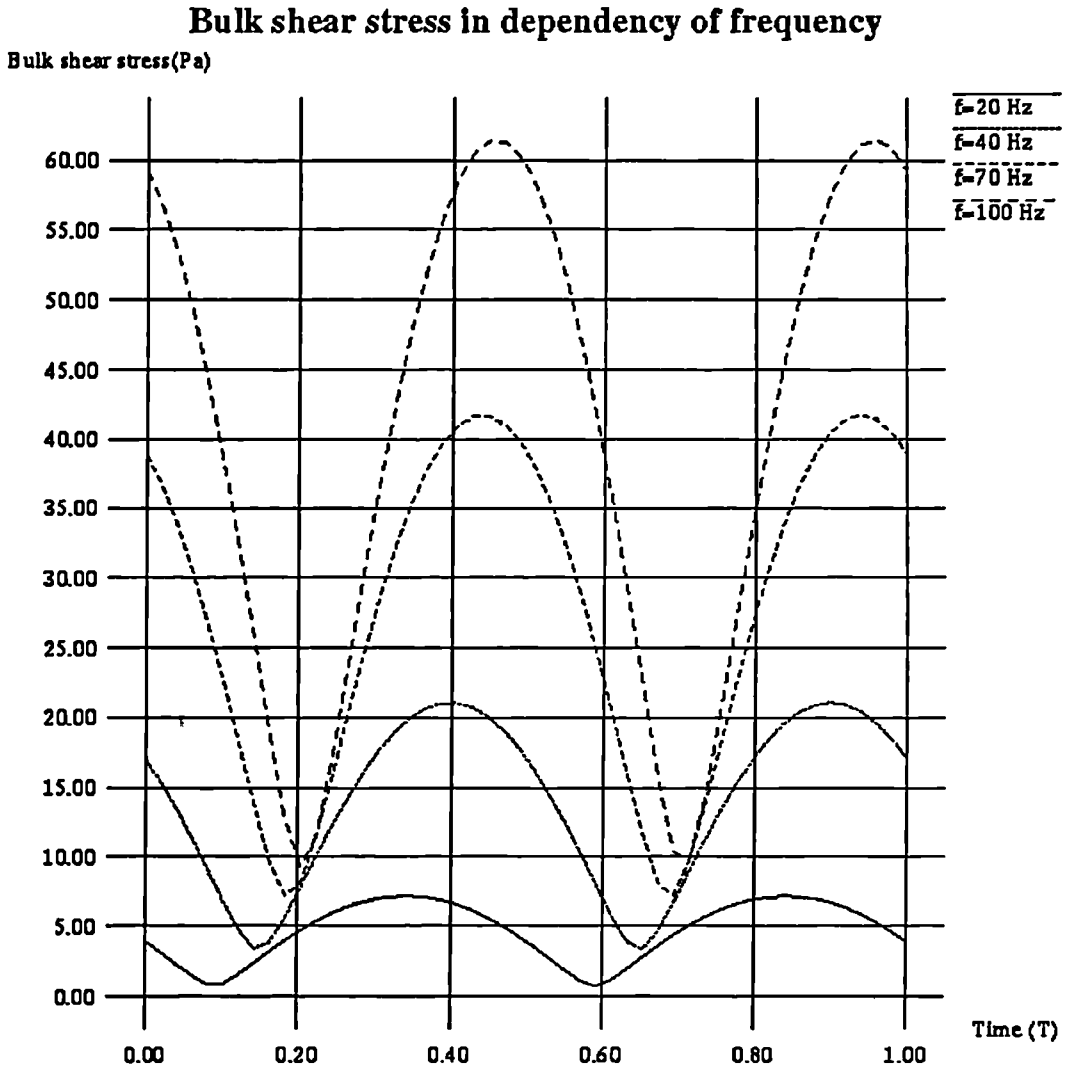

Figure B.6: Dependency of bulk shear stress amplitude on the oscillation frequency

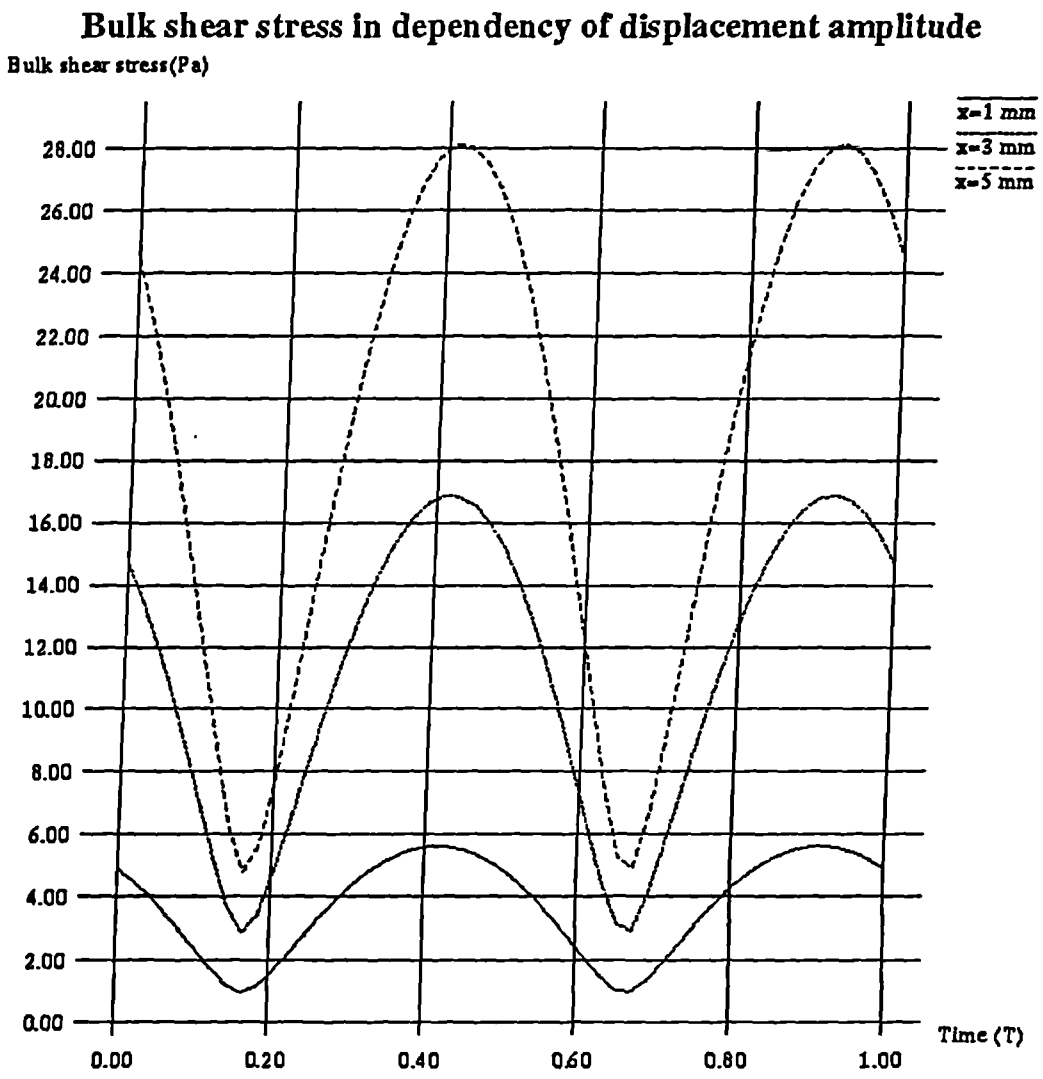

Figure B.7: Dependency of bulk shear stress amplitude on the displacement amplitude

Appendix C

Pump Dimensions

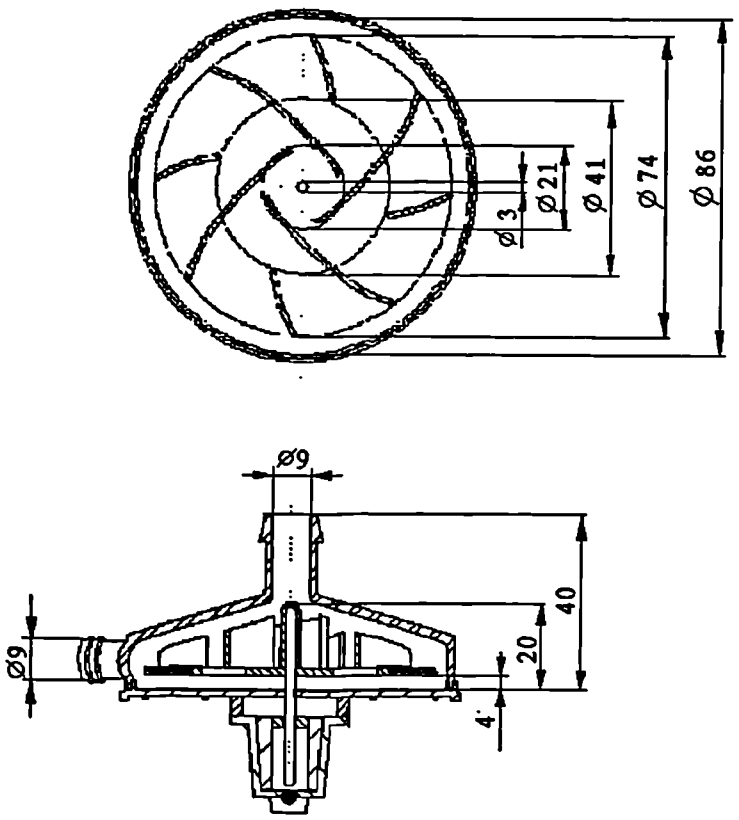

Figure C.1: Main dimensions of Isoflow ^{TM} centrifugal blood pump (Aries Medical). All dimensions in mm.

Appendix D

Grid Notations at Inflow Plane

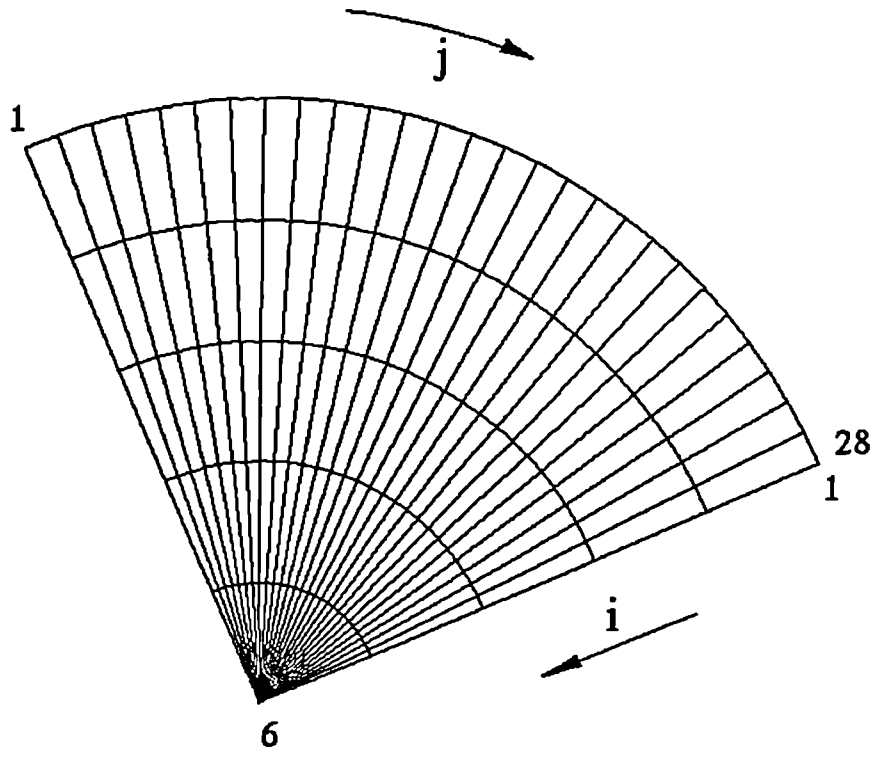

Figure D.1: Grid node notation (i,j) at inflow plane of inflow port for Isoflow ^{TM} centrifugal blood pump (Aries Medical).

Bibliography

[1] Lenihan J. Paradox and partnership - the engineer's contribution to medicine. The Hugh Macmillan Memorial Lecture. *Institution of Engineers and Shipbuilders in Scotland*, Paper No.1421, March 27, 1979.

[2] Kantrowitz A. State of the art - circulatory support. *Trans. ASAIO*, 1988, Vol.34, pp.445-449.

[3] United Kingdom Cardiac Surgical Register 1991.

[4] Norman J.C. Mechanical ventricular assistance : a review. *Artif. Organs*, 1981, Vol.5, No.2, pp.103-107.

[5] Jarvic R.K. The total artificial heart. *Scientific America*, January 1981, pp.66-72.

[6] Pae W.E., Pierce W.S. Combined registery for the clinical use of mechanical assist pumps and total artificial heart. Second Official Report - 1987. *The Journal of Heart Transplantation*, 1989, Vol.8, pp.1-4.

[7] Blackshear P.L. Mechanical engineering aspects of rotary blood pumps. *International Workshop on Rotary Blood Pumps*, Proc., Baden/Vienna, 1991.

[8] DePaulis R., Engelhardt H., Riebman J.B., Olsen D.B. Bloodpumps. *Int. J. of Artif. Organs*, 1966, Vol.9, No.6, pp.377-384.

[9] Hager J., Brandstätter F., Unger F., Klima G., Koller J. Experiences with the spindle pump as biventricular assist device in acute animal experiences. *Int. Workshop on Rotary Blood Pumps* Proc., Baden/Vienna, 1991, pp.165-171.

[10] Margreiter R., Schwab W., Klima G., Koller J., Baum M., Dietrich H., Hager J., Koenigsrainer A. Rotacor: a new rotary blood pump. *Trans. ASAIO*, 1990, Vol.36, No.3, pp.M281-M284.

[11] Monties J.R., Mesana T., Havlik P., Trinkl J., Demunck J.L., Candelon B. A way of pumping blood with a rotary but non-centrifugal pump for an artificial heart. *Trans. ASAIO*, 1990, Vol.36, No.3, pp.M258-M260.

[12] Affeld K., Poppe R., Ganter G. Flow in nutating centrifugal blood pumps. *Second World Symposium Artificial Heart*, Berlin, 1984.

[13] Akamatsu T., Shiroyama T., Fukumasu H. Development of nutating centrifugal blood pumps. In: *Artificial Heart 2; Proceedings of the 2nd Int. Symposium on Artif. Heart and Assist Devices.* Akatsu (ed.), Tokyo, 1987.

[14] Pfleiderer C. *Die Kreiselpumpen für Flüssigkeiten und Gase.* Springer-Verlag, 1961.

[15] Nose Y. The need for a nonpulsatile pumping system. *Artif. Organs*, 1988, Vol.12, pp.113-115.

[16] Westphal D., Reul H., Rau G. Development and in-vitro test results of the Helmholtz centrifugal pump. *Int. Workshop on Rotary Blood Pumps* Proc., Baden/Vienna, 1991, pp.132-136.

[17] Nishida H., Yamaki F., Nakatani H. Development of the Terumo Capiox centrifugal pump and its clinical application to open heart surgery: a comparative study with the roller pump. *Artif. Organs*, 1993, Vol.17, No.5, pp.323-327.

[18] Takatani S., Tanaka T., Noda H., Akutsu T. Development of a direct-drive centrifugal nonpulsatile blood pump. *Progress in Artif. Organs*, 1985, pp.373-378.

[19] Akamatsu T., Nakazeki T., Itoh H. Centrifugal blood pump with a magnetically suspended impeller. *Artif. Organs*, 1992, Vol.16, No.3, pp.305-306.

[20] Sakuma I., Takatani S., Nose Y. Development of a motor driven seal-less centrifugal blood pump. *Int. Workshop on Rotary Blood Pumps* Proc., Baden/Vienna, 1991, pp.48-53.

[21] Wampler R.K., Moise J.C., Frazier O.H., Olsen D.B. In vivo evaluation of a peripheral vascular access axial flow blood pump. *Trans. ASAIO*, 1988, Vol.34, pp.450-454.

[22] Butler K.C., Wampler R.K., Griffith B.P., Antaki J.F., Kormos R.L. Borovetz H.S. Development of an implantable axial flow LVAS. *Int. Workshop on Rotary Blood Pumps* Proc., Baden/Vienna, 1991, pp.148-153.

[23] Quian K.X., Kitamura T., Fukumasu H. Prototype design of an implantable nonpulsatile centrifugal diagonal pump. *Progress in Artif. Organs*, 1983, pp.148-151.

[24] Quian K.X., Pi K.D., Wang Y.P., Zhao M.J. Toward an implantable impeller total heart. *Trans. ASAIO*, 1987, Vol.33, pp.704-707.

[25] Wurzinger L.J., Opitz R. Hematological principles of hemolysis and thrombosis with special reference to rotary blood pumps. *Int. Workshop on Rotary Blood Pumps* Proc., Baden/Vienna, 1991, pp.19-25.

[26] Hochmuth R.M. Properties of red blood cells. In: *Handbook of Bioengineering.* R.Skalak, S.Chien (eds.), McGraw-Hill Book Company, 1987.

[27] Blackshear P.L., Blackshear G.L. Mechanical hemolysis. In *Handbook of Bioengineering.* R.Skalak, S.Chien (eds.), McGraw-Hill Book Company, 1987, p.501.

[28] Wurzinger L.J., Opitz R., Eckstein H. Mechanical blood trauma. *ESAO Workshop on Nonpulsatile Blood Pumps 1985*, TU Berlin, 1986, pp.30-44.

[29] Colantuoni G., Hellums J.D., Moake J.L., Alfrey C.P. The response of human platelets to shear stress at short exposure times. *Trans. ASAIO*, 1977, Vol.23, pp.626-631.

[30] Sutera S.P. Flow-induced trauma to blood cells. *Circ. Research*, 1977, Vol.41, No.1, pp.2-8.

[31] Schmid-Schönbein H., Born G.V.R., Richardson P.D. et al. Rheology of thrombotic processes in flow: the interaction of erythrocytes and thrombocytes subjected to high flow forces. *Biorheology*, 1981, Vol.18, pp.415-444.

[32] Olsen D.B. Evaluation of rotary blood pumps on animal experiments. *Int. Workshop on Rotary Blood Pumps* Proc., Baden/Vienna, 1991, pp.1-6.

[33] Schima H., Wohlfahrt A., Müller M.R. Vaneless or impeller rotary blood pumps: hydrodynamic and hemodynamic aspects and results. *Int. Workshop on Rotary Blood Pumps* Proc., Baden/Vienna, 1991, pp.32-38.

[34] Schima H., Müller M.R., Papantonis D. et al. Minimization of hemolysis in centrifugal blood pumps: influence of different geometries. *The Int. J. of Artif. Organs*, 1993, Vol.16, No.7, pp.521-529.

[35] Noon G.P., Sekela M., Glück J., Coleman C.L., Feldman L. Comparison of Delphin and BioMedicus pumps. *Trans. ASAIO*, 1990, Vol.36, pp.M616-M619.

[36] Hoerr H.R., Kraemer M.F. et al. In vitro comparison of the blood handling by the constrained vortex and Twin roller blood pumps. *J. Extra-Corpor. Techn.*, 1987, Vol.19, No.3, pp.316-320.

[37] Oku T., Harasaki H., Smith W., Nose Y. Hemolysis - a comparative study of four nonpulsatile pumps. *Trans. ASAIO*, 1988, Vol.34, pp.500-504.

[38] Müller M.R., Wohlfahrt A., Schima H. et al. Hematological parameters for in vitro testing of blood pumps - data analysis of two different principles. *Int. Workshop on Rotary Blood Pumps* Proc., Vienna, 1988, pp.82-86.

[39] Sasaki T., Jikuya T., Aizawa T. et al. A compact centrifugal pump for cardiopulmonary bypass. *Artif. Organs*, 1992, Vol.16, No.6, pp.592-598.

[40] Deleuze P.H., Liu Y., Tixier D. et al. Centrifugal pump or pneumatic ventricle for short-term mechanical circulatory support? *The Int. J. of Artif. Organs*, 1989, Vol.12, No.5, pp.327-332.

[41] Eastham R.D, Slade R.R. *Clinical Haematology*, Butterworth-Heinemann Ltd., 1992, p.54.

[42] Schlichting H. *Boundary-Layer Theory*, McGrawHill Book Company, 1979.

[43] Affeld K., Schichl K., Yoganathan A. Summary *ESAO Workshop on Non-pulsatile Blood Pumps 1985*, TU Berlin, 1986, pp.3-35.

[44] Papantonis D., Croba D. Numerical calculation of the performances and shear stresses developed on centrifugal blood pumps. *Int. Workshop on Rotary Blood Pumps* Proc., Vienna, 1988, pp.53-60.

[45] Papantonis D. Numerical prediction of the shear stresses and of the mean stay time for radial flow impellers. *Int. Workshop on Rotary Blood Pumps* Proc., Baden/Vienna, 1991, pp.63-69.

[46] Sakuma I., Fukui Y., Ohara Y., Makinouchi K., Takatani S., Nose Y. Flow visualization evaluation of secondary flow in a centrifugal blood pump. *ASAIO J.*, 1993, pp. M433-M437.

[47] Kerrigan J.P., Shaffer F.D., Maher T.R., Dennis T.J., Borovetz H.S., Antaki J.F. Flourescent image tracking velocimetry of the Nimbus Axipump. *ASAIO J.*, 1993, pp. M639-M643.

[48] Araki K., Taenaka Y., Masuzawa T. et al. A flow visualization study of centrifugal blood pumps developed for long-term usage. *Artif. Organs*, 1993, Vol.17, No.5, pp.307-312.

[49] Treichler J., Rosenow S.E., Damm G. et al. A fluid dynamic analysis of a rotary blood pump for design improvement. *Artif. Organs*, 1993, Vol.17, No.9, pp.797-808.

[50] Belenger J., Knight C.J. The origin of the failure of centrifugal pumps in cardiac support: an in-vitro approach. *Progress in Artif. Organs*, 1983, pp.74-78.

[51] Goldsmith H.L. Poiseuille medal award lecture: From papermaking fibres to human blood cells. *Biorheology*, 1993, Vol.30, pp.165-190.

[52] Blackshear P.L., Dorman F.D., Steinbach J.H. Some mechanical effects that influence hemolysis. *Trans. ASAIO*, 1965, Vol.2, pp.112-117.

[53] Bacher R.P., Williams M.C. Hemolysis in capillary flow. *J. Lab. Clin. Med.*, 1970, Vol.76, pp.485-496.

[54] Williams A.R. Viscoelasticity of the human erythrocyte membrane. *Biorheology*, 1973, Vol.10, pp.313-319.

[55] Beissinger R.L., Williams M.C. A dual mechanism for low-stress hemolysis in laminar flow. *AIChE*, 1984, Vol.30, No.4, pp. 569-577.

[56] Solen K.A., Whiffen J.D., Lightfood E.N. The effect of shear, specific surface and air interface on the development of blood emboli and hemolysis. *J. of Biomedical Material Research*, 1978, Vol.12, pp.381-399.

[57] Nevaril C.G., Lynch E.C., Alfrey C.P., Hellums J.D. Erythrocyte damage and destruction induced by shearing stress. *J. Lab. Clin. Med.*, 1969, Vol.71, pp.784-790.

[58] Leverett L.B., Hellums J.D., Alfrey C.P., Lynch E.C. Red blood cell damage by shear stress. *Biophysical J.*, 1972, Vol.12, p.257.

[59] Sutera S.P., Mehrjadi M.H. Deformation and fragmentation of human red blood cells in turbulent shear flow. *Biophysical J.*, 1975, No.15, pp.1-10.

[60] Blackshear P.L., Dorman F.D., Steinbach J.H. et al. Shear wall interaction and hemolysis. *Trans. ASAIO*, 1966, Vol.12, p.113.

[61] Sallam A.M. Hwang N.H.C. Human red blood cell hemolysis in a turbulent shear flow: contribution of Reynolds shear stresses. *Biorheology*, 1984, Vol.21, pp.783-797.

[62] Bluestein M., Mockros L.F. Hemolytic effects of energy dissipation in flowing blood. *Med. and Biol. Engng.*, 1969, Vol.7, pp.1-16.

[63] Rooney J.A. Hemolysis near an ultrasonically pulsating gas bubble. *Science*, 1970 Vol.169, pp.869-871.

[64] Williams A.R., Hughes D.E., Nyborg W.L. Hemolysis near a transversely oscillating wire. *Science*, 1970 Vol.169, pp.871-873.

[65] Hashimoto S. Erythrocyte destruction under periodically fluctuating shear rate: comparative study with constant shear rate. *Artif. Organs*, 1989, Vol.13, No.5, pp.458-463.

[66] Yarborough K.A., Mockros L.F., Lewis F.J. Hydrodynamic hemolysis in extracorporeal machines. *J. Thorac. Cardiovasc. Surg.*, 1960, Vol.52, pp.550-557.

[67] Nevaril C.G., Hellums J.D., Alfrey C.P., Lynch E.C. Physical effects in red blood cell trauma. *AIChE*, 1969, Vol.15, No.5, pp.707-711.

[68] Nakahara T., Yoshida F. Mechanical effects on rates of hemolysis. *J. of Biomedical Material Research*, 1986, Vol.20, pp.363-374.

[69] Hellums J.D., Hardwick R.A. Response of platelets to shear stress - a review. In *The Rheology of Blood, Blood Vessels and Associated Tissue*, Gross D.R., Hwang N.H.C. (eds.), Sijhoff & Noordhoff, 1981, p.160.

[70] Ramstack J.M., Zuckerman L., Mockros L.F. Shear-induced activation of platelets. *J. Biomechanics*, 1979, Vol.12, pp.113-124.

[71] Bernstein E.F., Marzec U., Johnston G.G. Structural correlations of platelet functional damage by physical forces. *Trans. ASAIO*, 1977, Vol.23, pp.616-625.

[72] Hung T.C., Hochmuth R.M., Joist J.H., Sutera S.P. Shear induced aggregation and lysis of platelets. *Trans. ASAIO*, 1976, Vol.22, p.285.

[73] Williams A.R. Release of serotonin from human platelets by acoustic microstreaming. *J. Acoust. Soc. Am.*, 1974, Vol.56, No.5, pp.1640-1644.

[74] Yu S.K., Latour J.G., Marchandise B., Pois M. Shear stress-induced changes in platelet reactivity. *Thrombos. Haemostas.*, 1978, Vol.40, pp.551-560.

[75] Goldsmith H.L., Marlow J.C., Yu S.K. The effect of oscillatory flow on the release reaction and aggregation of human platelets. *Microvasc. Research*, 1976, Vol.11, p.335.

[76] Dewitz T.S., McIntyre L.V., Martin R.R., Sybers H.D. Enzyme release and morphological changes in leucocytes induced by mechanical trauma. *Blood Cells*, 1979, Vol.5, pp.499-510.

[77] Evans E.A., Hochmuth R.M. Membrane viscoelasticity. *Biophys. J.*, 1976, Vol.16, pp.1-11.

[78] Richardson E. Red cell mechanics with application to haemolysis in shear. *PhD Thesis*, 1972, University of Strathclyde, Glasgow.

[79] Skalak R., Chien S. Rheology of blood cells as soft tissues. *Biorheology*, 1982, Vol.19, p.453.

[80] Rand R.P. Mechanical properties of the red cell membrane 2. Viscoelastic breakdown of the membrane. *Biophys. J.*, 1964, Vol.4, pp.303-316.

[81] Evans E.A., Hochmuth R.M. Membrane viscoplastic flow. *Biophys. J.*, 1976, Vol.16, pp.13-26.

[82] Schmid-Schönbein H., Wells R. Fluid drop-like transition of erythrocytes under shear. *Science*, 1969, Vol.165, pp.288-291.

[83] Goldsmith H.L., Marlow J. Flow behaviour of erythrocytes. 1. Rotation and deformation in dilute suspensions. *Proc. Royal Soc. London*, 1972, Vol.B182, pp.351-384.

[84] Sutera S.P., Tran-Son-Tay R. Mathematical model of the velocity field external to a tank-treading red cell. *Biorheology*, 1983, Vol.20, p.267.

[85] Sugihara M., Niimi H. Numerical approach to the motion of red blood cells in Couette flow. *Biorheology*, 1984, Vol.21, p.735.

[86] Richardson E. Deformation and haemolysis of red cells in shear flow. *Proc. Royal Soc. London*, 1974, Vol.338, pp.129-153.

[87] Niimi H., Sugihara M. Cyclic loading on the red cell membrane in shear flow: A possible cause of hemolysis. *J. of Biomechanical Eng.*, 1985, Vol.107, pp.91-95.

[88] Sugihara M. Motion and deformation of a red blood cell in a shear flow: a two-dimensional simulation of the wall effect. *Biorheology*, 1985, Vol.22, p.1.

[89] Johnson W. *Engineering Plasticity*, Van Norstrand Reinhold Company Ltd., 1973.

[90] Gnilke W. *Lebensdauerberechnung der Maschinenelemente*, VEB Verlag Technik Berlin, 1980.

[91] Hertzberg R.W., Manson J.A. *Fatigue of Engineering Plastics*, New York London Academic Press, 1980, p.41.

[92] Frost N.E.M, Marsh V.J., Pook L.P. *Metal Fatigue*, Clarendon Press, Oxford, 1974.

[93] Yokobori T. *An interdisciplinary approach to fracture and strength of solids*, Wolters-Noordhoff Scientific Publications Ltd. Groningen, 1968, p.249.

[94] Schott G. *Werkstoffermüdung*, VEB Deutscher Verlag für Grundstoffindustrie, Leipzig, 1985, p.87.

[95] Tillmann W., Reul H., Herold M., Bruss K.-H., VanGilse J. In-vitro wall shear measurements at aortic valve prostheses. *J. Biomechanics*, 1984, Vol.17, No.4, pp.263-279.

[96] Giersiepen M., Krause U., Knott E., Reul H., Rau G. Velocity and shear stress distribution downstream of mechanical heart valves in pulsatile flow. *Int. J. of Artif. Organs*, 1989, Vol.12, No.4, pp.261-269.

[97] Billington F.W. Coaxial cylinder viscometer for use under oscillatory and transient conditions. *J. Sci. Instrum.*, 1965, Vol.42, p.669.

[98] Copley A.L., King R.G., Chien S., Usami S., Skalak R., Huang C.R. Microscopic observations of viscoelasticity of human blood in steady and oscillatory shear. *Biorheology*, 1975, Vol.12, pp.257-263.

[99] Andereck C.D., Liu S.S., Swinney H.L. Flow regimes in a circular Couette system with independently rotating cylinders. *J. Fluid Mech.*, 1986, Vol.164, pp.155-183.

[100] Bowman F. *Introduction to Bessel Functions*, Longmans, Green and Co. Ltd., 1938.

[101] McLachlan N.W. *Bessel Functions for Engineers*, Clarondon Press, Oxford, 1955.

[102] Cokelet G.R. The rheology and tube flow of blood. In *Handbook of Bioengineering*. R.Skalak, S.Chien (eds.), McGraw-Hill Book Company, 1987, p.63.

[103] Mockros L.F., Leonhard R. Compact cross-flow tubular oxygenators. *Trans. ASAIO*, Vol.31, 1985.

[104] Johnson R., Wichern D. *Applied Multivariate Statistical Methods*. Second Edition, Prentice Hall, 1988.

[105] Kneschke A. *Differentialgleichungen und Randwertprobleme. Bd.3: Anwendungen der Differentialgleichungen*. B.G. Teubner Verlagsgesellschaft, Leipzig, 1968, pp.133-135.

[106] Hirsch C. *Numerical Computation of Internal and External Flows*. J. Wiley & Sons, New York, 1988.

[107] Panton R.L. *Incompressible Flow*. J. Wiley & Sons, New York, 1984, p.711.

[108] Launder B.E., Spalding D.B. *Mathematical Models of Turbulence.* Academic Press, 1972.

[109] Reynolds A.J. *Turbulent Flows in Engineering.* J. Wiley & Sons, London, 1974.

[110] Schönung B.E. *Numerische Strömungsmechanik - Inkompressible Strömungen mit komplexen Berandungen.* Springer-Verlag, Berlin, 1990.

[111] Krain H., Hoffmann W. Verification of an Impeller Design by Laser Measurements and 3D Viscous Flow Calculations. *ASME Paper 89-GT-159,* presented at the Gas Turbine and Aeroengine Congress and Exhibition, June 4-8, 1989, Toronto, Ontario, Canada.

[112] Thomas M.E. The development of an efficient turbomachinery CFD analysis procedure. *AIAA Joint Propulsion Conference,* Monterey, CA, July, 1989.

[113] *TASCflow - User Documentation,* Internal Report, Adv. Sc. Computing Ltd., 1994.

[114] Raithby G.D. Skew Upstream Differencing Schemes for problems involving fluid flow. *Comp. Meth. Appl. Mech. Eng.,* 1976, Vol.9, pp.153-164.

[115] Scheider G.E., Raw M.J. A Skewed Positive Influence Coefficient Upwinding Procedure for Control-Volume Based Finite-Element convection-diffusion computation. *Numerical Heat Transfer,* 1986, Vol.8, pp.1-26.

[116] Hutchinson B.R., Raithby G.D. A Multigrid method based on the Additive Correction strategy. *Numerical Heat Transfer,* 1986, Vol.9, pp.511-537.

[117] Schima H., Müller M.R., Papantonis D. et al. Minimization of hemolysis in centrifugal blood pumps : influence of different geometries. *The Int. J. of Artifical Organs* 1993, Vol.16, No.7, pp.521-529.

[118] Worster R.C., The flow in volutes and its effect on centrifugal pump performance. *Proc. Instn. Mech. Engrs.,* 1963, Vol.177, No.31, pp.843-875.

[119] Buxbaum O., *Betriebsfestigkeit,* 1988, Verlag Stahl-Eisen mbH, pp.11-26.